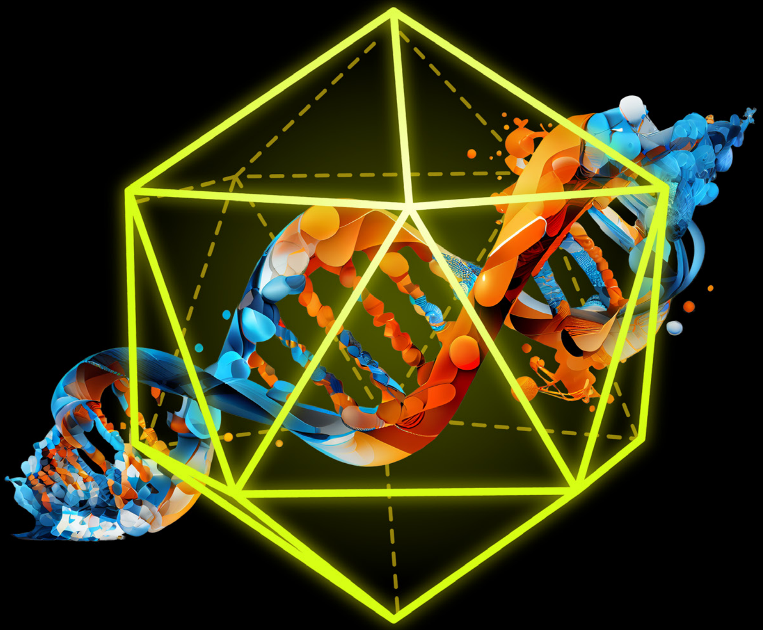

AAVs in Focus: Innovative Approaches to Guide Cutting-Edge Gene Therapy

Article Collection

Sponsored by SARTORIUS

WILEY Analytical Science

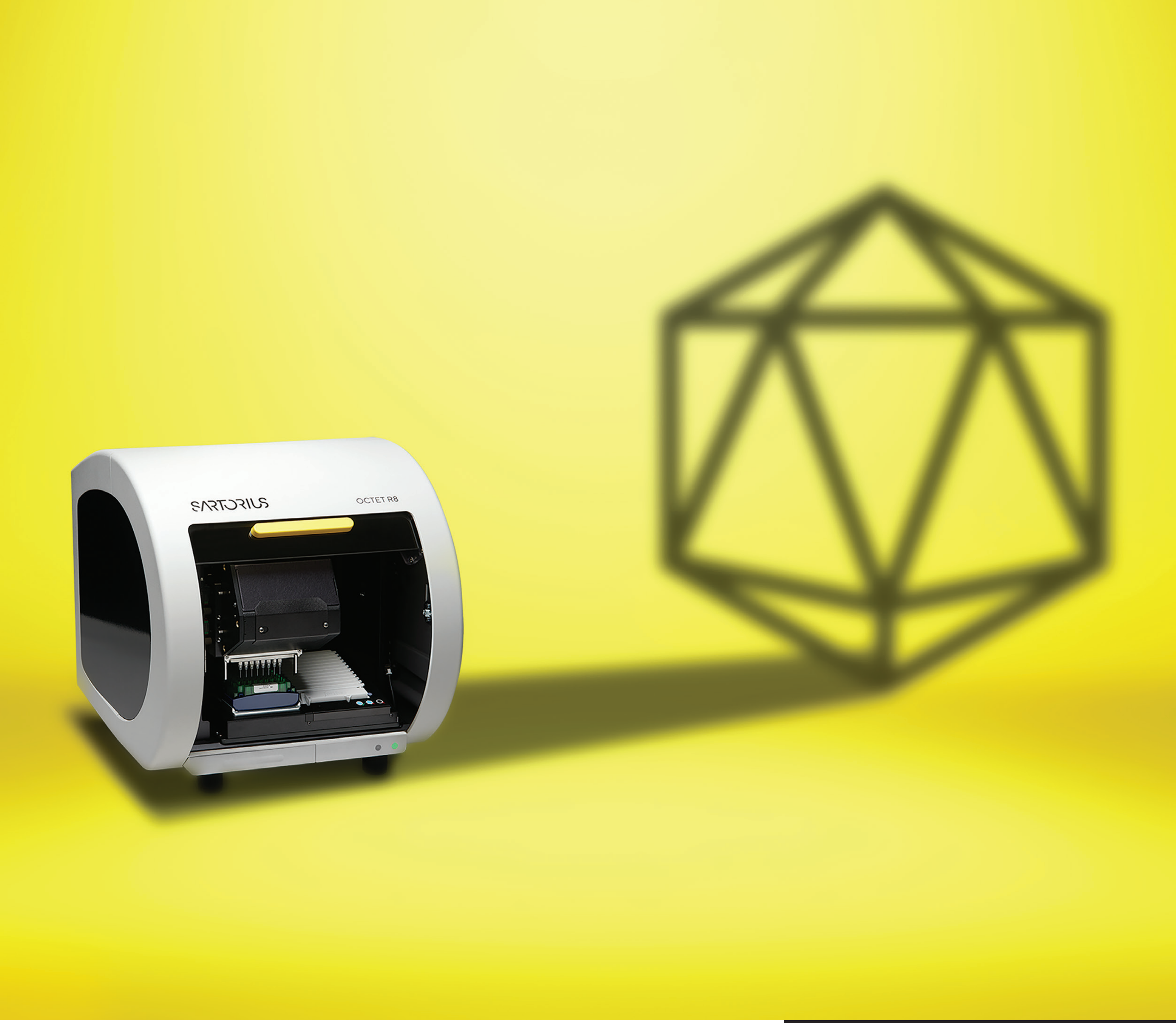
SARTORIUS
OCTET R8

Contents

Cover image © Sartorius

Introduction

Adeno-associated viruses (AAVs) have emerged as pivotal tools in gene therapy due to their ability to deliver genetic material safely and efficiently. This article collection delves into the latest research and applications of AAVs, highlighting advancements in production, characterization, and purification processes. By examining these studies, we aim to provide a comprehensive overview of the current status and future prospects of AAV technology in therapeutic applications.

This article collection begins with a comprehensive review of the current research status and applications of AAVs. Xia *et al.* summarizes the advancements and challenges faced in the field [1], providing a valuable resource for researchers looking to stay updated on the latest developments in AAV technology.

Next, Thomas *et al.* presents a study on the reversible shielding and immobilization of liposomes and viral vectors by tailored antibody-ligand interactions [2]. This research introduces innovative methods to enhance the stability and delivery efficiency of AAVs through reversible shielding techniques, which have significant implications for improving therapeutic outcomes.

Following this, Wang *et al.* reports on the transcriptomic features that reveal molecular signatures associated with recombinant AAV production in HEK293 cells [3]. This study provides valuable insights into the genetic and molecular mechanisms underlying AAV production, offering potential strategies for optimizing yield and quality.

In addition, Pistek *et al.* offers a comprehensive mRNA-sequencing-based characterization of three HEK-293 cell lines during an rAAV production process for gene therapy applications [4]. This research highlights the differences in gene expression profiles among the cell lines, contributing to a better understanding of the factors influencing AAV production and stability.

Finally, Meierrieks *et al.* introduces a novel and simplified anion exchange flow-through polishing approach for the separation of full from empty AAV capsids [5]. This innovative technique promises to enhance the purity and efficacy of AAV preparations, which is crucial for clinical applications.

Overall, this collection provides a detailed examination of the latest methodologies and technologies in AAV research. Through the innovative approaches and applications presented in this article collection, we hope to educate researchers on new technologies and techniques about AAVs. To gain a deeper understanding of available options for improving your research, we encourage you to explore the Octet® Biolayer Interferometry (BLI) technology from Sartorius, designed to streamline and optimize your AAV research and production processes. Visit the Sartorius website to learn more.

Dr. Christene A. Smith
Editor at Wiley

References

[1] Xia, K. *et al.* (2025). Research Status and Applications of Adeno-Associated Virus. *ChemBioChem.* https://chemistry-europe.onlinelibrary.wiley.com/doi/10.1002/cbic.202400856.

[2] Thomas, O.S. *et al.* (2022). Reversible Shielding and Immobilization of Liposomes and Viral Vectors by Tailored Antibody-Ligand Interactions. *Small.* https://doi.org/10.1002/smll.202105157.

[3] Wang, Y. *et al.* (2023). Transcriptomic features reveal molecular signatures associated with recombinant adeno-associated virus production in HEK293 cells. *Biotechnology Progress.* https://aiche.onlinelibrary.wiley.com/doi/10.1002/btpr.3346.

[4] Pistek, M. *et al.* (2023). Comprehensive mRNA-sequencing-based characterization of three HEK-293 cell lines during an rAAV production process for gene therapy applications. *Biotechnology Journal.* https://doi.org/10.1002/biot.202200513.

[5] Meierrieks, F. *et al.* (2024). A Novel and Simplified Anion Exchange Flow-Through Polishing Approach for the Separation of Full From Empty Adeno-Associated Virus Capsids. *Biotechnology Journal.* https://doi.org/10.1002/biot.202400430.

ChemBioChem
Review
doi.org/10.1002/cbic.202400856
Chemistry Europe
European Chemical Societies Publishing
www.chembiochem.org

Research Status and Applications of Adeno-Associated Virus

Ke Xia,[a] Shuangling Liu,[a] Zhenkun Wu,*[a] and Jian-Hui Jiang*[a]

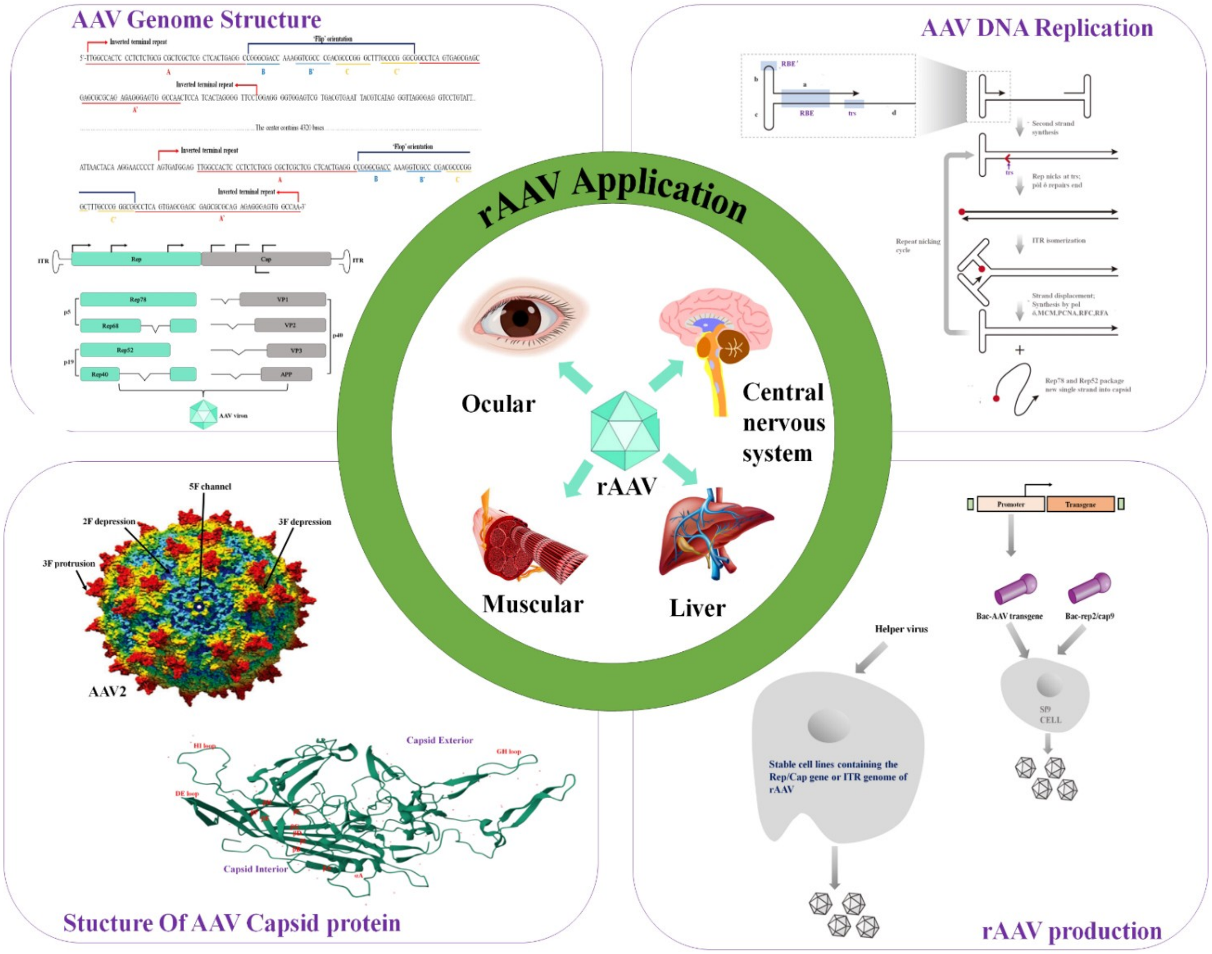

ChemBioChem
Review
doi.org/10.1002/cbic.202400856
Chemistry Europe
European Chemical Societies Publishing

Adeno-associated virus (AAV) has emerged as a powerful and effective tool for the delivery of exogenous genes into various cells or tissues. To improve the gene delivery efficiency, as well as the safety and specificity of AAV's cell-targeting capabilities, extensive investigations have been conducted into its molecular biological characteristics, including capsid structure, cellular tropism, and the mechanisms underlying its entry, replication, DNA packaging, and capsid assembly. Significant differences exist between human and non-human primate AAVs regarding tissue targeting and transduction efficiency. These differences are primarily attributed to the amino acid sequences of AAV capsid proteins, the structural characteristics of these proteins, and the interactions of AAV with surface factors on host cells, such as cell surface receptors, signaling molecules, and associated proteins. This review primarily focuses on several key aspects of AAV, including its genome, coat proteins and their structures, genome replication, virus assembly, and the role of helper viruses. Additionally, it examines the utilization of recombinant adeno-associated viruses (rAAV), detailing their production methods, mechanisms of cell entry and trafficking, and various serotypes. The review further interprets the role of rAAV by analyzing its current applications in research and therapy.

1. Introduction

AAV first discovered in the 1960s, is a non-enveloped, single-stranded DNA virus.[1] Thirteen distinct serotypes of AAV, designated AAV1 to AAV13, have been identified in human and nonhuman primate tissues.[2–12] These viruses share a common genomic structure consisting of an approximately 4.7 kb single-stranded DNA molecule that contains two open reading frames (ORFs): rep and cap. The rep ORF encodes four overlapping proteins that are essential for viral replication and DNA packaging, namely Rep78, Rep68, Rep52, and Rep40. The cap ORF encodes three capsid proteins through the use of two alternatively spliced mRNAs. One of these mRNAs retains the complete cap coding region, which encodes the VP1 protein, while the other mRNAs are derived from distinct start codons. Specifically, one mRNA initiates translation at the ACG start codon to produce VP2, and another mRNA begins translation at a downstream ATG start codon to produce VP3.[13]

AAV can be transmitted either as an integrated provirus or through lysogenic infectious viruses.[14–15] Generally, AAV requires the assistance of helper viruses, such as adenoviruses and herpesviruses, for its replication.[16] AAV is capable of crossing the nuclear membrane to enter the nucleus, where it sheds its coat protein and exists as naked linear single-stranded DNA. Subsequently, AAV integrates its DNA into a specific locus on chromosome 19 in human cells, known as AAVS1,[17] thereby establishing a latent infection.[18–19] AAV has the capacity to remain latent within mammalian cells for extended periods. During this latent phase, the integrated viral genome can be reactivated through reinfection with a helper virus, which triggers the production of viral particles. This ability to integrate and maintain latency is a key feature of AAV's lifecycle and contributes to its potential as a therapeutic vector in gene therapy applications.[15]

In this review, we examine the AAV through a comprehensive analysis of its genome, capsid protein structure, DNA replication, and viral packaging mechanisms. This understanding serves as a basis for discussing the manufacturing and production processes of rAAV, as well as the mechanisms by which they enter host cells. Furthermore, we explore the affinity of rAAV for cell surface receptors to elucidate the prevailing trends in AAV modification within the field.

2. Adeno-Associated Virus

AAV is a non-enveloped, single-stranded DNA virus classified within the Parvoviridae family. It features an icosahedral capsid composed of proteins, with an approximately diameter of 26 nm and contains single-stranded DNA that is approximately 4.7 kilobases in length[1] (Figure 1A).

2.1. Genome

Based on the previous reports, the full length of single-stranded genome of the wild-type adeno-associated virus AAV2 consists of 4,675 nucleotides.[13] This genome includes two open reading frames (ORFs): the Rep region (nucleotides 146–2,116) and the Cap region (nucleotides 2,117–4,530). Additionally, there are ITR sequences of 145 nucleotides at both ends (nucleotides 1–145 and 4,531–4,675). Notably, the first 125 nucleotides (nucleotides 1–43 and 83–125) of the two strands are complementary in reverse orientation, forming a palindromic sequence (Figure 1B).[13,20] The ITR sequence serves as the initiation point for viral gene replication and signals the packaging of the viral particles.[21–23] The Rep region encodes four nonstructural proteins,[20] classified based on their relative molecular masses as Rep78, Rep68, Rep52, and Rep40. These proteins are primarily involved in the replication of viral genes[24] and the regulation of viral gene expression.[25] The four Rep proteins are translated from transcripts synthesized from the p5 and p19 promoters, with Rep78 and Rep68 derived from the p5 promoter, and Rep52 and Rep40 originating from the p19 promoter.[13,26]

The Cap region of the wild-type AAV genome contains three genes encoding the coat proteins VP1, VP2, and VP3. These

---

[a] *K. Xia, S. Liu, Z. Wu, J.-H. Jiang*
State Key Laboratory of Chemo/Bio-Sensing and Chemometrics, College of Chemistry and Chemical Engineering, Affiliated Hospital of Hunan university, School of Biomedical Sciences
Hunan University
Changsha, Hunan 410082, China
E-mail: tomwu@hnu.edu.cn
jianhuijiang@hnu.edu.cn

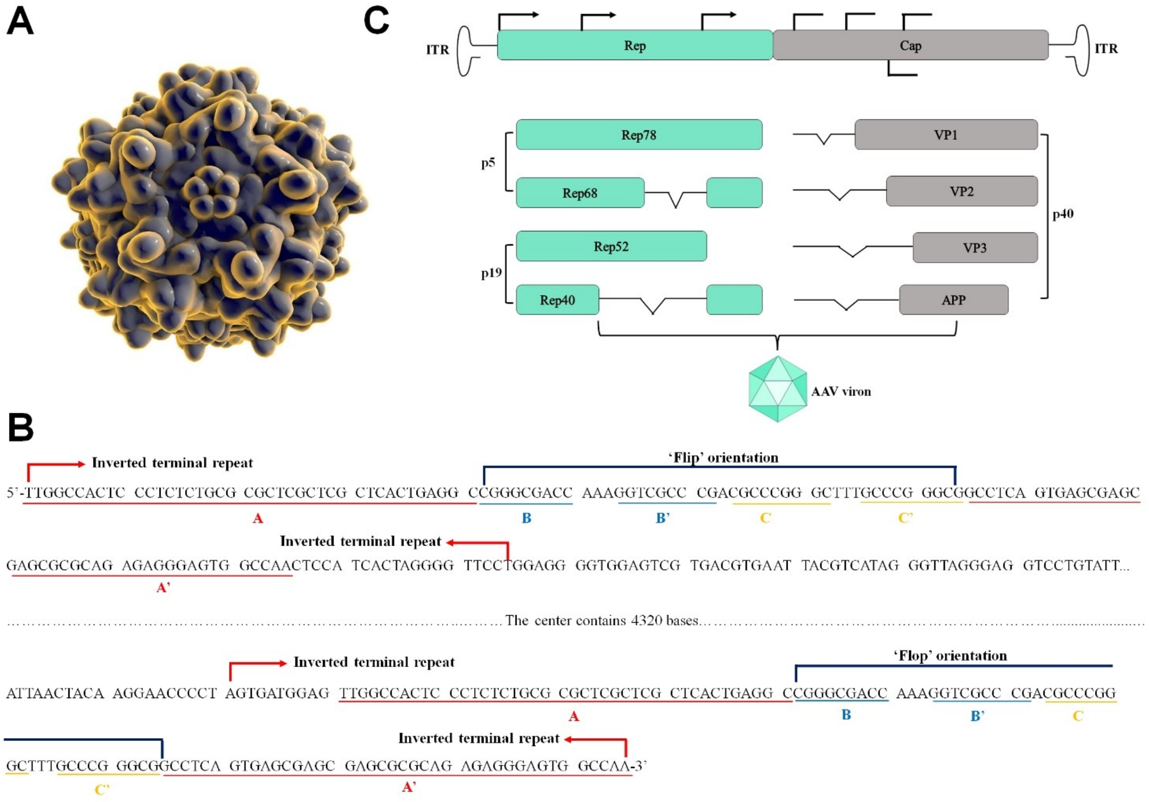

Figure 1. Adeno-associated virus and its genetic structure. (A) The adeno-associated virus is depicted as an icosahedron, with the graphical representation sourced from the Protein Data Bank. (B) The nucleotide sequences of the inverted terminal repeats (ITRs) in AAV2 DNA. (C) A schematic representation of the AAV genome.

proteins are generated through selective splicing of the mRNAs and differential translation initiated by specific start codons.[27–28]

The coat of wild-type AAV is composed of 60 coat protein monomers, with a typical copy number ratio of approximately

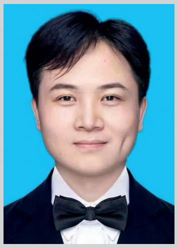

Dr. Ke Xia obtained his PhD degree in 2022 from Hunan University. Currently, he works at Hunan University. His research fields involve the application of adeno-associated viruses in gene-targeted delivery for tumor diagnosis and treatment.

Prof. Zhenkun Wu is currently an associate professor of State Key Laboratory of Chemo/Bio-Sensing and Chemometrics; College of Chemistry & Chemical Engineering at Hunan University. His research interests include the development of nucleic acids-based molecular recognition and chemical regulation strateiges.

Shuangling Liu is a graduate student of State Key Laboratory of Chemo/Bio-sensing and Chemometrics, College of Chemistry & Chemical Engineering at the Hunan University. Her research interests mainly focus on the engineering adeno-associated viruses for targeted gene delivery in vivo.

Prof. Jian-Hui Jiang is a professor of State Key Laboratory of Chemo/Bio-Sensing and Chemometrics; College of Chemistry & Chemical Engineering at Hunan University. He received his PhD degree from Hunan University in 1999. His group interests mianly include genetically programmed synthetic RNA and cells, chemically inducible gene expression and delivery platforms, as well as bioelectronic devices.

1:1:10 for VP1, VP2, and VP3.[27–29] However, the exact stoichiometry of these proteins remains unclear. One study has indicated that within a single AAV1 particle, there may be between 0 and 2 copies of VP1, 8 to 11 copies of VP2, and 48 to 51 copies of VP3. This suggests that the assembly of AAV coat proteins does not adhere to a fixed ratio but occurs in a stochastic manner that is influenced by the relative expression levels of these proteins.[30] Additionally, the Cap region of the wild-type AAV genome contains a third open reading frame (ORF) that features a selective splice site distinct from those of VP1, VP2, and VP3. This ORF encodes the assembly activating protein (AAP), which plays a critical role in facilitating the assembly of viral particles (Figure 1C).[31–32]

2.2. Capsid Protein

Among the various subtypes of AAV, the VP3 protein is predominantly located on the surface of the viral capsid, where it forms a pore with a fivefold symmetry axis. This structural feature is essential for the packaging of viral DNA and for the externalization of the N-termini of the VP1 and VP2 proteins during viral assembly. Moreover, VP3 functions as a cell adhesion factor, interacting with specific receptors on cell membranes, such as polysaccharides and the AAV receptor (AAVR), thereby mediating the adsorption and internalization of viral particles.[33–34] Additionally, both VP1 and VP2 proteins possess a cluster of three basic residues at their N-termini, which confer nuclear localization properties. This feature enhances the transduction of viral particles into the nucleus, thereby facilitating the subsequent stages of the viral life cycle.[35–36]

Taking AAV2 as a representative example, the relative molecular mass of the coat protein VP3 is approximately 61 kDa, accounting for about 90% of the total coat protein composition. In comparison, the relative molecular masses of VP1 and VP2 are 87 kDa and 73 kDa, respectively. The N-terminal sequence specific to VP1 comprises 137 amino acids and includes the PLA2 phospholipase region.[5,37] The N-terminal segment of VP2 consists of 65 amino acids that overlap with the VP1 sequence (amino acids 138–202), with both proteins featuring conserved nuclear localization sequences (NLS). This observation suggests that the N-terminus of VP1 is characterized by a distinct sequence of 137 amino acids.[20]

The region unique to VP1 (VP1u) contains a structural domain related to phospholipase A2[35] and an additional structural domain that interacts with GPR108, a significant host factor for multiple serotypes.[38] The N-terminal segment of VP3 includes 15 scrambled amino acid residues and is embedded within the coat structure. The VP proteins share a common C-terminus, and structural analyses have revealed that only the overlapping C-termini of the VPs (~520 amino acids) are observable, whereas the N-termini are likely not observed due to the predominance of VP3 and the fact that they may be buried within the interior of the coat.[34]

In our analysis, we classified tyrosine and glycine as neutral amino acids, capable of exhibiting either hydrophilic or hydrophobic characteristics. Based on this classification, we designated regions with four or more consecutive hydrophilic amino acids in blue and those with four or more hydrophobic amino acids in yellow. Notably, the regions spanning amino acids 401–520 and 561–600 exhibited a higher concentration of hydrophilic groups, containing binding sites for heparin proteoglycans (R588 and R585)[34] and an integrin recognition sequence (511-NGR-513)[39] (Figure 2).

2.2.1. Structure of Capsid Protein

The DNA sequences of VP1, VP2, and VP3 exhibit overlap within the Cap region, where the nucleotide sequences of all VP3 proteins are conserved. The structural topology of the VP3 region is highly conserved across AAV serotypes and other members of the genus Serratia. It features a core eight-stranded antiparallel β-barrel motif (βB-βI, based on the N- to C-terminal orientation of the VP3 structure) that forms a continuous capsid, in addition to an α-helix (αA) that is preserved among all known viral structures to date. Furthermore, the N-terminal segment, β-strand A, and other β-strands are also highly conserved among the various structures of AAVs and related viral entities.

The loops connecting the β-strands of the VP proteins are designated according to the strands they interlink. The most prominent loop is the GH-loop, encompassing nearly 230 amino acids, while the smallest loop is the FG-loop, which comprises only 2 to 3 amino acids[34] (Figure 3A).

AVV2-VP1 amino acid sequence（**4 or more consecutive hydrophobic amino acids - tan, hydrophilic amino acids labeled - blue**）
1-40：MAADGYLPDWLEDTLSEGIRQWWKLKPGPPPPKPAERHKD
41-80：DSRGLVLPGYKYLGPFNGLDKGEPVNEADAAALEHDKAYD
81-120：RQLDSGDNPYLKYNHADAEFQERLKEDTSFGGNLGRAVFQ
121-160：AKKRVLEPLGLVEEPVKTAPGKKRPVEHSPVEPDSSSGTG
PLA2 phospholipase region
161-200：KAGQQPARKRLNFGQTGDADSVPDPQPLGQPPAAPSGLGT
201-240：NTMATGSGAPMADNNEGADGVGNSSGNWHCDSTWMGDRVI
The nuclear localization sequence (NLS)
VP3 (Overlapping C-terminus of the VPs)
241-280：TTSTRTWALPTYNNHLYKQISSQSGASNDNHYFGYSTPWG
281-320：YFDFNRFHCHFSPRDWQRLINNNWGFRPKRLNFKLFNIQV
321-360：KEVTQNDGTTTIANNLTSTVQVFTDSEYQLPYVLGSAHQG
361-400：CLPPFPADVFMVPQYGYLTLNNGSQAVGRSSFYCLEYFPS
401-440：QMLRTGNNFTFSYTFEDVPFHSSYAHSQSLDRLMNPLIDQ
441-480：YLYYLSRTNTPSGTTTQSRLQFSQAGASDIRDQSRNWLPG
481-520：PCYRQQRVSKTSADNNNSEYSWTGATKYHLNGRDSLVNPG
521-560：PAMASHKDDEEKFFPQSGVLIFGKQGSEKTNVDIEKVMIT
561-600：DEEEIRTTNPVATEQYGSVSTNLQRGNRQAATADVNTQGV
601-640：LPGMVWQDRDVYLQGPIWAKIPHTDGHFHPSPLMGGFGLK
641-680：HPPPQILIKNTPVPANPSTTFSAAKFASFITQYSTGQVSV
681-720：EIEWELQKENSKRWNPEIQYTSNYNKSVNVDFTVDTNGVY
721-735：SEPRPIGTRYLTRNL

Figure 2. Amino acid sequence of AAV2. Four or more consecutive hydrophilic sequences were marked in blue and four or more consecutive hydrophobic sequences were marked in tan.

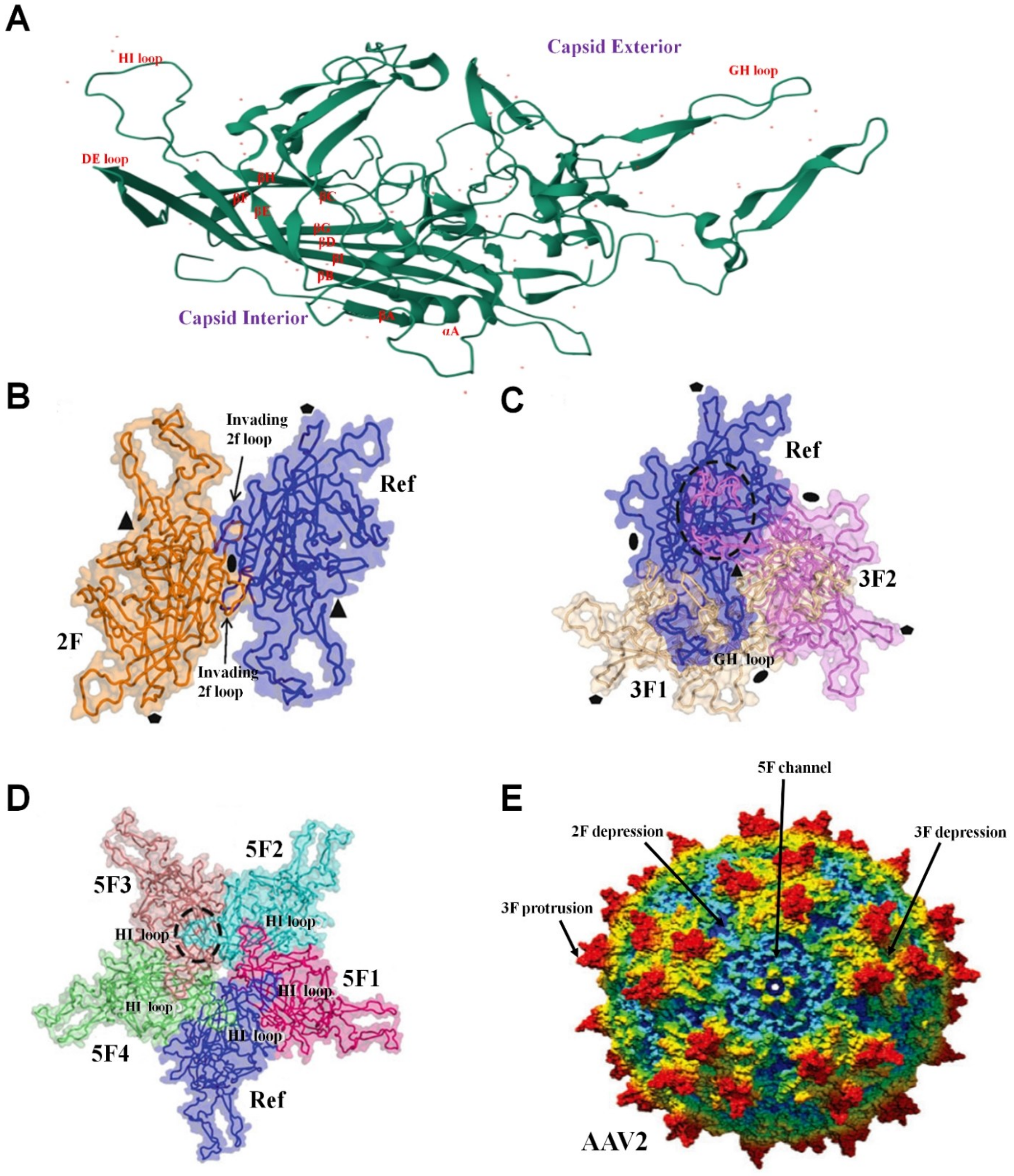

Figure 3. **(A)** The VP3 structure of AAV from the Protein Data Bank. (B–D) Coil diagrams of AAV2 VP3 presented in a transparent surface rendering, highlighting the interactions related to icosahedral symmetry. Specifically, these panels illustrate the twofold, threefold, and fivefold interactions, respectively. The reference monomers (Ref, blue), twofold-related monomers (2F, orange), threefold-related monomers (3F1 and 3F2, magenta and wheat, respectively), and fivefold-related monomers (5F1 to 5F4, red, cyan, brown, and green, respectively). Copyright 2011, Methods in Molecular Biology. (E) A view of the surface of the AAV capsid from a vantage point along the fivefold symmetry axis, with the central fivefold pore prominently displayed. This representation is a depth-cued space-filling model generated from the crystal structure of AAV2 using Chimera. Copyright 2014, Annual Review of Virology. The approximate locations of a twofold (2F) depression, threefold (3F) protrusion and depression, and a fivefold (5F) channel are indicated.

ChemBioChem
Review
doi.org/10.1002/cbic.202400856
Chemistry Europe
European Chemical Societies Publishing

14397633, 0

2.2.2. Two-Fold Symmetry Axes

The AAV capsids are composed of 60 copies of VP monomers, which interact through two-, three-, and fivefold symmetry-related interactions. A conserved sequence loop (amino acids 696–704) located at the C-terminus of the VPs extends into the loop region near the C-terminus of adjacent VP monomers, thereby creating a two-fold axial depression. In this region, the α-helix acts as the wall of the depression. This interaction area is characterized by its limited extent, being only one polypeptide chain thick, and is recognized as the thinnest and least buried region within the coat-symmetric interface[34] (Figure 3B).

2.2.3. Three-Fold Symmetry Axes

The most extensive interactions among the threefold-associated VP monomers involve amino acid residues located within the BC, EF, and GH loops. The GH loop intercalates to create a cusp-shaped protrusion that is offset from the threefold axes of the icosahedron. In contrast, the HI loop contributes significantly to the interactions between VP3 monomers associated with icosahedral pentafold symmetry (Figure 3C).[34]

2.2.4. Five-Fold Symmetry Axes

Interactions at the fivefold symmetry axes are established by the regions of the β-B, I, D, and G sheets, along with the ordered N-terminal residues of adjacent monomers. These interactions give rise to a cylindrical channel formed by the DE-loop, which serves as a conduit connecting the interior and exterior of the capsid. The N-terminal sequences of VP1, specifically the PLA2 and NLS motifs, are positioned at the base of this channel. Meanwhile, the β-A, B, I, D, and G chains constitute the inner surface of the capsid, while the loops are intercalated between the β chains, contributing to the formation of the outer surface of the capsid (Figure 3D).[34]

As previously described, it can be inferred that the coat of AAV comprises 12 pentagonal surfaces, corresponding to 12 fivefold symmetry axes. Each of these fivefold symmetry axes contains a channel, suggesting a potential connectivity between the channels of two symmetrically related fivefold axes. This connectivity may facilitate the injection of subsequent viral genes into the capsid protein. Additionally, the AAV capsid features 20 threefold symmetry axes, each characterized by three protrusions. These protrusions are primarily associated with the recognition of target cell receptors, as they are elevated relative to other subunits and are likely to be the first structures to interact with the cell surface (Figure 3E).

2.3. Replication

AAV DNA replication occurs via the rolling hairpin mechanism. In 2008, Nash, Chen, and colleagues successfully reconstituted AAV replication in vitro using purified components.[40] This DNA replication

process necessitates several factors, including the AAV-encoded Rep78 or Rep68 proteins, replication factor C (RFC), cellular DNA polymerase δ along with its accessory proteins, proliferating cell nuclear antigen (PCNA), the micro-chromosome maintenance complex (MCM), and single-stranded binding proteins.[41–42] Rep78 and Rep68 play crucial roles by binding to the Rep-binding element

(RBE) located in the terminal reverse sequence and the RBE′ in the 5′ end palindrome sequence, thereby facilitating viral DNA replication.[41] The cellular DNA polymerase δ complex not only promotes the continued synthesis of DNA strands but also possesses 3′-5′ exonuclease activity.[43] PCNA serves as a processing factor for cellular DNA replication, recruiting various protein factors to assemble on chromatin for the replication process,[44] Conversely, RFC acts as an auxiliary to PCNA, regulating the DNA replication protein complex by assisting in the loading and unloading of chromatin structures.[45] The MCM complex functions as a cellular DNA helicase, unwinding the double helix during DNA replication.[46] Single-stranded binding proteins play a critical role in stabilizing newly formed single-stranded DNA, preventing it from re-annealing into double-stranded DNA or being degraded by nucleases.[47] These proteins can either be replication protein A (RPA) from the host cell or encoded by helper viruses. Notably, the expression of adenovirus DNA-binding protein (DBP) has been shown to have minimal impact on AAV DNA replication.[48] This finding suggests that AAV replication primarily relies on cellular proteins as well as those encoded by its own genes (Figure 4A).

2.4. Packaging

The newly synthesized AAV coat proteins can exist as empty coat particles, facilitating the encapsulation of newly synthesized DNA into pre-assembled coats.[49] The AAV capsid exhibits an icosahedral geometry characterized by 12 pentagons, corresponding to 12 fivefold axes of symmetry. Each fivefold axis of symmetry features a small pore with a diameter of approximately 0.85 nm, which is widely recognized as the entry point for AAV DNA into the capsid (Figure 3E).[50] Concurrently, the Rep proteins (Rep78, Rep68, Rep52, and Rep40) engage in interactions with one another, exhibiting a particularly stable association with the capsid proteins (VPs) that precede coat assembly. Dubielzig et al. propose that Rep78 and Rep68 bind to the Rep-binding element (RBE) within the inverted terminal repeat (ITR) sequence at the 5′ end. They utilize the energy generated by the deconvolution of Rep52 and Rep40 to facilitate the packaging of DNA into the capsid in a 3′-5′ direction (Figure 4B).[51] In

this process, the Rep proteins are transcriptionally produced and subsequently bind to the newly replicated viral DNA. The interaction between the Rep proteins and the VPs enables the injection of the newly synthesized DNA into the empty capsid, employing the impetus derived from the deconvolution of Rep52 and Rep40 to assemble a new AAV viral particle.

ChemBioChem

Review
doi.org/10.1002/cbic.202400856

Chemistry Europe
European Chemical Societies Publishing

14397633, 0

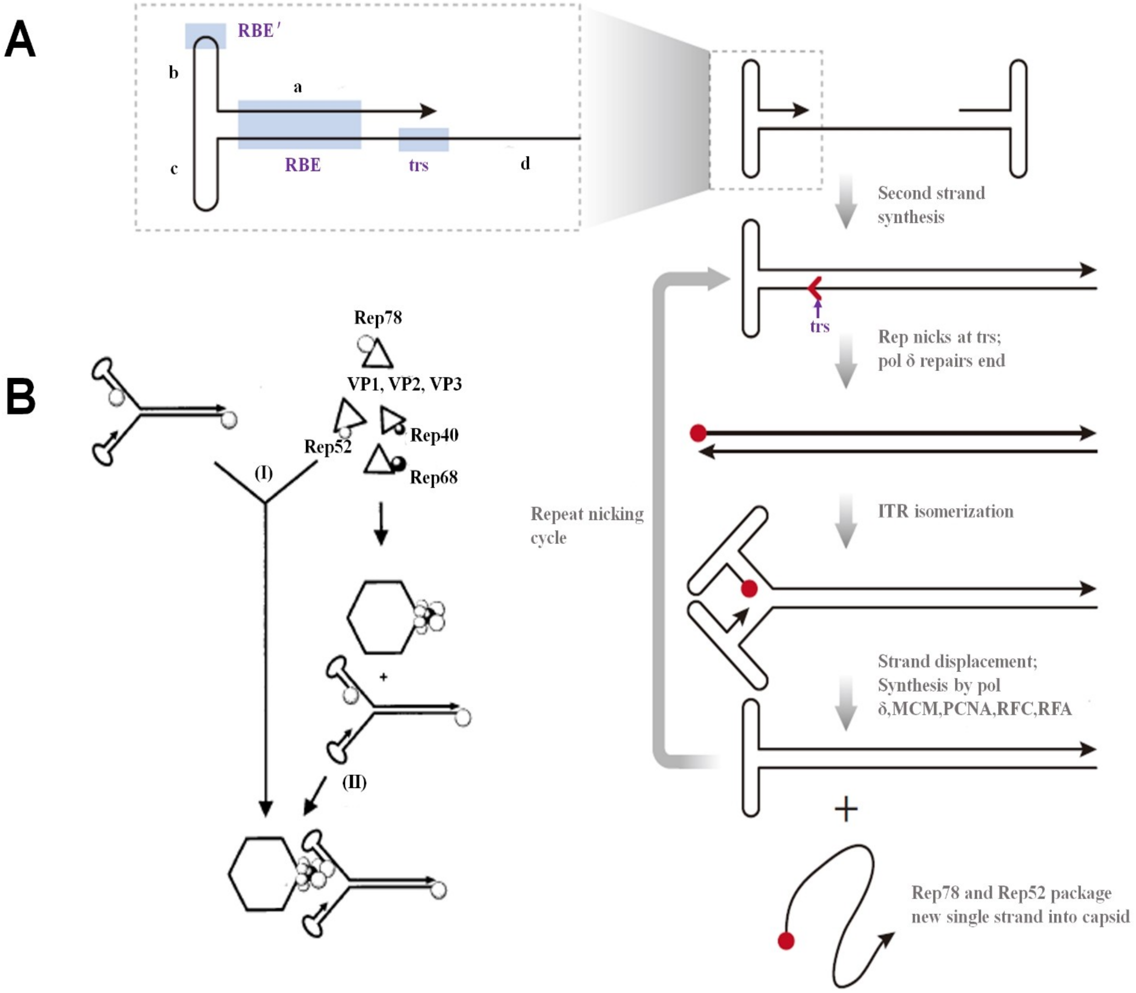

Figure 4. (A) ITR of AAV is comprised of two small palindromic sequences (b and c) that are flanked by a larger palindromic sequence (a) and an additional 20-base pair sequence (d), which is repeated at both termini. Copyright 2014, Annual Review of Virology. (B) A working hypothesis regarding the specific binding of AAV2 DNA to capsids is derived from the interactions observed within Rep-capsid complexes. Copyright 1999, Journal of Virology.

2.5. Helper Virus Function

AAV is classified within the family of replication-deficient Parvoviridae, characterized by its genomic DNA that relies on helper viruses (such as adenoviruses and herpesviruses) for efficient transcription. The paracrine functions of adenoviruses on AAV have been identified through several viral proteins, including E1a, E1b, E4orf6, the single-stranded DNA binding protein (DBP), and VA (viral-associated) RNA, as well as E2a. Notably, both E1a and DBP function as transcriptional activators, facilitating transcription from AAV's p5 promoter.[52–54] In instances of adenoviral co-infection, the Rep78/68 proteins can activate the three AAV promoters (p5, p19, p40), resulting in a transcriptional activation rate of up to 450-fold.[55–57] E1a induces host cells to enter the S phase of the cell cycle,[58] while E1b and E4 promote the maturation and cytoplasmic translocation of AAV mRNAs.[59] Additionally, E1b and E4 facilitate the degradation of Mer11, thus inhibiting the progression of cells through the G2/M phase, leading to extended retention in the S phase.[60–61] This coordinated action enhances the expression levels of enzymes involved in DNA replication within the host cells. In the absence of adenoviral infection, Rep78/68 exerts an inhibitory effect on the p5 promoter, resulting in negligible expression of Rep and other viral proteins, thereby placing the viral genes in a latent state.[62] E4 alone enhances both viral DNA replication and the synthesis of viral proteins while simultaneously shutting down host cell protein synthesis, consequently promoting the production of infectious viral particles.[63] VA RNA, in conjunction with DBP, plays a regulatory role in the expression of viral proteins such as the viral capsid proteins (VPs) .[64] Furthermore, E2a is implicated in increasing the formation of AAV loop intermediates, which refer to the configuration of the AAV genome characterized by looped double-stranded DNA appendages within the nucleus.[48] These loop intermediates allow for prolonged residence of the AAV genome in the cytosol, thereby favoring sustained gene expression.[65] Overall, it can be concluded that the adjuvant role of adenoviruses primarily involves prolonging the presence of the AAV genome and functioning as transcription factors to enhance AAV gene expression, as well as facilitating the replication of the AAV genome, rather than determining the conditions necessary for these processes. The proteins required for AAV replication can be fully supplied by AAV's own transcription of Rep proteins and single-stranded binding proteins derived from host cells. The role of helper viruses is to enhance the replication of the AAV genome and increase its transcription. Specifically, helper viruses help alleviate the inhibitory effects of Rep78/68 proteins on the P5 promoter of the viral genes. This relief promotes the synthesis of Rep78 and Rep68 proteins, which in turn accelerates the production of new AAV particles. Ultimately, this synergistic interaction between AAV and helper viruses facilitates both the replication and assembly of new viral progeny.

3. Recombinant Adeno-Associated Virus

Recombinant adeno-associated virus(rAAV) is engineered based on the structure of wild-type AAV (wtAAV), sharing both the gene sequence and coat protein structure of the native virus. Specifically, the coding region of the wtAAV genome is substituted with the target DNA of interest, which must not exceed 5 kilobases (Kb).[66] This modification retains only the ITR sequence, which is crucial for both the replication of the viral genome and the packaging process of the recombinant adeno-associated virus. Additionally, other essential genes, including those encoding for Rep, Cap, and other proteins involved in viral packaging, are incorporated into separate plasmid vectors. This construction strategy offers the notable advantage of allowing the vector genome containing the ITR from one serotype to be packaged within the capsid of a different serotype, thereby producing a recombinant pseudotyped viral vector.[67]

3.1. Production

In the early stages of research, the inherent inefficiencies associated with plasmid transfection, coupled with suboptimal coordination and functionality of the rep and cap genes, resulted in low yields of wtAAV. Furthermore, the co-transfection of helper viruses, such as adenovirus, led to the production of a mixture containing both rAAV and adenovirus.[37,68] Due to the lack of effective methods for purging adenovirus from the resulting preparations, the rAAV produced during A significant breakthrough occurred when three independent research groups successfully cloned the genes of the helper virus onto a single plasmid, while simultaneously eliminating the replication and coat protein genes associated with the adenovirus. This innovation effectively rendered the resultant rAAV independent of adenoviral particles.[69–70] Following this advancement, three distinct methods for producing rAAV were gradually developed, each incorporating various improvements to enhance the efficiency and safety of rAAV production. rAAV is engineered based on the structure of wtAAV, sharing both the gene sequence and coat protein structure of the native virus. Specifically, the coding region of the wtAAV genome is substituted with the target DNA of interest, which must not exceed 5 kilobases (Kb).[66] This modification retains only the ITR sequence, which is crucial for both the replication of the viral genome and the packaging process of the recombinant adeno-associated virus. Additionally, other essential genes, including those encoding for Rep, Cap, and other proteins involved in viral packaging, are incorporated into separate plasmid vectors. This construction strategy offers the notable advantage of allowing the vector genome containing the ITR from one serotype to be packaged within the capsid of a different serotype, thereby producing a recombinant pseudotyped viral vector.[67]

3.1.1. Triple Plasmid Cotransfection

This system is comprised of a transfer plasmid, a Rep and Cap expression plasmid (commonly referred to as the Rep-Cap plasmid), and a helper plasmid. The packaging process entails the co-transfection of HEK293T packaging cells with three components: the transfer plasmid, which carries the gene of interest (GOI) along with the ITR sequences; the Rep-Cap plasmid, which expresses capsid proteins of a specific serotype; and the helper plasmid, which encodes adenoviral genes (specifically E2, E2 A, and VA) that facilitate the replication of AAV. These three components work together to generate complete AAV viral particles in the cell.[70] The advantages of this method are the rapid and easy production of recombinant viruses and the relatively low rate of viral vacuoles. The disadvantage is that the method was created based on adherent cells, GOI, the Rep-Cap plasmid expresses serotype-specific AAV coat proteins, and the helper plasmid expresses components that aid in so the transducing plasmid expresses the AAV genome containing the scaling up production in these cells can present challenges. To address this issue, a novel production method utilizing suspension-cultured 293 cells for triple plasmid co-transfection has been developed (Figure 5A).

3.1.2. Stabilized Cell Line Production

rAAV can be generated by establishing a stable cell line that expresses either the Rep/Cap genes or the ITR sequences of rAAV, followed by infection with a helper virus. This approach enables the production of rAAV on a clinical scale, as the cell

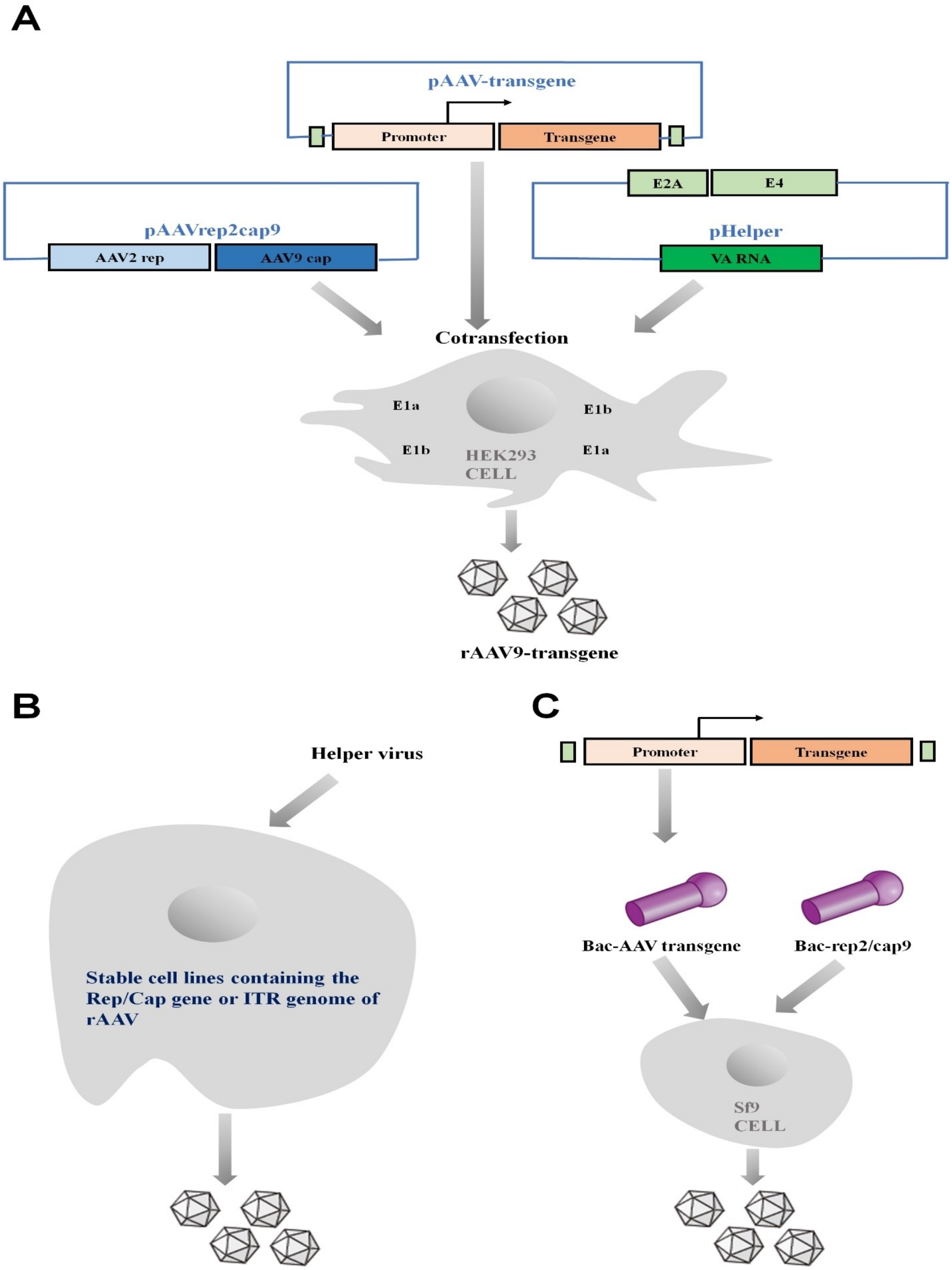

Figure 5. Schematic of rAAV production.(A) In the triple-plasmid method, HEK293 cells, which express adenovirus E1a and E1b, are cotransfected with an adenovirus helper plasmid (pHelper), a rep/cap plasmid that expresses AAV2 rep and AAV9 cap (pAAVrep2cap8), and a transgene plasmid that carries the rAAV-transgene cassette (pAAV-transgene). Copyright 2014 Annu. Rev. Virol (B) The stabilized cell line production method involves the establishment of a stable expression cell line containing either the Rep/Cap genes or the ITR genome of rAAV, followed by infection with a helper virus. (C) The viral infection method employs a baculovirus approach as an example. In this method, the rAAV-transgene cassette is integrated into a baculovirus, which is subsequently used to infect Sf9 insect cells. These cells are then coinfected with a second baculovirus that expresses rep2 and cap9, under the regulation of baculovirus promoters.

ChemBioChem

Review
doi.org/10.1002/cbic.202400856

Chemistry Europe
European Chemical Societies Publishing

14397633, 0

line can be cultured in suspension. However, the process of establishing and characterizing a stable cell line is time-consuming, and the stability of the cell line must be assessed over multiple passages. Additionally, it is crucial to ensure the complete inactivation of the helper virus during the subsequent purification of rAAV (see Figure 5B). In 2021, Joshi et al. reported the use of induced expression in an insect cell line as a novel method for producing rAAV, thereby expanding the potential avenues for rAAV production.[71]

3.1.3. Viral Infection

rAAV can be produced utilizing baculoviruses or recombinant herpes simplex viruses that contain the Rep/Cap genes and the rAAV genome. These viral vectors are employed to infect suspension-cultured insect or mammalian cells[72] (Figure 5C). This production method is particularly advantageous for large-scale industrial production, as well as for generating clinical-grade rAAV, thereby facilitating its application in therapeutic contexts.

3.2. Cell Entry and Trafficking

For rAAV particles to successfully enter cells, they must first adsorb to the cell membrane surface before being internalized via endocytosis. The adsorption of viral particles is facilitated by specific surface sugars on the cell membrane, referred to as primary receptors, including heparan sulfate proteoglycans,[73] N-chain sialic acid[74] and O-chain sialic acid.[75–76] The mechanism of viral entry can vary among different AAV serotypes (see Table 1). AAVs that utilize cytophagy for cell entry can escape late endosomes due to pH changes within these compartments.[36] It is speculated that this phenomenon may be associated with the acidification of the environment resulting from the

accumulation of multiple lysosomes. Such conditions lead to the exposure of the phospholipase A2 (PLA2) structural domain of the VP1 protein through small pores along the five-fold axis of symmetry. This exposure disrupts the phospholipid bilayer of the endosomes, allowing rAAV to escape into the cytoplasm, whereupon the viral particles become exposed to the nuclear localization sequences of VP1 and VP2, facilitating their transport into the nucleus.[36,77] While escaping from the endosomes, the viral particles may be susceptible to degradation by the cellular protease system; however, this degradation occurs to a limited extent.[87] Although some studies suggest that coat proteins of AAV cleave before the virus enters the nucleus, it is now more widely accepted that AAV enters the nucleus in an intact form.[88] This intact entry is considered a rate-limiting factor in the nuclear transport of AAV. The nuclear localization sequences present in the coat proteins VP1 and VP2 bind to importin β proteins on the nuclear membrane, facilitating the transport of AAV through the nuclear pore and into the nucleus.[89] Once inside the nucleus, AAV traverses the nuclear plasma and quickly reaches the nucleolus, where it interacts with nucleophosmin[90] and nucleolin[91] proteins. Although the precise functions of the nucleolus remain somewhat elusive, it is speculated that this interaction may be related to the shedding of coat proteins by AAV and the subsequent release of viral genes.

The viral genome then faces two potential pathways: one involves the synthesis of double-stranded DNA which has been described as a rate-limiting factor in transduction, using the hairpin structure of the inverted terminal repeat (ITR) as a

Table 1. Receptor types for AAV.

Serotype	Primary receptor	Secondary receptor
AAV1	N-linked sialic acid	AAVR/GPR108/TM9SF2
AAV2	Heparan sulfate proteoglycan	AAVR/GPR108/TM9SF2/LamR/αVβ5 integrin/αVβ1 integrin/FGFR1/CD9/HGFR
AAV3	Heparan sulfate proteoglycan	AAVR/GPR108/LamR/FGFR1 c-MET/HGFR
AAV4	O-linked sialic acid	GPR108
AAV5	N-linked sialic acid	AAVR/PDGFR/TM9SF2
AAV6	Heparan sulfate proteoglycan N-linked sialic acid	AAVR/GPR108/TM9SF2/EGFR
AAV7	–	GPR108/TM9SF2
AAV8	–	AAVR/GPR108/TM9SF2/LamR
AAVrh.8	–	GPR108
AAV9	Terminal N-linked galactose of SIA	AAVR/GPR108/TM9SF2/LamR
AAV10	–	–
AAVrh.10	–	GPR108/LamR
AAV11	–	–
AAV12	–	–
AAVrh32.33	–	GPR108

Date compiled from Refs. [1,11,34,38,78–86].

doi.org/10.1002/cbic.202400856

primer, ultimately resulting in the formation of a free-state gene in the form of dimers or multimers;[92–93] the other pathway involves the integration of the viral genome into the host cell's chromosome[17,94](Figure 6).

3.3. Serotypes

Serotypes, also referred to as seroproteotypes, are defined immunologically based on the principle that the binding of an antigen to its specific antibody results in the formation of an "antigen-antibody" immune complex. This principle serves as a basis for identifying distinct antigens and, in this context, for distinguishing between various subspecies of AAV. The isolation and characterization of new serotypes represent a significant advancement in rAAV vector technology. Historically, only five AAV serotypes were recognized, with AAV2 being the most extensively studied in clinical applications. However, in 1998, Rutledge et al. identified that AAV6 differs from AAV1 by a mere 14 amino acids yet exhibits distinct properties in vivo.[2] Furthermore, Gao et al. isolated the new serotype AAV8, which demonstrated a transduction efficiency in mouse liver that is 10 to 100 times greater than that of AAV2. They also identified over 100 novel coat mutants in human and non-primate tissues.[3,9] As of now, 13primate serotypes (AAV1-13) have been documented,[2–12] By exchanging the coding regions of the capsids in helper plasmids or helper viruses, researchers can package the same cassette constructed with the inverted terminal repeats (ITRs) of AAV2 into any serotype capsid. This methodology enables the rapid testing of various serotypes, including AAV4 and AAV8.[95–97] Below is a summary of some serotypes categorized according to their affinity for human tissue cells(Table 2).

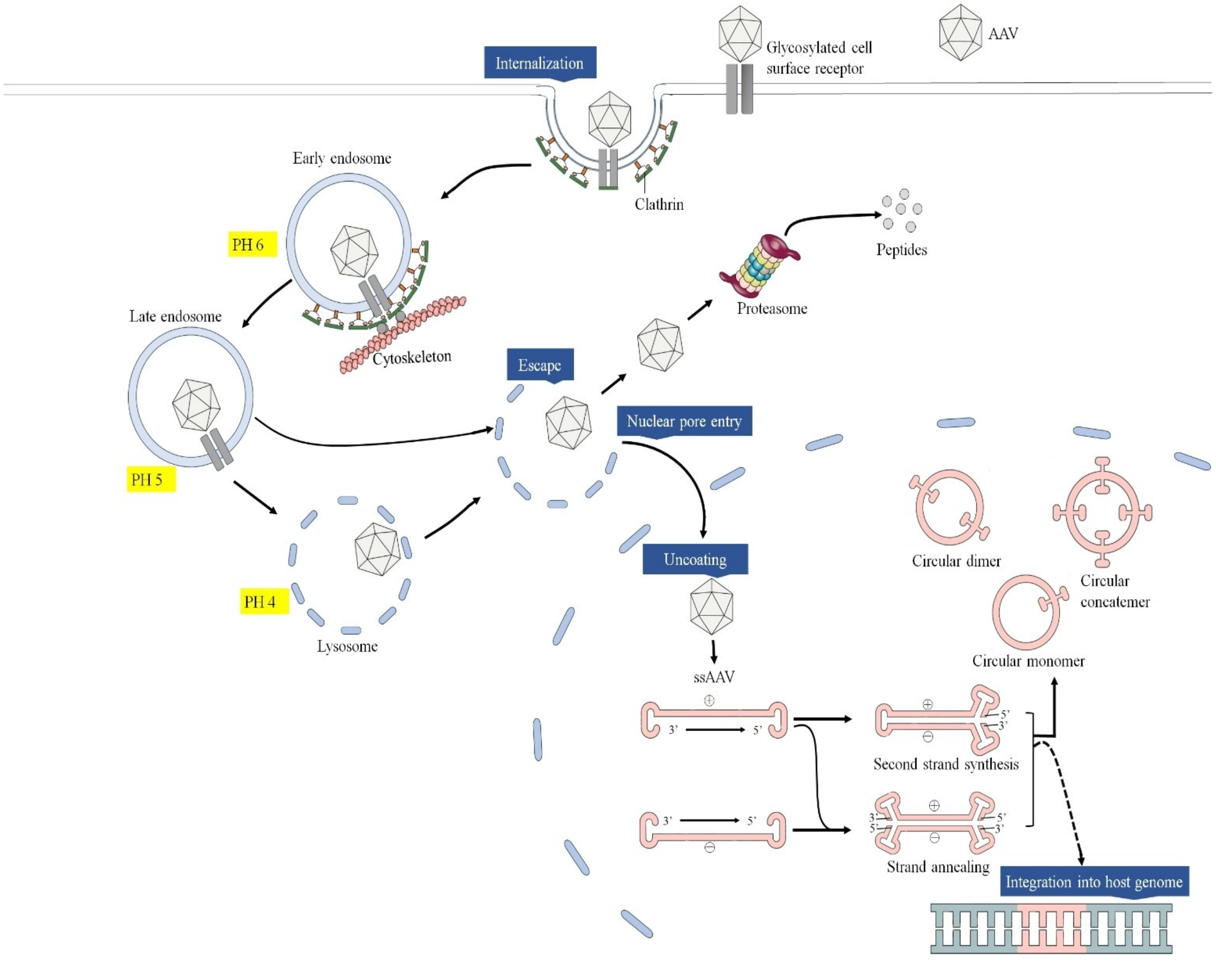

Figure 6. Schematic of rAAV transduction pathway. AAV is recognized by glycosylated receptors on the surface of host cells. This recognition initiates the internalization of the virus through clathrin-mediated endocytosis. Subsequently, AAV is transported through the cytosol with the assistance of the cytoskeletal network. Due to the relatively low pH environment within the endosome, the VP1/VP2 region of the virus undergoes a conformational change. Following the escape from the endosome, AAV is transported to the nucleus, where it undergoes uncoating. Additionally, AAV may be subjected to proteolysis by the proteasome.

ChemBioChem

Review
doi.org/10.1002/cbic.202400856

Chemistry Europe
European Chemical Societies Publishing

14397633, 0

Table 2. Serotypes and tissue affinities of adeno-associated viruses.

Tissue	Optimal Serotype
CHS	AAV1, AAV2, AAV3, AAV4, AAV5, AAV6, AAV7, AAV8, AAVrh.8, AAV9, AAVrh.10
Heart	AAV1, AAV4, AAV6, AAV8, AAV9, AAV10, AAVrh.10, AAV11
Kidney	AAV2, AAV4, AAV8, AAV9, AAV10, AAVrh.10, AAV11
Liver	AAV1, AAV2, AAV3, AAV5, AAV6, AAV7, AAV8, AAVrh.8, AAV9, AAV10, AAVrh.10
Lung	AAV1, AAV2, AAV4, AAV5, AAV6, AAV9, AAV10, AAVrh.10, AAV11
Pancreas	AAV1, AAV8, AAV9, AAVrh.10
Photoreceptor	AAV2, AAV5, AAV8
RPE (Retinal Pigment Epithelium)	AAV1, AAV2, AAV4, AAV5, AAV6, AAV7, AAV8, AAV9, AAVrh10,
Skeletal Muscle	AAV1, AAV6, AAV7, AAV8, AAV9, AAVrh.10, AAV11, AAV12
Uterus	AAV10
Testes	AAV9
Salivary glands	AAV12
stomach	AAV11
Spleen	AAV11
Airway	AAV6
Adipose tissue	AAV8
Joint	AAV2

Data compiled from Refs. [11,78–80,82–86,109–118].

3.4. Application

rAAV vectors offer significant advantages for gene therapy due to their low immunogenicity, minimal cytotoxicity, and efficient transduction capabilities, positioning them as one of the safest options available for gene therapy.

In the context of ocular diseases, rAAV has demonstrated promising therapeutic efficacy (Figure 7). For patients with Leber congenital amaurosis resulting from biallelic RPE65 mutations, subretinal injection of AAV2 vectors carrying the RPE65 cDNA has proven to be an effective treatment. Notably, after one year of therapy, patients exhibited significant improvements in visual acuity.[98] Similarly, in patients with retinitis pigmentosa caused by mutations in the RHO gene, subretinal injection of rAAV2 encoding vitelliform macular dystrophy 2 (VMD2)-hMERTK has shown favorable therapeutic outcomes. After one month of treatment, 50 % of these patients reported improved vision.[99] Furthermore, for individuals with Leber hereditary optic neuropathy due to mitochondrial DNA mutations, intravitreal injection of rAAV2-ND4 yielded excellent results in a cohort of nine patients, demonstrating safe and reliable efficacy, as confirmed by a subsequent 7-year follow-up study.[100] The safety and durability of this approach were further validated in a larger cohort of 142 additional patients.[101] In patients with achromatopsia resulting from biallelic pathogenic CNGA3 mutations, treatment with AAV8 vectors carrying CNGA3 also resulted in significant improvements in visual acuity after one year, with only mild side effects reported.[102] In the case of choroideremia patients with CHM gene mutations, subretinal injection of AAV2-REP1 has been shown to enhance retinal function in mouse models, and this efficacy was sustained for 3.5 years in clinical trials.[103] However, despite the widespread use of AAV vectors in treating ocular diseases and their established safety profile, challenges remain. For instance, in the case of X-linked retinitis pigmentosa, while the rAAV8 vector encoding a codon-optimizedversion of the human RPGR gene improved visual fields in mouse models, these outcomes were not replicated in clinical trials.[104] This discrepancy highlights the necessity for ongoing refinement and optimization of rAAV-based therapeutic approaches for various ocular disorders. Duchenne muscular dystrophy (DMD) is an X-linked recessive neuromuscular disorder characterized by progressive muscle weakness and atrophy resulting from the absence of dystrophin. Gene therapy represents an innovative approach for the treatment of DMD, with AAV emerging as one of the most prominent vectors due to its favorable safety profile and promising therapeutic outcomes. In a significant study published in 2018, Duan et al. demonstrated the efficacy of AAV in expressing micromyotrophic dystrophy proteins in a large animal model of DMD.[105] More recently, a clinical trial conducted in 2021 reported that 69 % of DMD patients in the high-dose treatment group exhibited positive dystrophin fiber expression (PF-06939926; NCT03362502).[106] The administration of AAV-expressing micromyotrophic dystrophy proteins has been shown to yield superior results and fewer side effects compared to conventional steroid therapies.[107] While some investigations have indicated that AAV therapy may lead to elevated levels of glutamyl transferase in DMD patients,[107] which could be attributed to the propensity of AAV to accumulate in the liver, this effect can be mitigated through concurrent steroid treatment. However, one significant limitation of this therapeutic strategy is the relatively large size of the gene encoding micromyotrophic dystrophy proteins, which approaches 11.5 Kb. This size exceeds the packaging capacity of AAV, which is approximately 4.5 Kb. Consequently, many researchers are focusing on expanding the capacity of AAV through homologous recombination strategies. In conclusion, AAV-mediated delivery of micro-dystrophin has demonstrated promising efficacy and a low toxicity profile in the treatment of DMD.[108]

In the central nervous system (CNS), the presence of the blood-brain barrier (BBB) poses significant challenges for the application of AAV gene therapies. Early design concepts focused on the targeted mutagenesis of exposed tyrosine residues on the surface of AAV coat proteins to enhance the transduction efficiency of AAV2 in the CNS.[119–120] These initial efforts were primarily serotype-specific, resulting in improved neuronal transduction in regions such as the hippocampus and striatum.[121] Subsequently, advances in understanding the original coat protein sequence led to the disruption of cell-binding sequences in the native coat proteins, which facilitated enhanced transduction of the CNS by serotypes AAV6,[122] AAV8,[123–124] and AAV9..[125] The study by Yao et al. in 2022

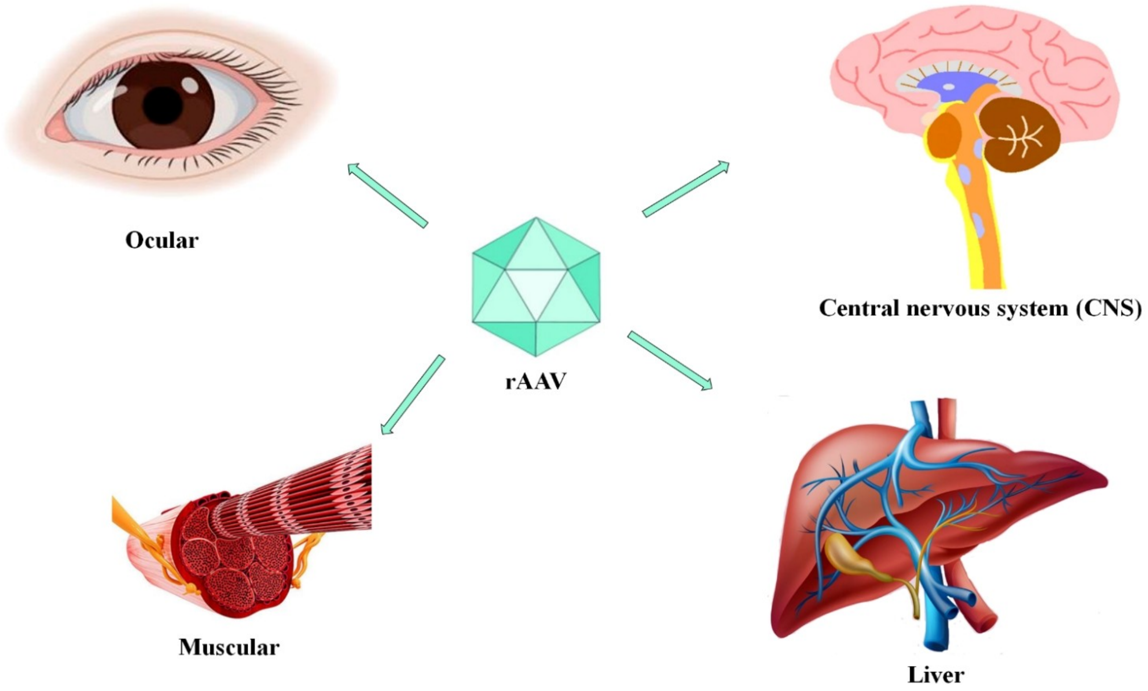

Figure 7. Current status of rAAV applications in four major organs: Ocular, Muscular, Central nervous system, and Liver.

highlights significant advancements in the modification of the AAV9 capsid protein to enhance its ability to cross the blood-brain barrier. By inserting specific peptides between amino acids Q588 and A589, they achieved a dramatic increase in transduction efficiency, with improvements noted in both mice and rhesus monkeys. This increased efficiency suggests potential for using these modified viruses in the treatment of neurological genetic disorders, offering new avenues for clinical application. The observed differences in transduction efficiencies between species also indicate that the mechanisms by which AAV9 crosses the blood-brain barrier may vary, prompting further research into species-specific applications and enhancements of AAV9 modifications. This research could pave the way for more effective gene therapies targeting the central nervous system.[126] While engineered capsids can significantly enhance the transduction efficiency of AAV, thereby improving the therapeutic potential of these viral vectors, studies have demonstrated an associated increase in immunogenicity following the transduction of human subjects with these modified capsids.[127–128] In 2016, Rosario et al. employed a specific combination of mutated surface tyrosine residues alongside a microglia-specific promoter (F4/80 or CD68) to successfully microenvironment within the CNS.[122] More recently, in 2024, Huang et al. engineered an AAV capsid, designated BI-Htfr1, which binds to the human transferrin receptor and is actively transported across human brain endothelial cells.[129] These developments have led to significant advancements in the field of CNS gene therapy using AAV vectors. These studies focus on the molecular characteristics of target cells and involve the modification of viral capsid proteins to enable the virus to achieve novel targeting capabilities. This indicates that it is feasible to design viral capsid proteins tailored to the molecular features of target cells, utilizing receptor-specific binding properties to facilitate the acquisition of new targets by the virus. However, the specific efficacy of these modified capsid proteins must be validated through more rigorous in vivo animal experiments.

The liver is the largest digestive organ in the human body and contains 10–15% of the total blood volume, positioning it as an ideal organ for the secretion of proteins into the circulation. Hemophilia A and B are coagulation disorders characterized by deficiencies in functional factor VIII (FVIII) and factor IX (FIX) protein expression, respectively. Both of these coagulation factors are naturally synthesized in the liver, specifically with FVIII produced in liversinusoidal endothelial cells (LSECs) and FIX produced in hepatocytes.[130] While plasma-derived or recombinant coagulation factor proteins are therapeutically effective, their high cost poses a significant burden for patients. In response, researchers have utilized the AAV2 vector to express the hemophilia B coagulation factor FIX transduce microglial compartments, thereby modulating the immune for therapeutic purposes, yielding promising results. This success has led to the development of additional AAV serotypes, such as AAV3,[131] AAV5,[132] AAV8,[133] and AAV9[133] for the treatment of both hemophilia A and B.[134] It is noteworthy that nearly all AAV serotypes accumulate in the liver following intravenous administration, although this phenomenon varies among different species.[130] To enhance the transduction efficiency of AAV in human liver cells, Mevel et al. modified the AAV coat protein by attaching GalNAc ligands to lysine residues on its surface, thereby increasing its ability to transduce hepatocytes.[135] In the context of inherited metabolic liver diseases (IMLD), the first application of AAV vectors was in the treatment of familial hypercholesterolemia (FH), which resulted in a 40 % reduction and stabilization of serum cholesterol and triglyceride levels in affected patients.[136] Since that initial success, there has been an exponential increase in therapeutic studies utilizing animal models of IMLD. Despite the diverse use of various serotypes, promoters, and delivery vehicles, all studies conducted thus far have demonstrated long-term therapeutic effects without significant adverse effects. This collective evidence suggests that AAV vectors have made substantial advancements in gene therapy for liver diseases and hold considerable promise for future applications.[137]

The rAAV vector is the most widely utilized viral gene delivery system undergoing exploration in clinical trials, with numerous therapeutic applications still under investigation.[138–139] In terms of clinical safety and efficacy, rAAV vectors have demonstrated significant success in both early and late-phase clinical trials for various monogenic diseases, including hemophilia,[140] hereditary blindness,[141] and muscular dystrophy.[142] Moreover, clinical approvals have been granted for gene transfer therapies employing rAAV vectors for the treatment of conditions such as congestive heart failure, hemophilia A and B, retinal diseases, X-linked myotubular myopathy, glioma, glioblastoma, and spinal muscular atrophy (SMA).[11] Notably, the world's first rAAV gene therapy product, alipogene tiparvovec (Glybera), received approval from the European Medicines Agency in 2012 for the treatment of lipoprotein lipase deficiency.[143] Five years later, voretigene neparvovec-rzyl (Luxturna), which became the first licensed rAAV gene therapy product in the United States, was also developed.

In 2019, Ogden et al. created the first comprehensive first-order fitness landscape for the AAV2 capsid, systematically characterizing all single-codon substitutions, insertions, and deletions across multiple functional domains. This work introduced a novel strategy for modifying AAV.[144] Subsequently, in 2023, Nyberg et al. employed a structure-guided evolution approach to develop an AAV variant with enhanced transduction efficiency in murine T cells.[145] These advancements indicate that by modifying the AAV coat protein, it is possible to better tailor its targeting capabilities to meet specific therapeutic needs. In the context of neurological diseases, AAV vectors have been explored for the treatment of Parkinson's disease, particularly in reversing access to axonal endings.[146] This suggests that AAV could be utilized to deliver genes or therapeutic agents more efficiently for treatment purposes.

Despite the rapid adoption of rAAV vectors, several challenges persist. These include innate humoral immunity against AAV coat proteins, limited transduction efficiency in certain tissues and cell types, low organ specificity, variable titers of AAV following expanded production, and dose-dependent toxicity of the vectors in patients. These limitations pose significant challenges to the application of rAAV vectors in specific therapeutic contexts.[78–79,147] Although Yuan et al. developed an immunosuppressive zwitterionic phosphoserine-containing polypeptide aimed at inducing AAV-specific immune tolerance and mitigating immunological responses,[148] the effectiveness of this approach in clinical settings has yet to be validated. Consequently, numerous obstacles remain to be addressed for the broader implementation and application of AAV vectors in gene therapy.

4. Summary and Outlook

AAV was discovered over sixty years ago and has since emerged as one of the most extensively utilized gene delivery tools in clinical development. When compared with other gene delivery methods (e.g., lentivirus, adenovirus, exosomes), rAAV offer several advantages:1)Replication-Deficient Nature: AAV is a replication-deficient virus. In the absence of helper viruses, its genome replicates slowly, and the efficiency of packaging its genome into new viral particles is low. 2)Structural Simplicity: The viral structure of rAAV is relatively simple, facilitating modifications. The coat protein is primarily composed of three proteins: VP1, VP2, and VP3. The C-termini of these proteins overlap, with VP3 accounting for over 90 % of the viral coat. This characteristic has led to a trend in modifying amino acids that target the overlapping hydrophilic regions on the outer surface of the viral coat proteins to enhance the targeting capabilities of rAAV, a strategy that has been validated through various approaches. 3) Limited Integration into Host Genome: The viral genome of rAAV rarely integrates into the genome of the host cell. Although some studies have indicated a 0.6 % probability of rAAV genes integrating into the host genome, these experiments were conducted in vitro rather than in vivo. Furthermore, current clinical trials involving rAAV have not reported any significant side effects, indicating a high level of safety in clinical applications.

rAAV has become the predominant gene delivery vector in clinical medicine due to its unique biological properties, simple viral structure, and lack of pathogenicity. Gene therapy regimens utilizing rAAV in clinical trials have demonstrated minimal side effects and good tolerability among patients. These findings suggest that rAAV has the potential for broader applications as research into the fundamental biological properties of AAV continues to advance.

In the future, the widespread adoption of recombinant adeno-associated viruses (rAAV) in gene therapy will necessitate overcoming several key challenges: First, it is essential to reduce the production costs of rAAV to alleviate the economic burden associated with its use. Both small-scale triple plasmid transfection systems and large-scale industrial production require significant financial investments. Additionally, the subsequent purification of the virus incurs considerable expenses, which hampers large-scale research and production efforts. Second, enhancing the precision and specificity of rAAV targeting is crucial in order to minimize the required dosage of these vectors. Currently, most approaches involve random mutations of the targeting sequences of capsid proteins to develop rAAV variants with new targeting capabilities. This method is both time-consuming and lacks direction, resulting in substantial investments of manpower and resources that hinder the widespread application of rAAV. Third, mitigating the immune response to rAAV in vivo is vital to reducing immune-mediated toxicity, particularly the severe hepatotoxicity associated with high doses of rAAV. This is because it not only leads to a weakening of the efficacy of the virus but also necessitates an increase in the viral dose to achieve the desired therapeutic effect. Administering large doses of the virus can pose significant risks, including severe adverse reactions and potential toxicity, which may result in serious harm to the patient's body or even death. Although immunosuppressive strategies aimed at T-cell responses have proven successful in some patients, they have failed in others, highlighting that the immune response remains a significant barrier to the broader utilization of rAAV. Furthermore, expanding the capacity of the rAAV genome to accommodate larger payloads, as well as improving the virus purification process to yield higher quantities of active virus, are also critical areas for advancement. Additionally, an interesting design of self-complementary adeno-associated virus (scAAV) has been reported.[149] scAAV is capable of circumventing the rate-limiting step of DNA synthesis, resulting in a more efficient and rapid gene expression process. However, these scAAV constructs are typically limited to approximately half the size of wild-type AAV. Finding a balance between gene expression efficiency and packaging capacity may represent a promising area for future research. Collectively, addressing these challenges will likely facilitate the broader application of rAAV in gene therapy.

Acknowledgements

This work was supported by National Key Research Program (2019YFA0905800), National Natural Science Foundation of China (22174043 and 22090050), Science and Technology Major Project of Hunan Province (2021SK1020) and Hunan Provincial Science Fund for Distinguished Young Scholars (2024JJ2011).

Conflict of Interests

The authors declare no conflict of interest.

Keywords: adeno-associated viral · Cellular tropism · Recombinant adeno-associated viral

[1] R. W. Atchison, B. C. Casto, W. M. Hammon, *Science* **1965**, *149*, 754–756.
[2] E. A. Rutledge, C. L. Halbert, D. W. Russell, *J. Virol.* **1998**, *72*, 309–319.
[3] G. Gao, L. H. Vandenberghe, M. R. Alvira, Y. Lu, R. Calcedo, X. Zhou, J. M. Wilson, *J. Virol.* **2004**, *78*, 6381–6388.
[4] W. Xiao, N. Chirmule, S. C. Berta, B. McCullough, G. Gao, J. M. Wilson, *J. Virol.* **1999**, *73*, 3994–4003.
[5] R. J. Samulski, A. Srivastava, K. I. Berns, N. Muzyczka, *Cell* **1983**, *33*, 135–143.
[6] S. Muramatsu, H. Mizukami, N. S. Young, K. E. Brown, *Virology* **1996**, *221*, 208–217.
[7] J. A. Chiorini, L. Yang, Y. Liu, B. Safer, R. M. Kotin, *J. Virol.* **1997**, *71*, 6823–6833.
[8] J. A. Chiorini, F. Kim, L. Yang, R. M. Kotin, *J. Virol.* **1999**, *73*, 1309–1319.
[9] G. P. Gao, M. R. Alvira, L. Wang, R. Calcedo, J. Johnston, J. M. Wilson, *Proc. Natl. Acad. Sci. USA* **2002**, *99*, 11854–11859.
[10] S. Mori, L. Wang, T. Takeuchi, T. Kanda, *Virology* **2004**, *330*, 375–383.
[11] S. Pipe, F. W. G. Leebeek, V. Ferreira, E. K. Sawyer, J. Pasi, *Mol. Ther.* **2019**, *15*, 170–178.
[12] M. Schmidt, A. Voutetakis, S. Afione, C. Zheng, D. Mandikian, J. A. Chiorini, *J. Virol.* **2008**, *82*, 1399–1406.
[13] E. W. Lusby, K. I. Berns, *J. Virol.* **1982**, *41*, 518–526.
[14] M. D. Hoggan, N. R. Blacklow, W. P. Rowe, *Proc. Natl. Acad. Sci. USA* **1966**, *55*, 1467–1474.
[15] F. B. Johnson, N. R. Blacklow, M. D. Hoggan, *J. Virol.* **1972**, *9*, 1017–1026.
[16] M. C. Geoffroy, A. Salvetti, *Curr. Gene Ther.* **2005**, *5*, 265–271.
[17] R. M. Linden, P. Ward, C. Giraud, E. Winocour, K. I. Berns, *Proc. Natl. Acad. Sci. USA* **1996**, *93*, 11288–11294.
[18] J. A. Rose, F. Koczot, *J. Virol.* **1972**, *10*, 1–8.
[19] R. M. Kotin, M. Siniscalco, R. J. Samulski, X. D. Zhu, L. Hunter, C. A. Laughlin, S. McLaughlin, N. Muzyczka, M. Rocchi, K. I. Berns, *Proc. Natl. Acad. Sci. USA* **1990**, *87*, 2211–2215.
[20] A. Srivastava, E. W. Lusby, K. I. Berns, *J. Virol.* **1983**, *45*, 555–564.
[21] E. Lusby, K. H. Fife, K. I. Berns, *J. Virol.* **1980**, *34*, 402–409.
[22] W. W. Hauswirth, K. I. Berns, *Virology* **1977**, *78*, 488–499.
[23] P. Senapathy, J. D. Tratschin, B. J. Carter, *J. Mol. Biol.* **1984**, *179*, 1–20.
[24] J. D. Tratschin, I. L. Miller, B. J. Carter, *J. Virol.* **1984**, *51*, 611–619.
[25] J. D. Tratschin, J. Tal, B. J. Carter, *Mol. Cell. Biol.* **1986**, *6*, 2884–2894.
[26] C. A. Laughlin, H. Westphal, B. J. Carter, *Proc. Natl. Acad. Sci. USA* **1979**, *76*, 5567–5571.
[27] J. A. Rose, J. V. Maizel Jr., J. K. Inman, A. J. Shatkin, *J. Virol.* **1971**, *8*, 766–770.
[28] F. B. Johnson, H. L. Ozer, M. D. Hoggan, *J. Virol.* **1971**, *8*, 860–863.
[29] R. M. Buller, J. A. Rose, *J. Virol.* **1978**, *25*, 331–338.
[30] J. Snijder, M. van de Waterbeemd, E. Damoc, E. Denisov, D. Grinfeld, A. Bennett, M. Agbandje-McKenna, A. Makarov, A. J. Heck, *J. Am. Chem. Soc.* **2014**, *136*, 7295–7299.
[31] F. Sonntag, K. Schmidt, J. A. Kleinschmidt, *Proc. Natl. Acad. Sci. USA* **2010**, *107*, 10220–10225.
[32] F. Sonntag, K. Kother, K. Schmidt, M. Weghofer, C. Raupp, K. Nieto, A. Kuck, B. Gerlach, B. Bottcher, O. J. Muller, K. Lux, M. Horer, J. A. Kleinschmidt, *J. Virol.* **2011**, *85*, 12686–12697.
[33] M. Mietzsch, J. J. Penzes, M. Agbandje-McKenna, *Viruses* **2019**, *11*(4), 362.
[34] M. Agbandje-McKenna, J. Kleinschmidt, *Methods Mol. Biol.* **2011**, *807*, 47–92.
[35] A. Girod, C. E. Wobus, Z. Zadori, M. Ried, K. Leike, P. Tijssen, J. A. Kleinschmidt, M. Hallek, *J. Gen. Virol.* **2002**, *83*, 973–978.
[36] F. Sonntag, S. Bleker, B. Leuchs, R. Fischer, J. A. Kleinschmidt, *J. Virol.* **2006**, *80*, 11040–11054.
[37] S. K. McLaughlin, P. Collis, P. L. Hermonat, N. Muzyczka, *J. Virol.* **1988**, *62*, 1963–1973.
[38] A. M. Dudek, N. Zabaleta, E. Zinn, S. Pillay, J. Zengel, C. Porter, J. S. Franceschini, R. Estelien, J. E. Carette, G. L. Zhou, L. H. Vandenberghe, *Mol. Ther.* **2020**, *28*, 367–381.
[39] M. A. Lochrie, G. P. Tatsuno, B. Christie, J. W. McDonnell, S. Zhou, R. Surosky, G. F. Pierce, P. Colosi, *J. Virol.* **2006**, *80*, 821–834.
[40] K. Nash, W. Chen, N. Muzyczka, *J. Virol.* **2008**, *82*, 1458–1464.
[41] T. H. Ni, W. F. McDonald, I. Zolotukhin, T. Melendy, S. Waga, B. Stillman, N. Muzyczka, *J. Virol.* **1998**, *72*, 2777–2787.
[42] P. Ward, F. B. Dean, M. E. O'Donnell, K. I. Berns, *J. Virol.* **1998**, *72*, 420–427.
[43] J. J. Byrnes, *Mol. Cell. Biochem.* **1984**, *62*, 13–24.
[44] G. Prelich, B. Stillman, *Cell* **1988**, *53*, 117–126.
[45] T. Miyata, T. Oyama, K. Mayanagi, S. Ishino, Y. Ishino, K. Morikawa, *Nat. Struct. Mol. Biol.* **2004**, *11*, 632–636.
[46] Y. Ishimi, *J. Biol. Chem.* **1997**, *272*, 24508–24513.
[47] A. H. Marceau, *Methods Mol. Biol.* **2012**, *922*, 1–21.
[48] B. J. Carter, B. A. Antoni, D. F. Klessig, *Virology* **1992**, *191*, 473–476.
[49] M. W. Myers, B. J. Carter, *J. Biol. Chem.* **1981**, *256*, 567–570.
[50] S. Bleker, F. Sonntag, J. A. Kleinschmidt, *J. Virol.* **2005**, *79*, 2528–2540.
[51] R. Dubielzig, J. A. King, S. Weger, A. Kern, J. A. Kleinschmidt, *J. Virol.* **1999**, *73*, 8989–8998.

[52] L. S. Chang, T. Shenk, *J. Virol.* **1990**, *64*, 2103–2109.
[53] Y. Shi, E. Seto, L. S. Chang, T. Shenk, *Cell* **1991**, *67*, 377–388.
[54] L. S. Chang, Y. Shi, T. Shenk, *J. Virol.* **1989**, *63*, 3479–3488.
[55] D. J. Pereira, N. Muzyczka, *J. Virol.* **1997**, *71*, 4300–4309.
[56] D. J. Pereira, N. Muzyczka, *J. Virol.* **1997**, *71*, 1747–1756.
[57] D. F. Lackner, N. Muzyczka, *J. Virol.* **2002**, *76*, 8225–8235.
[58] B. Aj, *In Fields Virology* **2007**, pp. 2355–2394.
[59] R. J. Samulski, T. Shenk, *J. Virol.* **1988**, *62*, 206–210.
[60] R. A. Schwartz, J. A. Palacios, G. D. Cassell, S. Adam, M. Giacca, M. D. Weitzman, *J. Virol.* **2007**, *81*, 12936–12945.
[61] C. T. Carson, R. A. Schwartz, T. H. Stracker, C. E. Lilley, D. V. Lee, M. D. Weitzman, *EMBO J.* **2003**, *22*, 6610–6620.
[62] M. Horer, S. Weger, K. Butz, F. Hoppe-Seyler, C. Geisen, J. A. Kleinschmidt, *J. Virol.* **1995**, *69*, 5485–5496.
[63] M. M. Huang, P. Hearing, *J. Virol.* **1989**, *63*, 2605–2615.
[64] J. E. Janik, M. M. Huston, K. Cho, J. A. Rose, *Virology* **1989**, *168*, 320–329.
[65] M. Penaud-Budloo, C. Le Guiner, A. Nowrouzi, A. Toromanoff, Y. Cherel, P. Chenuaud, M. Schmidt, C. von Kalle, F. Rolling, P. Moullier, R. O. Snyder, *J. Virol.* **2008**, *82*, 7875–7885.
[66] N. Muzyczka, *Curr. Top. Microbiol. Immunol.* **1992**, *158*, 97–129.
[67] J. E. Rabinowitz, F. Rolling, C. Li, H. Conrath, W. Xiao, X. Xiao, R. J. Samulski, *J. Virol.* **2002**, *76*, 791–801.
[68] R. J. Samulski, L. S. Chang, T. Shenk, *J. Virol.* **1989**, *63*, 3822–3828.
[69] X. Xiao, J. Li, R. J. Samulski, *J. Virol.* **1998**, *72*, 2224–2232.
[70] T. Matsushita, S. Elliger, C. Elliger, G. Podsakoff, L. Villarreal, G. J. Kurtzman, Y. Iwaki, P. Colosi, *Gene Ther.* **1998**, *5*, 938–945.
[71] P. R. H. Joshi, A. Venereo-Sanchez, P. S. Chahal, A. A. Kamen, *Biotechnol. J.* **2021**, *16*, e2000021.
[72] D. Grimm, A. Kern, K. Rittner, J. A. Kleinschmidt, *Hum. Gene Ther.* **1998**, *9*, 2745–2760.
[73] C. Summerford, R. J. Samulski, *J. Virol.* **1998**, *72*, 1438–1445.
[74] Z. Wu, E. Miller, M. Agbandje-McKenna, R. J. Samulski, *J. Virol.* **2006**, *80*, 9093–9103.
[75] R. W. Walters, S. M. Yi, S. Keshavjee, K. E. Brown, M. J. Welsh, J. A. Chiorini, J. Zabner, *J. Biol. Chem.* **2001**, *276*, 20610–20616.
[76] N. Kaludov, K. E. Brown, R. W. Walters, J. Zabner, J. A. Chiorini, *J. Virol.* **2001**, *75*, 6884–6893.
[77] J. S. Johnson, R. J. Samulski, *J. Virol.* **2009**, *83*, 2632–2644.
[78] S. Pillay, J. E. Carette, *Curr. Opin. Virol.* **2017**, *24*, 124–131.
[79] A. Asokan, D. V. Schaffer, R. J. Samulski, *Mol. Ther.* **2012**, *20*, 699–708.
[80] A. Srivastava, *Curr. Opin. Virol.* **2016**, *21*, 75–80.
[81] W. H. Meisen, Z. B. Nejad, M. Hardy, H. Zhao, O. Oliverio, S. Wang, C. Hale, M. M. Ollmann, P. J. Collins, *Mol. Ther.* **2020**, *17*, 601–611.
[82] L. Lisowski, S. S. Tay, I. E. Alexander, *Curr. Opin. Pharmacol.* **2015**, *24*, 59–67.
[83] B. H. Albright, C. M. Storey, G. Murlidharan, R. M. Castellanos Rivera, G. E. Berry, V. J. Madigan, A. Asokan, *Mol. Ther.* **2018**, *26*, 510–523.
[84] H. C. Brown, C. B. Doering, R. W. Herzog, C. Ling, D. M. Markusic, H. T. Spencer, A. Srivastava, A. Srivastava, *Hum. Gene Ther.* **2020**, *31*, 1114–1123.
[85] I. C. Han, J. L. Cheng, E. R. Burnight, C. L. Ralston, J. L. Fick, G. J. Thomsen, E. F. Tovar, S. R. Russell, E. H. Sohn, R. F. Mullins, E. M. Stone, B. A. Tucker, L. A. Wiley, *Hum. Gene Ther.* **2020**, *31*, 1288–1299.
[86] M. H. Kang, J. Hu, R. E. Pratt, C. P. Hodgkinson, A. Asokan, V. J. Dzau, *Biochem. Biophys. Res. Commun.* **2020**, *533*, 9–16.
[87] B. Akache, D. Grimm, X. Shen, S. Fuess, S. R. Yant, D. S. Glazer, J. Park, M. A. Kay, *Mol. Ther.* **2007**, *15*, 330–339.
[88] C. E. Thomas, T. A. Storm, Z. Huang, M. A. Kay, *J. Virol.* **2004**, *78*, 3110–3122.
[89] S. C. Nicolson, R. J. Samulski, *J. Virol.* **2014**, *88*, 4132–4144.
[90] J. M. Bevington, P. G. Needham, K. C. Verrill, R. F. Collaco, V. Basrur, J. P. Trempe, *Virology* **2007**, *357*, 102–113.
[91] J. Qiu, K. E. Brown, *Virology* **1999**, *257*, 373–382.
[92] H. Nakai, T. A. Storm, M. A. Kay, *J. Virol.* **2000**, *74*, 9451–9463.
[93] D. Duan, P. Sharma, J. Yang, Y. Yue, L. Dudus, Y. Zhang, K. J. Fisher, J. F. Engelhardt, *J. Virol.* **1998**, *72*, 8568–8577.
[94] C. H. Miao, R. O. Snyder, D. B. Schowalter, G. A. Patijn, B. Donahue, B. Winther, M. A. Kay, *Nat. Genet.* **1998**, *19*, 13–15.
[95] Q. Xie, W. Bu, S. Bhatia, J. Hare, T. Somasundaram, A. Azzi, M. S. Chapman, *Proc. Natl. Acad. Sci. USA* **2002**, *99*, 10405–10410.
[96] L. Govindasamy, E. Padron, R. McKenna, N. Muzyczka, N. Kaludov, J. A. Chiorini, M. Agbandje-McKenna, *J. Virol.* **2006**, *80*, 11556–11570.
[97] H. J. Nam, M. D. Lane, E. Padron, B. Gurda, R. McKenna, E. Kohlbrenner, G. Aslanidi, B. Byrne, N. Muzyczka, S. Zolotukhin, M. Agbandje-McKenna, *J. Virol.* **2007**, *81*, 12260–12271.
[98] S. Russell, J. Bennett, J. A. Wellman, D. C. Chung, Z. F. Yu, A. Tillman, J. Wittes, J. Pappas, O. Elci, S. McCague, D. Cross, K. A. Marshall, J. Walshire, T. L. Kehoe, H. Reichert, M. Davis, L. Raffini, L. A. George, F. P. Hudson, L. Dingfield, X. Zhu, J. A. Haller, E. H. Sohn, V. B. Mahajan, W. Pfeifer, M. Weckmann, C. Johnson, D. Gewaily, A. Drack, E. Stone, K. Wachtel, F. Simonelli, B. P. Leroy, J. F. Wright, K. A. High, A. M. Maguire, *Lancet* **2017**, *390*, 849–860.
[99] N. G. Ghazi, E. B. Abboud, S. R. Nowilaty, H. Alkuraya, A. Alhommadi, H. Cai, R. Hou, W. T. Deng, S. L. Boye, A. Almaghamsi, F. Al Saikhan, H. Al-Dhibi, D. Birch, C. Chung, D. Colak, M. M. LaVail, D. Vollrath, K. Erger, W. Wang, T. Conlon, K. Zhang, W. Hauswirth, F. S. Alkuraya, *Hum. Genet.* **2016**, *135*, 327–343.
[100] J. Yuan, Y. Zhang, H. Liu, D. Wang, Y. Du, Z. Tian, X. Li, S. Yang, H. Pei, X. Wan, S. Xiao, L. Song, X. Xiao, J. Sun, Z. Wang, B. Li, *Ophthalmology* **2020**, *127*, 1125–1127.
[101] Y. Zhang, X. Li, J. Yuan, Z. Tian, H. Liu, D. Wang, B. Li, *Clin Exp Ophthalmol* **2019**, *47*, 774–778.
[102] M. D. Fischer, S. Michalakis, B. Wilhelm, D. Zobor, R. Muehlfriedel, S. Kohl, N. Weisschuh, G. A. Ochakovski, R. Klein, C. Schoen, V. Sothilingam, M. Garcia-Garrido, L. Kuehlewein, N. Kahle, A. Werner, D. Dauletbekov, F. Paquet-Durand, S. Tsang, P. Martus, T. Peters, M. Seeliger, K. U. Bartz-Schmidt, M. Ueffing, E. Zrenner, M. Biel, B. Wissinger, *JAMA Ophthalmol* **2020**, *138*, 643–651.
[103] T. L. Edwards, J. K. Jolly, M. Groppe, A. R. Barnard, C. L. Cottriall, T. Tolmachova, G. C. Black, A. R. Webster, A. J. Lotery, G. E. Holder, K. Xue, S. M. Downes, M. P. Simunovic, M. C. Seabra, R. E. MacLaren, *N. Engl. J. Med.* **2016**, *374*, 1996–1998.
[104] J. Ou, C. Vijayasarathy, L. Ziccardi, S. Chen, Y. Zeng, D. Marangoni, J. G. Pope, R. A. Bush, Z. Wu, W. Li, P. A. Sieving, *J. Clin. Invest.* **2015**, *125*, 2891–2903.
[105] D. Duan, *Mol. Ther.* **2018**, *26*, 2337–2356.
[106] N. Elangkovan, G. Dickson, *J Neuromuscul Dis* **2021**, *8*, S303–S316.
[107] J. R. Mendell, Z. Sahenk, K. Lehman, C. Nease, L. P. Lowes, N. F. Miller, M. A. Iammarino, L. N. Alfano, A. Nicholl, S. Al-Zaidy, S. Lewis, K. Church, R. Shell, L. H. Cripe, R. A. Potter, D. A. Griffin, E. Pozsgai, A. Dugar, M. Hogan, L. R. Rodino-Klapac, *JAMA Neurol.* **2020**, *77*, 1122–1131.
[108] H. Wilton-Clark, T. Yokota, *Genes (Basel)* **2022**, *13*(2), 257.
[109] I. Kwon, D. V. Schaffer, *Pharm. Res.* **2008**, *25*, 489–499.
[110] Z. Wu, A. Asokan, R. J. Samulski, *Mol. Ther.* **2006**, *14*, 316–327.
[111] C. Burger, O. S. Gorbatyuk, M. J. Velardo, C. S. Peden, P. Williams, S. Zolotukhin, P. J. Reier, R. J. Mandel, N. Muzyczka, *Mol. Ther.* **2004**, *10*, 302–317.
[112] D. Grimm, M. A. Kay, *Curr. Gene Ther.* **2003**, *3*, 281–304.
[113] P. J. Xiao, T. B. Lentz, R. J. Samulski, *Ther. Delivery* **2012**, *3*, 835–856.
[114] R. Bates, W. Huang, L. Cao, *Mol. Ther.* **2020**, *19*, 236–249.
[115] Q. Chen, H. Luo, C. Zhou, H. Yu, S. Yao, F. Fu, R. Seeley, X. Ji, Y. Yang, P. Chen, H. Jin, P. Tong, D. Chen, C. Wu, W. Du, H. Ruan, *PLoS One* **2020**, *15*, e0243359.
[116] Y. Colon-Cortes, M. A. Hasan, G. Aslanidi, *Gene* **2020**, *763S*, 100037.
[117] Z. Liu, K. Klose, S. Neuber, M. Jiang, M. Gossen, C. Stamm, *J. Transl. Med.* **2020**, *18*, 437.
[118] K. L. Pietersz, R. M. Martier, M. S. Baatje, J. M. Liefhebber, C. C. Brouwers, S. M. Pouw, L. Fokkert, J. Lubelski, H. Petry, G. J. M. Martens, S. J. van Deventer, P. Konstantinova, B. Blits, *Gene Ther.* **2021**, *28*, 435–446.
[119] P. Wu, W. Xiao, T. Conlon, J. Hughes, M. Agbandje-McKenna, T. Ferkol, T. Flotte, N. Muzyczka, *J. Virol.* **2000**, *74*, 8635–8647.
[120] L. Zhong, B. Li, C. S. Mah, L. Govindasamy, M. Agbandje-McKenna, M. Cooper, R. W. Herzog, I. Zolotukhin, K. H. Warrington Jr., K. A. Weigel-Van Aken, J. A. Hobbs, S. Zolotukhin, N. Muzyczka, A. Srivastava, *Proc. Natl. Acad. Sci. USA* **2008**, *105*, 7827–7832.
[121] N. M. Kanaan, R. C. Sellnow, S. L. Boye, B. Coberly, A. Bennett, M. Agbandje-McKenna, C. E. Sortwell, W. W. Hauswirth, S. E. Boye, F. P. Manfredsson, *Mol. Ther. Nucleic Acids* **2017**, *8*, 184–197.
[122] A. M. Rosario, P. E. Cruz, C. Ceballos-Diaz, M. R. Strickland, Z. Siemienski, M. Pardo, K. L. Schob, A. Li, G. V. Aslanidi, A. Srivastava, T. E. Golde, P. Chakrabarty, *Mol. Ther.* **2016**, *3*, 16026.
[123] J. A. Gilkes, B. L. Judkins, B. N. Herrera, R. J. Mandel, S. L. Boye, S. E. Boye, A. Srivastava, C. D. Heldermon, *Gene Ther.* **2021**, *28*, 447–455.
[124] C. Ojano-Dirain, L. G. Glushakova, L. Zhong, S. Zolotukhin, N. Muzyczka, A. Srivastava, P. W. Stacpoole, *Mol. Genet. Metab.* **2010**, *101*, 183–191.

[125] Y. Meng, D. Sun, Y. Qin, X. Dong, G. Luo, Y. Liu, *Mol. Ther.* **2021**, *21*, 28–41.

[126] Y. Yao, J. Wang, Y. Liu, Y. Qu, K. Wang, Y. Zhang, Y. Chang, Z. Yang, J. Wan, J. Liu, H. Nakashima, S. E. Lawler, E. A. Chiocca, C. F. Cho, F. Bei, *Nat Biomed Eng* **2022**, *6*, 1257–1271.

[127] W. Shao, L. F. Earley, Z. Chai, X. Chen, J. Sun, T. He, M. Deng, M. L. Hirsch, J. Ting, R. J. Samulski, C. Li, *JCI Insight* **2018**, *3*.

[128] B. E. Deverman, B. M. Ravina, K. S. Bankiewicz, S. M. Paul, D. W. Y. Sah, *Nat. Rev. Drug Discovery* **2018**, *17*, 767.

[129] Q. Huang, K. Y. Chan, J. Wu, N. R. Botticello-Romero, Q. Zheng, S. Lou, C. Keyes, A. Svanbergsson, J. Johnston, A. Mills, C. Y. Lin, P. P. Brauer, G. Clouse, S. Pacouret, J. W. Harvey, T. Beddow, J. K. Hurley, I. G. Tobey, M. Powell, A. T. Chen, A. J. Barry, F. E. Eid, Y. A. Chan, B. E. Deverman, *Science* **2024**, *384*, 1220–1227.

[130] B. Palaschak, R. W. Herzog, D. M. Markusic, *Methods Mol. Biol.* **2019**, *1950*, 333–360.

[131] M. Biswas, D. Marsic, N. Li, C. Zou, G. Gonzalez-Aseguinolaza, I. Zolotukhin, S. R. P. Kumar, J. Rana, J. S. S. Butterfield, O. Kondratov, Y. P. de Jong, R. W. Herzog, S. Zolotukhin, *Mol. Ther.* **2020**, *19*, 347–361.

[132] S. Rangarajan, L. Walsh, W. Lester, D. Perry, B. Madan, M. Laffan, H. Yu, C. Vettermann, G. F. Pierce, W. Y. Wong, K. J. Pasi, *N. Engl. J. Med.* **2017**, *377*, 2519–2530.

[133] C. S. Manno, G. F. Pierce, V. R. Arruda, B. Glader, M. Ragni, J. J. Rasko, M. C. Ozelo, K. Hoots, P. Blatt, B. Konkle, M. Dake, R. Kaye, M. Razavi, A. Zajko, J. Zehnder, P. K. Rustagi, H. Nakai, A. Chew, D. Leonard, J. F. Wright, R. R. Lessard, J. M. Sommer, M. Tigges, D. Sabatino, A. Luk, H. Jiang, F. Mingozzi, L. Couto, H. C. Ertl, K. A. High, M. A. Kay, *Nat. Med.* **2006**, *12*, 342–347.

[134] A. C. Nathwani, E. G. Tuddenham, S. Rangarajan, C. Rosales, J. McIntosh, D. C. Linch, P. Chowdary, A. Riddell, A. J. Pie, C. Harrington, J. O'Beirne, K. Smith, J. Pasi, B. Glader, P. Rustagi, C. Y. Ng, M. A. Kay, J. Zhou, Y. Spence, C. L. Morton, J. Allay, J. Coleman, S. Sleep, J. M. Cunningham, D. Srivastava, E. Basner-Tschakarjan, F. Mingozzi, K. A. High, J. T. Gray, U. M. Reiss, A. W. Nienhuis, A. M. Davidoff, *N. Engl. J. Med.* **2011**, *365*, 2357–2365.

[135] M. Mevel, M. Bouzelha, A. Leray, S. Pacouret, M. Guilbaud, M. Penaud-Budloo, D. Alvarez-Dorta, L. Dubreil, S. G. Gouin, J. P. Combal, M. Hommel, G. Gonzalez-Aseguinolaza, V. Blouin, P. Moullier, O. Adjali, D. Deniaud, E. Ayuso, *Chem. Sci.* **2019**, *11*, 1122–1131.

[136] S. Maestro, N. D. Weber, N. Zabaleta, R. Aldabe, G. Gonzalez-Aseguinolaza, *JHEP Rep* **2021**, *3*, 100300.

[137] N. Zabaleta, M. Hommel, D. Salas, G. Gonzalez-Aseguinolaza, *Hum. Gene Ther.* **2019**, *30*, 1190–1203.

[138] S. H. Chen, J. Haam, M. Walker, E. Scappini, J. Naughton, N. P. Martin, *Curr Protoc Neurosci* **2019**, *87*, e67.

[139] J. Rabinowitz, Y. K. Chan, R. J. Samulski, *Viruses* **2019**, *11*(2), 102.

[140] A. C. Nathwani, U. M. Reiss, E. G. Tuddenham, C. Rosales, P. Chowdary, J. McIntosh, M. Della Peruta, E. Lheriteau, N. Patel, D. Raj, A. Riddell, J. Pie, S. Rangarajan, D. Bevan, M. Recht, Y. M. Shen, K. G. Halka, E. Basner-Tschakarjan, F. Mingozzi, K. A. High, J. Allay, M. A. Kay, C. Y. Ng, J. Zhou, M. Cancio, C. L. Morton, J. T. Gray, D. Srivastava, A. W. Nienhuis, A. M. Davidoff, *N. Engl. J. Med.* **2014**, *371*, 1994–2004.

[141] K. Miyadera, E. Santana, K. Roszak, S. Iffrig, M. Visel, S. Iwabe, R. F. Boyd, J. T. Bartoe, Y. Sato, A. Gray, A. Ripolles-Garcia, V. L. Dufour, L. C. Byrne, J. G. Flannery, W. A. Beltran, G. D. Aguirre, *Proc. Natl. Acad. Sci. USA* **2022**, *119*, e2117038119.

[142] D. E. Bowles, S. W. McPhee, C. Li, S. J. Gray, J. J. Samulski, A. S. Camp, J. Li, B. Wang, P. E. Monahan, J. E. Rabinowitz, J. C. Grieger, L. Govindasamy, M. Agbandje-McKenna, X. Xiao, R. J. Samulski, *Mol. Ther.* **2012**, *20*, 443–455.

[143] S. Yla-Herttuala, *Mol. Ther.* **2012**, *20*, 1831–1832.

[144] P. J. Ogden, E. D. Kelsic, S. Sinai, G. M. Church, *Science* **2019**, *366*, 1139–1143.

[145] W. A. Nyberg, J. Ark, A. To, S. Clouden, G. Reeder, J. J. Muldoon, J. Y. Chung, W. H. Xie, V. Allain, Z. Steinhart, C. Chang, A. Talbot, S. Kim, A. Rosales, L. P. Havlik, H. Pimentel, A. Asokan, J. Eyquem, *Cell* **2023**, *186*, 446–460 e419.

[146] Y. Chen, Z. Hong, J. Wang, K. Liu, J. Liu, J. Lin, S. Feng, T. Zhang, L. Shan, T. Liu, P. Guo, Y. Lin, T. Li, Q. Chen, X. Jiang, A. Li, X. Li, Y. Li, J. J. Wilde, J. Bao, J. Dai, Z. Lu, *Cell* **2023**, *186*, 5394–5410 e5318.

[147] W. Asaad, P. Volos, D. Maksimov, E. Khavina, A. Deviatkin, O. Mityaeva, P. Volchkov, *Heliyon* **2023**, *9*, e15071.

[148] Z. Yuan, B. Li, W. Gu, S. Luozhong, R. Li, S. Jiang, *J. Am. Chem. Soc.* **2022**, *144*, 20507–20513.

[149] D. M. McCary, P. E. Monahan, R. J. Samulski, *Gene Ther.* **2001**, *16*, 1248–1254.

Manuscript received: October 15, 2024
Revised manuscript received: December 21, 2024
Accepted manuscript online: December 26, 2024
Version of record online: ■■, ■■

RESEARCH ARTICLE

NANO · MICRO small
www.small-journal.com

Reversible Shielding and Immobilization of Liposomes and Viral Vectors by Tailored Antibody-Ligand Interactions

*Oliver S. Thomas, Balder Rebmann, Matthias Tonn, Ivo C. Schirmeister, Sarah Wehrle, Jan Becker, Gabriel J. Zea Jimenez, Sebastian Hook, Sarah Jäger, Melissa Klenzendorf, Mateo Laskowski, Alexander Kaier, Gerhard Pütz, Matias D. Zurbriggen, Wilfried Weber, Maximilian Hörner, and Hanna J. Wagner**

Controlling the time and dose of nanoparticulate drug delivery by administration of small molecule drugs holds promise for efficient and safer therapies. This study describes a versatile approach of exploiting antibody-ligand interactions for the design of small molecule-responsive nanocarrier and nanocomposite systems. For this purpose, antibody fragments (scFvs) specific for two distinct small molecule ligands are designed. Subsequently, the surface of nanoparticles (liposomes or adeno-associated viral vectors, AAVs) is modified with these ligands, serving as anchor points for scFv binding. By modifying the scFvs with polymer tails, they can act as a non-covalently bound shielding layer, which is recruited to the anchor points on the nanoparticle surface and prevents interactions with cultured mammalian cells. Administration of an excess of the respective ligand triggers competitive displacement of the shielding layer from the nanoparticle surface and restores nanoparticle-cell interactions. The same principle is applied for developing hydrogel depots that can release integrated AAVs or liposomes in response to small molecule ligands. The liberated nanoparticles subsequently deliver their cargoes to cells. In summary, the utilization of different antibody-ligand interactions, different nanoparticles, and different release systems validates the versatility of the design concept described herein.

1. Introduction

Nanotechnology allows the upgrade of existing and clinically proven drugs with sophisticated delivery vehicles in order to optimize pharmacokinetic parameters and ameliorate toxicity. Since long circulation times have been shown to be beneficial for bioavailability,[1–3] nanocarriers are often modified to reduce the binding of opsonizing agents, such as complement proteins or antibodies, or the uptake by sentinel cells of the immune system, such as macrophages.[4] A common strategy relies on decorating the surface of nanoparticles with polymers such as polyethylene glycol (PEG), which reduces interactions with proteins and cells by steric, enthalpic, and entropic effects.[5] Similarly, nanoparticles can be protected by incorporating them into hydrogels, whose high water content and viscoelastic properties resemble those of living tissues, making them ideally suited for use

---

O. S. Thomas, B. Rebmann,[+] M. Tonn, I. C. Schirmeister, S. Wehrle,
J. Becker, G. J. Zea Jimenez, S. Hook, S. Jäger, M. Klenzendorf,
M. Laskowski, A. Kaier, W. Weber, M. Hörner, H. J. Wagner
Faculty of Biology II
University of Freiburg
79104 Freiburg, Germany
E-mail: hanna.wagner@biologie.uni-freiburg.de

The ORCID identification number(s) for the author(s) of this article can be found under https://doi.org/10.1002/smll.202105157.

[+]Present address: Lipoid GmbH, 67065 Ludwigshafen, Germany

DOI: 10.1002/smll.202105157

O. S. Thomas, B. Rebmann, M. Tonn, I. C. Schirmeister, S. Wehrle,
J. Becker, G. J. Zea Jimenez, S. Hook, S. Jäger, M. Klenzendorf,
M. Laskowski, A. Kaier, W. Weber, M. Hörner, H. J. Wagner
Signalling Research Centres BIOSS and CIBSS
University of Freiburg
79104 Freiburg, Germany

O. S. Thomas, W. Weber
Spemann Graduate School of Biology and Medicine (SGBM)
University of Freiburg
79104 Freiburg, Germany

G. Pütz
University Medical Center Freiburg
Institute for Clinical Chemistry
79106 Freiburg, Germany

M. D. Zurbriggen
Institute of Synthetic Biology and CEPLAS
Heinrich Heine University Düsseldorf
40225 Düsseldorf, Germany

H. J. Wagner
Department of Biosystems Science and Engineering – D-BSSE
ETH Zurich
Basel 4058, Switzerland

as drug depots.[6–8] This combination of nanoparticles and hydrogel depots gave rise to a new class of delivery systems, termed nanocomposite systems.[9–12]

However, both PEGylation and entrapment in hydrogel depots also prevent efficient internalization of the nanocarrier and its cargo by the intended target cells, and a balance must be found between specific versus efficient uptake. To address this challenge, systems have been developed which enable induced release and targeted delivery by employing sheddable PEG coatings, degradable particles, or dissolvable gels.[12–15] These systems can be tailored to flexibly respond to their environment, for instance to exogenous stimuli such as induced local heating, ultrasonication, targeted magnetic fields, or illumination with light of a specific wavelength.[16–18] However, these triggers place high demands on available equipment and the expertise of trained personnel. The usage of bioavailable and tolerable small molecules as exogenous triggers, on the other hand, would be a suitable alternative, and upon further development could eventually allow temporally precise and controlled release in response to administration of a trigger compound.

To date, a number of delivery systems responding to endogenous small molecule metabolites such as ATP, glucose, or lactate have been developed. Typically, this is achieved by incorporating (often protein- or aptamer-based) binding partners into the material. Presence of the trigger molecule leads to a physicochemical rearrangement within the material, affecting cargo release.[19–22]

However, these endogenous substances are permanently present in human physiology at considerable and fluctuating concentrations, and are therefore unsuitable to exogenously trigger responsive nanoparticle and nanocomposite systems. Instead, the putative trigger substances employed in such a design should i) possess an excellent clinical safety profile, ii) have no other targeted pharmacological effects, iii) distribute across many tissue types, iv) be rapidly excreted after use, v) not be present at high concentrations in a regular diet, and vi) (ideally) already be licensed for clinical use. Furthermore, the interaction between the trigger molecule and its binding partner must be highly specific to avoid unintended release.

Here, we conducted a proof-of-concept study to develop prototype systems in agreement with these requirements. We exploited the exquisite specificity of antibody-antigen pairs for the reversible recruitment of functionalized antibody fragments to ligand-coupled nanoparticles. By first fusing polymeric tails to the antibody fragments, they acted as a non-covalently bound shielding layer. This was competitively removed by the addition of free ligand acting as a trigger molecule and converting the nanoparticles to their free and accessible state.

We chose two well-suited small molecule ligands as prospective triggers: fluorescein, which does not occur in human physiology, but is clinically used as a safe contrast agent,[23] and biotin, a naturally occurring vitamin,[24] which is present in plasma at concentrations below 10 nM—too low to inadvertently trigger stimulus-responsive systems.[25] Moreover, both molecules are bioavailable after oral administration and exhibit low toxicity.[23,24,26,27]

As a complementary component, antibody fragments are ideal building blocks for stimulus-triggered systems because antibodies have been in clinical use for over three decades,[28,29] can be raised against virtually any molecule of interest, and have been successfully applied for the generation of stimulus-responsive hydrogels.[30] Since F_C effector functions such as immune cell receptor activation or complement binding are both unnecessary and undesirable for our intended application, we used single-chain variable fragments (scFvs). scFvs comprise only the variable V_H and V_L domains of an antibody connected by a flexible peptide linker and therefore are devoid of the F_C part. They retain the specificity and affinity for their antigen and are functional without glycosylation, making them amenable for efficient production in prokaryotic expression hosts.[31–33]

In this study, we applied the same versatile design principle for rendering both nanocarrier and nanocomposite systems stimulus-responsive to exogenous small trigger molecules. We designed scFvs specifically tailored to achieve desirable stability properties and affinity for the trigger molecules. Subsequently, we covalently attached the respective trigger molecules to the surface of nanoparticles, thus enabling their non-covalent decoration with the scFvs. We validated this design principle with two representative classes of nanoparticles: liposomes (a versatile type of carrier suitable for encapsulation of hydrophilic and lipophilic cargo) and adeno-associated viral vectors (AAVs, a vector system for gene therapy applications). By functionally modifying the scFvs with polymeric tails, they acted as a recruitable shielding layer, and we characterized the systems by quantifying the association with (for liposomes) or the transduction of (for AAVs) cultured mammalian cells in the shielded and triggered free states. Using star-shaped multi-arm PEG for functionalization, the scFvs could also act as a backbone of dissolvable hydrogels into which nanoparticles were actively incorporated. We characterized these gels by measuring nanoparticle release in the stable and dissolved states.

The usability of our versatile design principle for the development of both a controlled deshielding system and stimulus-responsive hydrogel depots for nanoparticles demonstrated the advantage of combining tailored antibody-antigen interactions with the design of nanoparticles for the development of next-generation delivery systems.

2. Results and Discussion

2.1. Non-Covalent Reversible Shielding of Nanoparticles

In this study, we propose a versatile strategy to control nanoparticle-cell interactions by modifying the surface of nanoparticles with small molecules, thus allowing their reversible interaction with functionally modified scFvs directed against these small molecules.

To confer shielding properties on the cognate scFvs, we genetically fused them to PAS tails, thus avoiding chemical coupling to PEG, which is often used for shielding. PAS is a synthetic polypeptide sequence named after its constituent monomers proline, alanine, and serine, which are arranged in a repetitive fashion.[34] PAS repeats adopt a random coil structure, exposing the hydrophilic backbone and mimicking the biophysical characteristics of PEG.[35] Upon binding to the ligands exposed on the nanoparticle surface, the PASylated scFvs acted

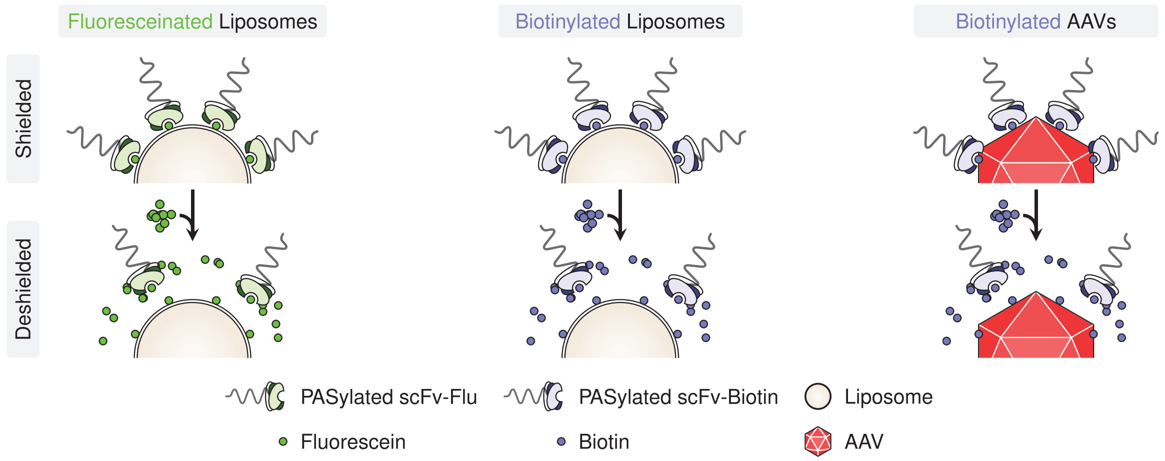

Figure 1. Shielding of liposomes or AAVs by exploitation of scFv-ligand interactions. Covalently modifying the surface of liposomes or AAVs with fluorescein or biotin allows their reversible decoration with specifically designed scFvs. By fusing the scFvs to a PAS tail (a polypeptide with biophysical properties similar to PEG), attachment of the scFvs to the nanoparticle surface results in *shielding* of the nanoparticles, preventing interaction with cells. Subsequent addition of the free ligand competes with the surface-attached ligand for binding to the scFv, resulting in *deshielding*. Illustrated components are not drawn to scale.

as a shielding layer. Since this interaction is reversible, addition of the free ligand competitively removed the scFvs, thus liberating the nanoparticle and enabling cell binding (**Figure 1**).

We first established the system exemplarily with liposomes whose deshielding could be controlled by fluorescein. We then verified the tailoring of the trigger ligand by generating biotin-responsive liposomes. Finally, we demonstrated the versatility of the approach by controlling the transduction of cells through biotin-responsive AAVs.

For the establishment of our system, we used empty liposomes with a lipid composition similar to that of Doxil (the clinically used PEGylated liposomal formulation of the anthracycline doxorubicin), but omitting the PEGylated lipid component (i.e., 60 mol% hydrogenated soy phosphatidyl choline (HSPC), 40 mol% cholesterol).[36] First, we investigated whether the presence of fluorescein (Flu) or biotin on the surface of liposomes would interfere with cellular association. For this purpose, we prepared liposomes marked with the fluorescent lipophilic tracer DiD and quantified their association with HeLa cells via flow cytometry (**Figure 2**A and Figure S1, Supporting Information). When comparing the area under the curves (AUCs) of cellular association over time for the different liposome species, modification with neither fluorescein nor biotin had a negative impact on cell association (AUCs of kinetic curves for modified liposomes compared

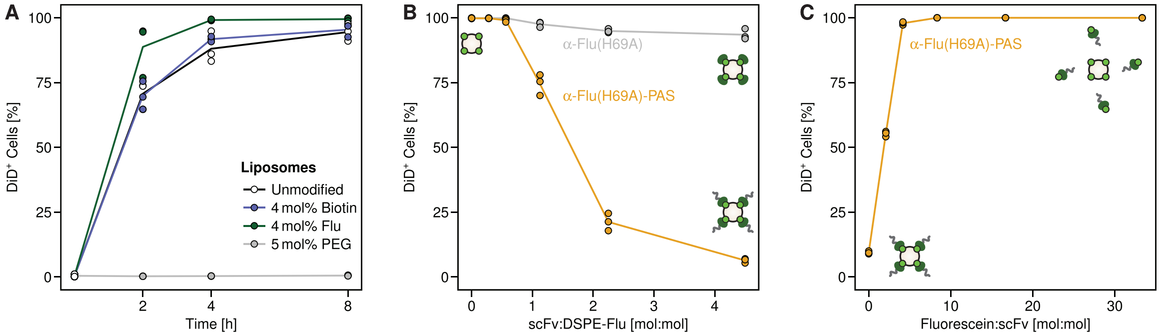

Figure 2. Shielding of fluorescein-modified liposomes by PASylated scFvs prevents association with cells. Liposomes labeled with the lipophilic fluorescent dye DiD are prepared and modified with 4 mol% distearoyl-phosphoethanolamine (DSPE)-Fluorescein, 4 mol% dipalmitoyl-phosphoethanolamine (DPPE)-Biotin, or 5 mol% DSPE-PEG2000. Liposomes (100 µM phospholipids, 167 µM total lipid) are incubated with HeLa cells and cell association is quantified by flow cytometry. A) Influence of liposome surface modification on cell association. Unmodified liposomes, or liposomes with ligands attached to lipid head groups (either biotin, fluorescein, or PEG2000) are incubated at 37 °C for the indicated time periods before cellular association is quantified. $n = 3$ per time point for each liposome type. B) Liposome shielding by scFvs. For the whole 24 h incubation period with fluoresceinated liposomes, an α-Flu scFv without or with a PAS tail of 11 PAS repeats is present at the indicated molar ratio relative to surface-accessible DSPE-Flu. The highest scFv:DSPE-Flu ratio corresponds to 15 µM α-Flu-PAS. $n = 3$ for each combination of scFv and scFv:DSPE-Flu ratio. C) Liposome deshielding by addition of free ligand. Fluoresceinated liposomes are shielded by incubation with PASylated α-Flu (molar ratio 4.5:1 relative to surface-accessible DSPE-Flu) and incubated with HeLa cells. After 2 h, fluorescein is added, and after 24 h, cellular association is quantified. $n = 3$ for each fluorescein:scFv ratio.

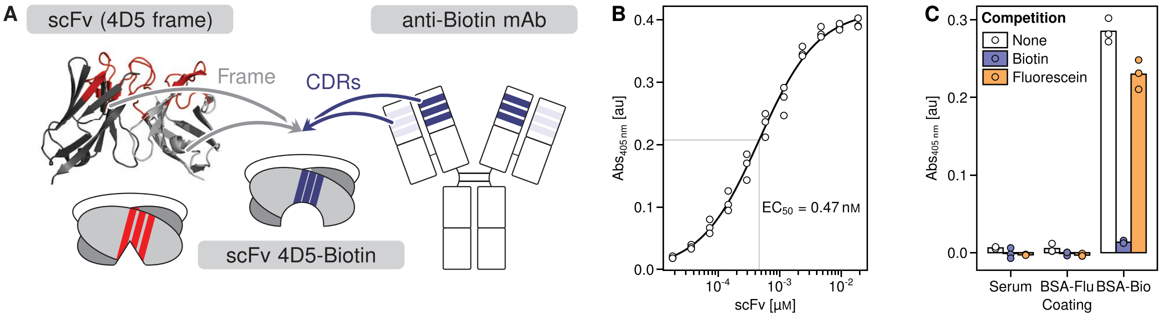

Figure 3. Design and characterization of a CDR-grafted biotin-binding scFv. A) Design of the CDR grafting. Framework regions are taken from the 4D5 V_H and V_L consensus sequences and combined with the CDR regions of a biotin-binding murine mAb. B) Binding curve of the grafted α-Biotin scFv. The binding capability of the grafted scFv to biotin-BSA is determined by ELISA. $n = 3$ for each scFv concentration. C) Specificity of the grafted α-Biotin scFv. Binding of the scFv to immobilized bovine serum, fluorescein-BSA, or biotin-BSA is measured by ELISA. For competition with the immobilized ligand, 500 µM free biotin or 500 µM free fluorescein is mixed with the scFv before addition to the coated wells. $n = 3$ for each combination of competition and coating.

to unmodified liposomes, $p > 0.9$, one-sided Dunnett test, $n = 3$ per group). In contrast, covalent PEGylation drastically reduced liposome association with cells as expected ($p < 0.001$ when AUCs of kinetic curves for PEGylated liposomes were compared to unmodified liposomes, one-sided Dunnett test, $n = 3$ per group).

Next, we tested whether we could shield fluoresceinated liposomes from cell association by non-covalent attachment of an scFv against fluorescein (α-Flu(H69A)), based on the FITC-E2 scFv[37] with an H69A mutation, facilitating production in *E. coli* at the expense of an increased K_D (from 0.75 to 8.9 nM).[38,39] To confer shielding properties on α-Flu(H69A), we fused 11 repeats of a 20 amino acid PAS sequence to its C terminus. α-Flu(H69A) and α-Flu(H69A)-PAS were produced in *E. coli* and purified by immobilized metal affinity chromatography (Figure S2A,B, Supporting Information).

To verify binding of the scFv to the liposomal surface, we measured the particle size of unshielded and shielded liposomes by dynamic light scattering (DLS; Figure S3, Supporting Information). Unshielded liposomes showed a Z average of (151 ± 2) nm, whereas this increased to (168 ± 7) nm for liposomes incubated with α-Flu(H69A), indicative of the increase in hydrodynamic radius by addition of the bulky PAS chains. This was in line with the previously reported hydrodynamic radius of a 200 amino acid (equivalent to 10 repeats) PAS peptide of approximately 4.9 nm.[35]

When the α-Flu(H69A) variants were allowed to bind to fluoresceinated liposomes and added to HeLa cells, α-Flu(H69A)-PAS dose-dependently reduced cellular association, whereas association remained high for α-Flu(H69A) without PAS (Figure 2B, Figure S4, Supporting Information). AUCs of the concentration curves differed significantly between both constructs when compared by *t*-test ($p < 0.001$, $n = 3$ per group), demonstrating that shielding of liposomes by attachment of a PASylated scFv is a feasible approach.

Next, we assessed the possibility of deshielding by addition of free ligand (Figures 1 and 2C and Figure S5, Supporting Information). To test this, we bound α-Flu(H69A)-PAS to fluoresceinated liposomes and incubated them with HeLa cells in the presence of different concentrations of free fluorescein. When association was quantified after 24 h, we found that fluorescein successfully deshielded the liposomes and reconstituted cellular association in a dose-dependent manner (Figure 2C and Figure S5, Supporting Information).

After we demonstrated (de)shielding with fluorescein, we tested whether we could adjust the system to respond to other trigger molecules by tailoring the small molecule-scFv affinity pair. For this purpose, we chose biotin as an alternative trigger molecule. In order to generate a biotin binder, we designed a humanized biotin-binding scFv from a biotin-binding murine monoclonal antibody (mAb).[40] We grafted the complementarity determining regions (CDRs) into the 4D5 scFv framework, a human consensus sequence originally applied to humanize the α-c-erbB2 mAb 4D5 (Herceptin)[41] (**Figure 3**A and Figure S6, Supporting Information). This antibody framework exhibits favorable folding and stability properties and has been successfully used for CDR grafting.[42,43] We produced the resulting α-Biotin scFv in *E. coli* and purified it by Protein L affinity chromatography (Figure S2C, Supporting Information). We measured the affinity of α-Biotin to biotinylated bovine serum albumin (BSA) by biolayer interferometry and determined its mean K_D at (66±21) nM (Figure S7A, Supporting Information). An ELISA experiment showed a half-maximal effective concentration (EC_{50}) of 0.47 nM (95% CI: 0.40–0.53 nM) (Figure 3B). Furthermore, competitive ELISAs revealed that free biotin competitively abolished binding of α-Biotin to BSA-Biotin, whereas fluorescein did not (Figure S7B, Supporting Information, and Figure 3C), confirming the specificity of α-Biotin to its ligand.

Next, we fused 11 PAS repeats to the C terminus of the biotin-binding scFv (α-Bio-PAS; Figure S2D, Supporting Information) and investigated its shielding capacity. Incubating biotinylated liposomes with α-Bio-PAS again reduced cellular association, and this effect was reversible by addition of free biotin (**Figure 4**A and Figure S8, Supporting Information). In contrast, α-Bio-PAS did not reduce cellular association of non-biotinylated liposomes, thus confirming specificity of the scFv binding (Figure S10A, Supporting Information).

Following these successful non-covalent shieldings of liposomes decorated with two distinct small molecules, we asked whether we could further extend our approach to another class of nanoparticle, and selected an adeno-associated viral

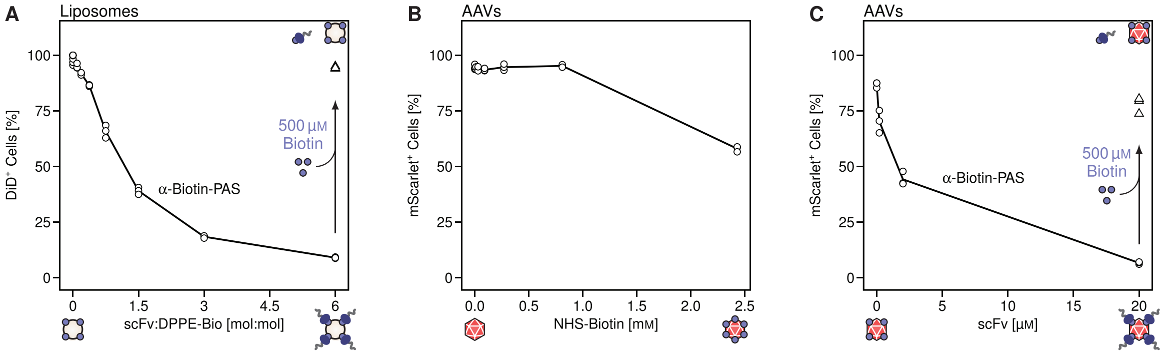

Figure 4. Shielding of biotin-modified liposomes or AAVs by PASylated scFvs prevents cellular association. A) Biotinylated DiD labeled liposomes are shielded (circles) with a PASylated (11 repeats) α-Biotin scFv (α-Biotin-PAS) and optionally deshielded (triangles) with 500 µM free biotin. After incubation with HeLa cells for 24 h, cell association is quantified by flow cytometry. The highest scFv:DPPE-Biotin ratio corresponds to 20 µM α-Biotin-PAS. For shielding, $n = 3$ for each scFv:DPPE-Bio ratio, except for the ratio of 0 ($n = 9$). For deshielding, $n = 3$. B) AAVs are surface-modified with NHS-biotin and the transduction efficiency is assessed by incubation with HEK-293T cells. After 24 h, mScarlet+ cells are quantified by flow cytometry. $n = 3$ for each NHS-Biotin concentration. C) Biotinylated AAVs (modified with 0.45 mM NHS-biotin) are shielded/deshielded as the liposomes in (A). Transduction efficiency is assessed by incubation with HeLa cells. For shielding, $n = 3$ for each scFv concentration. For deshielding, $n = 3$.

vector (AAV) for this purpose. AAV virions are approximately 25 nm in diameter and are a leading tool for therapeutic gene delivery.[44] We functionalized the surface of AAVs carrying a transgene for the fluorescent protein mScarlet[45] with NHS-biotin, which reacts with primary amines, and tested the effect on transduction (Figure 4B). At high NHS-biotin concentrations (>2.4 mM), transduction was markedly impaired, indicating modification of AAV surface structures crucial for transduction, or interference with AAV structure and/or stability. Therefore, we, chose an NHS-biotin concentration of 0.45 mM for labeling, which was not detrimental to AAV functionality. Shielding with α-Bio-PAS reduced the fraction of mScarlet+ transduced cells, whereas deshielding was accomplished after addition of free biotin (Figure 4C and Figure S9, Supporting Information). As for liposomes, addition of α-Bio-PAS to non-biotinylated liposomes did not decrease their transduction rate (Figure S10B, Supporting Information).

In summary, we could show that shielding of nanoparticles by non-covalent attachment of PASylated scFvs is feasible for different types of small molecules, and likewise for different types of nanoparticles.

2.2. Development of Fluorescein-Responsive Nanocomposite Hydrogels

Drawing inspiration from our previous experience with small molecule-responsive hydrogels[46] and incorporating our outlined strategy for nanoparticles, we set out to combine both approaches to develop controllable hydrogel-based depots for the triggered release of nanoparticles. First, we established the system with the example of fluorescein-responsive nanocomposite hydrogels for the release of liposomes and then demonstrated the versatility of the system by adapting it for the release of AAVs. The architecture of the gels consisted of non-covalently interacting 8-arm PEG-Fluorescein and 8-arm PEG-scFv conjugates. Entrapping fluorescein-labeled nanoparticles would allow to control their release and cellular interaction by the addition of free fluorescein, competitively displacing 8-arm PEG-Fluorescein and dissolving the hydrogel (**Figure 5**).

2.2.1. Generation of a Fluorescein-Binding scFv with Enhanced Stability

The synthesis reaction of fluorescein-responsive nanocomposite hydrogels based on the α-Flu scFv requires transiently high protein concentrations of approximately 60 to 70 mg mL^{-1} in order to meet the target concentration requirements of all reagents. Typically, such high protein concentrations are stabilized by addition of surfactants and excipients.[47] However, for hydrogel synthesis, reformulation of the scFv with additives is limited by the requirements for a defined reaction buffer.

As an alternative approach and encouraged by the successful construction of α-Biotin by grafting, we explored the possibility of increasing the stability of the anti-fluorescein scFv FITC-E2[37] by grafting its CDR regions to the 4D5 framework, resulting in α-Flu graft (Figure S11, Supporting Information).

We produced the grafted scFv in the cytosol of *E. coli* and used affinity chromatography for purification. Purification via a protein A agarose-based matrix yielded a higher purity compared to Ni^{2+}-NTA affinity chromatography (Figure S2E,F, Supporting Information).

To evaluate the fluorescein binding of the grafted scFv, we recorded a binding curve on immobilized, fluorescein-conjugated bovine serum albumin (BSA-Flu) by ELISA and obtained an EC$_{50}$ of 1.5 nM (95% CI: 1.3–1.6 nM) (Figure S12A, Supporting Information). Calculation of the dissociation constant from association and dissociation rates measured by biolayer interferometry yielded a dissociation constant (K_D) of 2 nM (Figure S13A, Supporting Information). Because framework residues can also contribute to antigen binding,[48] we compared the K_D of α-Flu and α-Flu graft by fluorescence quenching of fluorescein at different scFv concentrations

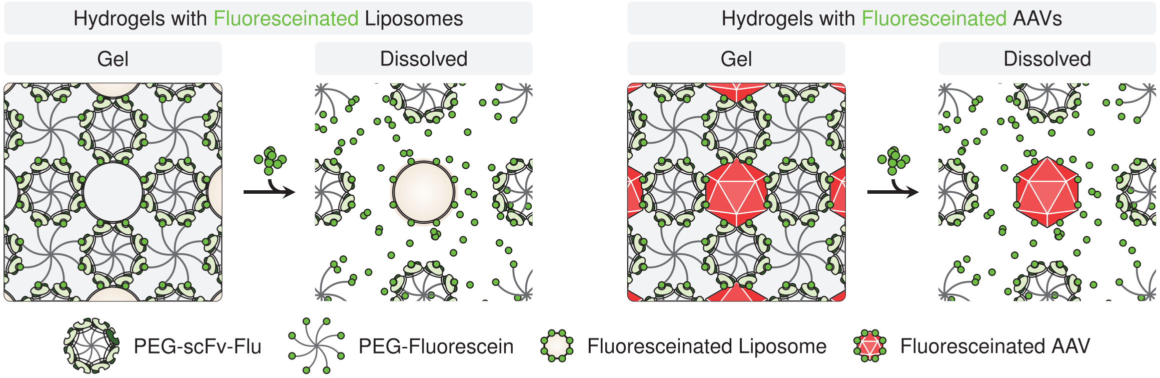

Figure 5. Active entrapment of liposomes or AAVs in fluorescein-responsive hydrogels. Multivalent interactions between 8-arm PEG fluorescein and 8-arm PEG-scFv conjugates result in the formation of a polymeric hydrogel network. Fluoresceinated liposomes or AAVs can actively participate in this interaction network and thus be immobilized. Addition of free fluorescein competes with the interactions stabilizing the hydrogel, resulting in its dissolution and release of its cargo. Illustrated components are not drawn to scale.

(Figure S13B, Supporting Information). Although we observed a slight decrease in affinity of α-Flu graft (K_D = 23.5 nM) in comparison to its ungrafted counterpart (K_D = 0.6 nM), the dissociation constant was still in the nanomolar range. Thus, the two methods were in good agreement within an order of magnitude and confirmed nanomolar affinity of the grafted scFv. As with α-Bio, we confirmed the specific binding of α-Flu graft to fluorescein by performing a competitive ELISA experiment. α-Flu graft only bound to immobilized BSA-Flu, but not to serum or BSA-Biotin. Only competition with free fluorescein abolished binding of the grafted scFv to the immobilized BSA-Flu (Figure S12B, Supporting Information).

Next, we characterized the grafted scFv with respect to its stability. We determined the thermal stability in comparison to the α-Flu(H69A) scFv. To this end, melting curves were determined by using SYPRO Orange, a dye that fluoresces upon binding to hydrophobic regions of denatured proteins. The grafted scFv showed a higher melting temperature (T_M = 70 °C) and thus a higher thermal stability than the CDR donor scFv (T_M = 60 °C) (Figure S12C, Supporting Information). Similarly, analysis of the tryptophan fluorescence in equilibrium denaturation experiments with guanidine hydrochloride revealed higher thermodynamic stability for the grafted scFv compared to the CDR donor scFv (Figure S12D, Supporting Information). These enhanced stability characteristics were also reflected in the binding capacity to BSA-Flu after prolonged storage. Whereas the ungrafted version lost approximately 50% activity after storage at 40 °C compared to storage at 4 °C for 3 weeks (as determined by ELISA), this deterioration was markedly diminished for the grafted variant even after 6 weeks (Figure S13C, Supporting Information).

2.2.2. Synthesis of Fluorescein-Responsive Hydrogels using the Grafted scFv

Following the successful graft of the FITC-E2 CDR regions into the stable 4D5 frame, we synthesized fluorescein-responsive hydrogels using this new variant.[46] To enable the chemoselective coupling to PEG-vinyl sulfone (PEG-VS), we fused a cysteine via a flexible serine-glycine linker to the C-terminus of the scFv (Figure S2G, Supporting Information). After letting the scFv bind to 8-arm PEG-fluorescein, we started the reaction of the 8-arm PEG-VS with the terminal cysteine by applying a one-pot thiol-ene click approach.[49] As a result, the PEG-fluorescein and PEG-scFv conjugates formed a stable hydrogel network. We qualitatively assessed different synthesis conditions and opted for performing all gel syntheses at a final scFv concentration of 30 mg mL^{-1} and a 1.5:1 molar ratio of PEG-VS:scFv (Figure S14, Supporting Information).

Afterward, we evaluated the mechanical properties and stimulus-responsiveness of the material (**Figure 6**). Amplitude sweep measurements at 1 Hz showed constant storage and loss moduli over a deformation range of ≈0.2% to 20% (Figure 6A). Subsequently, we performed rheology frequency-sweep experiments within the linear viscoelastic regime at a constant deformation of 0.5% (Figure 6B). In accordance with typical hydrogel properties, the storage modulus G′ exceeded the loss modulus G″ over the complete frequency range measured (0.01 to 1 Hz). At low frequencies, G′ decreased and G″ increased, indicating rearrangements of the physical crosslinks of the polymeric network typical for non-covalently crosslinked hydrogels.

Next, we quantified gel dissolution by measuring the amount of released protein in the supernatant. Without addition of free fluorescein, we observed a basal level, likely indicative of scFv molecules which had failed to undergo coupling to PEG-VS. Upon addition of increasing concentrations of fluorescein, the gels dissolved and their constituent protein was released in a dose-dependent fashion (Figure 6C). Addition of biotin instead of fluorescein did not result in protein release beyond the basal level, confirming the specific response of the hydrogels to the intended ligand (Figure S15, Supporting Information).

2.2.3. Active Entrapment of Liposomes or AAVs in Fluorescein-Responsive Hydrogels

The scale of typical pore sizes for hydrogels ranges from tens of nanometers[50] to tens of micrometers.[51,52] This is sufficiently

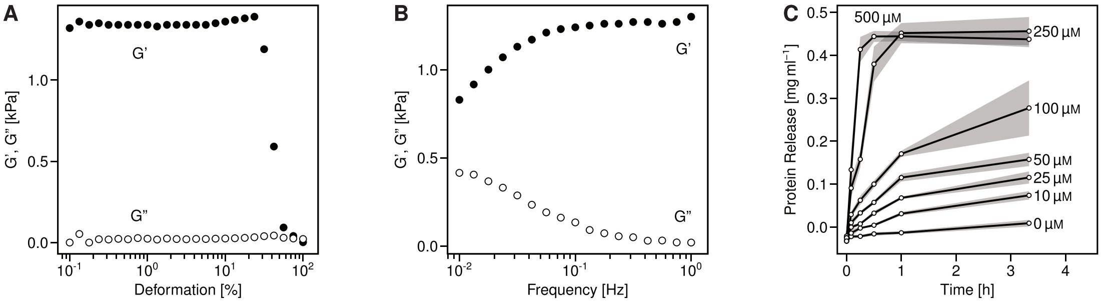

Figure 6. Synthesis and characterization of a fluorescein-responsive hydrogel. Hydrogels are synthesized using the grafted α-Flu scFv. A,B) Mechanical characterization. Hydrogel discs are pre-swollen in phosphate buffered saline (PBS). The storage (G′) and loss (G″) moduli are determined by small amplitude oscillatory shear rheology A) over a deformation range of 0.1 to 100% at 1 Hz, or B) over a frequency range of 0.01 to 1 Hz at a constant deformation of 0.5%. C) Fluorescein-triggered dissolution. Hydrogels are incubated in PBS with the indicated concentrations of free fluorescein. Dissolution is monitored by determining the released scFv in the supernatant with the bicinchoninic acid (BCA) assay. n = 6 gels per dissolution time course, symbols and lines mark the mean and ribbons show standard deviation.

small to passively entrap large complexes such as antigen-alum complexes,[46] which form micrometer-sized aggregates.[53] However, small molecules cannot be stably entrapped in this fashion because they would diffuse out of the hydrogel into the surrounding medium. This is apparent even for small proteins, which are released from porous hydrogels within a few hours.[54] Here, we investigated whether we could achieve liposome and AAV entrapment in fluorescein-responsive hydrogels.

When we added DiD labeled liposomes to the hydrogel synthesis reaction, we found that they did not remain stably associated, but passively diffused out of the gels even preceding addition of fluorescein to induce gel dissolution (**Figure** 7A and Figure S16A, Supporting Information). However, when we made fluorescein available on the surface of the liposomes by post-insertion[55] of DSPE-Flu (Figure S17, Supporting Information) and thus allowed the liposomes to be a structural component of the hydrogel framework, this leakiness was almost completely abolished, and release could still be triggered by free fluorescein (Figure 7A and Figure S16A, Supporting Information). The gels also tightly retained their cargo in synthetic body fluid (SBF, a buffer solution with ion concentrations closely mimicking acellular blood plasma[56]) and in complete cell culture medium with fetal calf serum (FCS). Fluorescein-triggered complete dissolution in these buffers was possible for at least 10 days after gel synthesis, although dissolution kinetics reduced slightly over time (Figure S16B, Supporting Information).

Next, we tested whether liposomes released from the gels would associate with cells. We prepared gels with different ratios of DSPE-Flu, placed the gels on HeLa cells, and measured liposome association after 24 h (Figure 7B and Figures S16C and S18, Supporting Information). Without a dissolution trigger, (49.9 ± 1.5)% of cells became DiD$^+$ upon incubation with hydrogels containing liposomes with 0.1 mol% DSPE-Flu, whereas this leakiness was reduced to (4.5 ± 2.6)% and (0.4 ± 0.2)% for liposomes with 0.25 mol% or 1.0 mol% DSPE-Flu, respectively. Dissolving the gels with 500 µM fluorescein increased the fraction of cells associated with liposomes to (95.4 ± 1.2)% for liposomes with 0.1 mol% and to (94.4 ± 0.3)% for liposomes with 0.25 mol% DSPE-Flu. Conversely, this increase only reached (52.8 ± 1.4)% for liposomes with 1 mol% DSPE-Flu. We hypothesize that this lower liposome-cell association was a consequence of residual PEG-scFv still attached to the liposomal surface, which acted as a shielding layer.

After establishing the gel system with empty liposomes, we extended it to cargo-loaded liposomes. We synthesized DiD labeled liposomes and performed remote-loading of doxorubicin via an ammonium sulfate gradient.[57] However, dry lipid cakes containing DSPE-Flu could not be hydrated in ammonium sulfate without the formation of aggregates, and the addition of doxorubicin to solutions containing DSPE-Flu likewise induced aggregation. To circumvent this issue, doxorubicin was first loaded into liposomes before addition of DSPE-Flu and subsequent post-insertion. This allowed encapsulation of doxorubicin into fluorescein-modified liposomes (Figure S19A, Supporting Information), but leakage was increased compared to unmodified liposomes (Figure S19B, Supporting Information).

The doxorubicin charged or empty liposomes were modified with 1 mol% DSPE-Flu by post-insertion and then used to synthesize hydrogels. After 24 h incubation with HeLa cells, we measured cell proliferation via WST-1 assay (Figure S20, Supporting Information). To avoid possible influences of physical contacts between cells and the gel matrix on the proliferation readout, the gels were placed in the upper compartment of a transwell insert without direct contact with the cell layer. We observed baseline toxicity of doxorubicin-charged hydrogels. Given that we observed negligible association between uncharged liposomes and cells without gel dissolution (Figure 7B), we speculated this was due to leakage of highly potent free doxorubicin from the charged liposomes, and not due to leakage of liposomes from the gel. Measurements of DiD and doxorubicin fluorescence in the supernatant supported this notion and revealed some leakage of doxorubicin, but not of liposomes (Figure S21, Supporting Information). Nevertheless, release of doxorubicin-loaded liposomes by addition of fluorescein significantly decreased cell viability ($p < 0.001$, t-test between conditions with and without addition of fluorescein, $n = 8$ per group), and the reduction in viability (to (49.8 ± 3.9)%) was in agreement with the previously observed fraction of cells

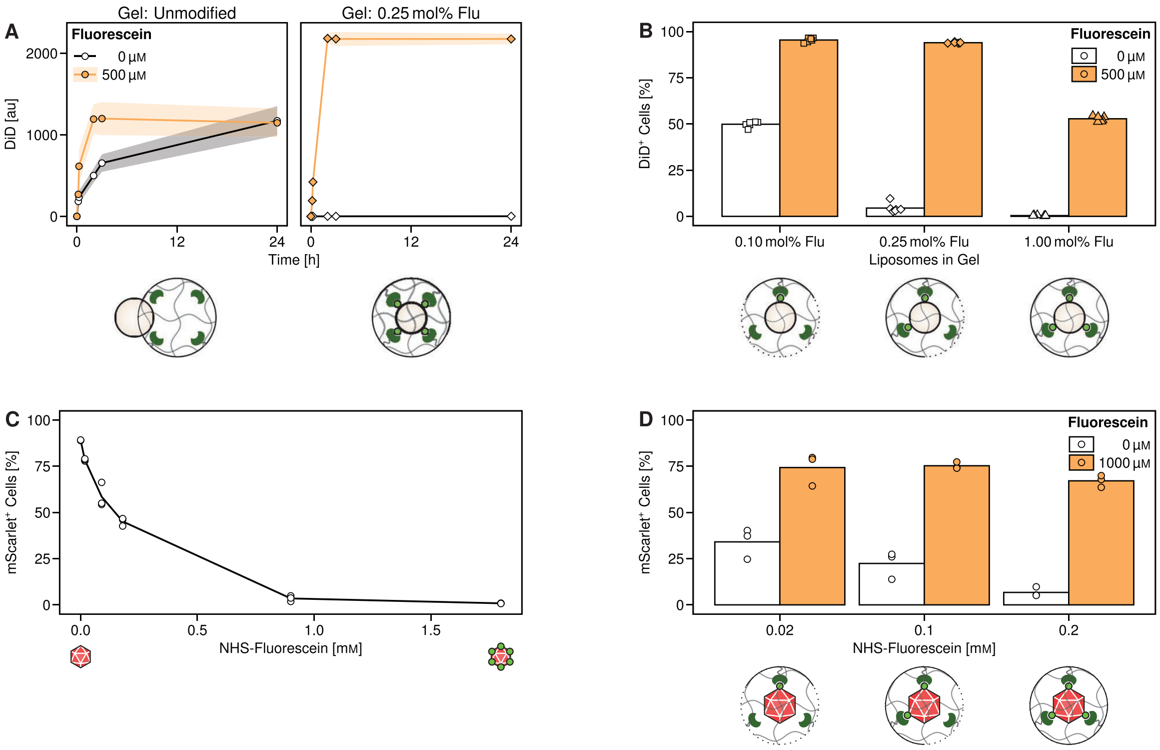

Figure 7. Entrapment of liposomes or AAVs in hydrogels and their fluorescein-dependent release. A) Fluorescein-dependent release kinetics of hydrogels with incorporated DiD labeled liposomes without (left panel) or with 0.25 mol% (right panel) surface-exposed fluorescein. Hydrogels are incubated in PBS with or without fluorescein and liposomal release is quantified by measuring DiD fluorescence in the supernatant. The difference in absolute values is due to loss of unmodified liposomes during wash steps (Figure S16A, Supporting Information). $n = 6$ gels for each dissolution time course, symbols mark the mean and ribbons show standard deviation. B) Availability of hydrogel-entrapped liposomes to cells. Hydrogels loaded with liposomes with the indicated amounts of surface-exposed fluorescein are placed on HeLa cells in complete medium with or without fluorescein. After 24 h, association of liposomes with cells is quantified by flow cytometry. $n = 6$ gels for each condition. C) AAVs carrying the mScarlet transgene are surface-modified with different concentrations of NHS-fluorescein. Transduction of HEK-293T cells is measured by flow cytometry after 24 h. $n = 3$ for each concentration of NHS-fluorescein. D) AAVs carrying the mScarlet transgene are surface-modified with different concentrations of NHS-fluorescein and concentrated via dialysis. The AAVs are entrapped in fluorescein-responsive hydrogels, which are placed on HeLa cells and incubated with or without fluorescein. After 24 h, transduction is quantified by flow cytometry. $n = 3$ gels for each condition.

associating with uncharged liposomes (52.8 ± 1.4%). In contrast, releasing empty liposomes did not significantly impact viability ($p > 0.3$, t-test between conditions with and without addition of fluorescein, $n = 8$ per group; Bonferroni corrected with prior t-test) (Figure S20, Supporting Information).

We next tested whether we could generalize our approach of releasing liposomes from a fluorescein-responsive hydrogel to another type of nanoparticle. As our experiments had demonstrated that scFvs could be used to confer shielding properties on AAVs, we chose this same type of AAV for our subsequent experiments.

We first verified if we could label AAV capsids with NHS-fluorescein and observed a dose-dependent decrease in transduction efficiency upon incubation with HEK-293T cells, compared to unmodified AAV (Figure 7C). For subsequent experiments, we chose NHS-fluorescein concentrations that did not abolish functionality of AAV (≤0.2 mM). We concentrated the fluoresceinated AAVs by ultrafiltration and prepared fluorescein-responsive hydrogels. When we placed these gels on HeLa cells, we saw a fluorescein dose-dependent increase in transduced mScarlet$^+$ cells, indicative of dissolution of the gels and release of AAVs (Figure S22, Supporting Information). However, incorporation of AAV into hydrogels was challenging, because ultrafiltration led to loss of a large fraction of input AAV. Consequently, transduction of only (18.7 ± 2.6)% of cells was achieved.

To address this limitation, we explored a more gentle approach for concentration: After coupling of AAVs with NHS-fluorescein, we placed them in a dialysis cassette and performed volume reduction by submersion in a buffer containing 40% (w/v) PEG-20. This allowed us to entrap a higher number of AAV particles in the hydrogels, resulting in high transduction ratios after dissolution of the gels (Figure 7D and Figure S23, Supporting Information). Of note, the transduction of HeLa cells by AAV released from the hydrogel depots was higher compared to the transduction of HEK-293T cells by "free" AAV labeled with the same concentration of NHS-fluorescein in Figure 7C. Since the AAV-2 transduction efficiency of both cell lines is comparable,[58,59] the difference is likely due to the higher concentration of AAV for gel synthesis and thus the entrapment and release of higher numbers of AAV particles per cell culture well. Similar to our observations for liposome-loaded gels, functionalization of AAV with higher amounts of fluorescein decreased leakiness, but also slightly impaired transduction after dissolution of the gels. This is likely a combination of the reduced AAV transduction efficiency after labeling and residual PEGylated scFvs acting as a shielding layer.

3. Conclusions

In this study, we demonstrated how the reversible interactions between scFvs and their ligands can be exploited for rational and modular nanoparticle design. By surface-functionalization of nanoparticles with scFv ligands, we upgraded the particles to allow attachment of functionally modified scFvs. Instead of pursuing further modification to the nanoparticles to accommodate different use cases, we customized the scFv component. Specifically, we showed shielding of nanoparticles from cellular binding by non-covalent attachment of a shielding polymer, and the active incorporation of nanoparticles into fluorescein-responsive hydrogels. We demonstrated the versatility of this approach by using the unrelated small molecules fluorescein and biotin, and two distinct types of nanoparticles, liposomes, and AAVs. Due to the reversibility of the exploited scFv-ligand interactions, we were able to detach the shielding layer or dissolve the hydrogels by the addition of a free trigger molecule, which was also used for the preceding functionalization of the nanoparticles. This form of exogenous stimulus-responsiveness provides a facile method for the scheduled activation of shielded nanoparticles, and for the dissolution of nanocomposite hydrogels.

Future efforts should be directed towards elucidating open questions regarding application of the prototypic systems presented herein for in vivo settings. For instance, the dose and the bioavailability of orally ingested or injected trigger molecules must be both tolerable and sufficient to induce release. Existing data for fluorescein suggests that this would be the case: In pigs, intravenous administration of 15 mg kg^{-1} fluorescein raised concentrations of fluorescein to approximately 10–20 g L^{-1} (30–60 µM) in a variety of tissues.[60] In a human patient, administration of an even higher dose (40 mg kg^{-1}) for delineation of a glioma during surgical resection was well tolerated,[61] although typically, lower doses (5–20 mg kg^{-1})[62,63] are used for this application. Importantly, there is direct evidence of the feasibility of administering high doses in mice: Four oral doses of ≈1000 mg kg^{-1}, given over three days, led to dissolution of a subcutaneously implanted fluorescein-responsive hydrogel.[46]

Likewise, the toxicity of biotin is low[24] and its LD_{50} value in rodents was >10 000 mg kg^{-1} (oral) or >1000 mg kg^{-1} (intravenous).[64] In rats, oral uptake of 1000 mg kg^{-1} day^{-1} over 36 weeks resulted in a peak plasma concentration of ≈10 µg mL^{-1} (40 µM).[64] On a functional level, it was shown that intraperitoneal administration of 100 mg kg^{-1} biotin could trigger a biotin-responsive gene switch in mice.[65]

Taken together, these data suggest that sufficient concentrations of fluorescein or biotin are attainable for triggering delivery systems responsive to these small molecules.

In summary, we showed that our system allows triggered delivery of small-molecule cargo in liposomes and of adeno-associated viral vectors in vitro.

4. Experimental Section

Plasmids and Protein Constructs: Plasmids and protein constructs used in this study are summarized in Table S1, Supporting Information, with DNA sequences, expression, and purification conditions. Buffer exchange of purified proteins into the respective assay buffer (as specified in the relevant experimental sections) was carried out by dialysis with SnakeSkin dialysis tubing (3.5 kDa MWCO, Thermo Fisher Scientific, #11532541). Proteins were concentrated by ultrafiltration in spin concentrators with a 10 kDa MWCO PES membrane (Sartorius, #VS15T02). Concentration of proteins in solution was determined with a NanoDrop 2000 spectrophotometer (Thermo Fisher Scientific), using theoretical extinction coefficients calculated by SnapGene (GSL Biotech).

Protein Production and Purification: For a summary of the expression and purification procedures used for different proteins, see Table S1, Supporting Information. After expression in *E. coli*, cells were harvested at 6000 g for 10 min and resuspended in 35 mL lysis buffer (50 mM NaH_2PO_4, 300 mM NaCl, 10 mM imidazole, pH 8.0) per 1 L culture. The cells were disrupted using a French press at 1000 bar and 4 °C. Insoluble material was removed by centrifugation at 30 000 g for 1 h at 4 °C. Optionally, proteins were precipitated in solutions of $(NH_4)_2SO_4$ for 1 h at 4 °C. The precipitate was pelleted by centrifugation at 30 000 g for 1 h at 4 °C and resuspended in lysis buffer. The resuspended precipitates or cleared lysates were purified by affinity chromatography with Ni-NTA agarose (Qiagen, #30450) or Capto L agarose (Cytiva, #17-5478-06) in manually packed gravity flow columns (bed volume 2 mL), or with a prepacked column of protein A agarose (GE Healthcare, #17-0403-01) on an Äkta Express fast protein liquid chromatography system (FPLC, GE Healthcare). Following sample loading, columns were washed with 20 column volumes of wash buffer and elution was performed with 6 column volumes of elution buffer.

For purification with Ni-NTA agarose, wash buffer was 50 mM NaH_2PO_4, 300 mM NaCl, 20 mM imidazole, pH 8.0, and elution buffer was 50 mM NaH_2PO_4, 300 mM NaCl, 250 mM imidazole, pH 8.0.

For purification with protein A or Capto L agarose, wash buffer was PBS (2.7 mM KCl, 1.5 mM KH_2PO_4, 8.1 mM Na_2HPO_4, 137 mM NaCl), and elution buffer was 0.1 M glycine, pH 3.0. After elution, the pH was neutralized by the addition of 1 column volume 1 M Tris-HCl (pH 8.0).

Purity was evaluated by sodium dodecyl sulfate (SDS)-polyacrylamide gel electrophoresis (SDS-PAGE) and subsequent Coomassie staining.

Preparation of Liposomes: Liposomes were prepared using the thin-film hydration method. Unmodified liposomes were prepared by mixing HSPC (Lipoid, #525600) and cholesterol (Sigma-Aldrich, #C3045) at a molar ratio of 60:40 in a 100 mL round bottom flask. Additional lipids were added at the expense of HSPC and cholesterol proportionally. The lipophilic tracer DiD (Thermo Fisher Scientific, #D7757) was included at a final concentration of 0.08 mol% for shielding experiments, or of 0.5 mol% for hydrogel experiments. For shielding experiments, final concentrations of 5 mol% DSPE-PEG2000 (Lipoid, #588200), 4 mol% DSPE-Flu or 4 mol% DPPE-Biotin (Avanti, #870285P), respectively, were also added. Chloroform was removed by rotary evaporation. The dry lipid film was hydrated in PBS at 70 °C with intermittent vortexing to achieve a final total lipid concentration of approximately 20 mM. The resulting heterogeneous liposome suspension was extruded using an Avanti Mini Extruder (Avanti, #610023) at 70 °C, with 23 passages through a 200 nm membrane (Cytiva, #10417004) and 12 passages through a 100 nm membrane (Cytiva, #800309). If required for downstream applications, liposomes were concentrated by ultrafiltration in spin concentrators with a 100 kDa MWCO RC membrane (Merck, #UFC810024). The lipid concentration of liposomes was determined by comparing the DiD fluorescence of the sample with a reference standard.

Fluorescence Measurements of Liposomes: All fluorescence measurements of DiD were made with an Infinite M200 pro microplate reader (Tecan) at 640 nm/680 nm (Ex/Em). Doxorubicin fluorescence was measured at 490 nm/580 nm (Ex/Em). If not specified otherwise, liposomes were lysed in PBS with 1% (v/v) Triton X-100 (Roth, #3051.4) at 70 °C for 15 min before measuring.

Post-Insertion and Doxorubicin Loading of Liposomes: For incorporation into hydrogels, liposomes were modified with DSPE-Flu by post-insertion, because DSPE-Flu was incompatible with hydration in 250 mM $(NH_4)_2SO_4$ required for doxorubicin loading.

DSPE-Flu was dried from chloroform and micellularly solubilized by hydration in PBS at 70 °C to a concentration of 3.84 mM. Micelles were added to liposomes in PBS (10 to 20 mM in 1 mL) to achieve the desired final mol% content of DSPE-Flu, assuming a post-insertion efficiency of 86% (Figure S17, Supporting Information). The mixture was incubated for 1 h at 70 °C, and unincorporated micelles were removed by gravity flow over 10 mL of a Sepharose CL-2B matrix (Cytiva, #17-0140-01).

For doxorubicin loading, liposomes were hydrated in 250 mM $(NH_4)_2SO_4$. After extrusion, a gradient was established by passage over a Sepharose CL-2B column equilibrated with PBS. Doxorubicin was added at a molar ratio of 1:3.5 (drug:lipid). Doxorubicin is carcinogenic and cardiotoxic, and must be handled with the necessary safety precautions. Loading was allowed to proceed for 30–45 min at 70 °C before performing post-insertion and removing unincorporated micelles and doxorubicin, as described above.

Cell Culture: HeLa cells and HEK-293T were cultured in DMEM (PAN Biotech, #P04-03550), supplemented with 10% (v/v) FCS (PAN Biotech, #P30-3602) and 1% (v/v) penicillin-streptomycin (PAN Biotech, #P06-07100) in a humidified atmosphere with 5% CO_2. If not specified otherwise, cells were seeded at a density of 5000 cells per well in a 96 well cell culture plate and assays were performed in a culture volume of 100 µL.

Flow Cytometry: The culture supernatant was removed, and cells were washed once with PBS before detachment with 50 µL Trypsin (PAN Biotech, #P10-023500). After incubation for 5 min at 37 °C, 50 µL FACS Buffer (PBS, 4% (v/v) FCS, 2 mM EDTA) were added, cells were centrifuged at 300 g for 5 min and resuspended in 200 µL FACS Buffer. Data were acquired on a Gallios flow cytometer (Beckmann Coulter) or an Attune NxT flow cytometer (Thermo Fisher Scientific) and analyzed with openCyto.[66] Association of liposomes with cells was quantified by gating for DiD^+ cells, whereas transduction by AAVs was quantified by gating for $mScarlet^+$ cells. Gates were constructed based on the untreated control after excluding debris and aggregates. Representative scatter plots illustrating the gating strategies are available in the Supporting Information.

Determination of Association Kinetics between Liposomes and Cells: Cells were seeded and allowed to adhere for 24 h. The culture medium was replaced by medium containing liposomes at phospholipid concentrations of 100 µM (167 µM total lipid) either 8, 4, or 2 h before analysis. Association of liposomes with cells was quantified via flow cytometry after incubation for the respective time spans at 37 °C.

Liposome Shielding and Deshielding: All proteins used for shielding were dialyzed against His Buffer (10 mM L-Histidine (Roth, #1696.2), 140 mM NaCl, pH 7.4) and concentrated to 5 to 10 mg mL^{-1}. Liposomes and shielding proteins were mixed in culture medium to achieve a final phospholipid concentration of 100 µM (167 µM total lipid) with varying molar ratios of protein to liposome-bound and surface-exposed ligand. For liposomes hydrated with DSPE-Flu or DPPE-Biotin, 50% of the incorporated ligand were assumed to be surface-exposed, with the other 50% facing the aqueous core of the liposome, rendering them inaccessible to proteins. For liposomes undergoing post-insertion, 100% of the ligand was assumed to be accessible. 100 µL of the liposome-protein mixture was added to cells 24 h after seeding and incubated for another 24 h before determination of liposome association with cells by flow cytometry. For deshielding experiments, free ligand was added 2 h after the start of the incubation period.

Viability Assay: Cells were seeded in MultiScreen 96 well receiver plates (Merck, #MATRNPS50), previously coated with 100 µg mL^{-1} rat collagen I (Thermo Fisher Scientific, #A1048301) in PBS for 3 h at room temperature. After 24 h, the culture supernatant was replaced with 300 µL fresh medium. A MultiScreen MESH Filter Plate (Merck, #MANMN2010) was placed on the plate, and 10 µL hydrogels were placed in the upper compartment before adding another 100 µL of medium. After 24 h, the culture supernatant was removed and replaced by 100 µL complete medium supplemented with a WST-1 based cell proliferation reagent (1:10 dilution; Sigma-Aldrich, #11644807001). The conversion of the tetrazolium salt WST-1 to a soluble formazan correlates with the metabolic activity of the cells and was monitored by measuring the increase in absorbance at 440 nm at 37 °C for 1 h.

Production and Purification of AAV-2 Vector: AAV-2 vector was produced using the adenovirus helper-free production system[67] and plasmids pHJW163 (AAV-2 rep-cap plasmid), pCMVmScarlet (vector plasmid; kind gift from Dirk Grimm), and pHelper (Cell Biolabs, #VPK-402) in a 1:1:2 molar ratio. Briefly, 5×10^6 HEK-293T cells (DSMZ, #ACC 635) were seeded in 15 cm cell culture dishes. After 48 h, the cells were transfected with 62.45 µg plasmid DNA, 206 µg polyethylene imine (25 000 Da), and 3 mL OptiMEM (Thermo Fisher Scientific, #22600-134). 5 h post-transfection, the cell culture medium was replaced with fresh medium. 72 h post-transfection, the cells were harvested by scraping them from the culture dishes and centrifuged at 400 g for 15 min. AAV-2 vector was purified from both the supernatant and cell pellet.

AAV-2 vector in the supernatant was precipitated by the addition of 25 mL PEG-8000 solution (40% (w/v), 0.41 M NaCl) per 100 mL of cell culture supernatant and stirring for 1 h at 4 °C, followed by an additional incubation step overnight without stirring. Precipitated vector was pelleted by centrifugation at 2818 g for 15 min at 4 °C and then resuspended in PBS. AAV-2 vector in the cells was released by washing the cell pellet first in PBS and then in virus lysis solution (50 mM Tris-HCl, 150 mM NaCl, pH 8.5), followed by five freeze-thaw cycles.

Vector preparations derived from the supernatant and cell pellet were combined and treated with benzonase (50 U mL^{-1}, Merck, #344 70664-3) at 37 °C for 1 h. Cellular debris was removed by three rounds of centrifugation at 4000 g for 15 min. The cleared AAV-2 vector sample was filtered through a 0.45 µm filter (Fisher Scientific, #15191499) and applied to a HiTrap AVB Sepharose column (Cytiva, #28411211) equilibrated with AVB wash buffer (20 mM Tris, 0.5 M NaCl, pH 8.0) using an Äkta Express FPLC system (GE Healthcare). After washing with 10 column volumes wash buffer, AAV-2 was eluted with 0.1 M sodium acetate, 0.5 M NaCl, pH 2.5, and the pH was neutralized with 1 M Tris, pH 8.7. Purified AAV-2 vector was dialyzed against 50 mM HEPES, 150 mM NaCl, and 2 mM $MgCl_2$, pH 7.4, supplemented with 10% (v/v) glycerol, and stored at −80 °C until use. Capsid titers were determined as described elsewhere.[68]

Synthesis of Biotin-rAAV-2 and Fluorescein-rAAV-2 Conjugates: NHS-biotin (Cayman Chemical, #Cay13315-100) and NHS-fluorescein (Thermo Fisher Scientific, #46410) were dissolved in *N*,*N*-Dimethylformamid (anhydrous; Sigma-Aldrich, #227056) to a final concentration of 20 mM. For the conjugation of biotin or fluorescein to rAAV-2, 1.12×10^{11} viral particles (VP) mL^{-1} were mixed with the indicated concentrations of NHS-biotin stock or NHS-fluorescein stock, respectively, and allowed to react for 3 h at room temperature. Unreacted NHS-biotin or NHS-fluorescein was removed by dialysis against 20 mM HEPES, 150 mM NaCl, 2 mM EDTA, 2 mM $MgCl_2$, 0.001% (v/v) Pluronic F-68, pH 7.4.

AAV Shielding and Deshielding: AAV shielding experiments were performed similarly to liposome shielding experiments, but 0.75 µL (8.4×10^7 VP) of biotinylated AAVs were used for transduction of each well. AAVs used for shielding experiments were biotinylated with 0.45 mM of NHS-biotin stock.

Determination of Particle Size by DLS: Liposomes (100 µM total lipid) were incubated with PASylated proteins (10 µM) in His buffer for 1 h at 37 °C. DLS was performed in a Zetasizer Nano S90 (Malvern) at 25 °C and a scattering angle of 90°.

Evaluation of Protein Stability: The thermal stability of scFvs was determined using the fluorescent SYPRO Orange dye (Thermo Fisher

Scientific, #S6650) in a real-time PCR thermal cycler (qTower 2.0/2.2, Analytik Jena). The scFv samples were prepared in PBS (4 µM final concentration) containing SYPRO Orange dye (diluted 1:1250). Thermal melting curves were recorded at 565 nm/606 nm (Ex/Em) by raising the temperature from 25 to 90 °C at intervals of 1 °C every 30 s.

Thermodynamic stabilities were determined by incubating the scFv constructs (0.8 µM of the grafted construct and 0.6 µM of the CDR donor scFv FITC-E2 (H69A) construct) with different concentrations of guanidine hydrochloride in 50 mM Tris-HCl, 100 mM NaCl, pH 7.2 at room temperature overnight. Tryptophan fluorescence maxima were determined by recording the emission intensities from 300 to 360 nm at an excitation wavelength of 280 nm in an Infinite M200 pro microplate reader (Tecan). Data analysis was conducted as described elsewhere.[69]

ELISA: ELISA was performed by coating 96 well plates (Corning, #CORN3590) with fluorescein- or biotin-conjugated BSA (Roth, #T844.3; 1 µg in 100 µL PBS per well) overnight at room temperature. Wells were washed 3× with 300 µL wash buffer (PBS, supplemented with 0.05% (v/v) Tween-20) and blocked with 300 µL blocking buffer (1% (w/v) BSA in PBS) for 1 h at room temperature. After washing 3× with wash buffer, the wells were incubated with scFv samples (diluted in blocking buffer) for 1 h at room temperature. Wells were washed 3× with wash buffer, probed with 100 µL anti-His antibody (1:1000 in blocking buffer; Merck, #70796) for 1 h at room temperature, washed again and incubated with anti-mouse IgG-HRP (1:2500 in blocking buffer; Santa Cruz, #sc-2005) for 1 h at room temperature. After washing 3× with wash buffer, the HRP activity was monitored by adding 100 µL 2,2′-azino-bis(3-ethylbenzothiazoline-6-sulphonic acid) (ABTS, Sigma-Aldrich, #A1888; 0.5 mM in 50 mM citric acid, pH 4.0, supplemented with 0.05% (v/v) H_2O_2) and measuring the absorbance at 405 nm in a microplate spectrophotometer. For competitive ELISA assays, the competing ligand was mixed with the scFv 30 min prior to addition to the coated wells.

Determination of Dissociation Constant by Fluorescence Titration: Dissociation constants of scFv-fluorescein affinity pairs were determined by fluorescence titrations.[38] Fluorescence spectra from 500 to 550 nm (440 nm excitation) were measured using dilutions of scFv (0 µM to 3 µM) and 0.1 µM fluorescein at room temperature. The fluorescence intensity maxima (at 516 nm) were plotted against the scFv concentrations and K_D values were calculated as described elsewhere.[38]

Biolayer Interferometry: Association and dissociation rates were determined by biolayer interferometry using the Octet RED96 System (Pall ForteBio LLC) at an assay temperature of 30 °C. Aminopropylsilane (APS) biosensors were loaded with unconjugated BSA, or with fluorescein- or biotin-conjugated BSA (10 µg mL^{-1} in PBS). After equilibration with assay buffer (PBS supplemented with 1% (w/v) BSA), the association of dilutions of scFv was monitored, followed by their dissociation in assay buffer. Control biosensors loaded with unconjugated BSA, which showed no association with the highest applied scFv concentrations, were used as reference for the biotin-binding scFv and were subtracted from the data. Similarly, the highest applied fluorescein-scFv showed no unspecific association to BSA. The background signal of biosensors loaded with fluorescein-BSA was subtracted from the data. Association and dissociation curves were locally fitted according to a 1:1 bimolecular interaction model (full fit for the α-Flu scFv, partial fit for the α-Biotin scFv).

Hydrogel Synthesis: For the synthesis of hydrogels, purified scFvs were dialyzed against hydrogel buffer (20 mM HEPES, 500 mM NaCl, pH 8.0). Typical 5 µL hydrogels were prepared by combining 150 µg scFv with tris-(2-carboxyethyl)-phosphine (TCEP; Roth, #HN95.1; TCEP:scFv = 0.7; mol:mol) and adding 0.5 µL 1 M triethanolamine (Roth, #6300.1), pH 8.0, and 8-arm PEG-fluorescein (scFv:fluorescein = *1:1.2;* mol:mol).[46] After incubation at room temperature for 30 min, 8-arm PEG-VS (40 kDa; NOF Europe, #Sunbright HGEOS-400VS) was added at a molar ratio of 1:1.5 (scFv:VS).

For the synthesis of liposome-loaded hydrogels, liposomes were added to the reaction mixture to a final concentration of 10 mM. For liposomes containing fluorescein, the total amount of fluorescein in the reaction was kept constant by reducing the amount of 8-arm PEG-fluorescein proportionally.

For the synthesis of rAAV-2 depots, purified rAAV-2 was concentrated by dialysis against 40% (w/v) PEG-20 (Sigma-Aldrich, #81300), 0.001% (v/v) Pluronic F-68, 20 mM HEPES, 500 mM NaCl, pH 8.0 for 40 min at room temperature using Slide-A-Lyzer dialysis cassettes (10 kDa MWCO, Thermo Fisher Scientific, #66383). The concentrated rAAV-2 (5×10^8 VP per 5 µL gel) was mixed with the hydrogel mixture prior to the addition of 8-arm PEG-VS.

The reactions were pipetted onto siliconized (Sigmacote; Sigma-Aldrich, #SL2) glass slides and incubated at room temperature in a humidified atmosphere for 20 h. After polymerization, the hydrogels were transferred into 300 µL hydrogel buffer supplemented with 100 mM monoethanolamine (Sigma-Aldrich, #E0135) to quench unreacted groups for 2 h at room temperature. Subsequently, gels were washed 3× in the buffer used for downstream applications for 1 h at room temperature.

Mechanical Hydrogel Characterization: 50 µL hydrogels were prepared between siliconized glass slides (1 mm height) and incubated in PBS at room temperature overnight. Small amplitude oscillatory shear measurements were conducted using an MCR301 rheometer (Anton Paar) with parallel plates at 25 °C. The hydrogels were placed between the plates (upper plate: 8 mm diameter, PP08, Anton Paar) and the gap was adjusted to 0.3 mm.

Statistics: Sample sizes in cell culture experiments reflect independently treated wells of a culture plate.

Statistical testing of liposome association was performed by calculating the AUC for each time course (for Figure 2A) or each concentration series (Figure 2B). AUCs were determined with the trapezoidal rule. For this purpose, individual data points were arbitrarily assigned to a replicate number for each x value, and AUCs were calculated for the curves formed by these replicates.

Data ranges in the text reflect mean ± standard deviation, except for EC_{50} and IC_{50} values.

To determine absolute EC_{50} and IC_{50} values by ELISA, the *drc* package[70] for R 4.1.1[71] was used. The indicated errors represent 95% confidence intervals.

Supporting Information

Supporting Information is available from the Wiley Online Library or from the author.

Acknowledgements

The authors are grateful for outstanding technical support by Denise Gaspar, Elke Wehinger-Welte, Susanne Knall, and Frauke Bartels-Burgahn. The authors would also like to thank Dirk Grimm (Heidelberg University, Germany) for providing the plasmid pCMVmScarlet. This work was supported by the Deutsche Forschungsgemeinschaft (DFG, German Research Foundation) under Germany's Excellence Strategy CIBSS – EXC-2189 – Project ID: 390939984 and under the Excellence Initiative of the German Federal and State Governments – EXC-294 and GSC-4, and in part by the Ministry for Science, Research and Arts of the State of Baden-Württemberg. This work was supported by the EU Framework Programme for Research and Innovation Horizon 2020 with a Grant from the European Research Council (ERC) Action No. 755369-DeShield.

Open access funding enabled and organized by Projekt DEAL.

Conflict of Interest

The University of Freiburg has filed a patent application of which B.R., M.D.Z., and W.W. are inventors. The remaining authors have no competing interests to declare.

Data Availability Statement

Research data are not shared.

Keywords

adeno-associated viruses, complementarity determining region grafting, hydrogels, nanoparticles, PAS, single-chain variable fragments, stimulus-responsive systems

Received: August 26, 2021
Revised: October 24, 2021
Published online: December 3, 2021

---

[1] T. M. Allen, C. Hansen, *Biochim. Biophys. Acta, Biomembr.* **1991**, *1068*, 133.
[2] D. Peer, J. M. Karp, S. Hong, O. C. Farokhzad, R. Margalit, R. Langer, *Nat. Nanotechnol.* **2007**, *2*, 751.
[3] E. Fleige, M. A. Quadir, R. Haag, *Adv. Drug Deliv. Rev.* **2012**, *64*, 866.
[4] E. Blanco, H. Shen, M. Ferrari, *Nat. Biotechnol.* **2015**, *33*, 941.
[5] A. Wörz, B. Berchtold, K. Moosmann, O. Prucker, J. Rühe, *J. Mater. Chem. B* **2012**, *22*, 19547.
[6] T. R. Hoare, D. S. Kohane, *Polymer* **2008**, *49*, 1993.
[7] C. J. Kearney, D. J. Mooney, *Nat. Mater.* **2013**, *12*, 1004.
[8] A. N. Zelikin, C. Ehrhardt, A. M. Healy, *Nat. Chem.* **2016**, *8*, 997.
[9] M.-T. Popescu, S. Mourtas, G. Pampalakis, S. G. Antimisiaris, C. Tsitsilianis, *Biomacromolecules* **2011**, *12*, 3023.
[10] B. E. B. Jensen, L. Hosta-Rigau, P. R. Spycher, E. Reimhult, B. Städler, A. N. Zelikin, *Nanoscale* **2013**, *5*, 6758.
[11] A. K. Gaharwar, N. A. Peppas, A. Khademhosseini, *Biotechnol. Bioeng.* **2014**, *111*, 441.
[12] P. Lavrador, M. R. Esteves, V. M. Gaspar, J. F. Mano, *Adv. Funct. Mater.* **2021**, *31*, 2005941.
[13] H. Hatakeyama, H. Akita, H. Harashima, *Adv. Drug Deliv. Rev.* **2011**, *63*, 152.
[14] H. Hatakeyama, H. Akita, H. Harashima, *Biol. Pharm. Bull.* **2013**, *36*, 892.
[15] M. C. Koetting, J. T. Peters, S. D. Steichen, N. A. Peppas, *Mater. Sci. Eng., R* **2015**, *93*, 1.
[16] S. Mura, J. Nicolas, P. Couvreur, *Nat. Mater.* **2013**, *12*, 991.
[17] N. Kamaly, B. Yameen, J. Wu, O. C. Farokhzad, *Chem. Rev.* **2016**, *116*, 2602.
[18] S. L. Pedersen, T. H. Huynh, P. Pöschko, A. S. Fruergaard, M. T. Jarlstad Olesen, Y. Chen, H. Birkedal, G. Subbiahdoss, E. Reimhult, J. Thøgersen, A. N. Zelikin, *ACS Nano* **2020**, *14*, 9145.
[19] R. Mo, T. Jiang, R. DiSanto, W. Tai, Z. Gu, *Nat. Commun.* **2014**, *5*, 3364.
[20] R. Mo, T. Jiang, Z. Gu, *Angew. Chem., Int. Ed.* **2014**, *53*, 5815.
[21] A. Matsumoto, T. Ishii, J. Nishida, H. Matsumoto, K. Kataoka, Y. Miyahara, *Angew. Chem., Int. Ed.* **2012**, *51*, 2124.
[22] K. R. Fruehauf, T. I. Kim, E. L. Nelson, J. P. Patterson, S.-W. Wang, K. J. Shea, *Biomacromolecules* **2019**, *20*, 2703.
[23] K. O'goshi, J. Serup, *Skin Res. Technol.* **2006**, *12*, 155.
[24] J. Zempleni, T. Kuroishi, *Adv. Nutr.* **2012**, *3*, 213.
[25] Institute of Medicine, *Dietary Reference Intakes: The Essential Guide to Nutrient Requirements*, National Academies Press, Washington, DC **2006**.
[26] S. L. Yankell, J. J. Loux, *J. Periodontol.* **1977**, *48*, 228.
[27] D. M. Mock, *J. Nutr.* **2017**, *147*, 1487.
[28] L. Chatenoud, J. A. Bluestone, *Nat. Rev. Immunol.* **2007**, *7*, 622.
[29] M. X. Sliwkowski, I. Mellman, *Science* **2013**, *341*, 1192.
[30] T. Miyata, N. Asami, T. Uragami, *Nature* **1999**, *399*, 766.
[31] J. F. Rippmann, M. Klein, C. Hoischen, B. Brocks, W. J. Rettig, J. Gumpert, K. Pfizenmaier, R. Mattes, D. Moosmayer, *Appl. Environ. Microbiol.* **1998**, *64*, 4862.
[32] L. Vaks, I. Benhar, in *Human Monoclonal Antibodies: Methods and Protocols* (Ed: M. Steinitz), Humana Press, Totowa, NJ **2014**, pp. 171–184.
[33] J. Lobstein, C. A. Emrich, C. Jeans, M. Faulkner, P. Riggs, M. Berkmen, *Microb. Cell Fact.* **2012**, *11*, 56.
[34] M. Schlapschy, U. Binder, C. Börger, I. Theobald, K. Wachinger, S. Kisling, D. Haller, A. Skerra, *Protein Eng., Des. Sel.* **2013**, *26*, 489.
[35] J. Breibeck, A. Skerra, *Biopolymers* **2018**, *109*, e23069.
[36] Y. Bavli, I. Winkler, B. M. Chen, S. Roffler, R. Cohen, J. Szebeni, Y. Barenholz, *J. Control. Release* **2019**, *306*, 138.
[37] T. J. Vaughan, A. J. Williams, K. Pritchard, J. K. Osbourn, A. R. Pope, J. C. Earnshaw, J. McCafferty, R. A. Hodits, J. Wilton, K. S. Johnson, *Nat. Biotech.* **1996**, *14*, 309.
[38] G. Pedrazzi, F. Schwesinger, A. Honegger, C. Krebber, A. Plückthun, *FEBS Lett.* **1997**, *415*, 289.
[39] A. Honegger, S. Spinelli, C. Cambillau, A. Plückthun, *Prot. Sci.* **2005**, *14*, 2537.
[40] F. Kohen, H. Bagci, G. Barnard, E. A. Bayer, B. Gayer, D. G. Schindler, E. Ainbinder, M. Wilchek, in *Methods in Enzymology*, Academic Press, Cambridge **1997**, pp. 451–463.
[41] P. Carter, L. Presta, C. M. Gorman, J. B. Ridgway, D. Henner, W. L. Wong, A. M. Rowland, C. Kotts, M. E. Carver, H. M. Shepard, *Proc. Natl. Acad. Sci. U. S. A.* **1992**, *89*, 4285.
[42] S. Jung, A. Plückthun, *Protein Eng., Des. Sel.* **1997**, *10*, 959.
[43] J. Willuda, A. Honegger, R. Waibel, P. A. Schubiger, R. Stahel, U. Zangemeister-Wittke, A. Plückthun, *Cancer Res.* **1999**, *59*, 5758.
[44] H. J. Wagner, W. Weber, M. Fussenegger, *Adv. Sci.* **2021**, *8*, 2004018.
[45] D. S. Bindels, L. Haarbosch, L. van Weeren, M. Postma, K. E. Wiese, M. Mastop, S. Aumonier, G. Gotthard, A. Royant, M. A. Hink, T. W. J. Gadella, *Nat. Methods* **2017**, *14*, 53.
[46] R. J. Gübeli, D. Hövermann, H. Seitz, B. Rebmann, R. G. Schoenmakers, M. Ehrbar, G. Charpin-El Hamri, M. Daoud-El Baba, M. Werner, M. Müller, W. Weber, *Adv. Funct. Mater.* **2013**, *23*, 5355.
[47] B. A. Kerwin, *J. Pharm. Sci.* **2008**, *97*, 2924.
[48] I. Sela-Culang, V. Kunik, Y. Ofran, *Front. Immunol.* **2013**, *4*, 302.
[49] M. W. Jones, G. Mantovani, S. M. Ryan, X. Wang, D. J. Brayden, D. M. Haddleton, *Chem. Commun.* **2009**, 5272.
[50] M. Hörner, K. Raute, B. Hummel, J. Madl, G. Creusen, O. S. Thomas, E. H. Christen, N. Hotz, R. J. Gübeli, R. Engesser, B. Rebmann, J. Lauer, B. Rolauffs, J. Timmer, W. W. A. Schamel, J. Pruszak, W. Römer, M. D. Zurbriggen, C. Friedrich, A. Walther, S. Minguet, R. Sawarkar, W. Weber, *Adv. Mater.* **2019**, *31*, 1806727.
[51] Y.-C. Chiu, M.-H. Cheng, H. Engel, S.-W. Kao, J. C. Larson, S. Gupta, E. M. Brey, *Biomaterials* **2011**, *32*, 6045.
[52] J. Yu, X. Xu, F. Yao, Z. Luo, L. Jin, B. Xie, S. Shi, H. Ma, X. Li, H. Chen, *Int. J. Pharm.* **2014**, *470*, 151.
[53] H. HogenEsch, D. T. O'Hagan, C. B. Fox, *npj Vaccines* **2018**, *3*, 51.
[54] M. S. Rehmann, K. M. Skeens, P. M. Kharkar, E. M. Ford, E. Maverakis, K. H. Lee, A. M. Kloxin, *Biomacromolecules* **2017**, *18*, 3131.
[55] P. S. Uster, T. M. Allen, B. E. Daniel, C. J. Mendez, M. S. Newman, G. Z. Zhu, *FEBS Lett.* **1996**, *386*, 243.
[56] S. Jalota, S. B. Bhaduri, A. C. Tas, *Mater. Sci. Eng., C* **2008**, *28*, 129.
[57] G. Haran, R. Cohen, L. K. Bar, Y. Barenholz, *Biochim. Biophys. Acta* **1993**, *1151*, 201.
[58] B. L. Ellis, M. L. Hirsch, J. C. Barker, J. P. Connelly, R. J. Steininger, M. H. Porteus, *Virol. J.* **2013**, *10*, 74.
[59] A. Westhaus, M. Cabanes-Creus, A. Rybicki, G. Baltazar, R. G. Navarro, E. Zhu, M. Drouyer, M. Knight, R. F. Albu, B. H. Ng, P. Kalajdzic, M. Kwiatek, K. Hsu, G. Santilli, W. Gold, B. Kramer, A. Gonzalez-Cordero, A. J. Thrasher, I. E. Alexander, L. Lisowski, *Hum. Gene Ther.* **2020**, *31*, 575.
[60] M. Kunes, J. Kvetina, J. Malakova, J. Bures, M. Kopacova, S. Rejchrt, *Neuroendocrinol. Lett.* **2010**, *31*, 57.
[61] E. Belykh, N. R. Onaka, X. Zhao, I. Abramov, J. M. Eschbacher, P. Nakaji, M. C. Preul, *Front. Neurol.* **2021**, *12*, 1169.
[62] F. Acerbi, C. Cavallo, M. Broggi, R. Cordella, E. Anghileri, M. Eoli, M. Schiariti, G. Broggi, P. Ferroli, *Neurosurg. Rev.* **2014**, *37*, 547.

[63] F. Acerbi, M. Broggi, K.-M. Schebesch, J. Höhne, C. Cavallo, C. D. Laurentis, M. Eoli, E. Anghileri, M. Servida, C. Boffano, B. Pollo, M. Schiariti, S. Visintini, C. Montomoli, L. Bosio, E. L. Corte, G. Broggi, A. Brawanski, P. Ferroli, *Clin. Cancer Res.* **2018**, *24*, 52.
[64] L. P. S. Paul, D. Debruyne, D. Bernard, D. M. Mock, G. L. Defer, *Expert Opin. Drug Metab. Toxicol.* **2016**, *12*, 327.
[65] W. Weber, J. Stelling, M. Rimann, B. Keller, M. D.-E. Baba, C. C. Weber, D. Aubel, M. Fussenegger, *Proc. Natl. Acad. Sci. U. S. A.* **2007**, *104*, 2643.
[66] G. Finak, J. Frelinger, W. Jiang, E. W. Newell, J. Ramey, M. M. Davis, S. A. Kalams, S. C. De Rosa, R. Gottardo, *PLoS Comput. Biol.* **2014**, *10*, e1003806.
[67] X. Xiao, J. Li, R. J. Samulski, *J. Virol.* **1998**, *72*, 2224.
[68] D. Grimm, A. Kern, M. Pawlita, F. Ferrari, R. Samulski, J. Kleinschmidt, *Gene Ther.* **1999**, *6*, 1322.
[69] E. Monsellier, H. Bedouelle, *Protein Eng., Des. Sel.* **2005**, *18*, 445.
[70] C. Ritz, F. Baty, J. C. Streibig, D. Gerhard, *PLoS One* **2015**, *10*, e0146021.
[71] R. Core Team, *R: A Language and Environment for Statistical Computing*, R Foundation For Statistical Computing, Vienna, Austria **2021**.

Received: 26 December 2022 | Revised: 21 March 2023 | Accepted: 9 April 2023
DOI: 10.1002/btpr.3346

BIOTECHNOLOGY PROGRESS

RESEARCH ARTICLE

Applied Cellular Physiology and Metabolic Engineering

Transcriptomic features reveal molecular signatures associated with recombinant adeno-associated virus production in HEK293 cells

Yongdan Wang[1] | **Qiang Fu**[2] | **Yong Suk Lee**[3] | **Sha Sha**[1] | **Seongkyu Yoon**[1]

[1]Department of Chemical Engineering, University of Massachusetts Lowell, Lowell, Massachusetts, USA

[2]Department of Biomedical Engineering and Biotechnology, University of Massachusetts Lowell, Lowell, Massachusetts, USA

[3]Department of Pharmaceutical Sciences, University of Massachusetts Lowell, Lowell, Massachusetts, USA

Correspondence
Seongkyu Yoon and Sha Sha, 1 University Avenue, Lowell, MA 01854, USA.
Email: seongkyu_yoon@uml.edu; xiami1117@gmail.com

Funding information
National Science Foundation, Grant/Award Number: 1624684 2100075; National Institute for Innovation in Manufacturing Biopharmaceuticals, Grant/Award Number: 70NANB17H002

Abstract

The development of gene therapies based on recombinant adeno-associated viruses (rAAVs) has grown exponentially, so the current rAAV manufacturing platform needs to be more efficient to satisfy rising demands. Viral production exerts great demand on cellular substrates, energy, and machinery; therefore, viral production relies heavily on the physiology of the host cell. Transcriptomics, as a mechanism-driven tool, was applied to identify significantly regulated pathways and to study cellular features of the host cell for supporting rAAV production. This study investigated the transcriptomic features of two cell lines cultured in their respective media by comparing viral-producing cultures with non-producing cultures over time in parental human embryonic kidney cells (HEK293). The results demonstrate that the innate immune response signaling pathways of host cells (e.g., RIG-I-like receptor signaling pathway, Toll-like receptor signaling pathway, cytosolic DNA sensing pathway, JAK-STAT signaling pathway) were significantly enriched and upregulated. This was accompanied by the host cellular stress responses, including endoplasmic reticulum stress, autophagy, and apoptosis in viral production. In contrast, fatty acid metabolism and neutral amino acid transport were downregulated in the late phase of viral production. Our transcriptomics analysis reveals the cell-line independent signatures for rAAV production and serves as a significant reference for further studies targeting the productivity improvement in the future.

Abbreviations: AAV, adeno-associated virus; ALDH6A1, aldehyde dehydrogenase 6 family member A1; ARSB, arylsulfatase B; BCAA, branched-chain amino acid; CCL5, CC chemokine ligand 5; cGAS, cyclic GMP-AMP synthase; CHO, Chinese hamster ovary; CLN6, ceroid-lipofuscinosis neuronal protein 6; CXCL9, CXC chemokine ligand 9; DAI, DNA-dependent activator of IFN-regulatory factors; DEG, differentially expressed gene; DOE, design of experiment; EIF2α, eukaryotic translation initiation factor 2A; ER, endoplasmic reticulum; GADD34, growth arrest and DNA damage inducible 34; GO, gene ontology; GOI, gene of interest; HEK, human embryonic kidney; HSPA6, heat shock protein family A (hsp70) member 6; HSV, Herpes simplex virus; ICP0, infected cell protein no. 0; IFIT, interferon-induced protein with tetratricopeptide repeats; IFITM, interferon-induced transmembrane; IFN, interferon; IFNAR, interferon alpha and beta receptor subunit 1; IFNB1, interferon beta 1; IKK2, inhibitor of kappa-B kinase; IRF, interferon regulatory factor; ISG, interferon-stimulated genes; JAK, Janus kinase; MDA5, melanoma differentiation-associated protein 5; NLRC5, Nod-like receptor family card domain containing 5; OAS, oligoadenylate synthetase; PEI, polyethylenimine; PERK, protein kinase R-like endoplasmic reticulum kinase; PLS-DA, partial least squares-discriminant analysis; POLR3C, RNA polymerase III subunit C; RIG, retinoic acid-inducible gene; RIN, RNA integrity number; RSAD2, radical S-adenosyl methionine domain containing 2; RSEM, RNA-Seq by expectation maximization; SLC43A2, solute carrier family 43 member 2; STAT, signal transducer and activator of transcription; TBK1, tank-binding kinase 1; TLR, toll-like receptor; TMEM106B, transmembrane protein 106B; TRIF, TIR domain containing adapter-inducing interferon-β; TRIM25, tripartite motif containing 25; UPR, unfolded protein response; XBP1, X-box binding protein 1.

Yongdan Wang and Qiang Fu equally contributed to this article.

Biotechnol. Prog. 2023;39:e3346.
https://doi.org/10.1002/btpr.3346

KEYWORDS
HEK293 cells, pathway analysis, rAAV production, transcriptomics, transient transfection

1 | INTRODUCTION

As more gene therapy drugs enter the market, AAV-mediated gene therapy has attracted particular interest due to its unique therapeutic advantages, including non-pathogenicity in humans, the ability to target different tissues with various serotypes, and long-term efficacy.[1–3] The most common method for clinical use and commercial production is the triple plasmid-based transient transfection of HEK293 cells in order to produce rAAV.[4] During rAAV production, three plasmids (GOI plasmid, RepCap plasmid, and helper plasmid) are co-transfected into HEK293 cells. This transient transfection process enables rAAV production for a limited time without integrating viral DNA into the host cell genome.[5–7] The major challenge of the rAAV manufacturing process is its limited production capability, which cannot meet the demand.[8] This increases the cost of AAV-mediated gene therapies.[8]

Several strategies have been attempted to improve rAAV productivity. Transient transfection is a complex process, so parameter optimization is one of the most commonly applied approaches.[9–11] The design of experiment (DoE) was conducted to improve the process.[11] However, these methods may be limited to specific cell lines or media. One mechanistic model was reported for the rAAV viral vector biosynthesis,[12] but an overall insufficient mechanism-directed understanding of transfection-based rAAV production still limited our ability to capture cellular or molecular features for more efficient production. For example, the rAAV production process is highly reliant on host cells: It requires the host's cellular machinery for its own genome replication, and this genome replication is regulated by the host cell's DNA replication system. However, very limited knowledge of AAV genome replication has been gained so far, especially from the perspective of the host cell.

The exploration of transcriptomes is an important approach to characterizing features of the host cell in terms of viral production. Previous studies have applied microarray and mRNA sequencing (RNA-seq) analysis for specific gene expression and cellular pathway identification in CHO cells[13,14] and in HEK293 cells,[15] thus consolidating our knowledge on pathway regulation in response to the production of therapeutic drugs. RNA-seq has become a more popular approach to exploring the HEK293 transcriptome, due to the limitations of microarray analysis and the availability of human and HEK293 cell transcriptome databases or reference materials.[16,17] In a recent study, RNA-seq was used to investigate various engineered viral production[18–20] and virus infection mechanisms.[21–23] However, the use of RNA-seq analysis of the transcriptome to characterize HEK293 cells for rAAV production has not been reported.

In this study, we compare the transcriptome of an AAV-producing group (referred to as the *viral-producing* group) to a non-producing group (the *negative control* group) from two parental HEK293 cell lines on different post-transfection days. These HEK293 cell lines originated from different sources and were adapted and cultured in their respective media. The differentially expressed genes were analyzed after obtaining the global transcriptome. First, the genes were screened by *fold change* (FC) and by *p*-adj. value thresholds. Then, their biological functions were further explored to understand their relevance to rAAV production. This work presents an attempt to understand the changes in host cell physiology for rAAV production. Based on the results of this study, potential medium supplementation strategies and cell line engineering strategies to enhance viral production are also proposed for future investigations.

2 | MATERIALS AND METHODS

2.1 | Plasmid preparation and cell culture

Escherichia coli stabs contained one backbone plasmid pcDNA3.1/Zeo (Plasmid #V86020, Invitrogen, USA) in addition to three AAV-related plasmids: pAdDeltaF6 (Plasmid #112867, Addgene, USA), pAAV2/2 (Plasmid #104963, Addgene, USA), and AAV-CMV-GFP (Plasmid #67634, Addgene, USA). The bacteria were amplified in Luria-Bertani (LB) broth media with 100 μg/mL ampicillin (Sigma-Aldrich, USA). The plasmids were extracted and purified using the Zymo Maxiprep kit (Zymo, USA). The purified plasmids were then sterilized using a 0.22 μm PES sterile syringe filter (VWR, USA). The quality of plasmids was inspected based on A230/260, A260/280 using Nanodrop (Thermo Fisher, USA), and DNA electrophoresis.

This study used two different media (AMBIC 1.0 HEK293 in-house media and BalanCD HEK293 media [Irvine, USA]) and two different sources of HEK 293 cells: (a) HEK293 cells from ATCC ([HEK-293] CRL—1573, ATCC) adapted in AMBIC media supplemented with 4 mM GlutaMax™ (Thermo Fisher, USA) and (b) HEK293 cells from Mass Biologics adapted in BalanCD HEK293 media with 4 mM glutamine (Thermo Fisher, USA) added. Both sources were cultured in shake flasks (5% CO_2, 37°C, and 125 rpm). For rAAV production, the transfection process utilized 30 mL of cell culture in a 125 mL shake flask.

2.2 | Transient transfection-rAAV vector production

Cells in the logarithmic growth phase were resuspended with fresh media to target predetermined cell density on the day of transfection. These cells were then transfected with three plasmids (pHelper, pAAV2/2, and pGoI) and the transfection reagent PEIpro® (PolyScience, USA). Transfection was conducted as follows: Three sterilized plasmids were mixed carefully in the fresh media with 10% of the cell culture volume. The PEIpro was then added to the plasmid diluted media. After 5–30 min of incubation, the PEIpro–DNA complex medium was added to the cell culture shake flasks. The culture was conducted in a shaker incubator (5% CO_2, 37°C, and 125 rpm). The specific transfection conditions are shown in Tables S1 and S2. To achieve statistical significance for RNA-seq data, biological triplicates were used for each cell culture condition.

2.3 | Cell count, viability, and AAV genome titer measurement

Cell count and viability were evaluated daily using a Cedex HiRes Analyzer (Roche Life Science, USA). The crude harvest was lysed using three freeze–thaw cycles (i.e., frozen in a dry ice–ethanol bath for 2 min and then thawed in 37°C water for 3 min) with vortexing at each thaw. Treatment with $MgCl_2$ (Sigma-Aldrich, USA) and Benzonase® (New England Biolabs, USA) was then performed, followed by 1 h of incubation and 40 min of centrifugation at 4100*g* at 4°C. The collected supernatant was treated with DNase I and DNase reaction buffer to eliminate any host proteins or unpackaged GFP (New England Biolabs, USA). This was followed by 1 h of incubation at 37°C. Then, the sample was treated with proteinase K to open the viral capsids (New England Biolabs, USA), followed by 1 h of incubation at 55°C, followed by 10-min inactivation process at 95°C. The sample underwent 125× serial dilution for the quantitative polymerase chain reaction (qPCR) reaction using CFX Real-Time PCR Detection system (Bio-Rad, USA).

A PrimeTime® qPCR Probe assay (Integrated DNA Technologies, USA) was designed using the PrimerQuest® Design Tool (Integrated DNA Technologies, USA). Each 20 μL sample of the qPCR reaction mixture contained 10.0 μL of TaqMan™ Universal PCR Master Mix, 1.0 μL of primer–probe mix (500 nM primer and 250 nM probe), 6.0 μL of molecular biology-grade water, and 3.0 μL of the diluted sample. The cycling conditions were 20 s at 95°C followed by 39 cycles of two-step thermal cycling (3 s at 95°C followed by 30 s at 60°C). For each run, the negative control (i.e., no primer–probe mixture), the no-template control (NTC), and the positive control (i.e., linearized GFP plasmids) were used along with six rAAV5 reference standards in triplicates (MassBiologics, USA) to achieve semi-quantification of viral titers. The primer and probe sequences used for the genome titer were:

Forward: 5′- GAA CCG CAT CGA GCT GAA -3′.

Reverse: 5′- TGC TTG TCG GCC ATG ATA TAG -3′.

Probe: /56-FAM/ATC GAC TTC/ZEN/AAG GAG GAC GGC AAC/3IABkFQ/.

2.4 | RNA isolation and sequencing

Approximately 1 × 10^6 cells were centrifuged from cell suspension at 1000 rpm for 5 min. The cell pellets were washed with iced PBS twice and then stored at −80°C. Total RNAs were extracted using RNeasy Mini Kit (QIAGEN, USA) with DNase digestion (QIAGEN, USA) following the manufacturer's instructions. RNA concentrations were quantified using a Qubit fluorometer (ThermoFisher Scientific, USA). The integrity of the total RNA was measured using a Bioanalyzer (Agilent, USA). RNA samples with RIN value greater than 7 were qualified for later cDNA library preparation. Messenger RNA purification and library preparation were performed under the guidance of Universal Plus™ mRNA-Seq with NuQuant® (Tecan Group Ltd., Switzerland). The adaptor-ligated libraries were quantified by quantitative PCR using a CFX Real-Time PCR Detection System (Bio-Rad, USA) and sequenced on a NextSeq 500 System (Illumina, USA) using a NextSeq 500 High-Output v2 Kit (at 150 cycles). Raw sequencing data (in.bcl format) were de-multiplexed according to their barcodes, then converted to FASTQ files using bcl2fastq2 Conversion Software (Illumina, USA). Approximately 10 million 150-base pair (bp) reads (pair-end) were generated for each sample (see Tables S4 and S5). The library size was normalized by DESeq2 in the later bioinformatics pipeline.

2.5 | Alignment to plasmid sequences and the human genome

AAV reference sequences (including *Rep* and *Cap* genes) are detailed in the Supporting Information. The annotation GTF file *Human genome* was used as the global reference. FastQC (Babraham Institute, UK) was used to evaluate the quality of the sequence reads. Artificial adaptors were removed, and reads with a quality below 15 per bp sequence were cropped using Trimmomatic.[24] Fewer than 2% of the total reads were aligned to the common RNAs, and these were excluded. Reads from each sample were aligned to PAdDeltaF6, *rep and cap plasmid sequences* using Bowtie2 as a aligner.[25] The remaining reads were aligned to the *Human genome* reference transcriptome using RNA-Seq by expectation maximization (RSEM)[26] to quantify transcript abundance using RNA-Seq data. Around 80% of the reads were aligned from each sample to the human genome. All bioinformatics data uploading was performed using Linux command lines in the Massachusetts Green High Performance Computer Center (MGHPCC).

2.6 | Differential gene expression, function analysis, pathway enrichment, and statistical analysis

First, principal component analysis (PCA) and *partial least-squares discriminant analysis* (PLS-DA) in SIMCA (Sartorius, USA) were used to cluster samples with the normalized expected counts output from RSEM. Then, those expected counts were imported to the DEBrowser, an interactive interface for data examination and differential expression.[27] DESeq2[28] was used to perform differential expression (DE) analyses between different sample groups. A list of differentially expressed genes was generated and filtered according to the fold change between the viral-producing groups and the negative control groups and *p*-adj. values.[29] The web-based tool Metascape and

DAVID were used for gene ontology (GO) enrichment and KEGG pathway analysis.[30] Origin software (OriginLab, USA) was used for plot generation.

2.7 | Quantitative polymerase chain reaction for relative gene expression quantification

Synthesized cDNA library samples (the same sample used for the RNA sequencing), were diluted 10 times, amplified, and detected in a qPCR using universal SYBR Green (Thermo Fisher, USA) protocol. The primer sequences were shown in the Table S10. The comparative cycle threshold ($2^{-\Delta\Delta Ct}$) method was used to analyze the relative gene expression level changes. The transcript level of each gene was normalized to the housekeeping gene *GAPDH*. The relative gene expression for each sample was quantified in technical duplicates.

3 | RESULTS AND DISCUSSION

3.1 | Post transfection cell growth, viability, and viral titer

For the viral-producing condition, parental HEK293 cells were transfected with helper, RepCap, and GOI plasmids. Two production systems were studied using the BalanCD and AMBIC media and their specific cell lines. Both cell culture systems lasted for 72 h after transfection. For the non-producing condition, parental HEK293 cells were

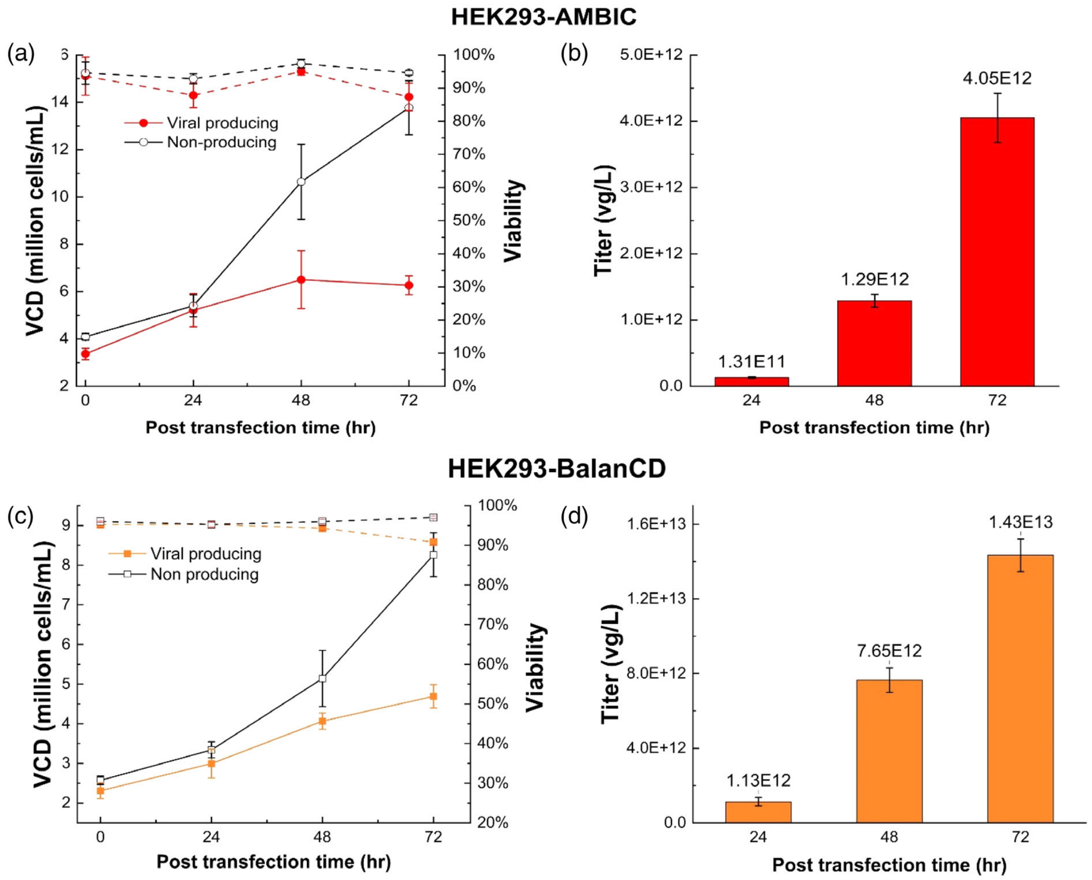

FIGURE 1 Cell growth profile and genome titer for both AMBIC and BalanCD cell cultures post-transfection. Left *y* axis in (a) and (c) represents viable cell density, expressed in million cells/mL. The right *y* axis represents viability expressed as a percentage. The *y* axis in (b) and (d) represents the viral titer expressed in viral genome per liter (vg/L). The closed circle and square represent the viral-producing condition. The open circle and square represent the non-producing condition. Data shown are the average of the triplicate cell cultures. The error bar represents the standard deviation among biological triplicates

transfected with backbone-sequence plasmids at a total mass of DNA equal to the amount used in the viral-producing condition. Each condition was conducted in biological triplicates. Figure 1 shows the cell growth, viability, and viral titer for both production systems. With a similar cell density prior to transfection, post-transfection cell growth and viability in the viral-producing condition were lower than in the non-producing condition for both systems. This phenomenon might be explained by the shift of nutrients and energy from supporting cell growth to rAAV production. At 72 h, the production conditions using the BalanCD and AMBIC systems reached a genome yield of 1.43×10^{13} vg/L and 4.05×10^{12} vg/L, respectively. The cell line adapted to the BalanCD medium achieved a virus titer three times higher than the cell line in the AMBIC medium. Specific productivities (vg/cell) for both viral producing conditions were calculated and shown in Table S3. As expected from the total genome titer, Q_p of HEK293-BalanCD cell culture was continuously higher than that of HEK293-AMBIC cell cultures over time, achieving peak specific productivity 48 h post transfection. Specific differences among cell lines themselves and different components supplemented in media both contributed to titer variations between the two production systems. During this experiment, cell pellet samples were taken 24 h ("D1"), 48 h ("D2"), and 72 h ("D3") after transfection. These samples were used in the transcriptomic study discussed below.

3.2 | Transcriptome overview differentiating the viral-producing and non-producing conditions

Figure 2 shows a cluster analysis using both PCA and PLS-DA for daily gene expression, which is the output of the normalized transcript counts from RSEM, for the viral-producing and non-producing conditions of each production system. PLS-DA, a supervised statistical method, was utilized and mainly analyzed here as it provided more efficient and better separation with defined and known groups of samples compared to unsupervised PCA analysis. PLS-DA has been recommended for use in omics data analysis since it can successfully reduce data dimensions and also be aware of the classification.[31] In our case, each biological triplicate set was defined as one distinct class in PLS-DA analysis. RNA-seq data was missing for one of the non-producing group samples in the BalanCD (NC2D2) system, so it was excluded from PLS-DA analysis. The first two main principals, shown as R2x [1] and R2x [2] in each plot in Figure 2c,d, accounted for about

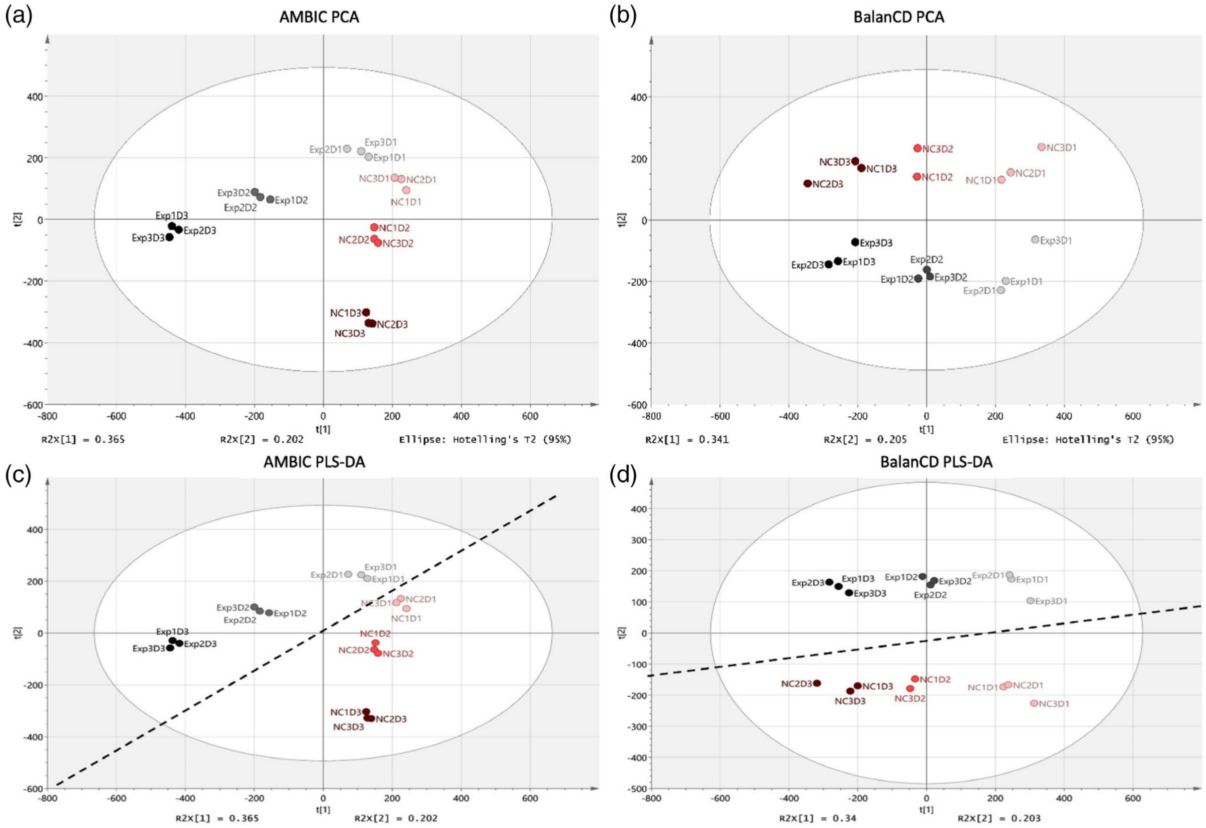

FIGURE 2 Principal component analysis and PLS-DA plots for both AMBIC and BalanCD cell cultures on different post-transfection days. Diagonal lines separate viral-producing (Exp) and non-producing (NC) groups for PLS-DA plots. Post-transfection times are represented as D1 (24 h), D2 (48 h), and D3 (72 h)

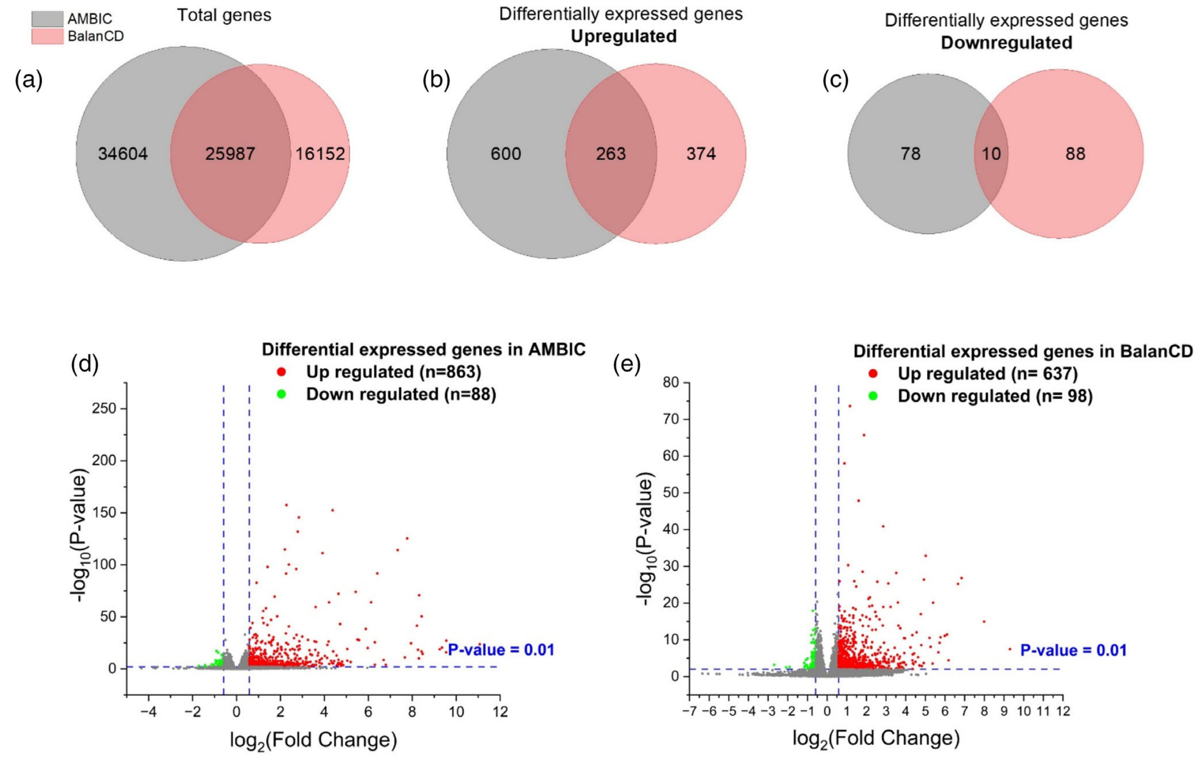

FIGURE 3 Venn diagram of the overall gene expression (a) and the differentially expressed genes (b) and (c). The overlapping region shows the number of genes shared by the AMBIC and BalanCD cell cultures. Volcano plots for differentially expressed genes in the AMBIC (d) and BalanCD cell cultures (e). The fold change threshold was set to 1.5, and the *p*-adj. value threshold was set to 0.01. The upregulated genes are represented by red dots, the downregulated genes are represented by green dots, and nonsignificant genes are represented by gray dots

55% of the variability in the data. It was noted that the biological replicates for each condition were clustered, and the viral-producing and non-producing groups could be separated by diagonal lines. This result indicates a distinct separation between the viral-producing and non-producing conditions, and the distance between the two conditions increased as the transfection continued over time from the beginning to harvest. This indicates a growing difference between the two groups in terms of cellular physiology after transfection. Further analysis was conducted to screen the differentiated gene expressions and to identify the host cell physiological changes accompanied with rAAV production.

The cellular mRNA from D1, D2, and D3 post-transfection were sequenced for both systems. A total of 60,591 and 42,141 genes were identified in the AMBIC and BalanCD cell cultures respectively. It was found that 25,987 genes overlapped between the two cell lines (see Figure 3a). Next, the differentially expressed genes (DEGs) were identified using DESeq2 analysis between the viral producers and non-producers, including all post-transfection time points, with a threshold of 1.5-fold changes and a *p*-adj. value <.01. As shown in Figure 3b,c, the viral-producing condition using the AMBIC medium resulted in 863 upregulated genes and 88 downregulated genes. The viral production system using the BalanCD medium resulted in 637 upregulated and 98 downregulated genes. Figure 3d,e illustrate the DEG distribution that corresponds to the FC and *p*-adj. values. Appendix A1 in Data S1 provides details on the overall DEG results for both systems.

The combined set of differentially expressed genes in the AMBIC system (951 genes) and the BalanCD system (735 genes) were processed using GO enrichment analysis. Figure 4 shows the top 20 upregulated and the top 20 downregulated GO gene clusters for viral production (see Figures S1 and S2 for the top 100 GO gene clusters). Among the upregulated GO gene clusters shown in Figure 4a, more than half were related either to the innate immune response of the host cell (e.g., interferon signaling), different virus infection responses, or the host cell's antiviral responses. This reveals that AAV production stimulates the HEK293 cellular immune response. A few common metabolic processes (e.g., the glycolipid metabolic process, glycosaminoglycan metabolism) were downregulated and clustered in the GO enrichment (see Figure 4b). The next several sections elaborate on further analysis related to AAV production.

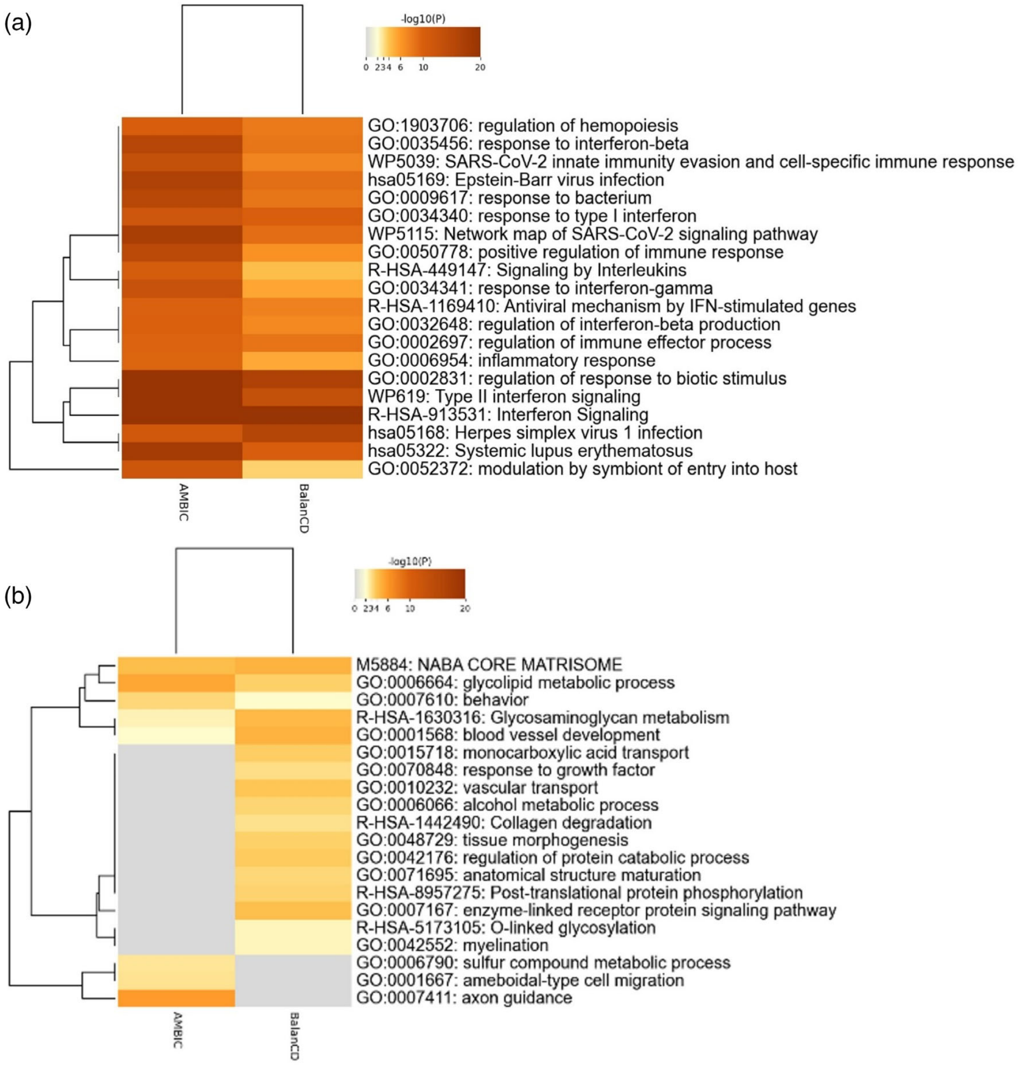

FIGURE 4 Enriched upregulated (a) and downregulated (b) clusters in the viral-producing states based on the gene ontology database for both AMBIC and BalanCD cell cultures. Differentially expressed genes in both systems with a 1.5-fold change threshold and *p*-adj. values <0.01 were processed for ontology analysis. The figure shows the comparison of the AMBIC and BalanCD cell cultures

3.3 | DEGs, functions, and pathway analysis

The transcriptomes of two viral producers were compared to their corresponding non-producing states on various post-transfection days to investigate the regulation of cell line-independent pathways for AAV viral production. The resulting list of DEGs with the threshold fold change (>1.5) and *p*-adj. value (<0.01) were enriched using the KEGG database (see Appendix A2 in Data S1 for the HEK-AMBIC system and A3 for the HEK-BalanCD system). The DEG and pathway analysis in this section focused on D2 (48 h post-transfection) because this was the most rapidly proliferating phase for AAV production as shown in Figure 2b,d. Transcriptome changes relating to viral production that arise over time for viral production are discussed briefly in the Table S9. The primary enriched pathways include antiviral immunity signaling pathways and cellular stress-associated pathways for both cell lines. Significantly enriched pathways were further investigated to evaluate their correlation with viral production and their potentials to regulate productivity. Detailed statistical results on pathway enrichment can be found in Appendix A6 in Data S1 for the HEK-AMBIC system and Appendix A7 in Data S1 for the HEK-BalanCD system. The official full names of genes and proteins mentioned below can be found in the list of abbreviations.

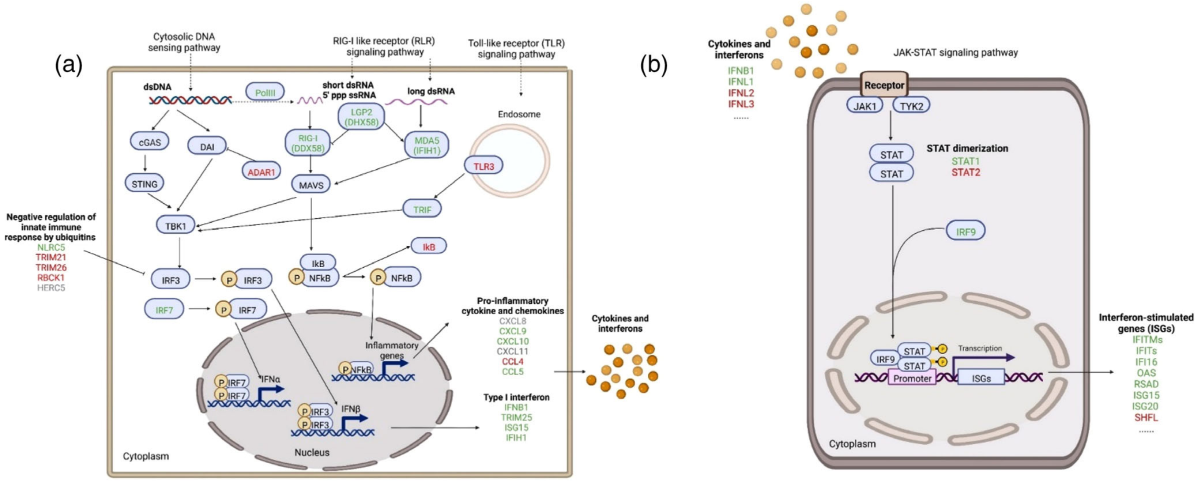

FIGURE 5 Innate immune response signaling pathways enriched in viral-producing states. (a) shows RIG-I like receptor (RLR) signaling, Toll-like receptor (TLR) signaling, and cytosolic DNA sensing pathways. (b) shows JAK-STAT signaling pathways. The genes shown in green were found to be common in both cell lines. Genes shown in red are specific to the HEK-AMBIC cell line. Genes shown in gray are specific to HEK-BalanCD cell line

3.4 | Innate immune responses

Several signaling pathways involved in the innate immune response, ranked as the top enriched KEGG pathways, were significantly upregulated in the viral-producing state. Host cell innate immunity often acts as the first line of defense against the spread of viruses. Once a pathogen-associated molecular pattern (e.g., viral nucleic acids) is recognized by the host's pathogen recognition receptor, a series of downstream signaling pathways is activated to stimulate the production of type I interferon (IFN), and the transcription of interferon-stimulated genes (ISGs).[32] The expression of these genes results in the negative regulation of viral replication and the restriction of the viral production.[32] The innate immune response signaling pathways shown in Figure 5 were enriched in the viral-producing state. These pathways include the *Toll-like receptor* (TLR) signaling pathway, the *retinoic acid-inducible gene-I-like receptor* (RLR) signaling pathway, and the downstream Janus kinase-signal transducer and activator of transcription (JAK-STAT) signaling pathway. Table S6 shows the FC and *p*-adj. values for these innate immune response signaling pathways in both cell lines. The JAK-STAT signaling pathway is downstream for all antiviral sensing pathways. The JAK-STAT signaling pathway describes all the commonly expressed genes in the downstream of the RLR, TLR, and cytosolic DNA sensing pathways (see Appendices A6 and A7 in Data S1 for the other enriched KEGG pathways).

3.4.1 | RLR signaling pathway

The RLR signaling pathway is the major sensing pathway for RNA viruses.[33] This study finds that this pathway was enriched for rAAV production (see Figure 5a). RIG-I (also referred to as DDX58) and MDA5 (IFIH1) are receptor proteins for short dsRNA and long dsRNA, respectively.[33] Besides RNA source directly from evading viruses, the conversion of dsDNA to 5'ppp ssRNA via RNA polymerase III (PolIII) also allowed for the activation of the RLR signaling pathway by sensing cytosolic DNA.[34,35] The overexpression of *DDX58*, *IFIH1*, and *POLR3C* (a subunit of *PolIII*) in both cell lines shown in the transcriptome data suggested the activation of the RLR signaling pathway. The detection of foreign nucleic acids facilitated the activation of the MAVS protein and the recruitment of the downstream transcription factor *TBK1*, triggering the phosphorylation of *IRF3* and *IRF7*. The transcriptome data indicate that *IRF7* in both the AMBIC ($FC = 15.102$, p-adj. $= 0$) and BalanCD ($FC = 10.753$, p-adj. $= 2.92 \times 10^{-45}$) cell lines was upregulated in the viral-producing state. Then, phosphorylated *IRF7* translocated to the nucleus and triggered the production of type I IFNs and pro-inflammatory cytokines. The production of type I IFNs, pro-inflammatory cytokines, and chemokines was confirmed by the upregulated expression of multiple genes, including *IFNB1*, *TRIM25*, *CCL5*, and *CXCL9* (see Figure 5a).

3.4.2 | TLR signaling pathway

There are two categories of *Toll-like receptors* (TLR). One category consists of receptors on the cellular surface that detect viral proteins. The other category consists of receptors in the intracellular endosome that recognize viral nucleic acids. The transcriptome data demonstrate the enrichment of the TLR signaling pathway in both cell lines. Specifically, in the AMBIC cell line, *TLR3* ($FC = 2.8$, p-adj. $= 3.74 \times 10^{-7}$), which is one type of endosome receptor, was found to be upregulated in the viral-producing state. This upregulation has been shown to be a host cell defense mechanism against viruses by limiting viral replication via the type I IFN production.[36] The recognition of foreign components by TLR3 triggers the activation of *TRIF* (*TICAM1*). Enhanced TRIF expression was observed in both the BalanCD ($FC = 10.232$, p-adj. $= 1.034 \times 10^{-4}$) and the AMBIC ($FC = 1.547$, p-adj. $= 1.214 \times 10^{-4}$) cell lines. The activation of TRIF recruited the downstream transcription factor TBK1 and phosphorylated IRF7. Similarly, the TLR signaling pathway can also produce type I IFN and cytokine release, which further triggers the downstream JAK-STAT signaling pathway.

3.4.3 | Cytosolic DNA sensing pathway

cGAS, together with DAI, are major cytosolic DNA sensors or receptor proteins that initiate the production of type I IFNs via phosphorylated IRF3 or IRF7.[37] The DEG data and KEGG pathway analysis showed that the cytosolic DNA sensing-signaling pathway was enriched in both cell lines. The overexpression of *POLR3C*, *ADAR1*, and the production of interferons and proinflammatory cytokines, activating the downstream JAK-STAT signaling pathway, may result in this enrichment (see Figure 5a). Detailed fold changes and p-adj. value can be found in Table S6.

3.4.4 | JAK-STAT signaling pathway

Secreted IFNs bind to recognition receptors embedded in the cell surface, which triggers the activation of the JAK-STAT pathway.[32,38] Significant upregulation of IFN expression (e.g., *IFNB1*, *IFNL1*) was observed in the viral-producing state in both cell lines. As shown in Figure 5b, phosphorylated STAT proteins formed heterotrimeric transcription factor complexes with IRF9. This was confirmed by the highly upregulated STAT protein and IRF9 expression. The complex translocated to the nucleus, bound to the promoter, and initiated the expression of ISGs such as the IFITM family, the IFIT family, the OAS family, or *RSAD2*.

ISGs were shown to be indicators of the host cell's defense against viruses. The ISGs common to both cell lines are shown in green text in Figure 5b. These genes were induced by IFN production, and they have their own mechanisms to negatively regulate viral genome replication and thus limit the spread of the virus.[39–45] Among the ISGs, the IFITM family of genes was found to be upregulated in the viral-producing condition, exhibiting an expression level five times higher than in the non-producing condition. These changes were more prominent in the AMBIC cell line (IFITM1, $FC = 70.95$, p-adj. $= 0$) than in the BalanCD cell line (IFITM1, $FC = 10.265$, p-adj. $= 3.92 \times 10^{-71}$). These interferon-induced transmembrane proteins act as virus restriction factors via viral entry-dependent or viral entry-independent inhibition, such as suppressing viral protein synthesis or limiting viral replication.[46,47] IFIT5 is another interferon-induced binding protein involved in innate immune responses ($FC = 5.098$, p-adj. $= 5.39 \times 10^{-250}$ in the AMBIC cell line; $FC = 2.448$, p-adj. $= 4.4 \times 10^{-23}$ in the BalanCD cell line). This protein could inhibit viral replication through multiple mechanisms, such as restraining translation initiation, sequestering viral nucleic acids or proteins in the cytoplasm, or binding to uncapped (or incompletely capped) viral RNA.[47] Table S6 provides more details on the FC and gene information of the ISGs involved in the enriched JAK-STAT pathway.

This significant enrichment in the host's immune response against viruses provides insight into the changes observed in cellular physiology that relate to rAAV production. This study proposes a few control strategies to modulate this response pathway. Virus replication is largely determined by two factors: the spread of virus replication and the induction of the antiviral state. Therefore, interferon-sensitive viruses can be difficult to cultivate to high titer in cells that produce IFNs.[48] In order to restrict IFN production and ISG expression, Stewart et al. proposed the use of inhibitors of the signaling proteins involved in IFN signaling pathways, such as BX795 (a TBK1 inhibitor), TPCA-1 (an IKK2 inhibitor), or ruxolitinib (a JAK1 inhibitor).[48] These small molecular inhibitors were utilized to block specific interferon pathways, and they were tested to successfully lower the innate immune response and enhance replication for Respiratory Syncytial Virus, Influenza Virus, and so on.[48] Similarly, the enrichment of the antiviral signaling pathway in rAAV production suggests the hypothesis that control of the IFN signaling pathway can contribute to enhanced viral production. The promising results in the literature on IFN inhibitors mentioned above supply a proof-of-concept that these IFN inhibitors can be used as media supplements to block or decrease the innate immune response pathways in HEK293 cells and enhance rAAV genome replication, thus improving cellular productivity.

Furthermore, the literature also reports that the critical genes triggered by the innate immune response (e.g., *RSAD2*,[42,44,49] OAS family genes,[40] IFIT family genes),[50] affect virus genome replication. For example, the expression of the enzyme RSAD2 could deplete cellular nucleotide pools and decrease the mitochondrial respiration rate via its radical activity, thereby restricting the genome replication of various RNA or DNA viruses.[44] Cell line engineering strategies (e.g., gene silencing, gene knockout) might be used to lower or eliminate the expression of those genes. However, the biological functions of these genes in terms of maintaining basic cellular activities must be explored further.

3.4.5 | Ubiquitin in the attenuation of the innate immune response

In addition to enriched innate immune response signaling pathways, some clustered genes function as negative regulators of the innate immune response via the ubiquitin modification system (see Figure 5a). FC, p-adj. values, and detailed biological functions of these genes can be found in Table S7. This ubiquitin modification strategy is often utilized by other viruses to evade antiviral signaling pathways and suppress IFN-I expression.[51–53] For example, ICP0 is a viral protein expressed by the herpes simplex virus 1 (HSV1) with E3 ubiquitin ligase activity. ICP0 has been shown to play an important role in minimizing the production of IFN and ISGs during HSV1 viral infections.[53] Specifically, ICP0 targets activated IRF3/IRF7 for degradation, inhibits the activation of STAT proteins, and suppresses the expression of TRIMs.[53] Other than the result shown in this transcriptomic study, no literature has been reported about the ubiquitin modification system utilized by host cells for AAV production. One promising—but challenging—approach to enhancing virus productivity may be imitating other viruses' strategies to evade antiviral responses during the transfection process and eliminate the negative impacts of immune responses on viral genome replication. Co-transfection with predesigned plasmids allows for the expression of foreign viral proteins (e.g., ICP0) in HEK293 cells, so they can serve their biological function and reduce the production of IFN and ISGs during rAAV production. However, we need to be aware that plasmids as foreign DNAs, could also result in toxicity and other stresses to host cells. Another approach to promoting efficient rAAV production can be amplifying innate-associated ubiquitin behaviors by overexpression, thus further restricting antiviral responses. Both methods are aimed at eliminating or lowering the viral components induced innate immune responses, thus benefiting for viral replication.

3.5 | Host cell stress responses

The AAV viral production cycle relies on the host cell's replication and translation machinery. Viral proteins and viral nucleic acids are foreign components that could trigger a series of host cell stress responses, such as autophagy, ER stress, or apoptosis. These were all found to be upregulated in the viral-producing states. The transcriptomic results regarding ER stress induced UPR are mainly discussed in this section. Table S7 provides details of the GO enrichment results and the FC values for the DEGs in both cell lines. Appendices A4 and A5 in Data S1 show more GO enrichment results.

ER stress stimulated by viral production and UPR: Viruses rely on host ER machinery for viral protein synthesis and modification. To ensure the cell's survival and viral replication, host cells have to respond to this stress and trigger the activation of unfolded protein response (UPR).[54] GO enrichment analysis shows the cellular response to ER stress and the activation of UPR in the viral-producing state. PERK-mediated UPR, serving as one major UPR pathway, was found closely related to AAV production in this study. In PERK-mediated UPR, the activation of PERK by the accumulation of unfolded or misfolded proteins, phosphorylates translation initiation factor EIF2α, resulting in temporary protein synthesis attenuation. To ensure proper mRNA translation and protein synthesis, phosphorylated EIF2α in host cells can be deactivated by downstream negative feedback signaling molecules, such as *EIF2AK2* and *PPP1R15A* (which encodes for GADD34).[55] It was observed that both *EIF2AK2* and *PPP1R15A* were upregulated for viral production in both cell lines. This demonstrates that viral production indeed induces ER stress, and host cells can resolve ER stress and restore protein synthesis by overexpressing negative feedback signaling genes such as GADD34. Furthermore, the overexpression of the heat shock protein HSPA6 was observed in both the AMBIC (FC $= 4.376$, *p*-adj. $= 7.67 \times 10^{-10}$) and the BalanCD (FC $= 13.454$, *p*-adj. $= 4.94 \times 10^{-13}$) cell lines. In this case, stressful conditions induced the upregulation of HSPA6, which serves as an essential modulator to promote correct protein folding and ensure host cell survival in stressful environments.[56,57]

To modulate the UPR, and to relieve ER stress, the small molecules that enhance the expression of the heat shock protein (i.e., HSPA6 activators) and inhibit the expression of the UPR receptor protein (i.e., PERK inhibitors) can be evaluated for their impact on viral productivity.[58,59] Overexpression of genes involved in ER protein processing has been proved to achieve up to 97% volumetric titer improvement in the recombinant retroviral vector production.[60] Similar small molecule additives or cell line engineering approaches can be evaluated to resolve ER stress and recover AAV-related protein synthesis, thereby improving rAAV productivity. Additionally, ER stress and UPR pathways have also been reported for biologics production in Chinese Hamster Ovary (CHO) cells.[61,62] Reported strategies might also offer another good starting point for relieving ER stress and therefore improving yield in the vector production: for example, chemical chaperones (e.g., trehalose, proline, glycerol) have been reported to increase recombinant protein productivity and decrease protein aggregation.[63,64] Overexpression of genes encoding molecular chaperones also enhanced the expression of difficult-to-express recombinant proteins in HEK293 cell lines.[65,66]

Apoptosis is another host stress response to defend against viral replication. From GO analysis, both cell lines exhibit the enrichment of the positive regulation of apoptotic process (GO:004305 and GO:0006915). See Appendix 4 in Data S1 for GO enrichment in HEK293-AMBIC and Appendix 5 in Data S1 in HEK293-BalanCD. The expression of *rep* and helper genes has been shown to induce cytotoxicity: Rep78 protein, the most toxic protein, was found to activate caspase-3 and induce cell apoptosis[67]; E4orf4 was the major E4 product responsible for induction of p53-independent apoptosis.[68] Upon transfection, host cells were exposed not only to external pathogen components but also to transfection reagents (e.g., PEI pro). Within a relatively short 3-day cultivation period, viability for both cell lines was maintained above 80%. However, when compared to non-producing conditions, there was an obvious upregulation of apoptosis pathways induced by viral vector production (Appendices 4 and 5 in Data S1). In order to alleviate apoptosis-induced stress, small molecules such as antioxidants,[69] can be used as media supplements. Another potential strategy to facilitate rAAV production may be the overexpression of anti-apoptotic genes via cell engineering methods to delay apoptosis in the HEK293 cell line.[18] A study has been confirmed the improvement of r-RV productivity via overexpression of B-cell lymphoma 2 (*Bcl2*) protein gene (anti-apoptotic).[60]

Other GO-enriched cellular responses to stress were observed (e.g., the cellular response to glucose starvation, the response to the presence of reactive oxygen species, or enriched oxidant detoxification) to cope with such stressful conditions. FC, *p*-adj. value and biological functions of associated genes can be found in Table S7. More GO enrichment results can be found in Appendix 4 in Data S1 (HEK293-AMBIC) and 5 (HEK293-BalanCD).

3.6 | Metabolism

In both cell lines, *SLC43A2* was slightly overexpressed in the viral-producing state, as shown in Table S7. This encoded transmembrane protein was involved in transporting neutral amino acids. This overexpression could be related to the increased demand for the raw materials required for viral capsid synthesis in the viral-producing condition. More importantly, in the late stage of viral production, fatty acid metabolism was found to be downregulated in both cases (see Appendices A4 and A5 in Data S1). Furthermore, two genes involved in the *branched-chain amino acid* (BCAA) catabolic process, *ALDH6A1* and *ACADSB*, were found to be downregulated in the viral-producing state in both cell lines. BCAAs functioned as signaling molecules that regulate levels of glucose and lipids, the synthesis of proteins, and the immunity.[70] Further studies may be necessary to explore specific correlations between downregulated metabolism and viral production.

3.7 | Transcriptomic results validation by qPCR

The analysis and hypothesis elaborated above were based on the transcriptomic study. To validate the changes in the expression of main genes and enriched pathways for viral production, transcript levels of selected genes were further quantified using qPCR. Genes involved in mainly enriched pathways were chosen for the validation test. Since our transcriptomic analysis was mainly built upon the samples from post-transfection day 2 (D2), the most rapidly proliferating phase for rAAV production, D2 cDNA libraries were then utilized for validation experiments. Table S8 showed the normalized gene expression changes between viral producing and non-producing conditions for both HEK293-BalanCD and HEK293-AMBIC. Standard deviation (SD) and coefficient of variance (CV) were calculated based on the biological replicates.

Large upregulation of IFN-β, IRF7&9, and ISGs (*OAS1*, *RSAD2*, and *ISG15*) expression further confirmed the enrichment of innate immune responses. Overexpression of heat shock proteins (*HSPA6* and *PPP1R15A*) confirmed the activation of UPR and their beneficial functions of relieving the ER stress for viral vector production. qPCR results were comparable to those shown in the transcriptomic data. It cross-validated the transcriptomic results and analysis, and confirmed the common enriched pathways we identified for the parental HEK293 cell lines.

4 | CONCLUDING REMARKS

This study compares the transcriptomes of AAV-producing and non-producing groups over time using different sources of parental HEK293 cells adapted and cultured in their respective media. A transcriptomic variance was observed between the viral-producing and non-producing groups in both systems. Their transcriptomic features reveal pathways, including innate immune responses, cell stress responses, and specific metabolisms that potentially impact rAAV production in parental HEK293 cells.

These transcriptomic results provide a mechanistic understanding to guide rational modifications (including cell line development and media optimization) to enhance rAAV production. The antiviral immune response is one of the most significant bottlenecks identified in viral production. This study proposes multiple strategies to inhibit this response: The first recommendation is to supplement the medium with small molecules that inhibit interferon-signaling proteins. This has the potential to effectively lower the production of interferon and eliminate its negative regulation of viral replication. Second, gene silencing or knockout methods can be attempted to restrict the expression of ISGs (e.g., *RSAD2*, the OAS family, the IFITM family) to eliminate their detrimental impact on viral production. Last, viral productivity may be modified by imitating the strategies used by other viruses to escape the innate immune response signaling pathways via co-transfection with plasmids that express specific viral proteins.

It has been reported that the host's cellular metabolism is reprogrammed during viral production and viral infection.[71,72] However, our transcriptomic study provides limited insights into these changes in the host cell's metabolism. Future investigations should consider host cell metabolism for AAV production. It is also critical to understand the metabolic pathways related to viral production and the accumulation of inhibitory metabolites that restrict viral productivity.

AUTHOR CONTRIBUTIONS

Yongdan Wang: Conceptualization (equal); data curation (equal); formal analysis (equal); investigation (equal); methodology (equal); validation (equal); visualization (equal); writing – original draft (equal); writing – review and editing (equal). **Qiang Fu:** Conceptualization (equal); data curation (equal); formal analysis (equal); investigation (equal); methodology (equal); validation (equal); visualization (equal); writing – original draft (equal); writing – review and editing (equal). **Yong Suk Lee:** Data curation (supporting); investigation (supporting); methodology (supporting); writing – review and editing (supporting). **Sha Sha:** Conceptualization (lead); funding acquisition (lead); supervision (lead); writing – review and editing (supporting). **Seongkyu Yoon:** Funding acquisition (supporting); project administration (lead); supervision (equal); validation (equal); visualization (equal); writing – review and editing (equal).

ACKNOWLEDGMENTS

This work was funded and supported by the Advanced Mammalian Biomanufacturing Innovation Center (AMBIC) by means of the Industry-University Cooperative Research Center Program under the U.S. National Science Foundation (Grant numbers 1624684 and 2100075). The authors would like to express our gratitude to all AMBIC member companies for their mentorship and financial support. This work was conducted for a doctoral thesis, and it was partially funded by The National Institute for Innovation in Manufacturing Biopharmaceuticals (NIIMBL, Grant/Award Number: 70NANB17H002). The authors also appreciate Sartorius Data

Analytics for providing MODDE and SIMCA licenses for this study. The authors gratefully thank Dr. David McNally for the kind provision of HEK293 cell line. The authors also thank Jack Lepine from the UMass Lowell Core Research Facility (CRF) for his kind support.

CONFLICT OF INTEREST STATEMENT

The authors declare no conflict of interest.

PEER REVIEW

The peer review history for this article is available at https://www.webofscience.com/api/gateway/wos/peer-review/10.1002/btpr.3346.

DATA AVAILABILITY STATEMENT

The data that support the findings of this study are provided in the supplemental files.

ORCID

Seongkyu Yoon https://orcid.org/0000-0002-5330-8784

REFERENCES

1. Ferrari FK, Xiao X, Mccarty D, Samulski RJ. New developments in the generation of ad-free, high-titer rAAV gene therapy vectors. *Nat Med*. 1997;3(11):1295-1297.
2. Athanasopoulos T, Fabb S, Dickson G. Gene therapy vectors based on adeno-associated virus: characteristics and applications to acquired and inherited diseases. *Int J Mol Med*. 2000;6(4):363-438.
3. Patel A, Zhao J, Duan D, Lai Y. *Adeno-Associated Virus Vectors*. Springer; 2019:19-33.
4. Clément N, Grieger JC. Manufacturing of recombinant adeno-associated viral vectors for clinical trials. *Mol Ther-Meth Clin Dev*. 2016;3:16002.
5. Weitzman MD, Linden RM. *Adeno-Associated Virus*. Springer; 2012: 1-23.
6. Meier AF, Fraefel C, Seyffert M. The interplay between adeno-associated virus and its helper viruses. *Viruses*. 2020;12(6):662.
7. Sha S, Maloney AJ, Katsikis G, et al. Cellular pathways of recombinant adeno-associated virus production for gene therapy. *Biotechnol Adv*. 2021;49:107764.
8. Wang D, Tai PWL, Gao G. Adeno-associated virus vector as a platform for gene therapy delivery. *Nat Rev Drug Discov*. 2019;18(5):358-378. doi:10.1038/s41573-019-0012-9
9. Grieger JC, Soltys SM, Samulski RJ. Production of recombinant adeno-associated virus vectors using suspension HEK293 cells and continuous harvest of vector from the culture media for GMP FIX and FLT1 clinical vector. *Mol Ther*. 2016;24(2):287-297. doi:10.1038/mt.2015.187
10. Bingnan Gu VB, Dong W, Pham H, et al. Establishment of a scalable manufacturing platform for in-silico-derived ancestral adeno-associated virus vectors. *Cell Gene Ther Insights*. 2018;4:741-751. doi:10.18609/cgti.2018.078
11. Zhao H, Lee K-J, Daris M, et al. Creation of a high-yield AAV vector production platform in suspension cells using a Design of Experiment Approach. *Mol Ther-Meth Clin Dev*. 2020;18:312-320.
12. Nguyen TN, Sha S, Hong MS, et al. Mechanistic model for production of recombinant adeno-associated virus via triple transfection of HEK293 cells. *Mol Ther-Meth Clin Dev*. 2021;21:642-655.
13. Sha S, Bhatia H, Yoon S. An RNA-seq based transcriptomic investigation into the productivity and growth variants with Chinese hamster ovary cells. *J Biotechnol*. 2018;271:37-46.
14. Kang S, Ren D, Xiao G, et al. Cell line profiling to improve monoclonal antibody production. *Biotechnol Bioeng*. 2014;111(4):748-760.
15. Rodrigues A, Formas-Oliveira A, Bandeira V, Alves P, Hu W, Coroadinha A. Metabolic pathways recruited in the production of a recombinant enveloped virus: mining targets for process and cell engineering. *Metab Eng*. 2013;20:131-145.
16. Futschik ME, Morkel M, Schäfer R, Sers C. The human transcriptome: implications for understanding, diagnosing, and treating human disease. *Mol Pathol*. 2018;135-164.
17. Lin Y-C, Boone M, Meuris L, et al. Genome dynamics of the human embryonic kidney 293 lineage in response to cell biology manipulations. *Nat Commun*. 2014;5(1):1-12.
18. Abaandou L, Quan D, Shiloach JJC. Affecting HEK293 cell growth and production performance by modifying the expression of specific genes. *Cells*. 2021;10(7):1667.
19. Ye Q, Phan T, Hu W-S, et al. Transcriptomic characterization reveals attributes of high influenza virus productivity in MDCK cells. 2021; 13(11):2200.
20. Bell TA, Velappan N, Gleasner CD, et al. Nonclassical autophagy activation pathways are essential for production of infectious influenza a virus in vitro. 2022;117(2):508-524.
21. Yu G, Lin Y, Tang Y. Diao YJljoms. *Comparative transcriptomic analysis of immune-related gene expression in duck embryo fibroblasts following duck tembusu virus infection*. 2018;19(8):2328.
22. Almuqrin A, Davidson AD, Williamson MK, et al. SARS-CoV-2 vaccine ChAdOx1 nCoV-19 infection of human cell lines reveals low levels of viral backbone gene transcription alongside very high levels of SARS-CoV-2 S glycoprotein gene transcription. 2021;13(1):1-17.
23. Havranek KE, White LA, Lanchy J-M, Lodmell JSJPO. Transcriptome profiling in rift valley fever virus infected cells reveals modified transcriptional and alternative splicing programs. 2019;14(5):e0217497.
24. Bolger AM, Lohse M, Usadel BJB. Trimmomatic: a flexible trimmer for illumina sequence data. 2014;30(15):2114-2120.
25. Langmead B, Salzberg SLJN. Fast gapped-read alignment with bowtie 2. 2012;9(4):357-359.
26. Li B, Dewey CNJB. RSEM: accurate transcript quantification from RNA-Seq data with or without a reference genome. 2011;12(1):1-16.
27. Kucukural A, Yukselen O, Ozata DM, Moore MJ, Garber MJB. DEBrowser: interactive differential expression analysis and visualization tool for count data. 2019;20(1):1-12.
28. Love MI, Huber W, Anders SJG. Moderated estimation of fold change and dispersion for RNA-Seq data with DESeq2. 2014;15(12):1-21.
29. Benjamini Y, Hochberg YJJ. Controlling the false discovery rate: a practical and powerful approach to multiple testing. 1995;57(1): 289-300.
30. Huang DW, Sherman BT, Tan Q, et al. DAVID bioinformatics resources: expanded annotation database and novel algorithms to better extract biology from large gene lists. 2007;35(suppl_2):W169-W175.
31. Ruiz-Perez D, Guan H, Madhivanan P, Mathee K, Narasimhan G. So you think you can PLS-DA? *BMC Bioinformatics*. 2020;21(1):1-10.
32. Raftery N, Stevenson NJ. Advances in anti-viral immune defence: revealing the importance of the IFN JAK/STAT pathway. *Cell Mol Life Sci*. 2017;74(14):2525-2535.
33. Brisse M, Ly H. Comparative structure and function analysis of the RIG-I-like receptors: RIG-I and MDA5. *Front Immunol*. 2019;10:1586.
34. Jia J, Fu J, Tang H. Activation and evasion of RLR signaling by DNA virus infection. *Front Microbiol*. 2021;12:1-9.
35. Chiu Y-H, MacMillan JB, Chen ZJ. RNA polymerase III detects cytosolic DNA and induces type I interferons through the RIG-I pathway. *Cell*. 2009;138(3):576-591.
36. Kawai T, Akira S. The role of pattern-recognition receptors in innate immunity: update on toll-like receptors. *Nat Immunol*. 2010;11(5): 373-384.

37. Lin Y, Zheng C. A tug of war: DNA-sensing antiviral innate immunity and herpes simplex virus type I infection. *Front Microbiol*. 2019;10:2627.
38. Sadler AJ, Williams BR. Interferon-inducible antiviral effectors. *Nat Rev Immunol*. 2008;8(7):559-568.
39. Jønsson K, Laustsen A, Krapp C, et al. IFI16 is required for DNA sensing in human macrophages by promoting production and function of cGAMP. *Nat Commun*. 2017;8(1):1-17.
40. Drappier M, Michiels T. Inhibition of the OAS/RNase L pathway by viruses. *Curr Opin Virol*. 2015;15:19-26.
41. Gusho E, Baskar D, Banerjee S. New advances in our understanding of the "unique" RNase L in host pathogen interaction and immune signaling. *Cytokine*. 2020;133:153847.
42. Honarmand Ebrahimi K, Vowles J, Browne C, McCullagh J, James WS. ddhCTP produced by the radical-SAM activity of RSAD2 (viperin) inhibits the NAD+-dependent activity of enzymes to modulate metabolism. *FEBS Lett*. 2020;594(10):1631-1644.
43. Perng Y-C, Lenschow DJ. ISG15 in antiviral immunity and beyond. *Nat Rev Microbiol*. 2018;16(7):423-439.
44. Ebrahimi KH, Howie D, Rowbotham JS, McCullagh J, Armstrong FA, James WS. Viperin, through its radical-SAM activity, depletes cellular nucleotide pools and interferes with mitochondrial metabolism to inhibit viral replication. *FEBS Lett*. 2020;594(10):1624-1630.
45. Wu Y, Yang X, Yao Z, et al. C19orf66 interrupts Zika virus replication by inducing lysosomal degradation of viral NS3. *PLoS Negl Trop Dis*. 2020;14(3):e0008083.
46. Yánez DC, Ross S, Crompton T. The IFITM protein family in adaptive immunity. *Immunology*. 2020;159(4):365-372.
47. Diamond MS, Farzan M. The broad-spectrum antiviral functions of IFIT and IFITM proteins. *Nat Rev Immunol*. 2013;13(1):46-57.
48. Stewart CE, Randall RE, Adamson CS. Inhibitors of the interferon response enhance virus replication in vitro. *PloS One*. 2014;9(11):e112014.
49. Dumbrepatil AB, Ghosh S, Zegalia KA, et al. Viperin interacts with the kinase IRAK1 and the E3 ubiquitin ligase TRAF6, coupling innate immune signaling to antiviral ribonucleotide synthesis. *J Biol Chem*. 2019;294(17):6888-6898.
50. Zhou X, Michal JJ, Zhang L, et al. Interferon induced IFIT family genes in host antiviral defense. 2013;9(2):200.
51. Heaton SM, Borg NA, Dixit VM. Ubiquitin in the activation and attenuation of innate antiviral immunity. *J Exp Med*. 2016;213(1):1-13.
52. Viswanathan K, Früh K, DeFilippis V. Viral hijacking of the host ubiquitin system to evade interferon responses. *Curr Opin Microbiol*. 2010;13(4):517-523.
53. Zhu H, Zheng CJM, Reviews MB. The race between host antiviral innate immunity and the immune evasion strategies of herpes simplex virus 1. 2020;84(4):e00099.
54. He B. Viruses, endoplasmic reticulum stress, and interferon responses. *Cell Death Diff*. 2006;13(3):393-403.
55. Hetz C, Zhang K, Kaufman RJ. Mechanisms, regulation and functions of the unfolded protein response. *Nat Rev Mol Cell Biol*. 2020;21(8):421-438.
56. Su Y-S, Hwang L-H, Chen C-J. Heat shock protein A6, a novel HSP70, is induced during enterovirus A71 infection to facilitate internal ribosomal entry site-mediated translation. *Front Microbiol*. 2021;12:664955.
57. Iyer K, Chand K, Mitra A, Trivedi J, Mitra D. Diversity in heat shock protein families: functional implications in virus infection with a comprehensive insight of their role in the HIV-1 life cycle. *Cell Stress Chaperones*. 2021;26(5):743-768.
58. Calamini B, Silva MC, Madoux F, et al. ML346: a novel modulator of proteostasis for protein conformational diseases. *Probe Reports from the NIH Molecular Libraries Program [Internet]*. 2013.
59. Smith AL, Andrews KL, Beckmann H, et al. Discovery of 1 h-pyrazol-3 (2 h)-ones as potent and selective inhibitors of protein kinase r-like endoplasmic reticulum kinase (PERK). *J Med Chem*. 2015;58(3):1426-1441.
60. Formas-Oliveira AS, Basílio JS, Rodrigues AF, Coroadinha AS. Overexpression of ER protein processing and apoptosis regulator genes in human embryonic kidney 293 cells improves gene therapy vectors production. *Biotechnol J*. 2020;15(9):1900562.
61. Omasa T, Takami T, Ohya T, et al. Overexpression of GADD34 enhances production of recombinant human antithrombin III in Chinese hamster ovary cells. *J Biosci Bioeng*. 2008;106(6):568-573.
62. Prashad K, Mehra S. Dynamics of unfolded protein response in recombinant CHO cells. *Cytotechnology*. 2015;67:237-254.
63. Onitsuka M, Tatsuzawa M, Asano R, et al. Trehalose suppresses antibody aggregation during the culture of Chinese hamster ovary cells. 2014;117(5):632-638.
64. Hwang SJ, Jeon CJ, Cho SM, Lee GM, SKJBp Y. Effect of chemical chaperone addition on production and aggregation of recombinant flag-tagged COMP-angiopoietin 1 in chinese hamster ovary cells. 2011;27(2):587-591.
65. Gong Y, Jiang JH, Li ST. Functional expression of human α7 nicotinic acetylcholine receptor in human embryonic kidney 293 cells. *Mol Med Rep*. 2016;14(3):2257-2263.
66. Cain K, Peters S, Hailu H, et al. A CHO cell line engineered to express XBP1 and ERO1-Lα has increased levels of transient protein expression. *Biotechnol Prog*. 2013;29(3):697-706.
67. Schmidt M, Afione S, Kotin RM. Adeno-associated virus type 2 Rep78 induces apoptosis through caspase activation independently of p53. *J Virol*. 2000;74(20):9441-9450.
68. Marcellus RC, JeN L, Boivin D, Shore GC, Ketner G, Branton PE. The early region 4 orf4 protein of human adenovirus type 5 induces p53-independent cell death by apoptosis. *J Virol*. 1998;72(9):7144-7153.
69. Fernández-Frías I, Pérez-Luz S, Díaz-Nido JJMT. Enhanced production of herpes simplex virus 1 amplicon vectors by gene modification and optimization of packaging cell growth medium. 2020;17:491-496.
70. Nie C, He T, Zhang W, Zhang G, Ma X. Branched chain amino acids: beyond nutrition metabolism. *Int J Mol Sci*. 2018;19(4):954.
71. Thaker SK, Ch'ng J, Christofk HR. Viral hijacking of cellular metabolism. *BMC Biol*. 2019;17(1):1-15.
72. Prusinkiewicz MA, Mymryk JS. Metabolic reprogramming of the host cell by human adenovirus infection. *Viruses*. 2019;11(2):141.

SUPPORTING INFORMATION

Additional supporting information can be found online in the Supporting Information section at the end of this article.

Received: 11 October 2022 | Revised: 20 April 2023 | Accepted: 10 May 2023
DOI: 10.1002/biot.202200513

Biotechnology Journal

RESEARCH ARTICLE

Comprehensive mRNA-sequencing-based characterization of three HEK-293 cell lines during an rAAV production process for gene therapy applications

Martina Pistek[1] | **Carolin-Isabel Kahlig**[1] | **Matthias Hackl**[2] | **Sabine Unterthurner**[1] | **Barbara Kraus**[1] | **Reingard Grabherr**[3] | **Johannes Grillari**[2,3,4] | **Juan A. Hernandez Bort**[1]

[1]Biotherapeutics Process Development, Baxalta Innovations GmbH, a part of Takeda companies, Orth an der Donau, Austria

[2]TAmiRNA, Vienna, Austria

[3]Department of Biotechnology, University of Natural Resources and Life Sciences, Vienna, Austria

[4]Ludwig Boltzmann Institute for Traumatology, The Research Center in Collaboration with AUVA, Vienna, Austria

Correspondence
Juan A. Hernandez Bort, Biotherapeutics Process Development, Baxalta Innovations GmbH, a part of Takeda companies, Uferstraße 15, 2304 Orth an der Donau, Austria.
Email: juan.hernandezbort@takeda.com

Abstract

Human embryonal kidney cells (HEK-293) are the most common host cells used for transient recombinant adeno-associated virus (rAAV) production in pharmaceutical industry. To better cover the expected gene therapy product demands in the future, different traditional strategies such as cell line sub-cloning and/or addition of chemical substances to the fermentation media have been used to maximize titers and improve product quality. A more effective and advanced approach to boost yield can be envisaged by characterizing the transcriptome of different HEK-293 cell line pedigrees with distinct rAAV productivity patterns to subsequently identify potential gene targets for cell engineering. In this work, the mRNA expression profile of three HEK-293 cell lines, resulting in various yields during a fermentation batch process for rAAV production, was investigated to gain basic insight into cell variability and eventually to identify genes that correlate with productivity. Mock runs using only transfection reagents were performed in parallel as a control. It finds significant differences in gene regulatory behaviors between the three cell lines at different growth and production stages. The evaluation of these transcriptomics profiles combined with collected in-process control parameters and titers shed some light on potential cell engineering targets to maximize transient production of rAAV in HEK-293 cells.

KEYWORDS
gene therapy, HEK-293 cells, rAAV, transcriptomics, transient transfection, virus production

1 | INTRODUCTION

Gene therapy offers the opportunity to cure diseases which originate due to defective or missing genes. Since the conception of the technology to either introduce genetic material into target cells to correct for defective genes or add missing genes was born more than 50 years ago, large effort has been put into the development and clinical trials of such therapeutic strategies.

Today, there are viral[1] and non-viral vectors[2] known to enable efficient gene delivery and more than 20 gene therapy products were already approved in different countries.[3] Although, non-viral vectors are advantageous due to low immunogenicity and higher delivery

---

Martina Pistek and Carolin-Isabel Kahlig contributed equally to this study.

Biotechnol. J. 2023;18:2200513.
https://doi.org/10.1002/biot.202200513

capacity.[4–7] Around 70% of all worldwide gene therapy clinical trials (>2300) are carried out with viral vectors, because of their high efficiency in cell transduction.[6,7]

The type of treatment that will be administered to patients depends largely on the type of disease and target cells. Different viral vectors such as retroviruses, adenoviruses, or adeno-associated viruses (AAV) were established and further developed; each of them with unique advantages and limitations. rAAVs for example are frequently used for targeting dividing and non-dividing cells and are typically transiently produced by HEK-293 cell lines.

The importance of HEK-293 cells in biomanufacturing became inevitable with the breakthrough of Frank Graham when he first immortalized the cells in 1973, and later, stably introduced adenoviral genes into the host genome.[8] This paved the way for the beginning of gene therapy since production of viral vectors became possible without the use of adenoviruses as a helper virus.[9,10]

Transient transfection is the gold standard for fast production of rAAV material. Numerous studies have shown that transfection triggers various cellular responses, in addition to cellular adaption of their transcriptome for viability.[11,12] These cellular adaptions are influenced by the genomic characteristics of each HEK-293 cell line strain. Hence, the high genetic variability within HEK-293 strains can lead to different productivity patterns.[13] However, there is surprisingly little information available on their transcriptome and its adaption to an rAAV production process.

In this study, we aimed to characterize three different HEK-293 cell line strains exhibiting different metabolic and transient rAAV8 productivity patterns during a fermentation process by RNA-sequencing. We investigated the variations in their gene expression patterns at different timepoints between pre- and post-transfection phase and observed notable differences between all three cell line strains.

2 | METHODS

2.1 | Cell culture, fermentation, and transfection

Three different HEK-293 suspension cell line strain stocks stored at −130°C were cultivated at +37°C in chemically defined serum-free media (FreeStyle F17, ThermoFisher, NY, USA) and supplemented with 8 mM L-Glutamine and 1.0 (1.2 = total) g L^{-1} Lutrol in a HERA Cell 150 (Thermo Fisher Scientific) incubator with 5% CO_2 gassing. For improved statistical analysis, four biological replicates per cell line were cultivated in Single Use Spinner flasks (Corning, Germany) with increasing volume from 61 mL up to 1600 mL during the cell expansion phase. After 12 days, cells were transferred into an ambr250 Modular fermentation system (Sartorius, Germany) under controlled conditions (pH, CO_2, O_2) for transient rAAV particle production. Before transfection, all cells were diluted to a common cell density of 4.0 × 106 cells per mL for better comparison. Each biological replicate was split in two fermentation vessels, one for plasmid and the other for mock (w/o plasmids) transfection. A triple-plasmid transfection containing Adenovirus 5 Helper genes, Rep2Cap8, and a FIX Transgene sequence, respectively, was performed using Polyethylenimine (Merck KGaA, Darmstadt, Germany) following the supplier transfection. After transfection, the cells were cultivated for 72 h at +37.0°C and sampled for analytical purposes at five different timepoints: before (0 h) and after transfection (4, 24, 48, and 72 h) resulting in 120 samples.

2.2 | RNA sequencing analysis

2.2.1 | RNA isolation

Suspension cells were sampled between a concentration of 0.5–2.0 × 106 cells per mL. Following 5 different timepoints RNA isolation was conducted using the miRNeasy Mini Kit (Qiagen, Germany). Cell pellets were homogenized in 1 mL Qiazol at room temperature. Chloroform extraction was performed and precisely 550 μL aqueous phase were used for Ethanol precipitation. Precipitated RNA was applied to the miRNeasy columns, washed twice, dried, and eluted in 30 μL nuclease-free water. Spectrophotometric analysis (Nanodrop, Thermo Fisher) and capillary electrophoresis (Agilent Bioanalyzer RNA 6000 nano) were used for determining RNA -concentration, -integrity, and purity. All samples achieved RNA integrity numbers (RIN) above 9 and an RNA concentration of >500 ng μL^{-1}.

2.2.2 | Library preparation

Library preparation was performed with Lexogen QuantSeq 3′ mRNA-Seq Library Prep Kit FWD for Illumina (Lexogen, Austria) using 500 ng of total RNA input. Both Library yield and concentration was confirmed by RT-qPCR as well as size range using the Agilent Bioanalyzer (Agilent, United States). Equimolar pooling was performed and DNA sizes between 100–700 nucleotides were selected by capillary gel electrophoresis using a BluePippin instrument (Sage Biosciences, United States).

2.2.3 | Next-generation sequencing

Next-generation sequencing (NGS) analysis of the QuantSeq libraries was performed in the NGS Facility at Vienna Biocenter Core Facilities (VBCF, Austria). First, a test run was performed using paired-end 150 bp reads on an iSeq 100 instrument. Following a quality check for read length, adapter content and unique mapping, a NovaSeq SP run with 100 bp single-end reads was performed to generate more than 800 million 100 bp reads. Demultiplexing was performed and fastq files were generated.

2.2.4 | Genomic mapping and normalization

Demultiplexed NGS data were analyzed according to the protocols provided by the manufacturer (Lexogen, Austria). Reads were filtered with the open-source tool bbduk (v 38.69) from the bbmap suite[14] to remove adapter contamination, poly-A read-throughs, and low-quality tails. Overall sequencing quality was assessed with FASTQC (v 0.11.8).[15] Alignment of reads against the GRCh38 genome[16] using STAR Aligner (v 2.7)[17] was followed by quantification of features and generation of count matrices using HTSeq-count (v 0.12).[18]

2.2.5 | Differential expression analysis

Cut-off was applied by the EdgeR function "filter by expression," with a min. count of 5. Normalization inclusive log2 scaling was performed using EdgeR function voom from the limma package with default parameters.

2.2.6 | Gene set enrichment analysis

The desktop application version of GSEA (version 4.1.0.) from Broad Institute (https://www.gsea-msigdb.org/gsea) was used to perform a gene set enrichment analysis (GSEA).[19,20] Expression dataset contained normalized (RPM) non-logarithmic sequencing reads, including gene names mapped to HGNC IDs. Genes with low expression values (selection criteria: mean of each sample group $n = 4$ (per cell line, per timepoint, per transfection condition); sum of means from all timepoints per condition per cell line <100) were excluded from analysis. Following settings were applied: Gene sets database: c5.go.bp.v7.2.symbols.gmt; Number of permutations: 1000; Collapse: No; Permutation type: gene set; Metric for ranking genes: Signal2Noise; Enrichment statistics: weighted.

2.2.7 | Sequencing verification (qRT-PCR)

1 mL of cell suspension was harvested, washed with PBS once and pelleted at 2500 x g. RNA isolation was performed with PureLink RNA Mini Kit (Invitrogen) using 96% ethanol according to the manufacturer instruction. The nucleic acid concentration was determined by nanodrop. Transcriptor High Fidelity cDNA Synthesis Kit (Roche) was used according to protocol, and reverse transcription took place at +48°C for 60 min, followed by inactivation of RT for 5 min at +85°C. qRT duplex PCR was performed with Quantstudio 5 Software (Thermo Fisher) using TaqMan assays and ΔΔCT method to determine fold change of target gene expression. Assays for target genes were acquired from Thermo Fisher as follows. Housekeeping Genes: IPO8 (Hs00914057_m1), TBP (Hs00427620_m1), target genes: SNHG1 (Hs00411543_m1), SNHG12 (Hs00414754_m1), CRELD2 (Hs00911477_m1), IER2 (Hs01109355_m1), IGFBP5 (Hs00181213_m1), PRDX1 (Hs00602020_m1), and TXNIP (Hs00197750_m1).

2.3 | Statistics

PCR and ELISA statistics titer analysis were determined with ordinary one-way-ANOVA and Tukey multiple comparisons adjusted *p*-value, 95% confidence interval. Metabolite data were based on two-way-ANOVA with fitted full model and a Tukey adjusted *p*-value to multiple testing, $p < 0.05$, 95% confidence interval. Simple linear regression for mRNA PCR validation was conducted with 95% confidence interval.

2.4 | Analytics

2.4.1 | Droplet digital PCR (ddPCR)

For vector genome quantification, a Bio-Rad based droplet digital PCR method was used, applying the fully automated QX One System or semi-automated QX 200 AutoDG system. This method provides absolute quantification of vector genome without the use of standard curves. The sample is partitioned into oil droplets and each droplet becomes an independent compartment for PCR reaction. Degeneration of capsids takes place in the initial phase of the PCR in the thermal cycler and DNA becomes accessible for amplification. Vector genome titer is then determined using a droplet reader. Samples were treated with DNase I (NEB) to remove extraneous DNA sequences. Prior the treatment, samples were prediluted to increase the efficiency of the DNase I activity. After droplet generation, PCR was performed with Bio-Rad ddPCR Supermix (no dUTP) and transgene-specific primers and probe:—Fwd 5′-GGC ATC TAC ACC AAA GTC TCC AG -3′, Rev 5′-CAG CGA GCT CTA GGC ATG CT -3′, probe 5′-6FAM-AGA CCA AGC TGA CCT GAT-MGBNFQ -3′. Vector genome concentration was calculated by the appropriate Bio-Rad software.

2.4.2 | ELISA

The commercially available enzyme-linked immunosorbent assay (ELISA; Progen AAV8 titration ELISA kit, cat. No. PRAAV8) was used with a monoclonal antibody (ADK8) specific for a conformational epitope on assembled AAV8 capsids. Captured particles are then detected by the binding of biotinylated anti-AAV8 ADK8 since epitope targeted is repeatedly expressed on the assembled AAV8 capsid. Streptavidin peroxidase and a peroxidase substrate is then used for measuring bound anti-AAV8 and thus, the concentration of AAV8 capsid. The color reaction was measured photometrically at 450 nm. The kit contains an AAV2/8 particle preparation as calibration standard with a labeled AAV8 particle concentration.

3 | RESULTS

For transcriptome analysis, we selected three different HEK-293 suspension cell line strains exhibiting varying productivity pat-

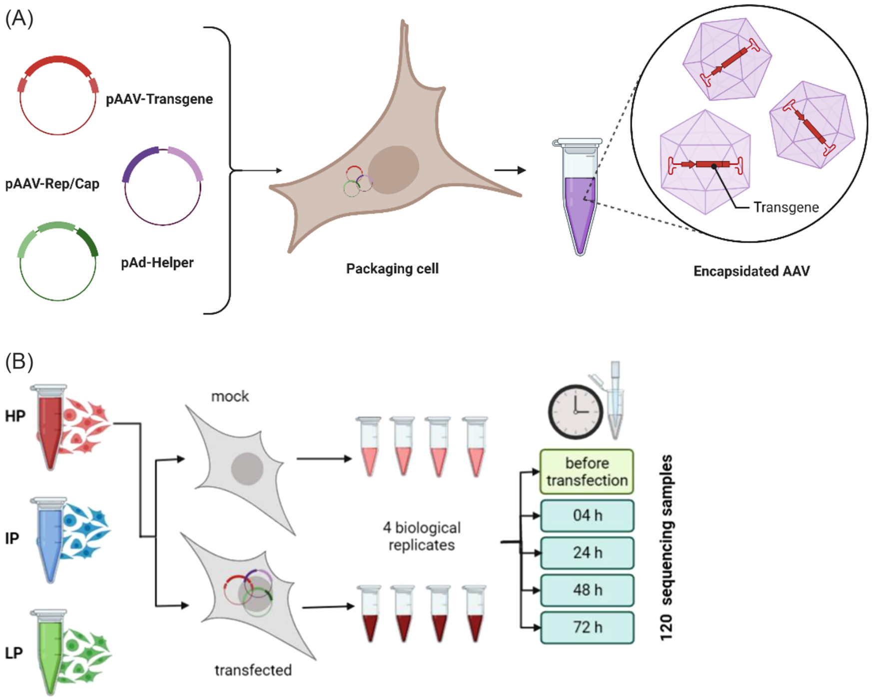

FIGURE 1 Experimental design of this study. (A) Schematic principle of the triple transfection process used in this study. (B) Three different HEK293 cell line strains, high (HP), intermediate (IP), and low producer (LP) were investigated. Each of four biological replicates (independently thawed) were used for both conditions, transfected and mock (non-transfected). Sampling was carried out for each biological replicate at five different timepoints, resulting in 120 samples which were then sequenced with Illumina for mRNA expression. Pictures adapted from Biorender Template (1) and created with BioRender.com.

terns. All used strains were derived from the parental cell line generated by Graham.[8] The HEK-293 cell line strain CRL-1573 (ATCC) was adapted for suspension serum-free media and considered in this study as low producer cell line. Further, two HEK-293 parental cell line strains used in-house in suspension and displaying increased transfectability properties were compared to the reference strain.

The aim of this study was to compare the dynamic mRNA expression patterns at different timepoints during a rAAV8 production process and identify whether specific gene regulatory pathways can be assigned to higher rAAV8 titers. An overview of the experimental setup is described in Figure 1

To determine the transient productivity, we analyzed samples collected at 48 and 72 h timepoints post-transfection via ELISA using specific antibodies complementary only to fully assembled particles, discriminating against free unassembled capsid proteins. Since certain subsets of HEK-293 cell lines tend to retain rAAV intracellularly compared to the norm, we analyzed both supernatant and lysed cell suspension. The latter was considered to represent the total number of assembled particles: the sum of released and non-released into the fermentation broth.

For the quantification of produced FIX transgene, we analyzed the specimens with droplet digital PCR (ddPCR) using specific primer pairs for the DNA as above mentioned.

3.1 | Assessment of productivity, growth and metabolic patterns in high, intermediate, and low producer HEK-293 cell line strains

The relative rAAV8 yields achieved after 72 h of transfection from supernatant and whole cell suspension lysates were normalized (considering 100% as the mean yield) from four biological replicates of the reference HEK-293 cell line strain (Low Producer, from now on termed LP). The further two HEK-293 cell line strains used in this study were labeled as high producer (HP) and intermediate producer (IP) based on in-house experience with those cell lines. As shown in Figure 2, HP was significantly superior in both, rAAV8 particle (2A) and FIX transgene (2B) production, which is applicable for both, rAAV8 released particles and total produced rAAV8 (cell suspension).

Principally, HP released +180% and IP about +62% more particles into the supernatant as compared to LP, respectively. In the case of cell suspension lysates, the difference in yield was similar for HP (+152%) but not as pronounced for IP (+15%). These results suggested that the total amount of produced rAAV8 between IP and LP was similar, but LP showed limitations in regard to rAAV8 release. By contrast, HP was superior in total particle production and release.

A similar pattern was observed when comparing the produced FIX transgene. Figure 2B shows the results for the supernatant and cell suspension lysate samples. After 72 h of transfection, HP cell line

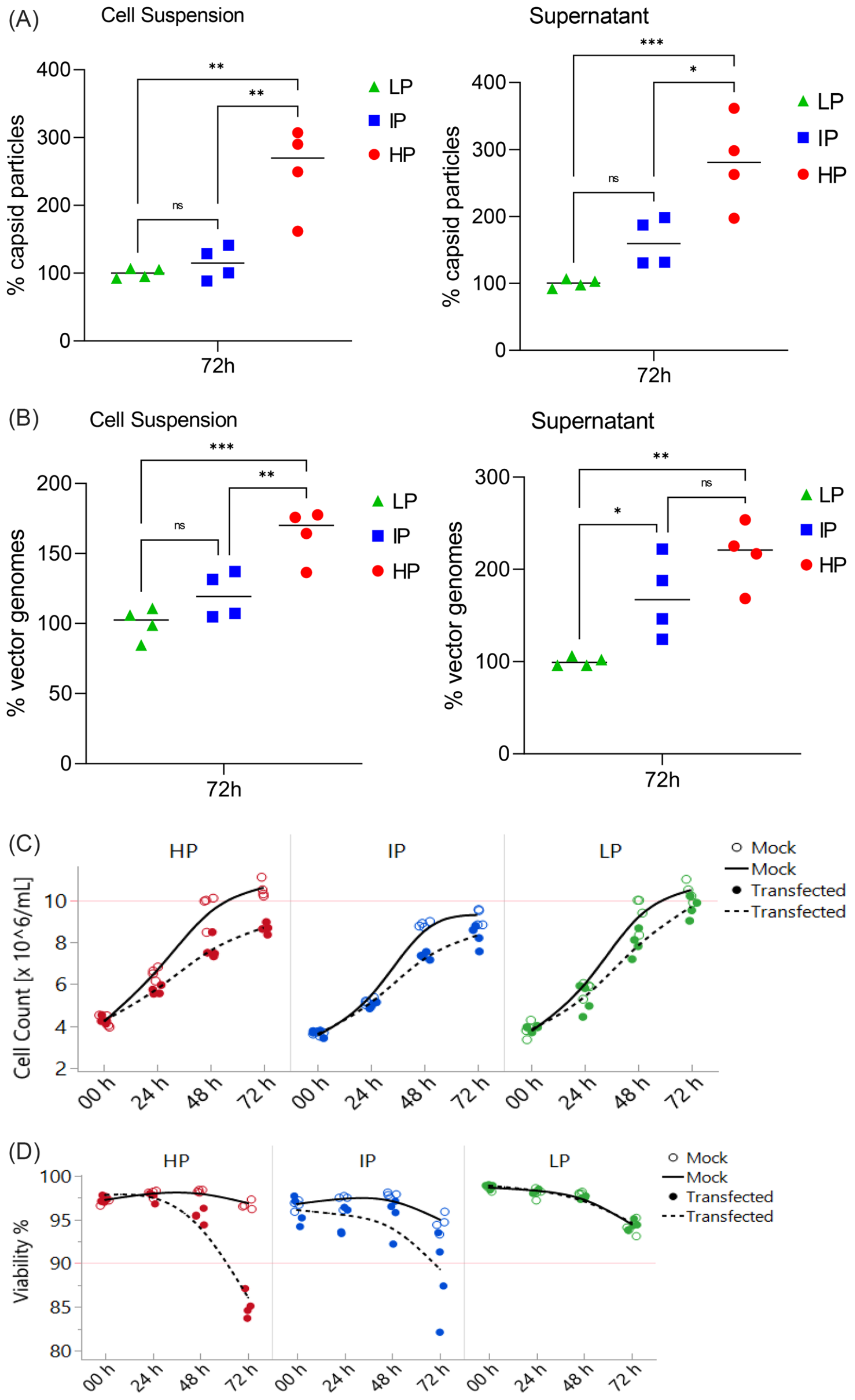

FIGURE 2 Comparison of productivity, growth and metabolic patterns for HP, IP, and LP cell line strains. Differences between HP, IP, and LP strain patterns are shown in regards of (A) assembled rAAV8 capsid production in total cell suspension (left) and secreted (right), (B) transgene production in total (left) and secreted (right), (A) and (B) were evaluated by one-way-ANOVA and Tukey's multiple comparisons test (CI = 95%, $p < 0.05$), (C) cell counts, (D) viability, and (E) selected metabolites indicated above the graphs (glucose, glutamine, lactate, glutamine, and ammonia) at three different timepoints after plasmid and mock transfection throughout the rAAV production process. Error bars indicate Mean ± SEM, significances were evaluated by two-way ANOVA with Tukey's multiple comparisons test, (CI = 95%, $p < 0.05$).

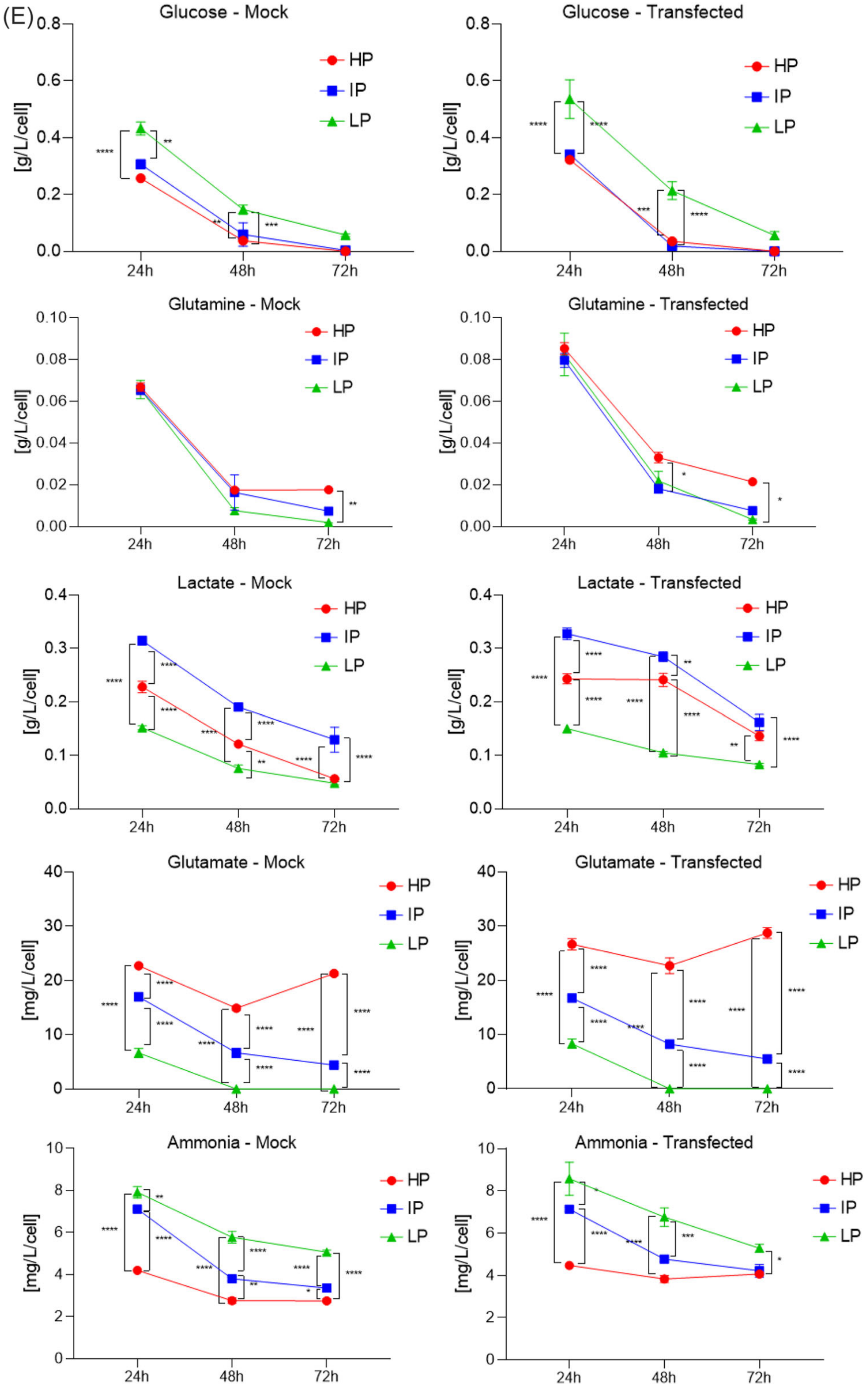

FIGURE 2 Continued

produced +115% (supernatant) and +63% (cell suspension lysate) of the transgene compared to LP, whereas IP provided +70% (supernatant) and +20% (cell suspension) more FIX transgene.

During rAAV8 production, cells tended to decrease their growth rates most likely due to increased energy consumption required for virus replication, assembly, and secretion. This effect was more prominent in the HP strain, whereby cell count fell to −17.7% (from 10.53×10^6 cells per mL in mock transfected cells to 8.66×10^6 cells per mL in producing cells), as shown in Figure 2C. IP reduced its cell growth by −9.8% when compared to mock (9.18×10^6 cells per mL) and transfected cells (8.28×10^6 cells per mL). In contrast, LP showed the smallest growth difference between mock (10.40×10^6 cells per mL) and transfected cells (9.66×10^6 cells per mL) with −7.1% difference. A similar pattern was observed for cell viability (Figure 2D), where HP showed a relative drop in −11.9% and IP of −6.3%, whereas LP did not exhibit any reduced viability at all.

Further differences were observed when comparing selected metabolites during the fermentation process as shown in Figure 2E. Metabolite analysis was performed with Cedex Bio HT analyzer (Roche) and values were normalized to the cell count to better compare consumption and production rates. We found that LP consumed lower amounts of glucose in general (Figure 2E) and this effect was more evident in transfected cells (Figure 2F). However, the transfected IP tended to metabolize glucose more rapidly than HP whilst showing similar consumption pattern. All three cell lines exhibited a higher glucose consumption in mock than in transfected cells. The glutamine consumption of LP cell line was higher compared to IP and HP cell line and was more evident in mock than in transfected cells. After transfection, the glutamine consumption pattern between IP and LP was comparable. IP and LP depleted nearly all glutamine 72 h after transfection, whereas HP had, in both conditions, consumed the remaining glutamine and still showed a 0.02 g L^{-1} per cell consumption rate. For all cell lines, we observed different amounts of lactate consumption, with variations between mock and transfected cells. (Figure 2F). During batch process, cells in general produced lactate as a result of glycolysis, but conversely, consumed it as an alternative energy source. In both conditions, IP showed the highest lactate accumulation, followed by HP and LP. A correlation between glucose depletion and lactate accumulation could be observed for all cell lines. However, transfected HP and IP cells remained at a relatively high lactate levels until 48 h post-transfection, whereas post-transfection, LP and all three mock conditions displayed a constant decrease. Glutamate is a catabolic byproduct of glutamine metabolism and here, differences in the measured amounts were observed 24 h post-transfection as (Figure 2F). HP cell lines showed the highest glutamate concentration at all timepoints and the concentration displayed a relative increase at the 72 h post-transfection timepoint. In comparison to HP, the glutamate concentration for IP decreased consistently after transfection (Figure 2F), however, it was not depleted completely. LP showed the lowest glutamate concentration at the 24 h post-transfection and was already depleted 48 h post-transfection timepoints. Glutamate is further catabolized via the citric acid cycle into Ammonia. Ammonia is known to pass through the cellular membrane and intracellularly influence local pH in organelles, leading to perturbation of protein processing and even virus replication.[21] The highest ammonia production was detected in LP fermentation broth being 2-fold higher 24 h post-transfection (Figure 2F) as compared to the HP cell line. With the progression of transfection time, ammonia production decreased in LP whereas the level in HP slightly increased and in IP slightly decreased.

To summarize, these results showed metabolic differences within the three HEK-293 cell line strains investigated in this study during transient rAAV8 production. LP cell line showed the most significant differences for glucose, lactate, glutamate, and ammonia metabolism as compared to HP and IP cell line.

3.2 | Differences in gene expression pattern profiles

Despite differences in productivity and metabolite consumption patterns, we examined transcriptional activity to obtain a global picture of their cellular function, including the dynamic changes of gene expression during the rAAV8 production. Therefore, we performed 3′ analysis of c-DNA ends (3′MACE) sequencing to specifically analyze the transcriptome. The quality of the mRNA sequencing is shown in Figure S1 by RNA integrity after isolation (A) and a FastQC mapping reports (C). In total, we sequenced 120 samples, with a mean of 7,012,537 reads (min 4.9 mio, max 10.6 mio, Figure S1B). One sample was excluded (T107128; HP 72 h post-transfection mock replicate) due to low sequencing quality. To verify our sequencing data, control data was obtained by performing qRT-PCR. In order to establish an endogenous control, we tested different housekeeping genes, identifying IPO8 and TBP as appropriate controls as they are constitutively expressed in all three cell lines. For validation, a linear regression model including four replicates per timepoint of HP and LP, respectively, was aligned to correlate sequencing reads (reads per million, rpm) with PCR reads of selected genes according to ΔΔCT method. A confirmation of the sequencing results in general is shown in Figure 3.

To detect global differences and to achieve better data visualization and interpretation, we primarily opted for a reducing model. We chose principal component analysis (PCA) and used $\log_2$ transformed normalized counts per million (CPM) sequencing data to visualize major differences. Interestingly, highest variations could be observed between the cell lines, whereas alterations of gene expression patterns within a cell line, regardless of the comparison between mock and transfected cells or between timepoints were less prominent, and therefore could not be distinguished in this reduced model (Figure 4A).

To examine the select three cell lines based on normalized sequencing data in more detail, we started with analyzing differential gene expression before transfection (t = 0 h). We used normalized TPM (transcript per million) sequencing data ($n = 4$ per cell line) and applied a threshold of CPM ≥ 100 per gene for the sum of each comparison group (HP vs. LP and HP vs. IP). Selected genes were clustered according to predicted biological processes, using GO terms of the C5BP set of the Molecular Signature Database (Broad Institute). A subsequent GSEA of the cell lines' mRNA expression profile revealed major differences in expression patterns, indicated by positive or negative normalized enrichment scores (NES) of respective GO terms. Enrichment scores and affiliated significance of resulting gene sets were combined to determine their Manhattan distance. The top 30 hits are highlighted in a volcano dot blot (Figure 4B), where positive NES imply higher expression in HP. In comparison between HP and LP, the majority of the top 30 dissimilar GO terms belong to a few biological processes, whereas differences between HP and IP identified gene sets of more dispersed functions.

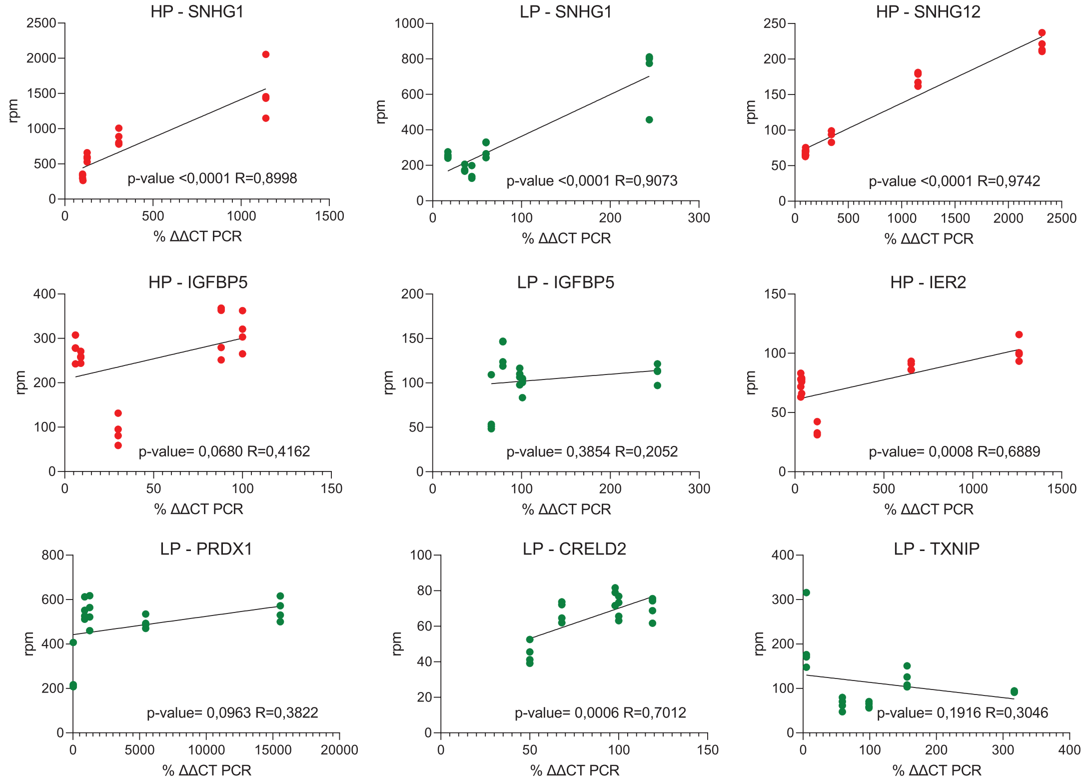

FIGURE 3 Confirmation of sequencing data by qRT-PCR. Linear regression models represent correlations between sequencing data (reads per million, rpm) and qRT-PCR data evaluated with the ΔΔCT method of selected mRNAs. Gene expression changes over time are shown per gene for all timepoints (0, 4, 24, 48 and 72 h). Data includes biological replicates, $n = 4$.

One of the most significant findings indicated substantial enrichment of endoplasmic reticulum (ER)-related GO terms in HP (GO REGULATION OF RESPONSE TO ER STRESS ID1, GO ENDOPLASMIC RETICULUM UNFOLDED PROTEIN RESPONSE ID7) when compared to LP. Interestingly, although 5 out of 19 ER-related gene sets were amongst the top 30 regulated GO terms (above 4.9 score of Manhattan distance), neither of them could be found in the comparison between HP and IP. Upon closer examination, we found that HP was more closely related to IP in terms of expression profiles of designated genes than to LP, as Manhattan distance for IP was below 2.4, which is shown in Figure S2. Additionally, the higher transcription rates of genes involved in sterol metabolism (GO STEROL BIOSYNTHETIC PROCESS ID2905, GO STEROLE METABOLIC PROCESS ID2903, ISOPRENOID METABOLIC PROCESS ID2815) in both, IP and LP were significant. Although differences between these two cell lines are not as evident as for ER-related gene sets, we again, found greater distances between HP and LP than between HP and IP (Figure S2). Furthermore, in comparison to LP, HP showed higher transcription rates regarding genes involved in amino acid biosynthesis (GO NEUTRAL AMINO ACID TRANSPORT ID2; GO ALPHA AMINO ACID BIOSYNTHETIC PROCESS ID4), while in contrast LP had a higher activity electron transport (GO ATP SYNTHESIS COUPLED ELECTRON TRANSPORT ID2898, GO RESPIRATORY ELECTRON TRANSPORT CHAIN ID2890).

We further examined differential single gene expression levels, identifying genes with the highest expression variance between cell lines. We examined normalized CPM sequencing data and calculated the $\log_2$ fold change between HP and IP or LP, respectively, at timepoint 0 h ($n = 8$ per cell line) for genes that achieved a threshold for an average expression of 10 CPM per sample. The significance was determined via *t*-test, and results are summarized in a volcano dot blot shown in Figure 4C. Again, Manhattan distance was used to determine the top 20 genes. Both comparisons showed a different pattern but shared four common genes that were higher expressed in IP and LP when both compared to HP: (i) SRY-Box Transcription Factor 11 (SOX11 ID9073), which is known to play a role in embryogenesis, certain cancers[22] and epigenetic regulation,[23] (ii) Ubiquitin specific peptidase 32 Protein 2 (USP32P2 ID9078), and (iii) Zinc Finger Protein 682 (ZNF682 ID9068), a transcriptional regulator. Moreover, in contrast to HP, LP showed significantly higher expression of keratin 19 (KRT19 ID9076), Gamma-Aminobutyric Acid Type A Receptor Subunit Beta3 (GABRB3 ID9077), a subunit of chloride channels and receptor for gamma-aminobutyric acid, but lower expression of Glycogenin 2 (GYG2 ID5), protein kinase X gene (PRKX ID4) and Patatin-like phospholipase domain-containing protein 4 (PNPLA4 ID7). In comparison to IP, HP showed the most significant difference in the higher expression of Microsomal Glutathione S-Transferase 1 (MGST1 ID2),

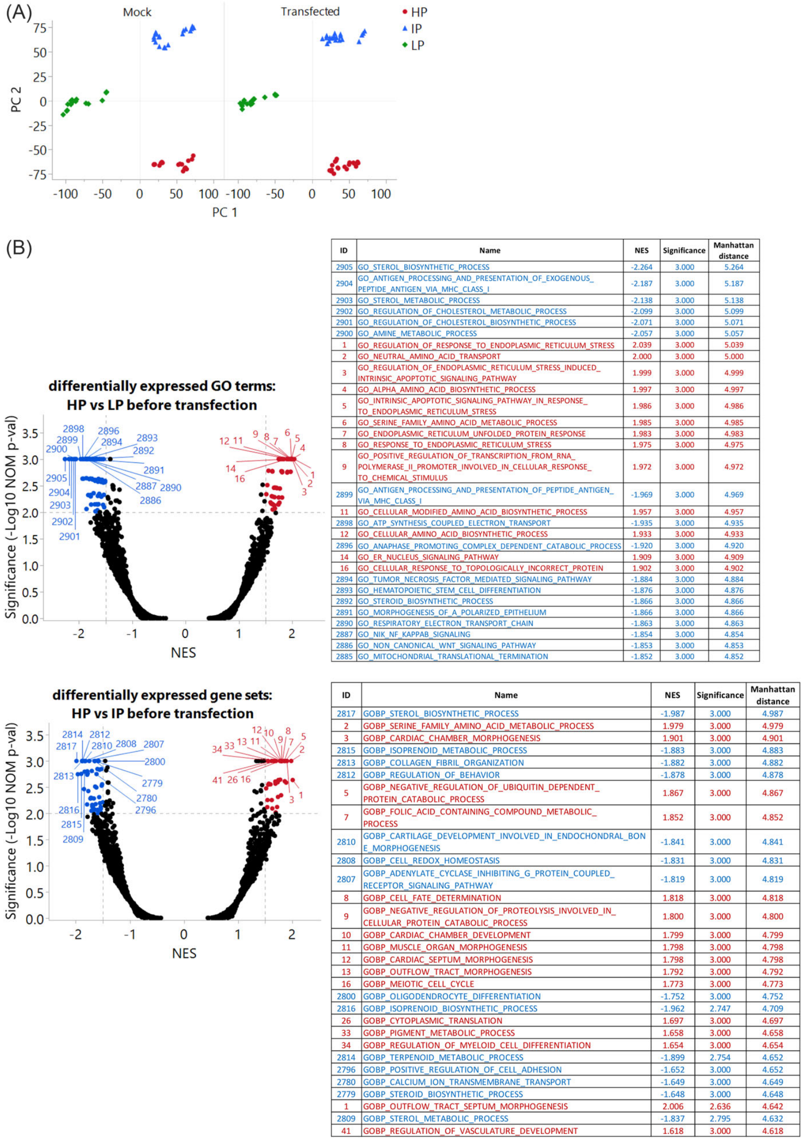

ID	Name	NES	Significance	Manhattan distance
2905	GO_STEROL_BIOSYNTHETIC_PROCESS	-2.264	3.000	5.264
2904	GO_ANTIGEN_PROCESSING_AND_PRESENTATION_OF_EXOGENOUS_PEPTIDE_ANTIGEN_VIA_MHC_CLASS_I	-2.187	3.000	5.187
2903	GO_STEROL_METABOLIC_PROCESS	-2.138	3.000	5.138
2902	GO_REGULATION_OF_CHOLESTEROL_METABOLIC_PROCESS	-2.099	3.000	5.099
2901	GO_REGULATION_OF_CHOLESTEROL_BIOSYNTHETIC_PROCESS	-2.071	3.000	5.071
2900	GO_AMINE_METABOLIC_PROCESS	-2.057	3.000	5.057
1	GO_REGULATION_OF_RESPONSE_TO_ENDOPLASMIC_RETICULUM_STRESS	2.039	3.000	5.039
2	GO_NEUTRAL_AMINO_ACID_TRANSPORT	2.000	3.000	5.000
3	GO_REGULATION_OF_ENDOPLASMIC_RETICULUM_STRESS_INDUCED_INTRINSIC_APOPTOTIC_SIGNALING_PATHWAY	1.999	3.000	4.999
4	GO_ALPHA_AMINO_ACID_BIOSYNTHETIC_PROCESS	1.997	3.000	4.997
5	GO_INTRINSIC_APOPTOTIC_SIGNALING_PATHWAY_IN_RESPONSE_TO_ENDOPLASMIC_RETICULUM_STRESS	1.986	3.000	4.986
6	GO_SERINE_FAMILY_AMINO_ACID_METABOLIC_PROCESS	1.985	3.000	4.985
7	GO_ENDOPLASMIC_RETICULUM_UNFOLDED_PROTEIN_RESPONSE	1.983	3.000	4.983
8	GO_RESPONSE_TO_ENDOPLASMIC_RETICULUM_STRESS	1.975	3.000	4.975
9	GO_POSITIVE_REGULATION_OF_TRANSCRIPTION_FROM_RNA_POLYMERASE_II_PROMOTER_INVOLVED_IN_CELLULAR_RESPONSE_TO_CHEMICAL_STIMULUS	1.972	3.000	4.972
2899	GO_ANTIGEN_PROCESSING_AND_PRESENTATION_OF_PEPTIDE_ANTIGEN_VIA_MHC_CLASS_I	-1.969	3.000	4.969
11	GO_CELLULAR_MODIFIED_AMINO_ACID_BIOSYNTHETIC_PROCESS	1.957	3.000	4.957
2898	GO_ATP_SYNTHESIS_COUPLED_ELECTRON_TRANSPORT	-1.935	3.000	4.935
12	GO_CELLULAR_AMINO_ACID_BIOSYNTHETIC_PROCESS	1.933	3.000	4.933
2896	GO_ANAPHASE_PROMOTING_COMPLEX_DEPENDENT_CATABOLIC_PROCESS	-1.920	3.000	4.920
14	GO_ER_NUCLEUS_SIGNALING_PATHWAY	1.909	3.000	4.909
16	GO_CELLULAR_RESPONSE_TO_TOPOLOGICALLY_INCORRECT_PROTEIN	1.902	3.000	4.902
2894	GO_TUMOR_NECROSIS_FACTOR_MEDIATED_SIGNALING_PATHWAY	-1.884	3.000	4.884
2893	GO_HEMATOPOIETIC_STEM_CELL_DIFFERENTIATION	-1.876	3.000	4.876
2892	GO_STEROID_BIOSYNTHETIC_PROCESS	-1.866	3.000	4.866
2891	GO_MORPHOGENESIS_OF_A_POLARIZED_EPITHELIUM	-1.866	3.000	4.866
2890	GO_RESPIRATORY_ELECTRON_TRANSPORT_CHAIN	-1.863	3.000	4.863
2887	GO_NIK_NF_KAPPAB_SIGNALING	-1.854	3.000	4.854
2886	GO_NON_CANONICAL_WNT_SIGNALING_PATHWAY	-1.853	3.000	4.853
2885	GO_MITOCHONDRIAL_TRANSLATIONAL_TERMINATION	-1.852	3.000	4.852

ID	Name	NES	Significance	Manhattan distance
2817	GOBP_STEROL_BIOSYNTHETIC_PROCESS	-1.987	3.000	4.987
2	GOBP_SERINE_FAMILY_AMINO_ACID_METABOLIC_PROCESS	1.979	3.000	4.979
3	GOBP_CARDIAC_CHAMBER_MORPHOGENESIS	1.901	3.000	4.901
2815	GOBP_ISOPRENOID_METABOLIC_PROCESS	-1.883	3.000	4.883
2813	GOBP_COLLAGEN_FIBRIL_ORGANIZATION	-1.882	3.000	4.882
2812	GOBP_REGULATION_OF_BEHAVIOR	-1.878	3.000	4.878
5	GOBP_NEGATIVE_REGULATION_OF_UBIQUITIN_DEPENDENT_PROTEIN_CATABOLIC_PROCESS	1.867	3.000	4.867
7	GOBP_FOLIC_ACID_CONTAINING_COMPOUND_METABOLIC_PROCESS	1.852	3.000	4.852
2810	GOBP_CARTILAGE_DEVELOPMENT_INVOLVED_IN_ENDOCHONDRAL_BONE_MORPHOGENESIS	-1.841	3.000	4.841
2808	GOBP_CELL_REDOX_HOMEOSTASIS	-1.831	3.000	4.831
2807	GOBP_ADENYLATE_CYCLASE_INHIBITING_G_PROTEIN_COUPLED_RECEPTOR_SIGNALING_PATHWAY	-1.819	3.000	4.819
8	GOBP_CELL_FATE_DETERMINATION	1.818	3.000	4.818
9	GOBP_NEGATIVE_REGULATION_OF_PROTEOLYSIS_INVOLVED_IN_CELLULAR_PROTEIN_CATABOLIC_PROCESS	1.800	3.000	4.800
10	GOBP_CARDIAC_CHAMBER_DEVELOPMENT	1.799	3.000	4.799
11	GOBP_MUSCLE_ORGAN_MORPHOGENESIS	1.798	3.000	4.798
12	GOBP_CARDIAC_SEPTUM_MORPHOGENESIS	1.798	3.000	4.798
13	GOBP_OUTFLOW_TRACT_MORPHOGENESIS	1.792	3.000	4.792
16	GOBP_MEIOTIC_CELL_CYCLE	1.773	3.000	4.773
2800	GOBP_OLIGODENDROCYTE_DIFFERENTIATION	-1.752	3.000	4.752
2816	GOBP_ISOPRENOID_BIOSYNTHETIC_PROCESS	-1.962	2.747	4.709
26	GOBP_CYTOPLASMIC_TRANSLATION	1.697	3.000	4.697
33	GOBP_PIGMENT_METABOLIC_PROCESS	1.658	3.000	4.658
34	GOBP_REGULATION_OF_MYELOID_CELL_DIFFERENTIATION	1.654	3.000	4.654
2814	GOBP_TERPENOID_METABOLIC_PROCESS	-1.899	2.754	4.652
2796	GOBP_POSITIVE_REGULATION_OF_CELL_ADHESION	-1.652	3.000	4.652
2780	GOBP_CALCIUM_ION_TRANSMEMBRANE_TRANSPORT	-1.649	3.000	4.649
2779	GOBP_STEROID_BIOSYNTHETIC_PROCESS	-1.648	3.000	4.648
1	GOBP_OUTFLOW_TRACT_SEPTUM_MORPHOGENESIS	2.006	2.636	4.642
2809	GOBP_STEROL_METABOLIC_PROCESS	-1.837	2.795	4.632
41	GOBP_REGULATION_OF_VASCULATURE_DEVELOPMENT	1.618	3.000	4.618

FIGURE 4 Inherent differences between HP and LP in gene expression. (A) Principal component analysis of HP and LP, separated into mock (M) and transfected (T) conditions, PC 1 captures 21.1% of variances and PC 2 16.7% volcano blot of (B) gene set enrichment analysis (GSEA) representing GO terms and (C) differential expression analysis of genes that are most different between HP and LP, respectively, before transfection ($t = 0$ h). Top 30 GO terms and top 20 genes according to Manhattan distance are displayed in the tables beneath. Positive scores correlate with higher expression in HP.

which plays an important role in cellular defense against oxidative stress, and a lower expression of Major Histocompatibility Complex, Class I, A (HLA-A ID9067) and G-protein-coupled Receptor 50 (GPR50 9071).

In summary, all three selected cell lines exhibited a highly distinctive expression pattern in their native state, and therefore, they seem to be equipped with different genetic characteristics. From those findings, we inferred that our cells may also react differently to transient transfections and subsequent rAAV production.

3.3 | Changes in gene expression 24 h after transfection highly depends on the expression pattern the three cell lines display in their native state

Transient transfection is known to induce stress responses because of introduction of foreign DNA with the help of cationic molecules known as transporters. Additional challenges for the cell synthesis machinery arise when a recombinant protein must be produced, and even more

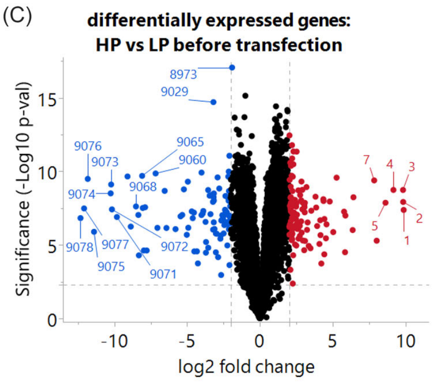

ID	Name	FC (log2)	Significance	Manhattan distance
9076	KRT19	-11.826	9.492	21.318
9077	GABRB3	-12.078	7.483	19.562
9073	SOX11	-10.221	9.113	19.333
8978	USP32P2	-12.322	6.828	19.150
8973	CCND1	-1.918	1.707	18.985
9074	TSTD1	-10.251	8.509	18.760
9070	TNFRSF10A	-9.096	9.658	18.754
3	ITPRIPL1	9.815	8.740	18.555
9029	SIM1	-3.200	14.713	17.913
4	PRKX	9.155	8.742	17.897
9065	PEG10	-8.094	9.698	17.792
2	PCDH11X	9.825	7.924	17.749
9072	FAM111B	-10.166	7.418	17.585
1	LOC389906	9.859	7.381	17.240
7	PNPLA4	7.835	9.390	17.225
9060	BEX1	-7.169	9.864	17.033
9070	CCDC144B	-9.825	6.902	16.727
5	GYG2	8.611	7.871	16.482
9068	ZNF682	-8.517	7.618	16.135

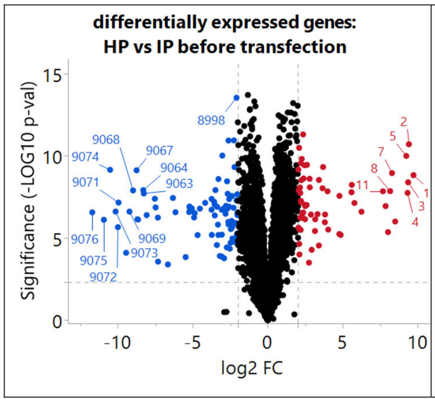

ID	Name	FC (log2)	Significance	Manhattan distance
2	MGST1	9.405	10.705	20.110
9074	CRYGD	-10.515	9.148	19.663
5	ZNF544	9.234	9.994	19.227
1	NRXN3	9.715	8.825	18.540
3	SLC6A11	9.355	8.388	17.743
7	CLMP	8.280	8.949	17.230
9071	GPR50	-9.954	7.155	17.109
4	NEFM	9.320	7.746	17.066
9075	SOX11	-10.936	6.109	17.044
9068	STC1	-8.987	7.896	16.883
9073	KLHL4	-10.152	6.611	16.763
9064	TCEAL7	-8.306	7.914	16.220
8	PKP3	8.154	7.852	16.006
9063	PEG10	-8.271	7.711	15.982
9069	ZNF682	-9.227	6.606	15.833
9072	USP32P2	-9.998	5.663	15.661
8998	PKIB	-2.089	13.530	15.618
11	ZSCAN18	7.675	7.842	15.516

FIGURE 4 Continued

so, when entire particles must be made and assembled. Numerous vital pathways may be affected by this metabolic burden. Although, we analyzed all timepoints, we were relatively more interested in immediate changes that would occur within 24 h after transfection. Interestingly, upon investigation, we also found that most changes occur at this early timepoint (t = 24 h) compared to the steady state of the cells at initial testing (t = 0 h) (Figure S3), implying the importance of a rapid adaption to changing conditions.

Thus, a GSEA analysis was performed with our sequencing data, comparing the CPMs for each timepoint after (04, 24, 48, 72 h) against and before (00 h) transfection (n = 4), to indicate relative changes within each cell line. For a better overview, we only show enrichment scores of selected gene sets in Figure 5A, clustered according to their biological functions. Notably, HP cell line upregulate gene sets related to ATP activity (GO REGULATION OF ATPASE ACTIVITY, GO ATP BIOSYNTHETIC PROCESS) and sterol metabolism (GO STEROL METABOLIC PROCESS ID2903, GO REGULATION OF CHOLESTEROL METABOLIC PROCESS ID2902) higher than the other two cell lines. However, this was already hypothesized, considering our comparisons before transfection where we mentioned that those pathways were not as active in HP when compared to LP or IP in their native state. Interestingly, for the aforementioned GO terms, we also describe a more prominent response in transfected HP and IP than in mock cells, which we could not confirm for LP. Similarly, for sterol-related GO terms we observed higher enrichment scores for HP transfected cells, but in juxtaposition, for IP and LP transfection seemed to have a negative impact on these genes' expression. Another vital property for a cell is to overcome ER stress, often induced by the transfection reagents.[24] LP had a low expression baseline for genes involved in ER stress response, which resulted in significant increase of NES for those gene sets (GO RESPONSE TO ER STRESS ID8, GO REGULATION OF ER UNFOLDED PROTEIN RESPONSE ID7, GO PROTEIN EXIT FROM ER). We found these to be stronger regulated for transfected than for mock cells for LP. Surprisingly, HP and IP, both transfected and mock showed negative enrichments of corresponding gene sets. We emphasize that these results represent just a relative view of changes within each cell line. Hence, these data do not describe relations between our three cell lines. In addition, we analyzed absolute changes on single transcript levels from top candidates of biological processes mentioned above.

When focusing on expression fold changes for timepoint 24 h, we identified Homocysteine Inducible ER Protein with Ubiquitin Like Domain 1 (HERPUD1) and X-Box Binding Protein 1 (XBP1) as members of ER-associated genes to be strongly downregulated in HP. Although, lower expressed in general, a similar trend could be observed for the sensor molecule endoplasmic reticulum to nucleus signaling 1 (ERN1). However, their absolute expression levels remained above those of LP at all timepoints. An opposing pattern was recognized for certain

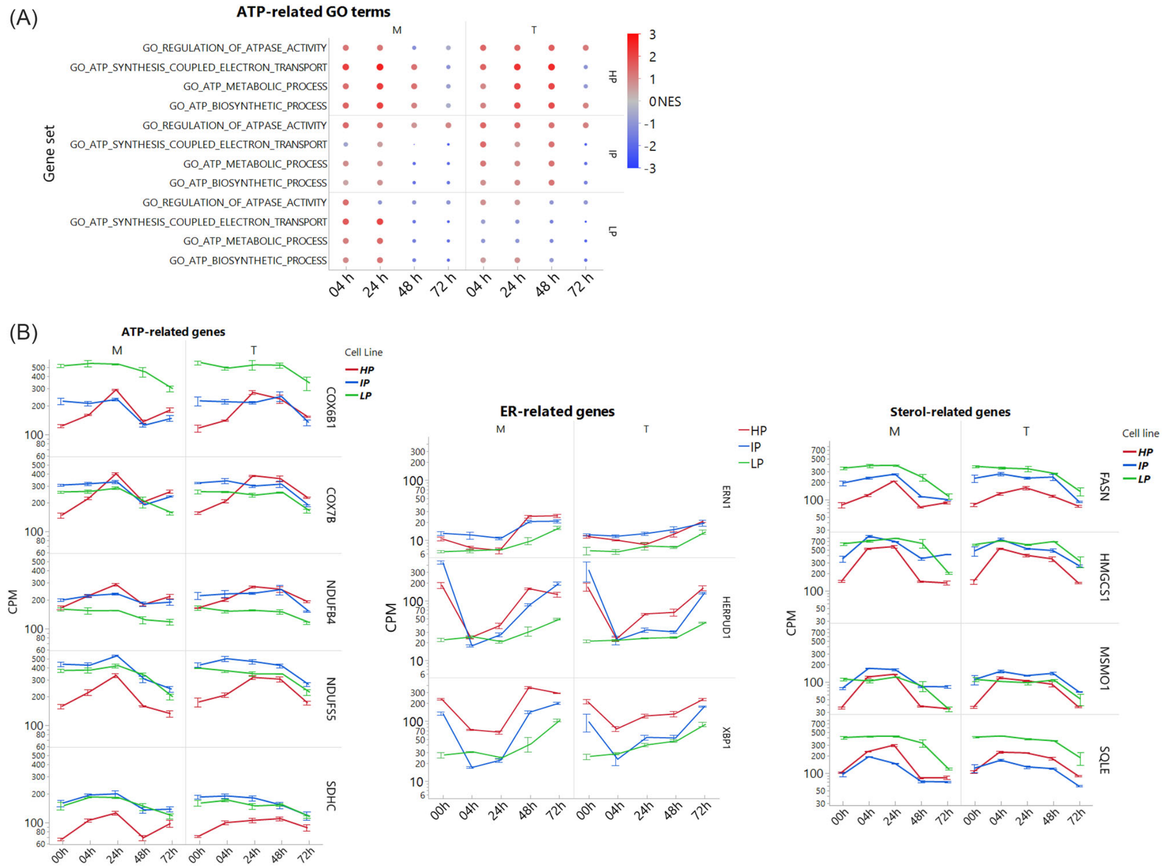

FIGURE 5 Differential gene expression during rAAV production process. (A) Overview of gene expression changes according to gene set enrichment analysis (GSEA) from 04 to 72 h post-transfection. Normalized enrichment scores (NES) are shown for selected pathways. A comparison of gene expression pattern for a subset of genes of above mentioned GO terms between transfected (T) and mock (M) is shown in (B) using normalized counts per million (CPM). Error bars indicate Mean ± SEM, $n = 4$.

ATP/electron transport (Figure 5B) and sterol metabolism-related genes, where HP indicated weaker gene expression. As aforementioned, related GO terms started with higher enrichments in LP compared to HP, but relative changes were more significant in HP. Highlighting the timepoint 24 h after transfection, our data reflect this pattern also on gene expression levels for Cytochrome C Oxidase Subunit 6B1 (COX6B1), NADH Dehydrogenase [Ubiquinone] Iron-Sulfur Protein 5 (NDUFS5) and Succinate Dehydrogenase Complex Subunit C (SDHC). For these genes, expression levels were constantly higher in LP than HP. This was also observed for important members of the cholesterol synthesis pathway, like 3-Hydroxy-3-Methylglutaryl-CoA Synthase 1 (HMGCS1) and Squalene Epoxidase (SQLE) as well as selected genes from fatty acid metabolism like Fatty Acid Synthase (FASN). On the other hand, for ER-stress related Cytochrome C Oxidase Subunit 7B (COX7B) and NADH Dehydrogenase [Ubiquinone] 1 Beta Subcomplex Subunit 4 (NDUFB4), as well as Methylsterol Monooxygenase 1 (MSMO1) involved in sterol metabolism, the mRNA levels in HP surpassed those of LP after strong upregulation, whereas in LP remained at comparable constant levels.

Notably, for above mentioned genes only slight differences were observed between mock and transfected conditions. As we specifically were interested in beneficial traits for productivity, we additionally screened for gene expression patterns that profoundly differ between mock and transfected cells and additionally, correlate with the productivity pattern of high and low yield. Again, we focused on the early timepoint 24 h after transfection for our selection and applied rigid selection criteria (average CPM > = 2 per sample for HP ($n = 40$); difference in fold changes between mock and transfected at 24 h post-transfection > = 1.5; CPM of HP > LP). We only identified four genes that met our criteria. The Histone Cluster 1 H2B Family Member K (H2BC12), known to be involved in transcription regulation and DNA replication, is most significantly differentially expressed ($p < 0.0001$) between transfected (FC 0–24 h = 10.3) and mock (FC 0–24 h = 2.2) and peaks at 24 h post-transfection. Tubulin Beta 3 Class III (TUBB3), a member of the microtubule family, already increased its expression 4.7-times at 24 h, but continued to elevate until a 6.6-times level is reached at 48 h. Notably, both genes moreover follow our productivity pattern, signifying high expression in HP, medium in IP and low in LP.

A similar pattern could be seen for Regulator of G-protein signaling 2 (RGS2), a GTPase Activating Protein (GAP), with highest fold change of 4.3 at 48 h after transfection, in comparison to its steady expression in mock cells. When compared to LP, HP exceeds expression of Tumor Protein 73 (TP73), a transcription factor participating in apoptotic response to DNA damage, nevertheless, highest mRNA levels are found in IP cells 48 h after transfection. Nevertheless, further studies will be needed to understand the influence of these genes on rAAV productivity.

4 | DISCUSSION

During this study, we characterized three different HEK-293 cell line strains at transcriptomics and productivity level collecting samples at different timepoints within a standard rAAV8 transient production fermentation. If transcriptome patterns change in response to rAAV8 production, we investigated the changes in gene expression along the post-transfection phase, with focus on 24 h after inducing rAAV production.

All three cell lines displayed a high variation throughout the post-transfection phase (24 to 72 h) especially for the accumulation of metabolic by-products that negatively influence productivity such as lactate, glutamate, and ammonia.[25] Particularly ammonia is associated with cellular toxic effects and can interfere in protein processing and virus replication.[26] We detected the highest ammonia concentrations in LP cell line, which may indicate an innate metabolic-based disadvantage for virus production in this cell line.

A PCA on non-transfected cells suggested that HP and IP cells are more closely related to each other, and that LP is most distant from HP. Since this reflects their ranking according to productivity, we were interested in closer characterization to identify possible traits that could be beneficial for high yield rAAV production.

Those predicted distances between those cell line strains were further confirmed by GSEA for important biological functions such as ATP synthesis, electron transport, ER stress, unfolded protein response, and sterol biosynthesis. The ability to overcome transfection-induced ER stress is essential for an effective production process of gene therapeutic particles.[27,28] Cationic macromolecules used in the transfection process are known to have cytotoxic properties, causing organelles like mitochondria or ER to destabilize.[24,29] Our GSEA data indicated that starting from low expression levels, LP induced ER-stress-response related to gene expression immediately 4 h post-transfection. This observation supports the evidence from literature,[24,27,28,29] and appears to be predominantly caused by the transfection reagent itself, as we observed elevations in both, mock and transfected LP cells. Unlike LP, HP and IP revealed a down-regulation of respective ER-stress related genes immediately.

However, as this comparison only reflects their relative change over time referring to their individual expression levels before transfection, we performed closer data evaluation of absolute transcription level changes. Out of ER-related gene sets, one of the most significantly down-regulated genes within the first 24 h after transfection of cell line HP was X-box binding protein 1 (*XBP1*), a transcription factor involved in the unfolded protein response (UPR).[30] This rescuing pathway, which prevents the cell from programmed cell death when unfolded proteins accumulate in the ER, can be activated in multiple ways. One of them involves the sensor molecule inositol-requiring enzyme 1 α (IRE1α), encoded by the *ERN1* gene, which activates the constitutively expressed XBP1 by splicing. The mature transcription factor in turn facilitates target gene expression, for instance chaperones and proteins involved in ER-associated protein degradation (ERAD) pathway.[31] Homocysteine-inducible ER stress-inducible ubiquitin-like domain member 1 (*HERPUD1*) has been identified as downstream target of XBP1 and mediates ER homeostasis by targeting ubiquitinated substrates to the proteasome for degradation.[9] Furthermore, the important role of XBP1 in gene therapy vector production has already been demonstrated and its overexpression can be linked directly to remarkable yield increase.[32] Although, mock and plasmid transfection, both reduced XBP1 expression significantly in HP an IP, the cell lines immediately restored their expression levels after 48 h in mock and 72 h in transfected cells. We interpreted these facts as an immediate recovery from the negative effects caused by the transfection agent. Nevertheless, the total mRNA levels of HP remained higher throughout all timepoints as compared to LP, suggesting their potential superior capability for clearing un- and misfolded proteins from the ER.

An additional characteristic of these three cell lines that may contribute to the transcriptional distance between them could be the difference in mRNA expression of genes involved in sterol metabolism and biosynthesis. Cholesterol is the major form of sterols found in mammalian cells and important to maintain membrane integrity and intra-cellular communication.[33,34] An additional characteristic of these three cell lines that may contribute to the transcriptional distance between them could be the difference in mRNA expression of genes involved in sterol metabolism and biosynthesis. Cholesterol is the major form of sterols found in mammalian cells and important to maintain membrane integrity and intra-cellular communication.[35,34] Through their ability to induce membrane bending and fission, sterols are essential for endocytosis and intracellular vesicle formation.[36] Their occurrence and distribution throughout membranes and various organelles are relevant to maintain many cellular functions including signal transduction and protein trafficking.[35,37] Their occurrence and distribution throughout membranes and various organelles are relevant to maintain many cellular functions including signal transduction and protein trafficking.[35,34] However, keeping a balance of intracellular sterol levels is vital for cells, as either too low or excessive amounts of those lipids may reduce or impair membrane and signaling functions.[38,39]

In our comparative transcriptome analysis, we identified LP as the cell line with highest and HP as the cell line with lowest sterol biosynthesis levels. Higher upregulation of respective gene sets within the first 24 h after transfection occurred in HP followed by IP, both compensating for their lower starting levels. We speculate that the transfection reagent itself induces membrane distortion that requires immediate restoration.[40] Have already shown that cholesterol can have protective properties when cells experience chemical damage. This would explain the need to elevate cholesterol synthesis pathways immediately after chemical exposure. Furthermore, in plasmid transfected cells, upregulation is prolonged to at least 48 h. One possible explanation could be an increased demand in cholesterol required for endocytic uptake of plasmid DNA,[41] intracellular signal transduction, and vesicle-mediated protein traffic as a result of rAAV production.[42,43] However, the constitutive high activity of sterol biosynthesis in LP combined with the fact that this particular cell line strain shows weaker regulation of genes in general, give rise to the question whether high cellular cholesterol levels may be disadvantageous for our batch process. Evidence of such effects can be found in a review by,[39] describing repression of cell signaling cascades because of high cellular sterols in two modalities: on one hand, high membrane rigidity does not allow conformational changes of residing membrane proteins to activate subsequent signaling pathways, on the other hand, inhibition can be caused through direct sterol-protein interaction. However, in order to confirm this hypothesis additional experiments will be required.

Another observation was the expression patterns of Adenosine triphosphate (ATP) -related genes. ATP is one major source of energy and considered the “energy currency” of the cell.[44] It is produced during aerobic respiration, which occurs in three stages: glycolysis, the tricarboxylic acid (TCA) cycle, and oxidative phosphorylation. Since glycolysis and the TCA cycle can only extract 2 molecules of ATP from each molecule of glucose, the highest yield is obtained by the last step of the respiratory chain generating 30–34 molecules of ATP. The so-called electron transport chain is a highly efficient multistep procedure involving five core complexes (I: NADH dehydrogenase, II: Succinate dehydrogenase, III: cytochrome c reductase, IV: cytochrome c oxidase, V: ATP synthase). Through multiple subsequent redox reactions, electrochemical gradients are created, providing operating power for the proton pump ATP synthase.[45–47]

By screening the transcriptome of all three cell line strains for genes involved in ATP synthesis and coupled electron transport, we observed patterns similar to those of sterol-related gene sets: low starting expression levels resulted in immediate upregulation past transfection in HP and IP. Interestingly, for all genes shown, increased mRNA levels in transfected cells were detected 24 h longer than in mock cells, indicating a possible additional energy requirement due to rAAV8 production. Unlike in HP and IP, mainly negative enrichments in transfected LP cells were observed, but since gene expression was high prior to transfection, numerous mRNAs were still more abundant in LP than HP cells. For example, although more tightly regulated in HP, expression of COX6B1, a member of the cytochrome c oxidase subunit VIb, remained highest in LP cells throughout all timepoints. This might although be disadvantageous since subunit VIb was found to interfere with the active center of cytochrome c oxidase, a key player of the respiratory chain.[48]

Another core member of cytochrome c oxidase, COX7B, shows similar levels as COX6B1 in HP, but is notably less abundant in LP. Unlike COX6B1, COX7B mediates beneficial functions for ATP-synthesis, as it is involved in establishing a proton gradient across the inner mitochondrial membrane. Furthermore, not only genes involved in complex IV of the electron transport chain seemed to be regulated with the effect to contribute to the performance of HP. Further beneficial differences in the electron transport chain were observed throughout all five complexes. Summarizing those findings, we suggest further investigations regarding possible differences in the cells’ efficiency to produce ATP, since our data might support the hypothesis that LP cells may encounter severe limitations.

Based on our results, we found that our three producer cell lines not only showed a high variation in their initial gene expression profile before transfection, but consequently respond differently to transfection events by individually adapting their transcriptome immediately within 24 h. Although, we detected numerous changes, not many of them were specific for transfected cells. Instead, most changes were observed under transfected and non-transfected conditions, but at different levels. Therefore, expression patterns essential for a high productivity cannot easily be identified and thus further examination on a deeper level is required to identify specific genes that have a direct influence on rAAV production titers.

In conclusion, the authors opted for mRNA profiling over total RNA profiling, encompassing ncRNA and small RNA profiling, as it serves as a cutting-edge analytical approach for initially examining the ncRNAs’ response to viral proteins. While investigating the role of small RNAs, such as miRNA, in antiviral mechanisms presents an intriguing comparison, the study’s emphasis on wild-type AAV and AdV, rather than an actual infection, may restrict the relevance of incorporating ncRNA and small RNA profiling. The authors hypothesize that the expression of cap and/or rep could potentially have adverse effects on cells in general; however, they anticipate fewer discrepancies in ncRNA expression across cell lines. Future research endeavors are required to delve deeper into this particular aspect.

AUTHOR CONTRIBUTIONS

Martina Pistek & Carolin-Isabel Kahlig: Conceptualization, data curation, formal analysis, methodology, validation, visualization, writing – original draft, and writing – review & editing. Matthias Hackl: Conceptualization, and writing – review & editing. Sabine Unterthurner: resources, writing – original draft. Barbara Kraus: Conceptualization, resources, and writing – review & editing. Reingard Grabherr: Conceptualization, writing – original draft, and writing – review & editing. Johannes Grillari: Conceptualization, writing – original draft, and writing – review & editing. Juan A. Hernandez Bort: Conceptualization, methodology, supervision, writing - original draft, and writing - review & editing.

ACKNOWLEDGMENTS

The authors would like to thank Brian Parkinson, MSc for carefully proofreading this manuscript.

CONFLICT OF INTEREST STATEMENT

Martina Pistek, Carolin-Isabel Kahlig, Sabine Unterthurner, Barbara Kraus, and Juan A. Hernandez Bort are all employees of Baxalta Innovations GmbH, a part of Takeda companies, which are involved in the development of gene therapy products and may be owner of stock options. The presented work was funded by Baxalta Innovations GmbH. Matthias Hackl is employee of TAmiRNA company. Reingard Grabherr and Johannes Grillari are employees of the University of Natural Resources and Applied Life Sciences, whereas Johannes Grillari is also affiliated to Ludwig Boltzmann Institute for Traumatology and TAmiRNA company.

DATA AVAILABILITY STATEMENT

The data that support the findings of this study are openly available in NCBI database at [https://urldefense.com/v3/__https://www.ncbi.nlm.nih.gov/geo/query/acc.cgi?acc=GSE226054__;!!KDurfCY!_jco4lIx4I3fCxt9XIYHV0zSFaJX_C10RNfS31KWDVbsk3JYal-XUSZGyCFn5SxB_rgS1TSFsikdXxPNqVtA7Q$]], reference number [GSE226054].

REFERENCES

1. Zhao, Z., Anselmo, A. C., & Mitragotri, S. (2022). Viral vector-based gene therapies in the clinic. *Bioengineering & Translational Medicine*, *7*, e10258.
2. Sarvari, R., Nouri, M., Agbolaghi, S., Roshangar, L., Sadrhaghighi, A., Seifalian, A. M., & Keyhanvar, P. (2020). A summary on non-viral systems for gene delivery based on natural and synthetic polymers. *International Journal of Polymeric Materials and Polymeric Biomaterials*, *71*, 246–65.
3. Shahryari, A., Saghaeian Jazi, M., Mohammadi, S., Razavi Nikoo, H., Nazari, Z., Hosseini, E. S., Burtscher, I., Mowla, S. J., & Lickert, H. (2019). Development and clinical translation of approved gene therapy products for genetic disorders. *Front Genet*, *10*, 868.
4. Kimberly, D. (2008). Toward development of artificial viruses for gene therapy: A comparative evaluation of viral and non-viral transfection. *Biotechnology Progress*, *24*, 871–83.
5. Patil, G., Lin, L., Dang, T., Zhang, J., & Qadir, Q. (2019). The development of functional non-viral vectors for gene delivery. *International Journal of Molecular Sciences*, *20*(21), 5491.
6. Ramamoorth, M. (2015). Non viral vectors in gene therapy- an overview. *Journal of Clinical and Diagnostic Research*, *9*, GE01–6.
7. Ren, S., Wang, M., Wang, C., Wang, Y., Sun, C., Zeng, Z., Cui, H., & Zhao, X. (2021). Application of non-viral vectors in drug delivery and gene therapy. *Polymers (Basel)*, *13*(19), 3307.
8. Graham, F. L., Smiley, J., Russell, W. C., & Nairn, R. (1977). Characteristics of a human cell line transformed by DNA from human adenovirus type 5. *Journal of General Virology*, *36*, 59–74.
9. Acosta-Alvear, D., Zhou, Y., Blais, A., Tsikitis, M., Lents, N. H., Arias, C., Lennon, C. J., Kluger, Y., & Dynlacht, B. D. (2007). XBP1 controls diverse cell type- and condition-specific transcriptional regulatory networks. *Molecular Cell*, *27*, 53–66.
10. Oxgene. 2023. The role of HEK293 cells in gene therapy. *New-Medical life sciences*. Retrieved on March 15, 2023 from https://www.news-medical.net/whitepaper/20200520/The-Role-of-HEK293-Cells-in-Gene-Therapy.aspx
11. Fiszer-Kierzkowska, A., & Vydra, N. (2011). Liposome-based DNA carriers may induce cellular stress response and change gene expression pattern in transfected cells. *BMC Molecular Biology*, *12*(1), 10.1186/1471-2199-12-27
12. Jacobsen, L., Calvin, S., & Lobenhofer, E. (2009). Transcriptional effects of transfection: The potential for misinterpretation of gene expression data generated from transiently transfected cells. *Biotechniques*, *47*, 617–24.
13. Lin, Y. (2014). Genome dynamics of the human embryonic kidney 293 lineage in response to cell biology manipulations. *Nature Communications*, *5*(1), 4767. https://doi.org/10.1038/ncomms5767
14. Bushnell, B. (2013). "BBMap." In, BBMap: Short read aligner for DNA and RNA-seq data. Capable of handling arbitrarily large genomes with millions of scaffolds. Handles Illumina, PacBio, 454, and other reads; very high sensitivity and tolerant of errors and numerous large indels.
15. Andrews, S. (2010). "FASTQC." In, FastQC aims to provide a simple way to do some quality control checks on raw sequence data coming from high throughput sequencing pipelines. It provides a modular set of analyses which you can use to give a quick impression of whether your data has any problems of which you should be aware before doing any further analysis.
16. Yates, A. D., Achuthan, P., Akanni, W., Allen, J., Allen, J., Alvarez-Jarreta, J., Amode, M. R., Armean, I. M., Azov, A. G., Bennett, R., Bhai, J., Billis, K., Boddu, S., Marugán, J. C., Cummins, C., Davidson, C., Dodiya, K., Fatima, R., Gall, A., … Flicek, P. (2020). Ensembl 2020. *Nucleic Acids Research*, *48*, D682–D88.
17. Dobin, A., Davis, C. A., Schlesinger, F., Drenkow, J., Zaleski, C., Jha, S., Batut, P., Chaisson, M., & Gingeras, T. R. (2013). STAR: Ultrafast universal RNA-seq aligner, *Bioinformatics*, *29*, 15–21.
18. Putri, G H., Anders, S., Pyl, P. T., Pimanda, J E., Zanini, F., & Boeva, V. (2022). Analysing high-throughput sequencing data in Python with HTSeq 2.0. *Bioinformatics*, *38*, 2943–45.
19. Mootha, V. K., Lindgren, C. M., Eriksson, K.-F., Subramanian, A., Sihag, S., Lehar, J., Puigserver, P., Carlsson, E., Ridderstråle, M., Laurila, E., Houstis, N., Daly, M. J., Patterson, N., Mesirov, J. P., Golub, T. R., Tamayo, P., Spiegelman, B., Lander, E. S., Hirschhorn, J. N., … Groop, L. C. (2003). PGC-1α-responsive genes involved in oxidative phosphorylation are coordinately downregulated in human diabetes. *Nature Genetics*, *34*(3), 267–273.
20. Subramaniana, A. (2005). Gene set enrichment analysis: A knowledge-based approach for interpreting genome-wide expression profiles. *Proceedings of the National Academy of Sciences*, *102*(43), 15545–15550.
21. Schneider, M., & Marison, I. (1996). The importance of ammonia in mammalian cell culture. *Journal of Biotechnol*, *46*, 161–85.
22. Tsang, S. M., Oliemuller, E., & Howard, B. A. (2020). Regulatory roles for SOX11 in development, stem cells and cancer. *Seminars in Cancer Biology*, *67*, 3–11.
23. Decaesteker, B., Louwagie, A., Loontiens, S., De Vloed, F., Roels, J., Vanhauwaert, S., De Brouwer, S., Sanders, E., Denecker, G., D'haene, E., Van Haver, S., Van Loocke, W., Van Dorpe, J., Creytens, D., Van Roy, N., Pieters, T., Van Neste, C., Fischer, M., Van Vlierberghe, P., … Speleman, F. (2020). SOX11 is a lineage-dependency factor and master epigenetic regulator in neuroblastoma. bioRxiv, 2020, S. 2020.08. 21.261131.
24. Dabbaghi, M., Kazemi Oskuee, R., Hashemi, K., & Afkhami Goli, A. (2018). Evaluating polyethyleneimine/DNA nanoparticles-mediated damage to cellular organelles using endoplasmic reticulum stress profile. *Artif Cells Nanomed Biotechnol*, *46*, 192–99.
25. Roman, R., Farras, M., Camps, M., Martinez-Monge, I., Comas, P., Martinez-Espelt, M., Lecina, M., Casablancas, A., & Cairo, J. J. (2018). Effect of continuous feeding of CO2 and pH in cell concentration and product titers in hIFNγ producing HEK293 cells: Induced metabolic shift for concomitant consumption of glucose and lactate. *Journal of Biotechnology*, *287*, 68–73.
26. Lavorgna, M., Russo, C., D'Abrosca, B., Parrella, A., & Isidori, M. (2016). Toxicity and genotoxicity of the quaternary ammonium compound benzalkonium chloride (BAC) using Daphnia magna and Ceriodaphnia dubia as model systems. *Environmental Pollution*, *210*, 34–9.
27. Moghimi, S. M., Symonds, P., Murray, J. C., Hunter, A. C., Debska, G., & Szewczyk, A. (2005). A two-stage poly(ethylenimine)-mediated cytotoxicity: Implications for gene transfer/therapy. *Molecular Therapy*, *11*, 990–5.
28. Parhamifar, L., Larsen, A. K., Hunter, A. C., Andresen, T. L., & Moghimi, S. M. (2010). Polycation cytotoxicity: A delicate matter for nucleic acid therapy—focus on polyethylenimine. *Soft Matter*, *6*, 4001–09.

29. Unfried, K., Albrecht, C., Klotz, L.-O., Mikecz, A. V., Grether-Beck, S., & Schins, R P. F. (2009). Cellular responses to nanoparticles: Target structures and mechanisms. *Nanotoxicology*, *1*, 52–71.
30. Yoshida, H., Matsui, T., Yamamoto, A., Okada, T., & Mori, K. (2001). XBP1 mRNA is induced by ATF6 and spliced by IRE1 in response to ER stress to produce a highly active transcription factor. *Cell Press*, *107*, 881–91.
31. Park, S. M., Kang, T.-I., & So, J.-S. (2021). Roles of XBP1s in transcriptional regulation of target genes. *Biomedicines*, *9*(7), 791.
32. Formas-Oliveira, A. S., Basilio, J. S., Rodrigues, A. F., & Coroadinha, A. S. (2020). Overexpression of ER protein processing and apoptosis regulator genes in human embryonic kidney 293 cells improves gene therapy vectors production, *Biotechnology Journal*, *15*, e1900562.
33. Maxfield, F. R., & van Meer, G. (2010). Cholesterol, the central lipid of mammalian cells. *Current Opinion in Cell Biology*, *22*, 422–9.
34. Sheng, R., Chen, Y., Yung Gee, H., Stec, E., Melowic, H. R., Blatner, N. R., Tun, M. P., Kim, Y., Källberg, M., Fujiwara, T. K., Hye Hong, J., Pyo Kim, K., Lu, H., Kusumi, A., Goo Lee, M., & Cho, W. (2012). Cholesterol modulates cell signaling and protein networking by specifically interacting with PDZ domain-containing scaffold proteins. *Nature Communications*, *3*, 1249.
35. Maxfield, F. R., & Menon, A. K. (2006). Intracellular sterol transport and distribution. *Current Opinion in Cell Biology*, *18*, 379–85.
36. Anderson, R. H., Sochacki, K. A., Vuppula, H., Scott, B. L., Bailey, E. M., Schultz, M. M., Kerkvliet, J. G., Taraska, J. W., Hoppe, A. D., & Francis, K. R. (2021). Sterols lower energetic barriers of membrane bending and fission necessary for efficient clathrin-mediated endocytosis. *Cell reports*, *37*, 110008.
37. Mesmin, B., & Maxfield, F. R. (2009). Intracellular sterol dynamics. *Biochimica Et Biophysica Acta*, *1791*, 636–45.
38. Xu, F., Rychnovsky, S. D., Belani, J. D., Hobbs, H. H., Cohen, J. C., & Rawson, R. B. (2005). Dual roles for cholesterol in mammalian cells. *Biochemistry*, *102*, 14551–56.
39. Yeagle, P. L. (1991). Modulation of membrane function by cholesterol. *Biochimie*, *73*, 1303–10.
40. Zhang, X., Barraza, K. M., & Beauchamp, J. L. (2018). Cholesterol provides nonsacrificial protection of membrane lipids from chemical damage at air–water interface. *PNAS*, *115*, 3255–60.
41. Pichler, H., & Riezman, H. (2004). Where sterols are required for endocytosis. *Biochimica Et Biophysica Acta*, *1666*, 51–61.
42. Ouweneel, A. B., Thomas, M. J., & Sorci-Thomas, M. G. (2020). The ins and outs of lipid rafts: Functions in intracellular cholesterol homeostasis, microparticles, and cell membranes. *Journal of Lipid Research*, *61*, 676–86.
43. Runz, H., Miura, K., Weiss, M., & Pepperkok, R. (2006). Sterols regulate ER-export dynamics of secretory cargo protein ts-O45-G. *Embo Journal*, *25*, 2953–65.
44. Dunn, J., & Grider, M. H. (2022). *Physiology, Adenosine triphosphate.* StatPearls.
45. Alabduladhem, T. O., & Bordoni, B. (2022). *Physiology, Krebs cycle.* StatPearls.
46. Chaudhry, R., & Varacallo, M. (2022). *Biochemistry, glycolysis.* StatPearls.
47. Deshpande, O. A., & Mohiuddin, S. S. (2022). *Biochemistry, oxidative phosphorylation.* StatPearls.
48. Weishaupt, A., & Kadenbach, B. (1992). Selective removal of subunit VIb increases the activity of cytochrome c oxidase. *Biochemistry*, *31*, 11477–81.

SUPPORTING INFORMATION

Additional supporting information can be found online in the Supporting Information section at the end of this article.

Biotechnology Journal

WILEY-VCH

Biotechnology Journal

RESEARCH ARTICLE OPEN ACCESS

A Novel and Simplified Anion Exchange Flow-Through Polishing Approach for the Separation of Full From Empty Adeno-Associated Virus Capsids

Frederik Meierrieks[1] | Alisa Weltken[1,2] | Karl Pflanz[3] | Andreas Pickl[1] | Benjamin Graf[1] | Michael W. Wolff[4]

[1]Lab Essentials Applications Development, Sartorius Lab Instruments GmbH & Co. KG, Göttingen, Germany | [2]University of Applied Sciences Aachen, Campus Jülich, Jülich, Germany | [3]Lab Essentials Applications Development, Sartorius Stedim Biotech GmbH, Göttingen, Germany | [4]Institute of Bioprocess Engineering and Pharmaceutical Technology, University of Applied Sciences Mittelhessen (THM), Giessen, Germany

Correspondence: Frederik Meierrieks (frederik.meierrieks@sartorius.com)

Received: 12 July 2024 | **Revised:** 9 September 2024 | **Accepted:** 11 September 2024

Keywords: adeno-associated virus (AAV) | anion exchange chromatography | downstream processing | flow-through mode | full-empty separation | gene therapy | polishing

ABSTRACT

Adeno-associated viruses (AAV) are widely used viral vectors for in vivo gene therapy. The purification of AAV, particularly the separation of genome-containing from empty AAV capsids, is usually time-consuming and requires expensive equipment. In this study, we present a novel laboratory scale anion exchange flow-through polishing method designed to separate full and empty AAV. Once the appropriate conditions are defined, this method eliminates the need for a chromatography system. Determination of optimal polishing conditions using a chromatography system revealed that the divalent salt $MgCl_2$ resulted in better separation of full and empty AAV than the monovalent salt NaCl. The efficacy of the method was demonstrated for three distinct AAV serotypes (AAV8, AAV5, and AAV2) on two different stationary phases: a membrane adsorber and a monolith, resulting in a 4- to 7.5-fold enrichment of full AAV particles. Moreover, the method was shown to preserve the AAV capsids' functional potency and structural integrity. Following the successful establishment of the flow-through polishing approach, it was adapted to a manual syringe-based system. Manual flow-through polishing using the monolith or membrane adsorber achieved 3.6- and 5.4-fold enrichment of full AAV, respectively. This study demonstrates the feasibility of separating full and empty AAV without complex linear or step gradient elution and the necessity of specialized equipment. Flow-through polishing provides a rapid and easy-to-perform platform for polishing multiple vector preparations, addressing a critical aspect in the research and development of novel gene therapies.

1 | Introduction

Viruses find application in a variety of therapeutic areas, including vaccines, oncolytic viruses, and as vectors in gene therapeutic treatments [1]. Among these, adeno-associated virus (AAV) vectors have emerged as particularly promising for in vivo gene therapy [2, 3], due to their nonpathogenicity [4], low immunogenicity [5], ease of production [6], and transgene

---

Abbreviations: AAV, adeno-associated virus; AdV, adenovirus; AEX, anion exchange chromatography; CV, column volumes; dPCR, digital polymerase chain reaction; FDA, food and drug administration; FPLC, fast protein liquid chromatography; GC, genomic copy; GFP, green fluorescent protein; GOI, gene of interest; HEK, human embryonic kidney; IAC, immunoaffinity chromatography; IEX, ion exchange chromatography; MA, membrane adsorber; pI, isoelectric point; ssDNA, single-stranded DNA; TFF, tangential flow filtration; VG, viral genome; VP, viral protein.

Benjamin Graf and Michael W. Wolff contributed equally to this study.

Biotechnology Journal, 2024; 19:e202400430
https://doi.org/10.1002/biot.202400430

Summary

- Separation full from empty AAV can be achieved in a flow-through mode.
- Flow-through polishing holds potential for large-scale processes and can be adapted to small scale laboratory settings without the need for FPLC systems.
- A divalent salt ($MgCl_2$) resulted in better separation of full and empty AAV than a monovalent salt (NaCl).

expression in various quiescent cell types [7]. To date, the US Food and Drug Administration (FDA) has granted approval to five AAV-based gene therapies: Elevidys (Sarepta), Hemgenix (CSL), Luxturna (Spark), Roctavian (BioMarin), and Zolgensma (Novartis).

Discovered in 1965 within adenovirus (AdV) preparations [8], AAV belongs to the *Parvoviridae* family and the genus of *Dependoparvovirus* [9]. Its replication is dependent on the presence of a helper virus, such as an AdV [10]. AAV is a non-enveloped [11], 4.7 kb single-stranded DNA (ssDNA) virus with an icosahedral capsid of 25 nm in diameter [12–14]. The AAV capsid consists of 60 subunits of the three viral proteins (VP)—VP1, VP2, and VP3—which are organized in an icosahedral symmetry in a ratio of 1:1:10 [2, 15]. To date, 13 different human serotypes have been identified [16]. These serotypes are characterized by variations in their capsid proteins and have specific tropisms for different types of cells [17, 18].

AAV are commonly produced by transient transfection of human embryonic kidney (HEK) 293 cells [11]. Alternative production methods include the transfection of HeLa cells, stable cell lines, or the use of a baculovirus-Sf9 cell system [19]. The purification of AAV typically involves multiple steps, beginning with cell lysis and nuclease treatment, followed by clarification through filtration [20]. This is succeeded by a chromatographic capture step using either immunoaffinity chromatography (IAC) or ion exchange chromatography (IEX) [21]. The final steps include a polishing step for the enrichment of full AAV particles, concentration, and formulation using tangential flow filtration (TFF), and sterile filtration [22].

Regardless of the manufacturing process, the encapsulation of DNA into the capsids during AAV production results in particles containing an intact genome (full), particles devoid of genomic content (empty), or particles comprising fragmented DNA (partially full) [22–24]. Although empty AAV particles have the same capsid structure as full AAV particles, they lack the therapeutic gene of interest (GOI) and are therefore not functionally relevant for the intended therapeutic effect [23]. Consequently, empty AAV particles are considered product-related impurities [21, 25], while their precise role in gene therapeutic treatments remains unclear [23]. It is discussed that empty capsids may serve as decoys for naturally occurring neutralizing anti-AAV antibodies, potentially enhancing the efficacy of a gene therapy drug [26, 27]. On the other hand, they may compete with full AAV particles for receptor binding sites, internalization, and intracellular cargo, which could reduce therapeutic efficacy [28, 29]. Beyond efficacy concerns, empty AAV particles may also affect the safety profile of AAV-based gene therapies by increasing the risk of immunogenicity [21]. For instance, Nathwani et al. observed that an excess of empty AAV8 particles could induce AAV8-capsid-specific T-cell responses, resulting in low-grade hepatotoxicity and partial loss of transgene expression [30]. In addition, Mingozzi et al. reported anti-capsid T-cell responses following ocular administration of AAV2 [31]. Therefore, in addition to the potency of an AAV gene therapy drug, it is crucial to ensure its safety profile through a manufacturing process that results in a final product with a low level of empty particles [32].

The separation of full and empty AAV particles is challenging due to their identical capsid structure, which renders IAC ineffective for separation [33]. The depletion of empty AAV particles is currently achieved by various methods, such as size exclusion chromatography (SEC), density gradient centrifugation, or anion exchange chromatography (AEX) [22]. Among these, density gradient centrifugation provides a serotype-independent approach to separate full and empty AAV particles based on their sedimentation characteristics [34]. However, density gradient centrifugation faces scalability challenges, is prone to operator error, and requires expensive equipment [21, 35].

As mentioned above, AEX is an effective method for separating full and empty AAV particles [32]. AEX is a method that exploits the interaction of the stationary phase with the surface charge of the viral particles [12, 36]. Empty AAV have an isoelectric point (pI) of 6.3, while full AAV have a pI of 5.9 due to their genomic payload [14]. This marginal difference in pI of 0.4 enables the separation of full AAV from their empty counterparts [32]. Unlike density gradient centrifugation, AEX provides a scalable solution for separating empty from full AAV particles [36–38]. Chromatographic separation is typically achieved using linear elution gradients or isocratic elution [22, 39–41]. A variety of chromatographic matrices, including resins [42, 43], membranes [44, 45], or monoliths [32, 46], can be used for AEX-based separation of empty and full AAV.

Traditionally, AEX-based methods for separating empty from full AAV depend on the use of fast protein liquid chromatography (FPLC) systems. In this work, we established a novel laboratory scale flow-through a polishing approach that can be performed without an FPLC. Empty particles do not bind to the stationary phase in this approach, while full AAV particles are retained and can be subsequently eluted by using a buffer of increased ionic strength. The design of this technique allows the use of syringes instead of an FPLC system to separate full from empty AAV particles. Flow-through polishing conditions were first determined using an FPLC system and then adapted to an FPLC-independent syringe approach. This method was successfully applied to both a monolithic column and a membrane adsorber for AAV8, AAV5, and AAV2.

2 | Materials and Methods

2.1 | AAV Production and Harvest

AAV2, AAV5, and AAV8 were produced via transient transfection of HEK293 cells (Expi293F Inducible Cells, Thermo Fisher Scientific, Waltham, Massachusetts, USA) in both non-baffled glass shake flasks and a 10 L glass Univessel bioreactor (Sartorius, Göttingen, Germany). Both systems used FreeStyle 293 Expression Medium (Thermo Fisher Scientific) as the growth medium. In the shake flask system, cells were cultivated at 130 rpm, 8% CO_2, and 80% humidity in an orbital shaker (Kuhner, Birsfelden, Switzerland). Within the 10 L bioreactor, the cultivation conditions were regulated by the BIOSTAT DCU controller unit (Sartorius) to maintain set points of 201 rpm, 40% dissolved oxygen, and pH 7.25. Furthermore, to prevent foaming within the bioreactor, the cultivation medium was supplemented with antifoam C (Sigma-Aldrich, Darmstadt, Germany) at a final concentration of 0.0002% (v/v). AAV production processes were inoculated at 3×10^5 viable cells/mL. After reaching a cell density of 1.3×10^6 viable cells/mL, transfection was performed using a dual plasmid system, with 0.55 µg/mL DNA per 10^6 viable cells and FectoVIR-AAV (Polyplus, Illkirch, France) as the transfection reagent in a 1:1 ratio. The plasmids pAAV-ssGFP (vector plasmid) and pDP2/pDP5/pDP8.ape (packaging and helper plasmid for each respective serotype) were used for transfection in a molar ratio of 4.5:1. Plasmids were sourced from PlasmidFactory (Bielefeld, Germany). At 72 h post-transfection, AAV vectors were harvested. To initiate cell lysis, the cell broth was treated with a 20× lysis buffer (1 M Tris pH 8.0, 40 mM $MgCl_2$ [both Carl Roth, Karlsruhe, Germany], 20% [v/v] Tween 20 [Sigma-Aldrich]) and Denarase (c-Lecta, Leipzig, Germany) at a final concentration of 50 U/mL. The mixture was then incubated at 37°C for 1.5 h. Subsequently, the lysed cultures were treated with 500 mM NaCl and incubated at 37°C for another 30 min.

2.2 | Purification of AAV From Crude Cell Lysates

Clarification of AAV crude cell lysates was performed by alluvial filtration as previously reported [47]. Briefly, the crude cell lysate was mixed with 11.25 g/L of Sartoclear Dynamics Lab Filter Aid (Sartorius) and clarified using Sartolab RF1000 filters (0.22 µm; PES; Sartorius). The clarified AAV sample was kept on ice and further purified by affinity chromatography using AAVX prepacked columns (1 mL, Thermo Fisher Scientific) and an ÄKTA avant 25 (Cytiva, Marlborough, Massachusetts, USA) chromatography system. Four distinct buffers were prepared as follows: (A) 25 mM Tris pH 8.5, 5 mM $MgCl_2$, 250 mM NaCl, (B1) 20 mM Glycine pH 2.3, 2 mM $MgCl_2$, 200 mM NaCl for AAV8, (B2) 20 mM Glycine pH 1.7, 2 mM $MgCl_2$, 200 mM NaCl for AAV2 and AAV5, and (C) 1 M Tris pH 8.5, hereafter referred to as binding (A), elution (B), and neutralization buffer (C). All chemicals were purchased from Carl Roth. The column was first equilibrated with 20 column volumes (CV) of binding buffer. Subsequently, a total of 750–1000 mL of clarified AAV sample was loaded per run in a downflow direction onto the column at a flow rate of 0.5–0.7 mL/min. Following sample application, the column was washed with 10 CV of binding buffer. Before elution, 50 µL of neutralization buffer was added to each well of the fraction collector plate. The AAV bound to the column were then eluted with elution buffer in an upflow direction in 0.45 mL fractions. Peak fractions were pooled, aliquoted, and stored at −80°C until further use.

2.3 | Anion Exchange Separation of Full From Empty AAV Capsids

For the separation of full from empty AAV capsids, three different AEX devices were applied. Experiments were performed using the multimodal monolithic column CIMmultus/CIMmic PrimaS (2 µm pore size, 1 mL, and 0.1 mL, Sartorius BIA Separations, Ajdovscina, Slovenia) that combines hydrogen bonding with weak AEX. Furthermore, the strong AEX monolithic column CIMmic QA (2 µm pore size, 0.1 mL, Sartorius BIA Separations) was used. The third device used was the strong AEX membrane adsorber (MA) Sartobind Lab Q (0.41 mL, Sartorius). For the $MgCl_2$ experiments, two different buffers were prepared as follows: (A) 50 mM Tris pH 8.5, 2 mM $MgCl_2$, and (B) 50 mM Tris pH 8.5, 50 mM $MgCl_2$, hereafter referred to as $MgCl_2$ loading and elution buffer. Only the loading buffer for the AAV2 experiments on the PrimaS column did not contain $MgCl_2$. For the NaCl experiments, two additional buffers were prepared: (C) 20 mM Bis-tris propane pH 9.0, and (D) 20 mM Bis-tris propane pH 9.0, 1 M NaCl, hereafter referred to as NaCl loading and elution buffer. For PrimaS experiments, the NaCl elution buffer contained 200 mM NaCl. Stationary phases were cleaned and regenerated based on manufacturer's recommendations. Experiments were conducted on an ÄKTA avant 25 (Cytiva) chromatography system at a flow rate of 2 mL/min. All chemicals were purchased from Carl Roth.

Sartobind Q: Linear and step gradient elution experiments for $MgCl_2$ and NaCl were conducted with a total of 8×10^{12}–2×10^{13} capsids of affinity-purified AAV8, AAV5, or AAV2. The AAV material was diluted 1:20–1:80 in the respective loading buffer and loaded onto the Sartobind Q. Linear gradient elution was performed from 0% to 100% of $MgCl_2$ elution buffer or from 0% to 20% of NaCl elution buffer over 4 min. Step gradient elution experiments employed 5% increments of $MgCl_2$ elution buffer or 2% increments of NaCl elution buffer. For the $MgCl_2$ flow-through polishing approach, 8×10^{12}–3.9×10^{13} capsids of affinity-purified AAV8, AAV5, or AAV2 were diluted 1:50–1:80 and $MgCl_2$ concentrations were adjusted to 24.6 mM for AAV8, 28.6 mM for AAV5, and 15.4 mM for AAV2 by appropriate mixing of the $MgCl_2$ loading and elution buffer. Sample application was performed with a loading and elution buffer mixture containing the same $MgCl_2$ concentration as during sample dilution. Isocratic elution was then achieved by increasing the $MgCl_2$ concentration to 30.8 mM for AAV8, 32.7 mM for AAV5, and 20.2 mM for AAV2.

CIMmultus PrimaS: Linear and step gradient elution experiments for $MgCl_2$ and NaCl were executed using 8×10^{12}–2.9×10^{13} capsids of affinity-purified AAV8, AAV5, or AAV2. The AAV preparations were diluted 1:10–1:20 in the respective loading buffer and loaded onto the PrimaS column. Linear gradient elution was performed from 0% to 30%–50% of $MgCl_2$ elution buffer over 3 min or from 0% to 100% of NaCl elution buffer over 5 min. For step gradient elution, 2%–3% increments of $MgCl_2$ elution buffer or 2%

increments of NaCl elution buffer were utilized. For the $MgCl_2$ flow-through a polishing method, 8 × 10^{12}–2.9 × 10^{13} capsids of affinity-purified AAV8, AAV5, or AAV2 were diluted 1:10–1:16 and $MgCl_2$ concentrations were adjusted to 3.6 mM for AAV8, 11.6 mM for AAV5, and 0.1 mM for AAV2 by appropriate mixing of the $MgCl_2$ loading and elution buffer. The sample application was performed with a loading and elution buffer mixture containing the same $MgCl_2$ concentration as during sample dilution. Isocratic elution was accomplished by increasing the $MgCl_2$ concentration to 9.2 mM for AAV8, 21.2 mM for AAV5, and 3 mM for AAV2.

CIMmic QA: Flow-through polishing was performed using a total of 1.9 × 10^{13} capsids of affinity-purified AAV8. The AAV8 material was diluted 1:20 in the respective loading buffer, and the $MgCl_2$ concentration was adjusted to 15.9 mM by appropriate mixing of the $MgCl_2$ loading and elution buffer. The sample was applied with a mixture of loading and elution buffer containing the same $MgCl_2$ concentration as during sample dilution. Isocratic elution was subsequently performed by increasing the $MgCl_2$ concentration to 22.6 mM.

Syringe approach: For AAV8 flow-through polishing, an FPLC-independent protocol with manual syringe operation was implemented using the Sartobind Lab Q and CIMmic PrimaS. All steps were performed at a flow rate of around one drop per second. A total of 2.3 × 10^{13}–3.6 × 10^{13} capsids of affinity-purified AAV8 were diluted 1:50 or 1:15 and adjusted to 24.6 mM or 3.6 mM $MgCl_2$ for the Sartobind Q and the PrimaS, respectively. For the sample application, a 10 mL Omnifix Luer Lock Solo syringe (B. Braun, Melsungen, Germany) was attached to the respective device. The subsequent wash step was achieved utilizing an additional syringe containing a loading and elution buffer mixture with the same $MgCl_2$ concentration as during the sample application. A third syringe was used for isocratic elution at an $MgCl_2$ concentration of 30.8 mM for the Sartobind Q and at 9.2 mM $MgCl_2$ for the PrimaS. A final elution step was performed with a fourth syringe with an $MgCl_2$ concentration of 50 mM.

2.4 | AAV Capsid Titer Determination

AAV capsid titer titration was performed employing the Octet R8 equipped with Octet AAVX Biosensors (both Sartorius). Quantitation was performed at 30°C and a shaking speed of 1000 rpm. The reading time during the quantitation step was set to 900 s. AAV reference standards were procured from Progen Biotechnik (Heidelberg, Germany).

2.5 | AAV Genome Titer Determination

AAV VG titers were determined by nanoplate digital polymerase chain reaction (dPCR) using the QIAcuity One with 24-well nanoplates (both Qiagen, Hilden, Germany). The samples were serially diluted in dPCR buffer composed of TE buffer (Thermo Fisher Scientific), 0.01% (v/v) Pluronic F-68 (Sigma-Aldrich, Darmstadt, Germany), and 100 mg/mL Poly A Carrier RNA (Roche, Basel, Switzerland). The diluted samples were then incubated at 95°C for 30 min. The dPCR was performed using the QIAcuity Probe Mastermix (Qiagen) along with specific forward and reverse primers (800 nM) and a specific probe (400 nM) targeting the SV40 polyadenylation signal (Integrated DNA Technologies, Coralville, Iowa, USA).

2.6 | AAV2 Transducing Titer Determination

AAV2 transducing unit titers were assessed by live-cell analysis. Adherent HEK293T cells (ACC 635; DSMZ, Braunschweig, Germany) were transduced with AAV2 samples. A total of 4 × 10^3 HEK293T cells per well were seeded in DMEM (Thermo Fisher Scientific) supplemented with 10% (v/v) fetal calf serum (FCS) and 0.5% (v/v) penicillin-streptomycin (both Sigma-Aldrich). The cells were seeded in a tissue culture treated, poly-L-lysine (Sigma-Aldrich) coated black 96-well plates with a clear bottom (Corning Inc., Corning, New York, USA). The cells were cultivated for 1 day at 36.5°C and 5% CO_2 in a static incubator. Before the transduction process, the spent culture medium was aspirated, and the cells were transduced by adding 50 µL of AAV2 samples. A medium exchange was performed 24 h post-transduction. The expression of green fluorescent protein (GFP) within the cells was monitored and quantitatively analyzed 48 h post-transduction using the Incucyte S3 live cell analysis system (Sartorius). Imaging was performed at 10× magnification, utilizing both the phase contrast and the green fluorescence channel at 3-h intervals to assess GFP expression dynamics.

2.7 | Western Blotting

AAV samples were diluted 6.25:1 in ddH_20 and loading dye and subjected to thermal denaturation at 95°C for 3 min. Loading dye was prepared using 900 µL of 4× Laemmli sample buffer and 100 µL of 2-mercaptoethanol (both Bio-Rad, Hercules, California, USA). A total AAV amount of 2.75 × 10^9 capsids was loaded per lane on a 10% Mini-Protean TGX gel (Bio-Rad). Electrophoretic separation was conducted at 200 V over 37 min. For western blot analysis, proteins were transferred to a 0.2 µm polyvinylidene fluoride membrane (Trans-Blot Turbo Transfer Pack, Bio-Rad). The membrane was then subjected to a blocking step using a solution of 5% (w/v) bovine serum albumin dissolved in TBS buffer (150 mM NaCl, 3 mM KCl, 25 mM Tris, all Carl Roth) supplemented with 0.1% (v/v) Tween 20 (Sigma-Aldrich) for a duration of 1 h. Following the blocking step, the membrane was incubated for 1 h with a primary antibody specifically targeting the AAV VP1/VP2/VP3 (Progen Biotechnik), at a dilution of 1:500 in TBS buffer containing 0.1% (v/v) Tween 20. Post-primary antibody incubation, the membrane was washed with TBS buffer and subsequently incubated with a secondary horseradish peroxidase conjugated anti-mouse antibody (diluted 1:5000 in TBS buffer, Thermo Fisher Scientific). Following a final TBS buffer wash step, the membrane was treated with 400 µL of SuperSignal West Pico Plus chemiluminescence substrate (Thermo Fisher Scientific). The resulting signal was imaged using an UVP ChemStudio imaging system (Analytik Jena, Jena, Germany).

3 | Results

3.1 | Monovalent and Divalent Cations for the Separation of Full From Empty AAV Capsids

Two different chromatographic stationary phases (Sartobind Q and PrimaS) were evaluated for their usability in separating full AAV from empty AAV capsids. To develop a flow-through polishing method for the separation of full AAV from empty AAV capsids, it was imperative to select a suitable cation for effective separation and to determine the conditions under which full AAV capsids still bind to the stationary phase, while empty AAV capsids elute from the column. Linear and step gradient elution experiments were performed to identify the appropriate cation and the respective concentration limits, as shown in Figure 1 for AAV8. Given that proteins absorb predominantly at 280 nm and nucleic acids at 260 nm, an increased 260:280 nm absorbance ratio indicates enrichment of the genome-containing AAV capsids. In addition, these results were verified by quantification of capsid and viral genome (VG) titers.

The first stationary phase evaluated was the Sartobind Lab Q MA. Linear gradient and isocratic elution experiments, as illustrated in Figure 1A–D, were performed using an AAV8 sample with a genomic copy (GC)/capsid ratio of 8.4%. Using NaCl as the elution salt (Figure 1A,B), AAV eluted between 125 and 195 mM NaCl during linear gradient elution. However, no separation of full and empty AAV particles was observed. In contrast, step gradient elution facilitated the separation of full and empty particles, resulting in the elution of empty AAV at 140 mM NaCl with a GC/capsid ratio of 4.4% and full AAV at 160 mM NaCl with a GC/capsid ratio of 32.7%. Subsequent elution experiments utilizing $MgCl_2$ for elution are shown in Figure 1C,D. AAV eluted over a concentration range of 23–38 mM $MgCl_2$. During the step gradient elution experiment in Figure 1D, a peak devoid of AAV was observed during sample application. Empty AAV capsids with a GC/capsid ratio of 1.3% eluted between 22 and 25 mM $MgCl_2$, while full AAV capsids with a GC/capsid ratio of 63.9% eluted between 25 and 27.5 mM $MgCl_2$. Due to the improved separation of the full and empty AAV particles achieved with $MgCl_2$, it was selected as the salt for flow-through polishing. Similar linear gradient and isocratic elution experiments were performed with $MgCl_2$ for AAV5 and AAV2 (data not shown). Based on these findings, the $MgCl_2$ concentrations for the flow-through polishing were determined to be 24.6 mM for AAV8, 28.6 mM for AAV5, and 15.4 mM for AAV2.

The evaluation of the monolithic PrimaS column as an alternative stationary phase for the chromatographic separation of full AAV capsids from their empty counterparts followed protocols analogous to those used for the Sartobind Q. Linear and isocratic NaCl elution experiments were conducted using an AAV8 sample with a GC/capsid ratio of 9.5%, with the corresponding chromatograms presented in Figure 1E,F. During the linear gradient elution experiment, AAV were eluted within a NaCl concentration range of 45–110 mM. The chromatographic profile indicated a separation of empty and full AAV particles, with empty AAV (GC/capsid = 0.1%) eluting at a lower NaCl concentration of 55 mM NaCl and full AAV (GC/capsid = 16.2%) eluting at a higher NaCl concentration of 75 mM. The application of a step gradient elution did not improve the separation between the full and empty AAV peaks. Step gradient elution resulted in the elution of empty AAV at 54 mM NaCl with a GC/capsid ratio of 0.1% and full AAV at 70 mM NaCl AAV with a GC/capsid ratio of 12.1%. Employing $MgCl_2$ as an elution salt resulted in different elution patterns as depicted in Figure 1G,H. It was observed that already during sample application, with a buffer containing 2 mM $MgCl_2$, mainly empty AAV8 with a GC/capsid ratio of 2.2% were found in the flow-through. The remaining AAV eluted within the range of 2–11 mM $MgCl_2$. The initial sample used for the step gradient elution experiment shown in Figure 1H had a GC/capsid ratio of 9.5%. We found that in addition to the empty AAV8 in the flow-through, an additional fraction of empty AAV8 was eluted between 3 and 4 mM $MgCl_2$ (GC/capsid ratio of 0.7%). Genome-containing AAV8 capsids were subsequently eluted between 4 and 10 mM $MgCl_2$. Similar to the observations with the Sartobind Q, $MgCl_2$ demonstrated improved separation of full and empty AAV peaks and was therefore selected as the salt for flow-through polishing. Comparable linear gradient and isocratic elution experiments with $MgCl_2$ were performed for AAV5 and AAV2 (data not shown). Based on these results, the $MgCl_2$ concentration of the samples for the flow-through polishing was adjusted to 3.6 mM for AAV8, 11.6 mM for AAV5, and 0.1 mM for AAV2.

3.2 | Membrane Adsorber-Based Flow-Through Separation of Full From Empty AAV Capsids

Flow-through polishing conditions for the Sartobind Q were determined by linear and step gradient elution experiments, as described in section 3.1. The chromatographic profiles resulting from the flow-through polishing of AAV8, AAV5, and AAV2 are shown in Figure 2A–C. Detailed process parameters can be found in Table 1 in the supplemental material. For AAV8 (Figure 2A), the flow-through polishing was performed at an $MgCl_2$ concentration of 24.8 mM, with elution of the genome-containing AAV8 capsids at 30.8 mM $MgCl_2$. The flow-through polishing resulted in a 5.3-fold enrichment of the full AAV8 particles, with the GC/capsid ratio increasing from 8.4% in the feed material to 44.9% in the eluted fraction at 30.8 mM $MgCl_2$. At the same time, the GC/capsid ratio in the flow-through was reduced to 1.9%. Flow-through polishing of AAV5 was achieved by sample application at 28.6 mM $MgCl_2$, with elution of the genome-containing AAV performed at 32.7 mM $MgCl_2$ (Figure 2B). The GC/capsid ratio was reduced from 10.1% in the starting material to 4.9% in the flow-through, while the GC/capsid ratio in the elution fraction at 32.7 mM $MgCl_2$ was increased by a factor of 7% to 71%. For AAV2 (Figure 2C), the flow-through polishing was performed at 15.4 mM $MgCl_2$, while the genome-containing AAV2 capsids were eluted at 20.2 mM $MgCl_2$. Flow-through polishing reduced the GC/capsid ratio from 5.9% in the feed material to 0.4% in the flow-through, while increasing it by a factor of 4%–23.8% in the elution at 20.2 mM $MgCl_2$.

The transduction efficiency of AAV2 following flow-through polishing was quantitatively assessed by the transduction of HEK293T cells, as shown in Figure 2D. The analysis revealed that 0.9% of the total transducing units were found in the

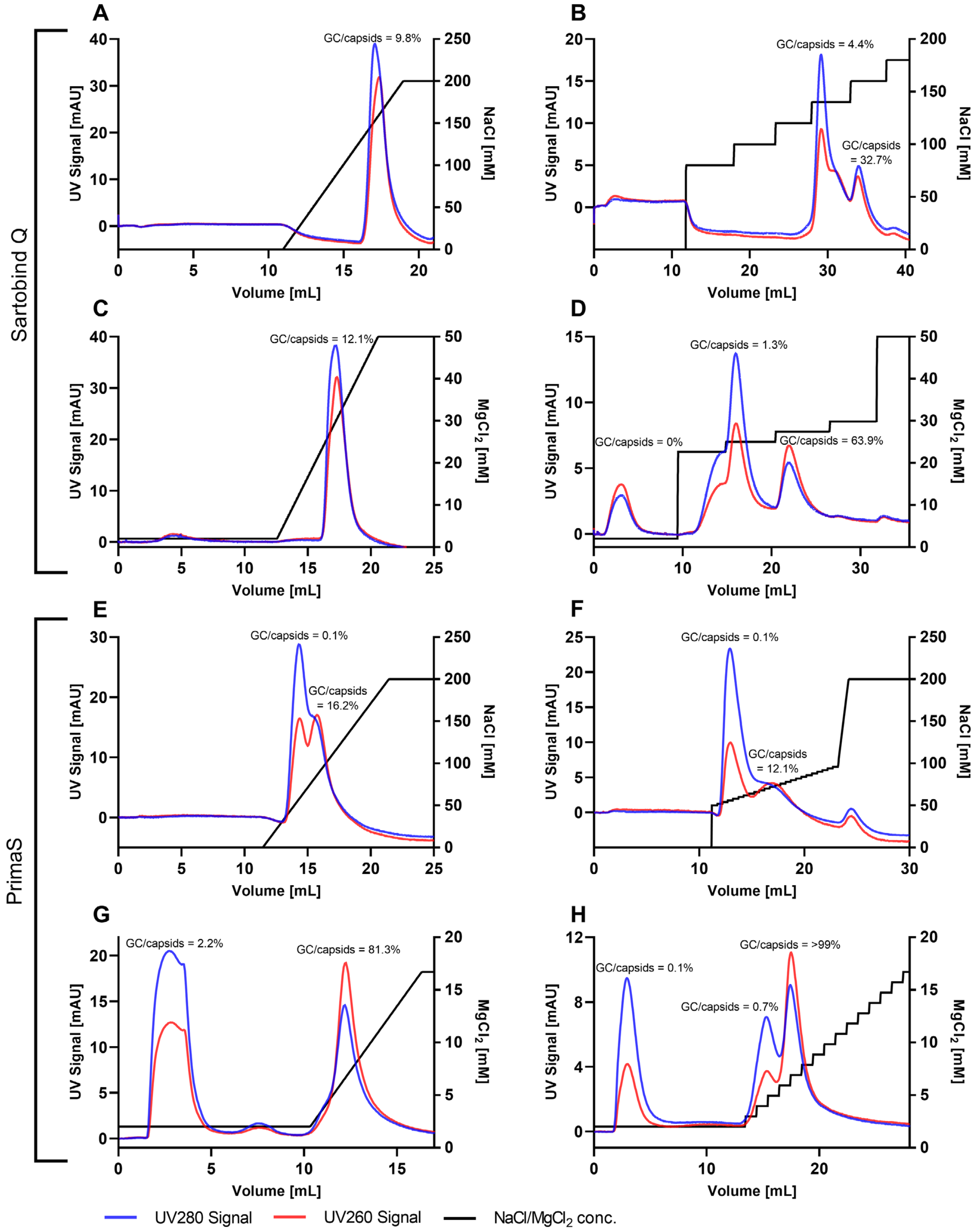

FIGURE 1 | Chromatographic profiles of linear and isocratic elution for the separation of full and empty AAV8 capsids. Panels A and B show the linear and isocratic NaCl elution profiles using the Sartobind Q, while Panels C and D depict the $MgCl_2$ elution profiles. In addition, Panels E and F illustrate the linear and isocratic NaCl elution profiles using the PrimaS, whereas Panels G and H show the $MgCl_2$ elution profiles. GC indicates genomic copies.

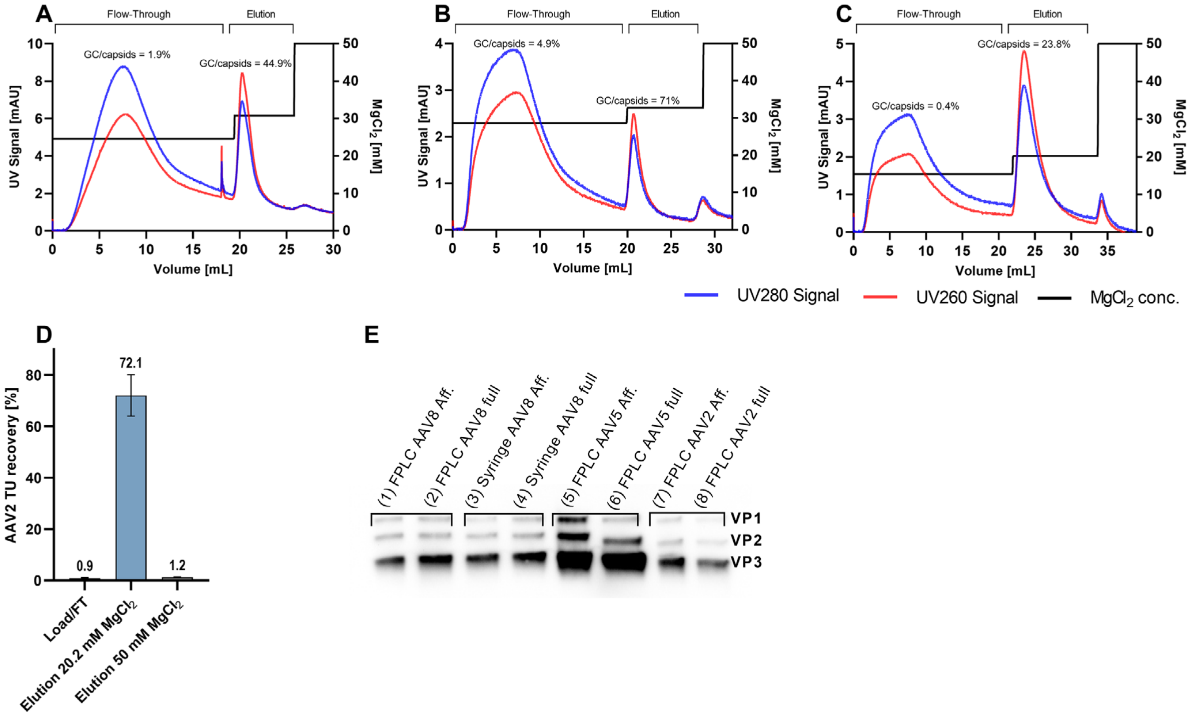

FIGURE 2 | Chromatographic profiles of Sartobind Q-based flow-through separation of full and empty AAV capsids. Panels A–C illustrate the flow-through polishing for the separation of full from empty AAV capsids for AAV8, AAV5, and AAV2, respectively. The $MgCl_2$ concentration during sample application was adjusted to 24.6 mM for AAV8, 28.6 mM for AAV5, and 15.4 mM for AAV2. Panel D provides information on the potency (n = 3) of AAV2 following the flow-through polishing. Additionally, Panel E shows a western blot analysis, using a monoclonal antibody against the AAV capsid proteins VP1-3, to validate the integrity of the capsid proteins after flow-through polishing. Lanes 1, 3, 5, and 7 represent affinity-purified AAV material, while lanes 2, 4, 6, and 8 correspond to the respective full AAV elution peaks. Aff. indicates affinity-purified AAV material; FPLC, fast protein liquid chromatography; FT, flow-through; GC, genomic copies; TU, transducing unit; VP, viral protein.

flow-through, while the 20.2 mM $MgCl_2$ elution showed a transducing unit recovery of 72.1%. Subsequently, the second elution peak at 50 mM $MgCl_2$ contained 1.2% of the total transducing units. In addition to potency, the integrity of AAV capsids before and after flow-through polishing was analyzed using a western blot targeting VP1, VP2, and VP3 (Figure 2E). The band intensity ratios for VP1, VP2, and VP3 remained constant at a ratio of 1:1:10 both before and after flow-through polishing, indicating no change in the composition of AAV8, AAV5, and AAV2 capsids.

3.3 | Monolith-Based Flow-Through Separation of Full From Empty AAV Capsids

The resulting chromatographic profiles of the PrimaS flow-through polishing (conditions determined in section 3.1) of AAV8, AAV5, and AAV2 are presented in Figure 3A–C, respectively. Detailed process characteristics are provided in the supplemental material in Table 1. For AAV8 (Figure 3A), the flow-through polishing was conducted at an $MgCl_2$ concentration of 3.6 mM, with the elution of genome-containing AAV8 capsids at 9.2 mM $MgCl_2$. This step resulted in an enrichment of the full AAV8 particles by a factor of 4.6 from a GC/capsid ratio of 10.4% in the starting material to 47.5% in the eluted fraction at 9.2 mM $MgCl_2$. The GC/capsid ratio in the flow-through could be reduced to 0.1%. The flow-through polishing of AAV5, depicted in Figure 3B, was executed at 11.6 mM $MgCl_2$, while the genome-containing AAV5 capsids were eluted at 21.2 mM $MgCl_2$. This led to a decrease in the GC/capsid ratio from 10.1% in the feed to 6.1% in the flow-through. In contrast, the elution fraction demonstrated an increase in the GC/capsid ratio to 76.2%, corresponding to an enrichment factor of 7.5 for the genome-containing AAV5 capsids. The flow-through polishing of AAV2 was achieved by sample application at 0.1 mM $MgCl_2$, with elution of the genome-containing AAV performed at 3 mM $MgCl_2$. The corresponding chromatographic profile is shown in Figure 3C. While the GC/capsid ratio decreased from 6.3% in the feed material to 1.1% in the flow-through, it increased by a factor of 1.9 to 12.1% in the elution at 3 mM $MgCl_2$. A second elution peak with a GC/capsid ratio of 5% was observed upon increasing the $MgCl_2$ concentration to 50 mM, similar to that of the feed material.

AAV2 transduction efficiency was determined (Figure 3D) with the flow-through comprising 2% of the total transducing units. The elution of full AAV2 particles at 3 mM $MgCl_2$ resulted in a transducing unit recovery of 48.2%. The second elution peak at 50 mM $MgCl_2$ contained 32.5% of the total transducing units. AAV capsid integrity was assessed by western blot analysis, as shown in Figure 3E. Consistent band intensity ratios of 1:1:10 for VP1, VP2,

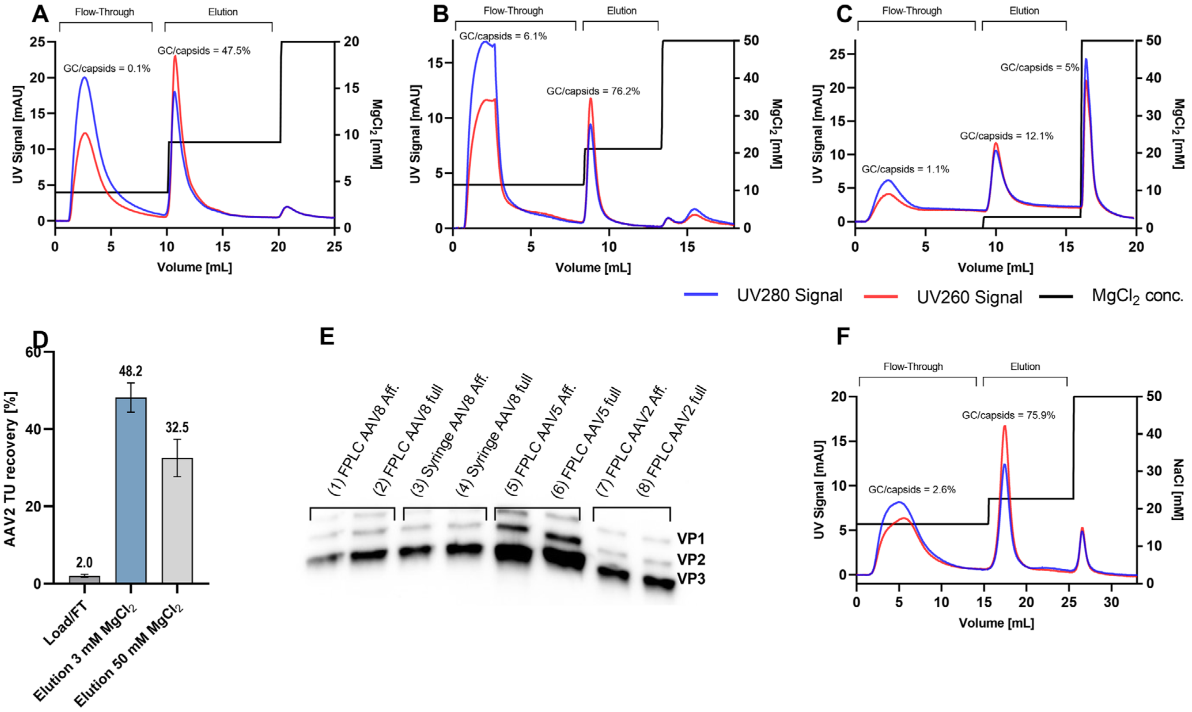

FIGURE 3 | Chromatographic profiles of monolithic PrimaS and QA-based flow-through separation of full and empty AAV capsids. Panels A–C show the flow-through polishing for the separation of full from empty AAV capsids for AAV8, AAV5, and AAV2 using the PrimaS. The $MgCl_2$ concentration during sample application was adjusted to 3.6 mM for AAV8, 11.6 mM for AAV5, and 0.1 mM for AAV2. Panel D shows the potency ($n = 3$) of AAV2 following the flow-through polishing. Additionally, a western blot analysis is shown in Panel E, using a monoclonal antibody against the AAV capsid proteins VP1-3, to validate the integrity of the capsid proteins post-flow-through polishing. Affinity-purified AAV material is represented in lanes 1, 3, 5, and 7, while the corresponding full AAV elution peaks are shown in lanes 2, 4, 6, and 8. Panel F shows the flow-through polishing for the separation of full from empty AAV8 capsids using the CIMmic QA. Aff. indicates affinity-purified AAV material; FPLC, fast protein liquid chromatography; FT, flow-through; GC, genomic copies; TU, transducing unit; VP, viral protein.

and VP3 were maintained both before and after-flow-through polishing. The capsid composition of AAV remained unchanged throughout the flow-through the polishing process.

Sartobind Q and PrimaS differ in both their stationary phases and ligands. To enable a direct comparison between MA and monoliths—both of which utilize a quaternary amine as the ligand—we conducted an additional flow-through polishing experiment using a CIMmic QA monolith with AAV8 (Figure 3F). Again, detailed process parameters can be found in Table 1 in the supplemental material. The CIMmic QA-based AAV8 flow-through polishing was performed at 15.9 mM $MgCl_2$, with the elution of full AAV8 capsids at 22.6 mM $MgCl_2$. The GC/capsid ratio decreased from 14.4% in the feed to 2.6% in the flow-through, while it increased to 75.9% in the elution fraction. This corresponds to an enrichment factor of 5.3 for the genome-containing AAV.

3.4 | FPLC-Independent Flow-Through Separation of Full From Empty AAV Capsids

The flow-through polishing conditions established for AAV8 in sections 3.2 and 3.3 using an FPLC were then adapted to an FPLC-independent system, utilizing separate syringes with varying $MgCl_2$ concentrations for each step (Figure 4). Details of the experimental setup and process information are provided in the supplemental material in Figure S5 and Table S1.

Flow-through polishing was performed at 3.6 mM $MgCl_2$ for PrimaS and at 24.6 mM $MgCl_2$ for Sartobind Q, followed by elution using separate syringes with an $MgCl_2$ concentration of 9.2 and 30.8 mM, respectively. Utilizing the PrimaS, 71.1% of the capsids were found in the flow-through, and 17.6% in the elution fraction at 9.2 mM $MgCl_2$. In contrast, <1% of VG was detected in the flow-through, while 62.9% of the VG were recovered in the elution fraction at 9.2 mM $MgCl_2$. This resulted in a decrease in the GC/capsid ratio from 10.4% in the feed to 0.1% in the flow-through. Conversely, the elution fraction demonstrated an increase in the GC/capsid ratio to 37.2%, corresponding to an enrichment factor of 3.6 for the genome-containing AAV8 capsids. Manual flow-through polishing of AAV8 with the Sartobind Q yielded a capsid recovery of 57.8% in the flow-through, 7.6% in the wash, and 4.6% in the elution fraction at 30.8 mM $MgCl_2$. A total of 35.8% of the VG were found in the flow-through, 10.4% in the wash, and 25.5% in the 30.8 mM $MgCl_2$ elution fraction. The GC/capsid ratio decreased from 9.3% in the starting material to 5.6% in the flow-through, while the elution

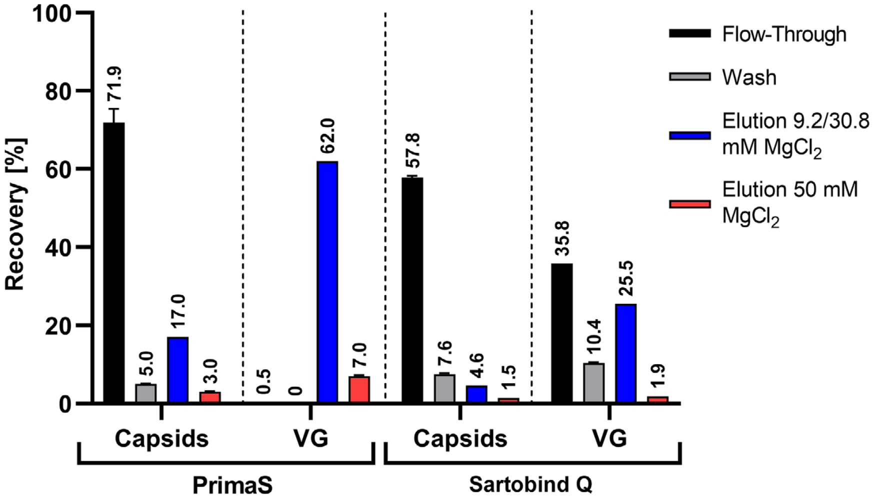

FIGURE 4 | Syringe-driven flow-through polishing of AAV8. Flow-through polishing of AAV8 was performed using either a PrimaS column or a Sartobind Q membrane adsorber. During sample application, the $MgCl_2$ concentration was adjusted to 3.6 mM for the PrimaS and 24.6 mM for the Sartobind Q. Elution of full AAV8 was achieved by using a separate syringe with an $MgCl_2$ concentration of 9.2 mM for the PrimaS and 30.8 mM for the Sartobind Q. A final elution was performed with 50 mM $MgCl_2$. VG indicates viral genomes.

fraction at 30.8 mM $MgCl_2$ demonstrated a 5.4-fold increase in the GC/capsid to 49.8% Additionally, the integrity of the AAV Capsid was assessed by western blot analysis and confirmed to be maintained throughout the flow-through polishing process, as evidenced in Figures 2E and 3E.

4 | Discussion

AAV is the leading vector platform for in vivo gene therapy [48]. Despite advances in AAV production and purification at larger process scales, there is still a lack of purification methods applicable at smaller laboratory scales. Apart from density gradient centrifugation, there are no easy-to-perform laboratory scale methods for the separation of empty and full AAV particles. Therefore, the objective of this study was to establish an AEX flow-through polishing method for the separation of full and empty AAV that can be adapted to a syringe setup following initial screening with an FPLC. Our flow-through polishing approach was evaluated using two separate AEX matrices and applied to three AAV serotypes, as they are known to differ in achieved titers, GC/capsid ratios, aggregation, and adsorption behavior [22].

In preliminary tests, various monoliths and MA were evaluated for their applicability in separating full and empty AAV (data not shown). The PrimaS monolithic column and the Sartobind Q MA demonstrated the best separation of empty and full AAV peaks for each device category and were selected for further study. These chromatography materials were chosen based on their improved convective mass transfer properties compared to conventional resins, due to their channels and porous structures, which allow for high flow rates and compatibility with syringe-based operations [32, 49]. While the PrimaS column is characterized by a monolithic structure with a multimodal ligand that combines hydrogen bonding with a weak anion exchanger, the Sartobind Q MA is characterized by a quaternary amine ligand and thus a strong anion exchanger. In addition, the monolithic CIMmic QA was used to facilitate direct comparison between monolith and MA. This monolith is also a strong anion exchanger due to the presence of a quaternary amine ligand.

In addition to the AEX matrix, the choice of elution salt is a factor that influences the elution behavior and separation of full and empty AAV. To assess the effect of cation valence on these parameters, we compared the use of NaCl and $MgCl_2$ as elution salts. The resulting chromatograms, illustrated in Figure 1A–D for the Sartobind Q and Figure 1E–H for the PrimaS, indicated a trend toward improved separation of full and empty AAV8 using the divalent cation Mg^{2+} compared to the monovalent Na^+. The variations in elution behavior can be attributed to the ion rather than the conductivity, as the conductivity differed between the $MgCl_2$ and NaCl concentrations required for elution. This trend is consistent with the findings of Joshi et al., who reported improved separation of full and empty AAV5 using divalent salts compared to monovalent chloride salts [46]. A potential rationale for the superior resolution achieved with $MgCl_2$ may be attributed to the stronger chaotropic effect of Mg^{2+} compared to Na^+. Based on the above data, we concluded that $MgCl_2$ is a more effective salt for separating full and empty AAV particles across various serotypes. Consequently, $MgCl_2$ was selected as the salt for the development of our flow-through polishing approach.

The $MgCl_2$ concentrations required for flow-through polishing of AAV8 were determined based on linear gradient and isocratic elution experiments using the Sartobind Q (Figure 1C,D) and PrimaS (Figure 1G,H). Similar experiments were performed for AAV5 and AAV2 (data not shown). The corresponding concentrations are given in Table S1. Due to distinct ligand properties, the $MgCl_2$ concentrations required for the Sartobind Q were higher than for the PrimaS. The $MgCl_2$ concentration needed was found to be influenced by both the ligand and the stationary phase, as well as the specific AAV serotype. For instance, AAV5 consistently required the highest $MgCl_2$ concentrations, followed by AAV8 and AAV2. The different physicochemical properties of the serotypes, particularly the variations in surface charge, underscore the need for serotype-specific protocols to achieve optimal separation of empty and full AAV particles [50–52]. As shown in Figures 2A–C and 3A–C,F, the flow-through polishing approach was successfully established for three different AAV serotypes on two distinct stationary phases. With the Sartobind Q, the genome-containing AAV8 could be enriched by a factor of 5.3 in the corresponding elution fraction with a VG recovery of 18%. For AAV5 and AAV2, full AAV particle enrichment factors of 7 and 4 were achieved with corresponding VG recoveries of 18% and 27%, respectively. In contrast, the use of PrimaS enabled full AAV enrichment factors of 4.6 for AAV8 and 7.5 for AAV5 in the particular full elution fraction, with corresponding VG recoveries of 33% and 42%, which were higher than those achieved with the Sartobind Q. However, the PrimaS was less effective for the flow-through polishing of AAV2 than for AAV8 and AAV5, with a full AAV enrichment factor of 1.9 and a VG recovery of 18% in the full AAV elution fraction. For both PrimaS and Sartobind Q, the lowest full enrichment factors were observed for AAV2. This reduced performance may be attributed to the tendency of AAV2 to aggregate at higher titers [53]. Since a uniform buffer system was used for all serotypes, optimization of the buffer conditions could potentially improve the performance of AAV2 polishing. Furthermore, the different capsid properties and structural variations among AAV serotypes suggest that the three-dimensional conformation of the AAV2 capsid may affect the accessibility of charge sites, thereby influencing its binding properties to the stationary phase [54, 55]. In addition, unlike AAV8 and AAV5, a second and larger elution peak was observed during PrimaS-based flow-through polishing of AAV2 at 50 mM $MgCl_2$, containing approximately 21% of the total loaded VG and exhibiting a GC/capsid ratio (5%) similar to that of the loaded starting material. As shown for AAV8 with the strong AEX monolithic column CIMmic QA (Figure 3F), flow-through polishing of AAV2 might also be achieved using a monolith, given its usual need for elevated salt concentrations.

Flow-through polishing using the Sartobind Q and PrimaS matrices resulted in different outcomes. While the enrichment of genome-containing AAV particles was comparable, the PrimaS demonstrated a higher VG recovery than the Sartobind Q. To allow for a direct comparison between MA and monoliths with the same ligand, the flow-through polishing of AAV8 was also conducted using a CIMmic QA monolith (Figure 3F). Similar to Sartobind Q, the CIMmic QA is a strong anion exchanger. It was observed that the $MgCl_2$ concentrations required for flow-through polishing and elution of full AAV8 were lower (15.9 and 22.6 mM, respectively) compared to those required for Sartobind Q. While the VG recovery of 28% was higher compared to Sartobind Q, the full AAV particle enrichment factors were identical at 5.3. The comparable performance on different stationary phases with the same ligand indicates that the different results between PrimaS and Sartobind Q are more likely due to the different ligands rather than the different stationary phases. The applicability of the flow-through polishing approach was demonstrated across two stationary phases for three serotypes, although limitations were observed for AAV2 using the PrimaS. Based on the data presented in Figures 2 and 3, this method holds promise for application to serotypes beyond AAV8, AAV5, and AAV2, although optimization of $MgCl_2$ concentrations may be required to account for the unique characteristics of each serotype.

During flow-through polishing (Figures 2A-C and 3A,B,F), an additional elution peak was observed upon increasing the $MgCl_2$ concentration to 50 and 20 mM for AAV8 with the PrimaS. This peak is likely capsid debris, potentially derived from low pH elution in the preceding IAC, the freeze-thaw step between IAC and flow-through polishing, or an AEX-derived on-column degradation product, as also observed in previous studies by Lavoie et al. [56] and Wang et al. [24]. According to Lavoie et al., these degradation products are hypothesized to be aggregates of full and empty AAV capsids and can be reduced by using stronger kosmotropic ions. During Sartobind Q flow-through polishing of AAV2 (Figure 2C,D), our findings confirmed that the second elution peak at 50 mM was indeed a degradation product, as it contained only 1.2% of the total transducing units.

Besides the separation of full and empty AAV and their VG recovery, the influence of flow-through polishing on the potency of AAV2 was analyzed by transduction of HEK293T cells (Figures 2D and 3D). As previously reported [57], the HEK293 cell-based transduction assay was exclusively applicable to AAV2, while AVV5 and AAV8 bind to other primary cell receptors and require other cell lines for potency determination [58]. For AAV2 flow-through polishing with the Sartobind Q, neither the flow-through nor the degradation product (50 mM $MgCl_2$ elution) showed any loss of transducing AAV2 particles, with recoveries of 0.9% and 1.2%, respectively. In contrast, the genome-containing AAV2 eluted at 20.2 mM $MgCl_2$ resulted in a 72.1% recovery of transducing units. The potential damage to AAV capsids, which affects viral potency, can be caused by various factors such as shear stress, extreme pH values, and salt concentrations. According to the transducing unit recovery results, the flow-through polishing method established in this work does not negatively affect the potency of AAV2. Given the similar buffers and $MgCl_2$ concentrations used for AAV8 and AAV5, flow-through polishing is not expected to have a negative effect on their potency. Comparable results were obtained with PrimaS flow-through polishing of AAV2, where only 2% of the total transducing units were found in the flow-through. Although flow-through polishing of AAV2 with the PrimaS was not as effective as with the Sartobind Q, elution of the full AAV2 particles at 3 mM $MgCl_2$ resulted in a transducing unit recovery of 48.2%, representing nearly half of the total transducing AAV2 loaded. The second elution peak at 50 mM $MgCl_2$ contained 32.5% of the total transducing units, indicating that this fraction was not exclusively composed of degradation products. This underscores the limited applicability of PrimaS for flow-through polishing in the case of AAV2.

In addition to the preservation of potency, western blot analysis of VP1, VP2, and VP3 in Figures 2E and 3E showed consistent band intensity ratios of 1:1:10 both before and after flow-through polishing. Given that the AAV capsid is typically composed of 60 subunits of VP1, VP2, and VP3 in a ratio of 1:1:10 [2], these data suggest that the novel flow-through polishing method does not result in the selective enrichment of improperly assembled AAV particles. The flow-through polishing method therefore does not affect the integrity of the AAV capsid.

The flow-through polishing conditions established for AAV8 using an FPLC system were then adapted to an FPLC-independent platform using syringes. As depicted in Figure 4, the syringe-based system resulted in a flow-through recovery of 71.9% for the capsids using the PrimaS, compared to a recovery of <1% for the VG. In comparison, 17.6% of capsids and 62.9% of VG were recovered in the elution fraction at 9.2 mM $MgCl_2$, corresponding to a 3.6-fold enrichment of the genome-containing AAV8. Manual flow-through polishing with the Sartobind Q resulted in a lower VG recovery, with only about 1/4 of the VG recovered in the 30.8 mM elution fraction (25.5%). The full AAV8 particles were enriched by a factor of 5.4. However, 35.8% of the genome-containing AAV8 was detected in the flow-through and thus did not bind to the membrane at 24.6 mM $MgCl_2$. By lowering the concentration of $MgCl_2$ used for flow-through polishing, the percentage of full AAV particles that do not bind to the membrane might be reduced. Compared to FPLC-mediated flow-through polishing of AAV8 in Figures 2 and 3, where the enrichment factors of full AAV8 were 4.6 for the PrimaS and 5.3 for the Sartobind Q, manual flow-through polishing achieved comparable full AAV8 enrichment factors of 3.6 and 5.4, respectively. VG recovery was higher with manual flow-through polishing compared to the FPLC-dependent approach for both the PrimaS (62.9% vs. 33%) and the Sartobind Q (25.5% vs. 18%). In summary, the findings support the feasibility of adapting the flow-through polishing approach to a syringe-based system for both PrimaS and Sartobind Q. The FPLC-independent syringe system, exemplified with AAV8, suggests potential applicability to AAV2 and AAV5. Besides that, the AEX-based flow-through polishing method is scalable and may be of interest for larger scale processes as it still relies on a bind-and-elute approach. Furthermore, it enables rapid full-empty separation on a smaller scale without relying on an FPLC, making it a valuable tool for academic research to polish many vector preparations with minimal effort. However, it is important to note that the flow-through polishing conditions must first be screened on an FPLC system before being adapted to a manual setup due to the limited monitoring capabilities of manual setups. In addition to syringes, chromatographic well plates can also be used in the manual setup.

The applicability of the flow-through polishing method depends on the precise alignment of the $MgCl_2$ concentration used in the preceding unit operation for AAV capture with those required for the flow-through polishing step. In this work, the method was demonstrated using $MgCl_2$; however, alternative salts such as NaCl and $MgSO_4$ may also be compatible with this approach [56]. The primary objective of this work was to develop and demonstrate a laboratory scale method that allows optimal separation of full and empty AAV and can also be performed without an FPLC system. The observed recovery rates of the FPLC-mediated flow-through polishing experiments of 18%–42% may be attributed to the small amounts of AAV loaded and the absence of additional buffer additives such as Pluronic-F68. Future work will focus on optimizing recovery and developing an alternative to IAC as a capture step that does not require an FPLC or other high-cost equipment. Furthermore, the robustness of the flow-through polishing approach will be evaluated using different GOIs and feed streams, as both are known to affect chromatographic behavior [39].

The phenomenon of empty AAV capsids passing through during AEX-based polishing was previously observed by Gagnon et al. [59]. In their study, empty AAV capsids did not bind to the stationary phase during sample application at pH 8.5. The authors achieved elution of the full AAV particles by lowering the pH to 7.5 and increasing the ionic strength. In contrast, our novel and innovative approach enables separation of full and empty AAV using only a single buffer system with varying salt concentrations. To the best of our knowledge, the systematic development and use of a flow-through polishing approach for the separation of full and empty AAV particles across multiple serotypes, which even shows the potential to be operated FPLC-independent, has not been reported before.

5 | Conclusion

In this study, we presented a novel laboratory scale flow-through polishing method for the separation of full and empty AAV particles, which holds potential for larger scale processes and is adaptable to a syringe setup without the need for FPLC systems. In conclusion, we found that the use of the divalent salt $MgCl_2$ resulted in better separation behavior than the monovalent salt NaCl and was therefore selected as the salt for our flow-through polishing approach. Furthermore, we demonstrated the efficacy of the flow-through polishing approach on two distinct stationary phases for the three serotypes: AAV8, AAV5, and AAV2. Flow-through polishing led to a 4- to 7.5-fold enrichment of the full AAV and showed limited applicability for AAV2 using the PrimaS. Furthermore, based on transduction experiments and western blot analysis, the flow-through polishing was shown to maintain potency and capsid integrity. The successful adaptation of this method to a syringe-based system, as demonstrated for AAV8, highlights its value as a tool for academic research. Once the appropriate conditions have been identified, it can be performed without specialized equipment and has the potential to facilitate rapid polishing of multiple vector preparations, thereby contributing to the development of novel gene therapies. Future work will focus on further optimization to improve recovery rates and to evaluate the impact of different GOIs and feed stream characteristics on chromatographic behavior.

Author Contributions

Frederik Meierrieks: conceptualization, methodology, investigation, formal analysis, visualization, writing–original draft. **Alisa Weltken**: methodology, investigation, formal analysis. **Karl Pflanz**: supervision. **Andreas Pickl**: supervision, writing–review and editing. **Benjamin Graf**: supervision, writing–review and editing, project administration. **Michael W. Wolff**: supervision, writing–review and editing.

Acknowledgments

This publication is part of a cumulative Ph.D. at "Graduate Centre for Engineering Sciences/Promotionszentrum für Ingenieurswissenschaften" under the aegis of the University of Applied Sciences Mittelhessen, Giessen, Germany. The work was funded by Sartorius Lab Instruments GmbH & Co. KG (Göttingen, Germany). This research did not receive any specific grant from funding agencies in the public, commercial, or not-for-profit sectors.

Conflicts of Interest

The authors declare no conflicts of interest.

Data Availability Statement

Data will be made available on request.

References

1. M. Bin Umair, F. N. Akusa, H. Kashif, et al., “Viruses as Tools in Gene Therapy, Vaccine Development, and Cancer Treatment,” *Archives of Virology* 167 (2022): 1387–1404.

2. M. Lu, Z. Lee, Y.-C. Lin, et al., “Enhancing the Production of Recombinant Adeno-Associated Virus in Synthetic Cell Lines Through Systematic Characterization,” *Biotechnology and Bioengineering* 121 (2024): 341–354.

3. D. Zhu, D. H. Brookes, A. Busia, et al., “Optimal Trade-off Control in Machine Learning–Based Library Design, With Application to Adeno-Associated Virus (AAV) for Gene Therapy,” *Science Advances* 10 (2024): eadj3786.

4. J.-S. Guan, K. Chen, Y. Si, et al., “Process Improvement of Adeno-Associated Virus Production,” *Frontiers in Chemical Engineering* 4 (2022): 830421.

5. D. Ail, H. Malki, E. A. Zin, and D. Dalkara, “Adeno-Associated Virus (AAV)—Based Gene Therapies for Retinal Diseases: Where Are We?,” *Application of Clinical Genetics* 16 (2023): 111–130.

6. A. Leray, P.-A. Lalys, J. Varin, et al., “Novel Chemical Tyrosine Functionalization of Adeno-Associated Virus Improves Gene Transfer Efficiency in Liver and Retina,” *Biomedicine & Pharmacotherapy* 171 (2024): 116148.

7. D. E. Sabatino, F. D. Bushman, R. J. Chandler, et al., “Evaluating the State of the Science for Adeno-Associated Virus Integration: An Integrated Perspective,” *Molecular Therapy* 30 (2022): 2646–2663.

8. R. W. Atchison, B. C. Casto, and W. M. Hammon, “Adenovirus-Associated Defective Virus Particles,” *Science* 149 (1965): 754–756.

9. T. B. Sant’Anna and N. M. Araujo, “Adeno-Associated Virus Infection and Its Impact in Human Health: An Overview,” *Virology Journal* 19 (2022): 173.

10. M. F. Naso, B. Tomkowicz, W. L. Perry, and W. R. Strohl, “Adeno-Associated Virus (AAV) as a Vector for Gene Therapy,” *BioDrugs* 31 (2017): 317–334.

11. G. Ronzitti, D.-A. Gross, and F. Mingozzi, “Human Immune Responses to Adeno-Associated Virus (AAV) Vectors,” *Frontiers in Immunology* 11 (2020): 670.

12. M. Penaud-Budloo, A. François, N. Clément, and E. Ayuso, “Pharmacology of Recombinant Adeno-Associated Virus Production,” *Molecular Therapy Methods and Clinical Development* 8 (2018): 166–180.

13. A. Bennett, J. Gargas, A. Kansol, et al., “Structural and Biophysical Analysis of Adeno-Associated Virus Serotype 2 Capsid Assembly Variants,” *Journal of Virology* 97 (2023): e0177222.

14. B. Venkatakrishnan, J. Yarbrough, J. Domsic, et al., “Structure and Dynamics of Adeno-Associated Virus Serotype 1 VP1-Unique N-Terminal Domain and Its Role in Capsid Trafficking,” *Journal of Virology* 87 (2013): 4974–4984.

15. B. J. Samelson-Jones and L. A. George, “Adeno-Associated Virus Gene Therapy for Hemophilia,” *Annual Review of Medicine* 74 (2023): 231–247.

16. M. I. Beloukhova, A. N. Lukashev, P. Y. Volchkov, A. A. Zamyatnin, and A. A. Deviatkin, “Robust AAV Genotyping Based on Genetic Distances in Rep Gene That Are Maintained by Ubiquitous Recombination,” *Viruses.* 14 (2022): 1038.

17. M. S. Weinberg, R. J. Samulski, and T. J. McCown, “Adeno-Associated Virus (AAV) Gene Therapy for Neurological Disease,” *Neuropharmacology* 69 (2013): 82–88.

18. B. Balakrishnan and G. R. Jayandharan, “Basic Biology of Adeno-Associated Virus (AAV) Vectors Used in Gene Therapy,” *Current Gene Therapy* 14 (2014): 86–100.

19. E. H. T. M. Ebberink, A. Ruisinger, M. Nuebel, M. Thomann, and A. J. R. Heck, “Assessing Production Variability in Empty and Filled Adeno-Associated Viruses by Single Molecule Mass Analyses,” *Molecular Therapy Methods and Clinical Development* 27 (2022): 491–501.

20. T. Dobrowsky, D. Gianni, J. Pieracci, and J. Suh, “AAV Manufacturing for Clinical Use: Insights on Current Challenges From the Upstream Process Perspective,” *Current Opinion in Biomedical Engineering* 20 (2021): 100353.

21. A. Srivastava, K. M. G. Mallela, N. Deorkar, and G. Brophy, “Manufacturing Challenges and Rational Formulation Development for AAV Viral Vectors,” *Journal of Pharmaceutical Sciences* 110 (2021): 2609–2624.

22. M. Hebben, “Downstream Bioprocessing of AAV Vectors: Industrial Challenges & Regulatory Requirements,” *Cell Gene Therapy Insights* 4 (2018): 131–146.

23. A. L. Hejmowski, K. Boenning, J. Huato, A. Kavara, and M. Schofield, “Novel Anion Exchange Membrane Chromatography Method for the Separation of Empty and Full Adeno-Associated Virus,” *Biotechnology Journal* 17 (2022): e2100219.

24. C. Wang, S. H. R. Mulagapati, Z. Chen, et al., “Developing an Anion Exchange Chromatography Assay for Determining Empty and Full Capsid Contents in AAV6.2,” *Molecular Therapy Methods and Clinical Development* 15 (2019): 257–263.

25. J. Smith, J. Grieger, and R. J. Samulski, “Overcoming Bottlenecks in AAV Manufacturing for Gene Therapy,” *Cell Gene Therapy Insights* 4 (2018): 815–825.

26. J. F. Wright, “AAV Empty Capsids: For Better or for Worse?,” *Molecular Therapy* 22 (2014): 1–2.

27. F. Mingozzi and K. A. High, “Immune Responses to AAV Vectors: Overcoming Barriers to Successful Gene Therapy,” *Blood* 122 (2013): 23–36.

28. K. Gao, M. Li, L. Zhong, et al., “Empty Virions in AAV8 Vector Preparations Reduce Transduction Efficiency and May Cause Total Viral Particle Dose-Limiting Side-Effects,” *Molecular Therapy Methods and Clinical Development* 1 (2014): 20139.

29. S. Kurth, T. Li, A. Hausker, et al., “Separation of Full and Empty Adeno-Associated Virus Capsids by Anion-Exchange Chromatography Using Choline-Type Salts,” *Analytical Biochemistry* 686 (2024): 115421.

30. A. C. Nathwani, E. G. D. Tuddenham, S. Rangarajan, et al., “Adenovirus-Associated Virus Vector–Mediated Gene Transfer in Hemophilia B,” *New England Journal of Medicine* 365 (2011): 2357–2365.

31. F. Mingozzi, M. V. Maus, D. J. Hui, et al., “CD8+ T-Cell Responses to Adeno-Associated Virus Capsid in Humans,” *Nature Medicine* 13 (2007): 419–422.

32. R. Dickerson, C. Argento, J. Pieracci, and M. Bakhshayeshi, “Separating Empty and Full Recombinant Adeno-Associated Virus Particles Using Isocratic Anion Exchange Chromatography,” *Biotechnology Journal* 16 (2021): e2000015.

33. S. A. Nass, M. A. Mattingly, D. A. Woodcock, et al., “Universal Method for the Purification of Recombinant AAV Vectors of Differing Serotypes,” *Molecular Therapy and Methods Clinical Development* 9 (2018): 33–46.

34. A. K. Lam, P. L. Mulcrone, D. Frabutt, et al., “Comprehensive Comparison of AAV Purification Methods: Iodixanol Gradient Centrifugation vs. Immuno-Affinity Chromatography,” *Advances in Cell and Gene Therapy* 2023 (2023): 2339702.

35. M. Lock, M. Alvira, L. H. Vandenberghe, et al., "Rapid, Simple, and Versatile Manufacturing of Recombinant Adeno-Associated Viral Vectors at Scale," *Human Gene Therapy* 21 (2010): 1259–1271.

36. J. El Andari and D. Grimm, "Production, Processing, and Characterization of Synthetic AAV Gene Therapy Vectors," *Biotechnology Journal* 16 (2021): e2000025.

37. J. Gomis-Fons, B. Zee, D. Hurwit, J. Woo, J. Moscariello, and B. Nilsson, "Mechanistic Modeling of Empty-Full Separation in Recombinant Adeno-Associated Virus Production Using Anion-Exchange Membrane Chromatography," *Biotechnology and Bioengineering* 121 (2024): 719–734.

38. D. P. Chen, J. Y. Wei, J. C. Warren, and C. Huang, "Tuning Mobile Phase Properties to Improve Empty and Full Particle Separation in Adeno-Associated Virus Productions by Anion Exchange Chromatography," *Biotechnology Journal* 19 (2024): e2300063.

39. W. R. Keller, A. Picciano, K. Wilson, J. Xu, H. Khasa, and M. Wendeler, "Rational Downstream Development for Adeno-Associated Virus Full/Empty Capsid Separation—A Streamlined Methodology Based on High-Throughput Screening and Mechanistic Modeling," *Journal of Chromatography A* 1716 (2024): 464632.

40. M. K. Aebischer, H. Gizardin-Fredon, H. Lardeux, et al., "Anion-Exchange Chromatography at the Service of Gene Therapy: Baseline Separation of Full/Empty Adeno-Associated Virus Capsids by Screening of Conditions and Step Gradient Elution Mode," *International Journal of Molecular Sciences* 23 (2022): 12332.

41. W. Di, K. Koczera, P. Zhang, D. P. Chen, J. C. Warren, and C. Huang, "Improved Adeno-Associated Virus Empty and Full Capsid Separation Using Weak Partitioning Multi-Column AEX Chromatography," *Biotechnology Journal* 19 (2024): e2300245.

42. O. Khanal, V. Kumar, and M. Jin, "Adeno-Associated Viral Capsid Stability on Anion Exchange Chromatography Column and Its Impact on Empty and Full Capsid Separation," *Molecular Therapy Methods and Clinical Development* 31 (2023): 101112.

43. G. Qu, J. Bahr-Davidson, J. Prado, et al., "Separation of Adeno-Associated Virus Type 2 Empty Particles From Genome Containing Vectors by Anion-Exchange Column Chromatography," *Journal of Virological Methods* 140 (2007): 183–192.

44. T. Okada, M. Nonaka-Sarukawa, R. Uchibori, et al., "Scalable Purification of Adeno-Associated Virus Serotype 1 (AAV1) and AAV8 Vectors, Using Dual Ion-Exchange Adsorptive Membranes," *Human Gene Therapy* 20 (2009): 1013–1021.

45. J. Fan, E. Barbieri, S. Shastry, S. Menegatti, C. Boi, and R. G. Carbonell, "Purification of Adeno-Associated Virus (AAV) Serotype 2 From Spodoptera Frugiperda (Sf9) Lysate by Chromatographic Nonwoven Membranes," *Membranes* 12 (2022): 944.

46. P. R. H. Joshi, A. Bernier, P. D. Moço, J. Schrag, P. S. Chahal, and A. Kamen, "Development of a Scalable and Robust AEX Method for Enriched rAAV Preparations in Genome-Containing VCs of Serotypes 5, 6, 8, and 9," *Molecular Therapy Methods and Clinical Development* 21 (2021): 341–356.

47. F. Meierrieks, A. Pickl, and M. W. Wolff, "A Robust and Efficient Alluvial Filtration Method for the Clarification of Adeno-Associated Viruses From Crude Cell Lysates," *Journal of Biotechnology* 117 (2023): 3199.

48. D. Wang, P. W. L. Tai, and G. Gao, "Adeno-Associated Virus Vector as a Platform for Gene Therapy Delivery," *Nature Reviews Drug Discovery* 18 (2019): 358–378.

49. C. Teepakorn, K. Fiaty, and C. Charcosset, "Comparison of Membrane Chromatography and Monolith Chromatography for Lactoferrin and Bovine Serum Albumin Separation," *Processes* 4 (2016): 31.

50. B. Adams, H. Bak, and A. D. Tustian, "Moving From the Bench Towards a Large Scale, Industrial Platform Process for Adeno-Associated Viral Vector Purification," *Biotechnology and Bioengineering* 117 (2020): 3199–3211.

51. A. M. Davidoff, C. Y. C. Ng, S. Sleep, et al., "Purification of Recombinant Adeno-Associated Virus Type 8 Vectors by Ion Exchange Chromatography Generates Clinical Grade Vector Stock," *Journal of Virological Methods* 121 (2004): 209–215.

52. J. F. Wright, "Manufacturing and Characterizing AAV-Based Vectors for Use in Clinical Studies," *Gene Therapy* 15 (2008): 840–848.

53. J. F. Wright, T. Le, J. Prado, et al., "Identification of Factors That Contribute to Recombinant AAV2 Particle Aggregation and Methods to Prevent Its Occurrence During Vector Purification and Formulation," *American Society of Gene Therapy* 12 (2005): 171–178.

54. V. Rayaprolu, S. Kruse, R. Kant, et al., "Comparative Analysis of Adeno-Associated Virus Capsid Stability and Dynamics," *Journal of Virology* 87 (2013): 13150–13160.

55. M. Mietzsch, A. Jose, P. Chipman, et al., "Completion of the AAV Structural Atlas: Serotype Capsid Structures Reveals Clade-Specific Features," *Viruses* 13 (2021): 101.

56. R. A. Lavoie, J. T. Zugates, A. T. Cheeseman, et al., "Enrichment of Adeno-Associated Virus Serotype 5 Full Capsids by Anion Exchange Chromatography With Dual Salt Elution Gradients," *Biotechnology and Bioengineering* 120 (2023): 2953–2968.

57. F. Meierrieks, A. Kour, M. Pätz, K. Pflanz, M. W. Wolff, and A. Pickl, "Unveiling the Secrets of Adeno-Associated Virus: Novel High-Throughput Approaches for the Quantification of Multiple Serotypes," *Molecular Therapy Methods and Clinical Development* 31 (2023): 101118.

58. H. Zhang, Q. Zhan, B. Huang, Y. Wang, and X. Wang, "AAV-Mediated Gene Therapy: Advancing Cardiovascular Disease Treatment," *Frontiers in Cardiovascular Medicine* 9 (2022): 952755.

59. P. Gagnon, B. Goričar, S. Drmota Prebil, H. Jug, M. Leskovec, and A. Štrancar, "Separation of Empty and Full Adeno-Associated Virus Capsids From a Weak Anion Exchanger by Elution With an Ascending pH Gradient at Low Ionic Strength," *Bioprocessing Journal* 20 (2021): 1–7.

Supporting Information

Additional supporting information can be found online in the Supporting Information section.

AAV Empty/Full Ratio Assessment Using the Octet® AAVX Biosensors

Technical Note

Scope
A rapid, high-throughput assay for analyzing the ratio of empty to full Adeno-Associated Virus (AAV) capsids using Octet® AAVX biosensors during bioprocess development for gene therapy.

Introduction

Adeno-associated virus (AAV) is a leading modality for in vivo gene delivery. Full capsids containing the gene cargo deliver therapeutics to target cells. However, the presence of empty capsids in the AAV drug product can compromise therapeutic efficacy; hence, these need to be detected at different stages of the AAV production cycle. Conventional methods for determining Empty/Full (E/F) ratio, such as analytical ultracentrifugation (AUC), electron microscopy (EM) and chromatography (IEX, SEC) and emerging technologies such as mass photometry or UV-Vis/light scattering have limitations that include lack of throughput, time constraints or work only with purified samples. Methods that measure released viral DNA and total capsids such as dPCR/ELISA require extensive optimization. Therefore, a method that reliably measures crude AAV samples with high throughput is urgently needed.

This Technical Note introduces a method for a rapid, high-throughput E/F ratio determination on the Octet® BLI platform using the Octet® AAVX Biosensors. The method is particularly suited for screening both crude and purified AAV samples in the upstream and downstream bioprocessing stages of AAV development and manufacturing. It analyzes intact viral capsids thereby avoiding the challenges associated with releasing and measuring viral DNA. This method relies on the high precision and consistency of the Octet® AAVX biosensors and it involves the saturation of the biosensor surface with equal amount of AAV particles, effectively normalizing capsid titer between samples. As a result, only one measurement is used to determine E/F ratio, eliminating compounded error — a limitation intrinsic to other methods that rely on accurate determination of both capsid titer and DNA content (two-measurement approaches). While this method can provide absolute quantitation with high precision, under certain circumstances where the signal window may be too small, it is better suited for screening purposes (see the section "Factors that Determine Signal Window and Assay Precision" below).

Principles of AAV E/F Ratio Detection

Octet® Bio-Layer Interferometry (BLI) deciphers light interference between reflections from the molecular layer and an internal reference layer of the biosensor. Analyte binding to biosensor surface changes the thickness and density of the molecular layer, which in turn alters light reflected off it and the interference pattern that ensues. Capitalizing on the fact that empty and full capsids have nearly identical size and protein composition, the Octet® AAV E/F assay saturates the biosensor surface with sufficiently high concentrations of AAV (≥ 2E11 vp/mL) to normalize the thickness factor between samples. As a result, BLI signal difference is solely a result of density difference between bound AAV particles, with samples with a higher percentage of full capsids generating higher signal (Figure 1). A standard curve can be generated from mixtures of Full and Empty reference materials and used to determine the E/F ratio of unknown samples in a typical Octet® BLI dip-and-read assay.

Figure 1: *Schematic of the Octet® AAV E/F Assay Workflow*

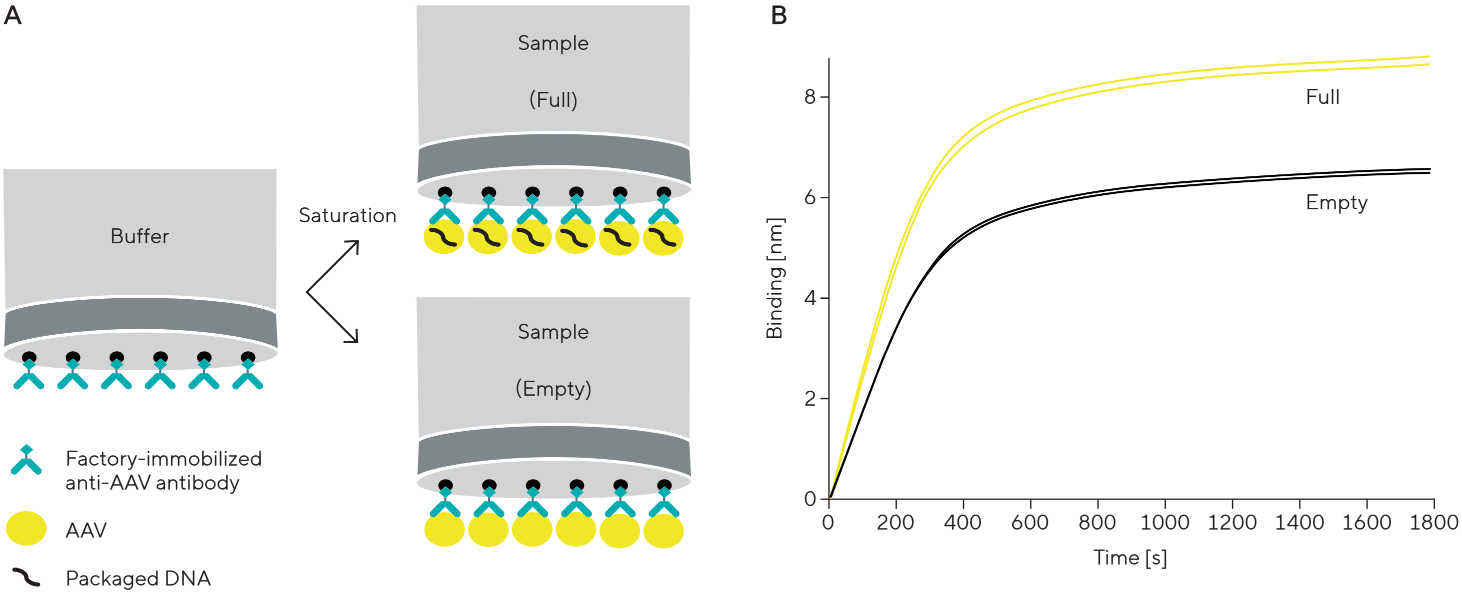

Note. (A) the AAVX biosensor is dipped into an AAV sample (Empty or Full). The unique aspect of the Octet® AAV EF assay is that AAV binding is allowed to reach saturation, at which point the amount of bound AAV is equal between samples, and the signal difference between a test sample and the matching Empty reference material can be attributed solely to density (in turn, E/F ratio) differences. (B) Example of binding response signal of Full (yellow) and Empty capsids (black) normalized to identical capsid titer (N = 2).

Materials Required

- Octet® BLI instrument with Octet® BLI Discovery and Analysis Studio Software, version 13.0.1 or newer

- Octet® AAVX Biosensors (Sartorius Part No. 18-5160)
  - Note: for best results, use the same lot of sensors within the same experiment

- For all Octet® instruments:
  - 96-well, black, flat bottom microplate, Greiner Bio-One Part No. 655209 (Minimum volume: 200 µL)

- Optional for Octet® RH16 and RH96 instruments:
  - 384-well, black, flat bottom, polypropylene microplate, Greiner Bio-One Part No. 781209 (Minimum volume: 80 µL)
  - Octet® 384 Well Tilted bottom Plate, Sartorius Part No. 18-5166 (pack); 18-5167 (case) (Minimum volume: 40 µL)

- Assay Buffer
  - Octet® Sample Diluent (Sartorius Part No. 18-1104) (recommended to dilute purified samples such as AAV reference materials)
  - Custom Assay Buffer (matches the sample matrix as closely as possible, recommended to dilute crude or in-process samples)

- Regeneration solution (10 mM Glycine, pH 1.7, Sartorius Part No. 18-1184)

- Neutralization solution (same as the Assay Buffer of choice)

- AAV Reference Materials to make calibration standards:
  - Capsid titer of the two paired reference materials (Full vs. Empty) needs to be accurately determined by validated methods using Octet® AAVX Biosensors or ELISA.
  - The E/F ratio of the reference materials should be pre-determined by an orthogonal method. There is no minimal requirement of the %Full level of reference materials, so long as they provide a test window to accommodate the expected %Full range of unknown samples.
  - The reference materials should be of the same serotype, contain the same or similarly sized genome (± 0.5 kb), and be produced from the same host cell line as the unknown samples.
  - Empty and Full AAV reference materials of various serotypes are readily available from third-party vendors, commonly with GFP as insert. It is recommended to purchase products with pre-determined capsid titer and E/F ratio. For other insert sizes, users are encouraged to use internally produced AAV as reference.

* Data showcased in this Tech Note were generated using reference materials from Progen (AAV2, 5, 8 produced in HEK293 cells) and Virovek (AAV2, 5, 8 produced in Sf9 cells).

- AAV Samples:
  - Capsid titer requirement to approach binding saturation under 30 minutes: ≥ 2E11 vp/mL for AAV5 or AAV8, ≥ 5E11 vp/mL for AAV2. Lower titer can be used but longer assay time should be expected.
  - Due to high binding variability, this assay is not recommended for AAV9.
  - For serotypes not listed here such as AAV1, AAV3, AAV4, AAV6, AAV7 and AAVrh10, the user is encouraged to determine optimal assay conditions with reference materials.

Assay Steps and Workflow

Step 1	Step 2	Step 3	Step 4
Quantitate sample titer using the AAVX biosensor	Normalize sample titer	Prepare standards from Full and Empty reference materials	Measure sample E/F ratio using the AAVX biosensor
30 min	15 min	30 min	30 min

Step 1: Quantitate Sample Titer Using the Octet® AAVX Biosensor

1. Choose one of the two AAV reference materials (Full or Empty) as the titer standard. The reference material of choice should be close to the expected % Full levels of the samples. For example, if the samples are expected to be 10% Full, the Empty reference should be used as titer standard; if the samples are expected to be 70% Full, the Full reference should be used.
2. Use the AAVX biosensors to determine titer of the unknown samples. Refer to the Technical Note: Octet® AAVX Biosensors for Quantitation of AAV Capsids (1).

Step 2: Normalize Sample Titer

1. Normalize unknown samples to the lowest capsid titer of the set (higher than the minimum titer requirement as outlined in the "Materials Required" section: ≥ 2E11 vp/mL for AAV5 or AAV8, and ≥ 5E11 vp/mL for AAV2). Unknown samples are best diluted in the same buffer that they are already in (referred to as "Custom assay buffer"). An example is provided in the Appendix.
2. Dilute Empty reference material to the same capsid titer as the normalized unknown samples using the same assay buffer. This material is to be analyzed simultaneously with the rest of the samples and to be used as reference for subtraction (referred hereinafter as Matching Reference, see Designing the Assay for more details).

Step 3: Prepare Standards from Full and Empty Reference Materials

The Octet® AAV EF Calculator App (requires Windows Operating System, version 10 or above) can be used to generate mixing scheme of standards with different %Full ratio using the steps below. Note that E/F ratio standards are created by taking two main steps: 1) normalizing capsid titer of the Full and Empty reference materials by diluting each stock in the same diluent, 2) mixing titer-normalized Full and Empty reference sample dilutions at volumes calculated by the EF Calculator App to make user-specified standards.

1. In Parameters tab, enter sample ID, pre-determined percent full value (%) and sample titer (vp/mL) for both Full and Empty reference materials (Figure 2A). Click Next (>>>) to proceed to the Standards tab.
2. In Standards tab, first define the desired normalized titer of standards (in vp/mL), the desired number of standards to construct standard curve, and the desired volume per standard (Figure 2B). Note that the normalized titer should be equal to or above the minimum titer requirement for the particular serotype (see Materials Required).
3. Next, enter desired %Full values at each standard level in Column 1 of the table below, which needs to be a number in-between the %Full value of Full and Empty references as defined in the previous tab (Figure 2B). The mixing volume of titer-normalized Full and Empty reference samples to form each standard (Column 2 and 3, respectively) and the total volume needed for each titer-normalized reference material (second table below) will automatically populate based on user inputs.

4. To prepare reference sample dilutions, enter "Volume to Prepare" based on the calculated "Total Volume Needed" from the step above, taking void volume into consideration according to specific user needs. Based on this, the required volume of reference material stock and diluent will be calculated.
5. To display and save all parameters and mixing scheme for the standards, click Next (>>>) to move to the Results tab. Right click inside the table to copy the %Full values of standards and paste into Octet® BLI Discovery Software under Plate Definition setup (inside the Concentration column of wells corresponding to the standards, see Assay Settings). To save or print the entire window, click Copy to take a screenshot.

Note: the capsid titer of standards does not need to match unknown samples, but each set (standards or unknowns) should maintain constant titer within themselves, each including a Matching Reference for subtraction purpose. This provides the user with flexibility to use a single saved standard curve to calibrate multiple batches of samples whose titer, buffer and experimental date are different, given that 1) the same Empty reference is used to make Matching References for both standards and unknown samples, and 2) assay settings are kept constant between experiments.

Step 4: Measure Sample E/F Ratio Using the AAVX Biosensor

Designing the Assay

One critical aspect of the assay is reference subtraction, in which the binding signal of a Matching Reference is subtracted from the rest of the samples. The subtraction step not only amplifies the relative signal change upon changes in %Full, but more importantly, it serves to normalize such variables as sample titer, buffer matrix, incubation time and experiment day. To properly implement reference subtraction, ensure that enough Empty reference wells are reserved to pair with each sample condition AND each sample read step. It is helpful to adopt the concept of "paired real-time reference subtraction" in assay design, requiring the Empty reference well used for subtraction (subtrahend) matches the samples for which it is to be subtracted from (minuend) as closely as possible in both composition (titer, matrix, volume, etc.) and detection conditions (plate, sensor lot, instrument time). Two examples are given below.

Figure 2: *AAV EF Calculator Interface*

A

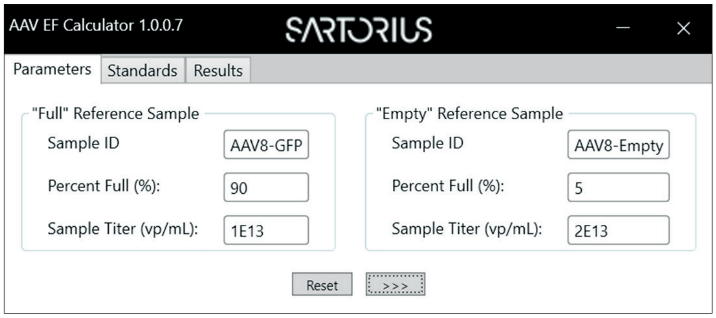

"Full" Reference Sample
Sample ID: AAV8-GFP
Percent Full (%): 90
Sample Titer (vp/mL): 1E13

"Empty" Reference Sample
Sample ID: AAV8-Empty
Percent Full (%): 5
Sample Titer (vp/mL): 2E13

B

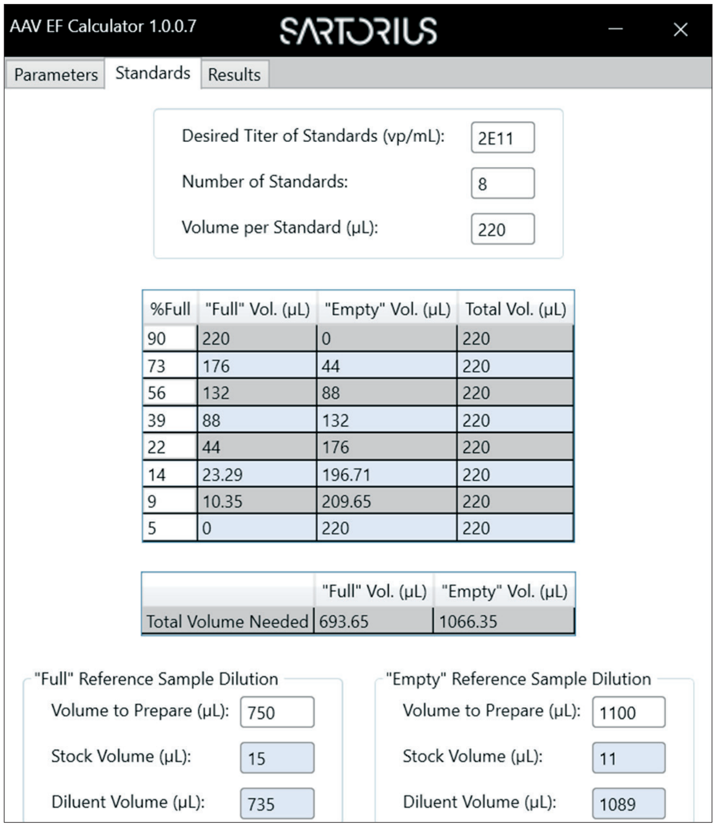

Desired Titer of Standards (vp/mL): 2E11
Number of Standards: 8
Volume per Standard (µL): 220

%Full	"Full" Vol. (µL)	"Empty" Vol. (µL)	Total Vol. (µL)
90	220	0	220
73	176	44	220
56	132	88	220
39	88	132	220
22	44	176	220
14	23.29	196.71	220
9	10.35	209.65	220
5	0	220	220

	"Full" Vol. (µL)	"Empty" Vol. (µL)
Total Volume Needed	693.65	1066.35

"Full" Reference Sample Dilution
Volume to Prepare (µL): 750
Stock Volume (µL): 15
Diluent Volume (µL): 735

"Empty" Reference Sample Dilution
Volume to Prepare (µL): 1100
Stock Volume (µL): 11
Diluent Volume (µL): 1089

Example 1:
If standards are diluted in Sample Diluent to titer A and unknown samples are diluted in cell lysis buffer to titer B, Empty reference diluted in Sample Diluent to titer A should serve as Matching Reference to subtract the standards, while the same Empty reference diluted in cell lysis buffer to titer B should serve as Matching Reference to subtract the unknowns. This is the example applied in Appendix: EXAMPLE WORKFLOW TO DETERMINE E/F RATIO OF AAV8-GFP SAMPLES.

Example 2:
To process 56 samples on the Octet® R8 system, ensure that one of the 8 channels is always reading the Matching Reference during each sample read step. Therefore, instead of designing the assay with 7 read steps (each processing 8 samples), run 8 read steps (each processing 7 samples and one Matching Reference) (Figure 3). This practice eliminates volume (and in turn, concentration) differences between sample read steps due to evaporation, ensuring a fair comparison.

Assay Settings

- In the Octet® BLI Discovery software version 13.0.1 or higher, select appropriate method template by clicking Experiment → New Experiment Wizard → Advanced Quantitation → AAV Quantitation.
- Under the "Plate Definition" tab, enter Sample ID and Replicate Group for standards and unknown samples. Enter %Full values of the standards (from Octet® AAV EF Calculator App) into the respective Concentration fields. Any concentration unit can be used but the actual unit is %Full.
- Ensure that each sample read step contains at least one Matching Reference and change its Type to Reference. Two examples of the Plate Map and Assay Settings are shown in Figure 3 to perform the assay on the Octet® R8 system (A - without regeneration; B – with regeneration). Two additional examples are shown in Figure 8 to perform the assay in high-throughput Octet systems (A - RH16; B- RH96).
- For the baseline step in Assay Buffer, assay time should be set in the range of 60 – 180 s to allow sufficient equilibration.
  - Note: If standards and samples have different matrix, the corresponding assay buffers in baseline wells should also be different to eliminate buffer mismatch between baseline and sample read steps. If this is the case, click on "Modify" under the "Plate Definition" tab to open the "Assay Parameters" window, then navigate to the "Assay Parameters" tab. Change Step Options of Buffer from "Reuse position" to "Use once" so that each baseline well is used only for the corresponding sample reading step.
- For the sample read step, time to reach saturation depends on AAV serotype and concentration. The default assay time of 1800 s is generally sufficient for saturation at the minimum titer requirement (see Materials Required). However, given the complexity of AAV material and titer determination methods, longer or shorter assay time may be optimal and should be evaluated on a case-by-case basis. For example, if shorter assay time such as 15 minutes is desired to accommodate large number of AAV8 samples, the titer needs to be increased to 5E11 vp/mL.
- (Optional) To regenerate biosensors, click on "Modify" under the "Plate Definition" tab to open the "Assay Parameters" window, then navigate to the "Assay Parameters" tab. Change the default Regeneration time from 5 s to 20 s, and the number of regeneration cycles at the "Pre-conditioning sensors" step from 10 cycles to 3 cycles. See Figure 6.

Performing the Assay

- Following the plate layout in the BLI Discovery Software, aliquot assay buffer, titer-normalized samples and | or standards from Assay Step 2 and 3 into corresponding plates.
- Aliquot regeneration and neutralization buffers to corresponding wells (if applicable).
- Confirm that the assay temperature is set to 30 °C under Experiment → Set Plate Temperature.
- Prepare a hydration tray in a 96-well plate by dispensing 200 µL of the matching assay buffer(s) in wells that match the locations of the biosensors and corresponding standard/sample wells in this assay.
- Place the hydration plate in the instrument with or without the plate holder (depending on instrument model). Place the green biosensor tip tray on top of hydration plate.
- Place the prepared sample plate(s) in the instrument.
- Set the delay to 10 minutes to allow the biosensors to hydrate and the samples to warm up to the assay temperature (30 °C).
- In the software select the location where the data should be stored. Click GO button to start the experiment.

Data Analysis

- Open the Octet® Analysis Studio Software version 13.0.1 or higher. Browse and load the data to be analyzed.
- In Preprocessed Data tab, select all wells corresponding to Matching Reference, and confirm or change its type to "Reference".
- Select all and only wells belonging to the same sample read step, of the same titer and share the same matrix, right click and select "Subtract Reference for Selected Wells → By Average".
  a. Note: the "By Average" command works even when only one reference well is present.
- Repeat the same for all other sample read steps/titers/ matrices combinations (if applicable).
- In the Quantitation Analysis tab, select the appropriate Standard Curve Equation to use. Typically, "Linear" or "Dose Response – 4PL unweighted" is suitable.
- Select "End Point" for Binding Rate Equation and verify that saturation is reached at the default or user-specified data analysis read time.
- Once the parameters are set, the standard curve and unknown values will be tabulated automatically.
- (Optional) If using previously saved standards, click "Load Standard" and select the saved Standard Curve File (.fsc) and click Open.
- Click Export button to generate and save a Microsoft Excel report of the data.

Figure 3: *Two examples of Plate Map and Assay Setting on the Octet® R8 Instrument*

A

Advanced Quantitation Experiment - AAVX_8CH_96W

In this step, all the information about the sample plate and its wel
First, check the assay settings. Then highlight one or more wells

Acquisition Rate: Standard (5.0 Hz)

Assay Settings
Assay: Advanced Quantitation
Standard Assay
Single analyte

	Time (s):	Shake speed (rpm):
Buffer	60	1000
Sample	1800	1000

B

Advanced Quantitation Experiment - AAVX_8CH_96W_with Regen

In this step, all the information about the sample plate and its wells
First, check the assay settings. Then highlight one or more wells o

Acquisition Rate: Standard (5.0 Hz)

Assay Settings
Assay: Advanced Quantitation
Standard Assay
Single analyte

	Time (s):	Shake speed (rpm):
Buffer	60	1000
Sample	1800	1000
Regeneration:	20	1000
Neutralization:	5	1000

5 cycles per regeneration
Pre-conditioning Enabled

Note. (A) Plate layout in R8 instrument without regeneration of biosensors. (B) With regeneration. Cyan: standards; Pink: samples; Red: matching reference wells. Assuming each sample read step consists of 8 wells (one column), each reference well is matched to the standards or samples within the same column because they share the same sample read step.

Representative Data

A representative Octet® AAV E/F Assay performed on AAV8 samples with %Full ranging from 9 – 90% is presented. Different %Full levels were obtained by mixing Full and Empty reference materials at different ratio, as designed by the Octet® AAV EF Calculator App. The samples were normalized to 2.5E11 vp/mL in Sample Diluent and captured onto the AAVX biosensor for 30 minutes. Figure 4 shows the binding curves before and after reference subtraction and the standard curve derived from curves post-subtraction. Table 1 shows accuracy (Recovery 100 ± 10%) and precision (%CV) of the 6 standards.

Table 1: *Results of the Octet® E/F Assay Analyzing AAV8 at Different %Full Levels (N = 2)*

Known %Full	**90%**	**73%**	**56%**	**39%**	**22%**	**9%**
Average Calculated %Full	89%	74%	55%	38%	21%	10%
%CV of Calculated %Full	1.8%	1.4%	2.5%	6.7%	8.3%	14.5%
%Recovery*	99%	102%	99%	98%	97%	108%

* Recovery refers to the percentage ratio of determined %Full (mean of two replicates) and theoretical %Full values.

Figure 4: *Representative Octet® AAV E/F Assay Analyzing AAV8*

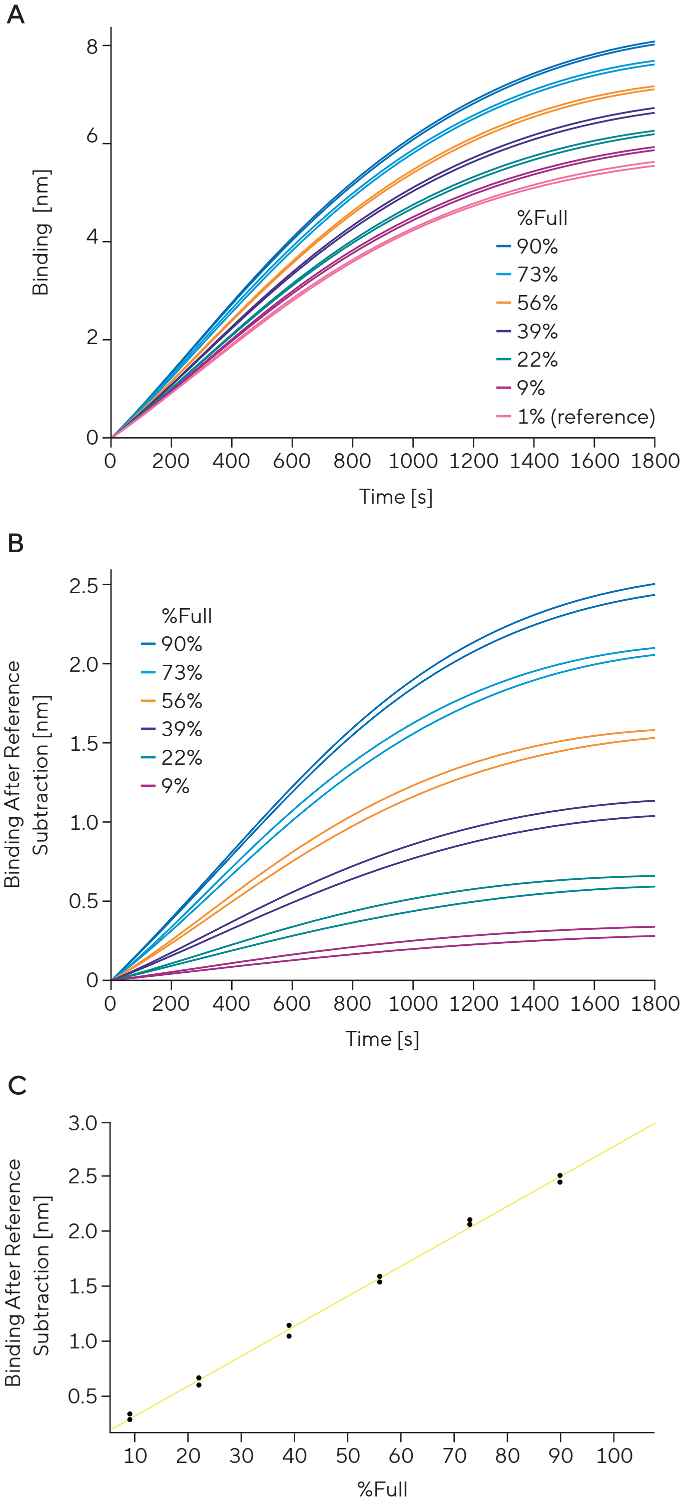

Note. (A) Raw binding traces of AAV8 standards at 90%, 73%, 56%, 39%, 22% and 9% full (N = 2 by the same color). The Empty reference traces are shown in pink. (B) Same dataset as A after reference subtraction. (C) Standard curve generated from end point signal in B using linear fit equation.

Assay Performance

Matrix Compatibility

Table 2: *Octet® AAV E/F Assay is Directly Compatible with Common Matrices in AAV Manufacturing*

Matrix Category	Matrix Type	AAV Serotype tested	Recommended Dilution Factor
Buffer	Octet® Sample Diluent	AAV2/5/8	Neat
Culture media	Chemically defined, protein-free medium (Viral Production Media*, FreeStyle 293 Expression Media*)	AAV5/8	Neat
	DMEM+10% Fetal Bovine Serum	AAV5/8	5-fold in Octet® Sample Diluent
Cell lysis solutions	1x Lysis Buffer with 1% Tween-20 in protein-free culture media	AAV5	Neat
	0.5 M NaCl in protein-free culture media	AAV5/8	Neat
Cell lysate	2 mg/mL HEK293 cell lysate with 1x Lysis Buffer and 0.5 M NaCl	AAV5/8	Neat

* Reagent from Thermo Fisher Scientific

The Octet® AAV E/F Assay analyzes the end point signal and is therefore more tolerant to matrix interference than the Octet® AAV Titer Assay. In addition, matrix effect can be normalized by subtracting a Matching Reference diluted in the same matrix. As a result, most matrices do not require dilution to maintain recovery comparable to the Sample Diluent (Table 2). Taking advantage of this, a single standard curve generated in Sample Diluent can be used to measure samples in different matrices. An example is shown in Figure 5 and Table 3.

Table 3: *Results of the Octet® AAV E/F Assay Analyzing AAV8 in Standards and Spiked Samples with Different %Full Levels (N = 2)*

	Known %Full	90%	73%	39%	22%	14%
Standards (in Octet® Sample Diluent)	Average Calculated %Full (N=2)	90%	72%	41%	21%	14%
	%CV of Calculated %Full (N=2)	1.4%	2.6%	0.3%	9.6%	0.7%
	%Recovery*	100%	99%	104%	94%	102%
Spiked samples (in cell lysate)	Average Calculated %Full (N=2)	84%	70%	38%	20%	14%
	%CV of Calculated %Full (N=2)	1.6%	1.9%	9.9%	15.0%	12.7%
	%Recovery*	93%	96%	97%	93%	98%

* Recovery refers to the percentage ratio of determined %Full (mean of two replicates) and theoretical %Full values.

Note. All standards and samples have a titer of 2.5E11 vp/mL.

Figure 5: *Octet® AAV E/F Assay Analyzing AAV8 in Cell Lysate Matrix Using Standard Curve Generated in the Octet® Sample Diluent*

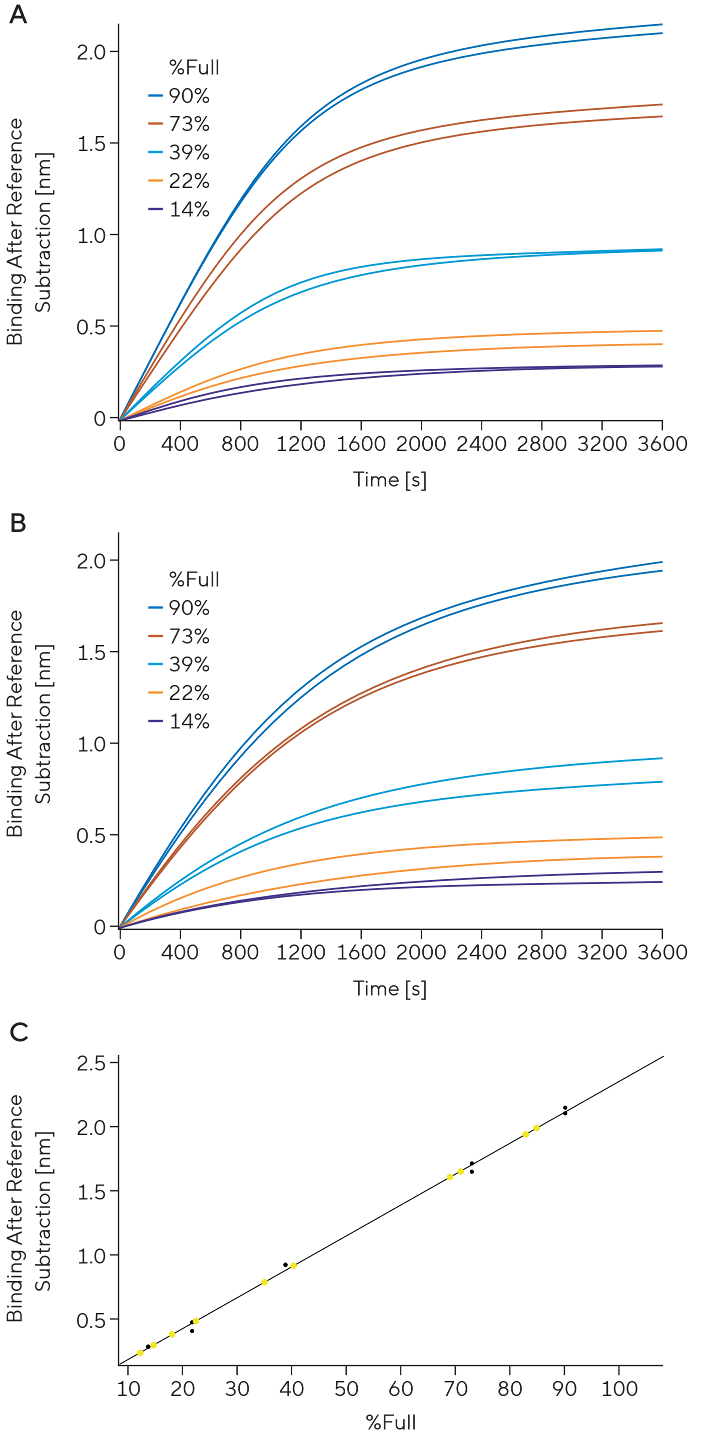

Note. (A) Reference-subtracted binding traces of AAV8 standards at 90%, 73%, 39%, 22% and 14% full (N = 2 by the same color). All standards were diluted in Sample Diluent. (B) Reference-subtracted binding traces of the same AAV8 standards spiked-in to neat HEK293 cell lysate (culture media supplemented with 1% Tween-20 and 0.5 M NaCl) at 1:160 ratio. (C) Spiked samples in B (yellow dots) and standards in A (black dots) generated comparable signal. Calculated %Full of the spiked samples (presented as the average recovery relative to the standards) and %CV is shown in Table 3.

Regeneration of the Octet® AAVX Biosensors for E/F Ratio Measurement

The Octet® AAVX Biosensors can be regenerated and re-used for E/F ratio measurement, providing an efficient and cost-effective solution for high-throughput applications (Table 4). The end point measurement requires more stringent removal of analyte captured in the previous cycle, therefore a modified regeneration scheme from the one outlined in Octet® AAV Titer Assay is recommended. The new scheme consists of 3 regeneration cycles before the experiment starts (pre-conditioning) and 5 regeneration cycles between assay steps. Each regeneration cycle consists of a regeneration step (10 mM glycine, pH 1.7 for 20 seconds) and a neutralization step (assay buffer for 5 seconds), as shown in Figure 6. Note that a Matching Reference should be dedicated to each regeneration round and used to subtract samples from the same sample read step (see Designing the Assay). The number of possible regeneration rounds should be determined by the user as it depends on the sample, buffer and assay conditions used, especially for serotypes that are prone to aggregation. Figure 7 and Table 5 show an example of AAV5 EF assay in which the biosensor is regenerated for 4 rounds.

Figure 6: *Recommended Regeneration Scheme for E/F Ratio Measurement*

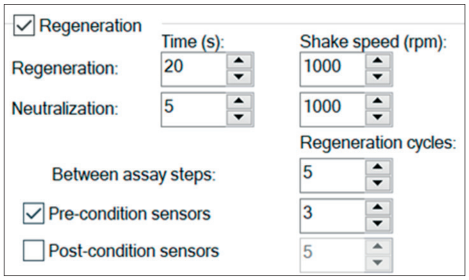
☑ Regeneration

	Time (s):	Shake speed (rpm):
Regeneration:	20	1000
Neutralization:	5	1000

Regeneration cycles:

Between assay steps: 5

☑ Pre-condition sensors 3

☐ Post-condition sensors 5

Table 4: *Regeneration Capacity Towards Different AAV Serotypes.*

AAV serotype	AAV2	AAV5	AAV8
Number of Rounds AAVX Biosensor can be Regenerated	2	4	*2*

Note. Assay buffer: Octet® Sample Diluent; Regeneration buffer: Octet® 10 mM glycine, pH 1.7.

Figure 7: *Octet® AAV E/F Assay with Biosensor Regeneration*

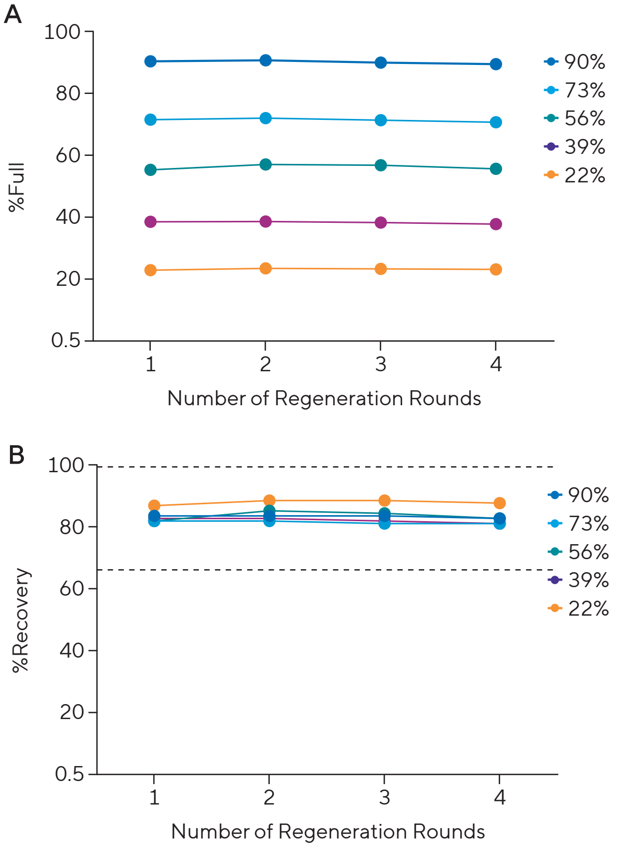

Note. (A) Four replicate wells of each of the five standards (at 90%, 73%, 56%, 39% and 22% full, respectively) were measured by the same biosensor over 4 rounds of regeneration. Round 1 denotes the first sample read step after the biosensors went through pre-conditioning and is used to generate the standard curve using linear fit equation. Rounds 2–4 were treated as unknowns. Calculated %Full values were plotted against the number of rounds of regeneration. (B) The same data plotted as %Recovery relative to the expected %Full.

Table 5: *Results of the Octet® AAV E/F Assay Analyzing AAV5 Samples with Different %Full Levels Over Four Biosensor Regeneration Rounds*

Known %Full	90%	73%	56%	39%	22%
Average Calculated %Full	91%	72%	57%	39%	23%
%CV of Calculated %Full	0.6%	0.7%	1.5%	1.0%	1.2%
%Recovery*	101%	98%	101%	99%	106%

* Recovery refers to the percentage ratio of determined %Full (mean of four replicates) and theoretical %Full values.

Note. All standards and samples have a titer of 2.5E11 vp/mL.

High-Throughput Compatibility

The Octet® AAV EF Assay can be performed on various Octet® BLI Systems, including R8, RH16 and RH96 that offer a wide range of sample throughput capabilities and allow to analyze 96 samples in as little as 30 min. Table 6 shows the comparison of total assay time required to analyze one fully filled 96-well plate depending on the Octet® instrument capacity. As outlined in the Assay Settings section, the assay time should be adjusted based on the AAV titer range. When using the Octet® R2, R4 or R8 system to analyze a large number of samples, it is important to consider the total experiment time. For example, if one fully filled 96-well plate is to be analyzed on the Octet® R8 instrument, the total assay time is 6 hours (30 min per assay x 11 assays). Evaporation resulting from the extended experiment time can be minimized either by using an Octet® Evaporation Cover, or by splitting the samples between two 96-well plates and analyze these plates consecutively. Data from the two plates can then be overlayed in the Octet® Analysis Studio Software for analysis.

Table 6: *Total Time Required to Analyze One Fully Filled 96-Well Plate on the Octet® BLI Platform*

Octet® BLI System (Acquisition Mode)	Octet® R8 (8-channel)	Octet® RH16 (16-channel)	Octet® RH96 (96-channel)
Number of Analyzed Samples in one 96-well plate	77 Samples + 11 Matching Reference + 8 Buffer[#]	90 Samples + 6 Matching Reference[^]	95 Samples + 1 Matching Reference[&]
Assay time × Number of Assays Required	30 min × 11	30 min × 6	30 min × 1
Total Assay Time	6 hours[*]	3 hours	30 min

[#] Figure 3A shows an example layout.
[^] Figure 8A shows an example layout. Buffer on separate plate.
[&] Figure 8B shows an example layout. Buffer on separate plate.
[*] With Octet® Evaporation Cover on; see text for details.

Note. As noted in Designing the Assay, it is highly recommended that at least one well containing Matching Reference is included in each sample read step, therefore the upper limit on the number of samples a 96-plate can accommodate is dependent on the BLI System in use. For example, in Octet® BLI R8, 11 assays are needed to process 77 samples, so at least 11 wells should be reserved to hold Matching Reference, each dedicated to one sample read step.

Figure 8: *Examples of Plate Map and Assay Settings on the High-Throughput Octet® Instruments*

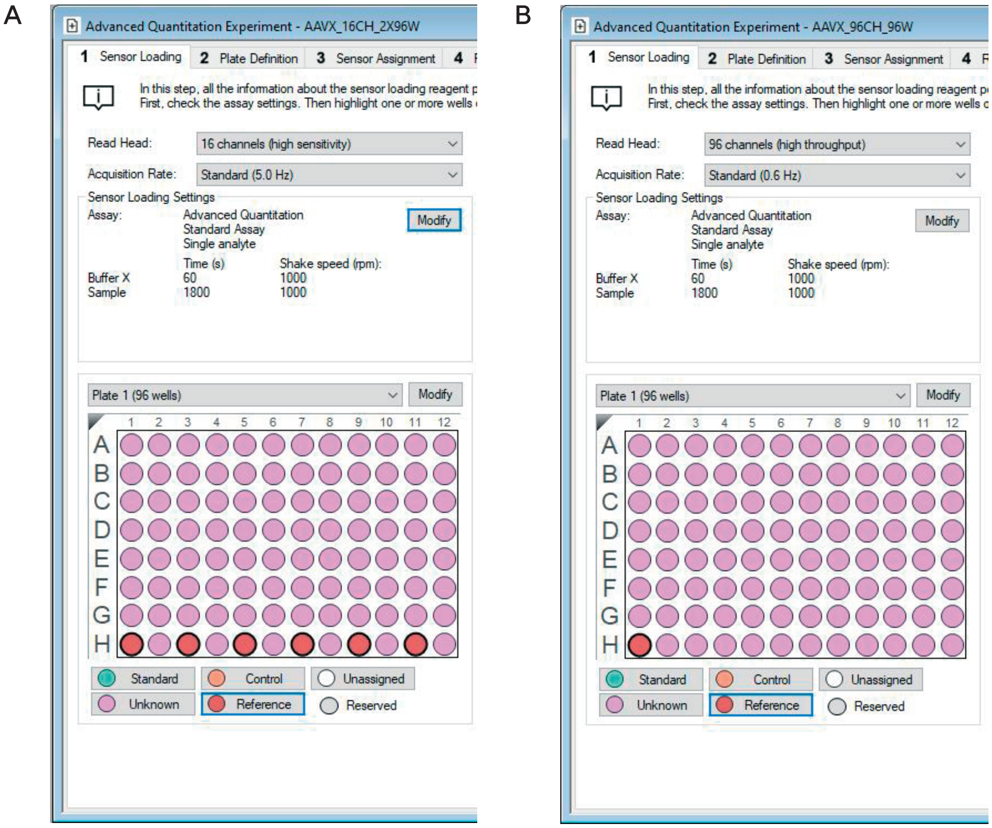

A

Advanced Quantitation Experiment - AAVX_16CH_2X96W

In this step, all the information about the sensor loading reagent p
First, check the assay settings. Then highlight one or more wells

Read Head: 16 channels (high sensitivity)
Acquisition Rate: Standard (5.0 Hz)

Sensor Loading Settings
Assay: Advanced Quantitation
Standard Assay
Single analyte

	Time (s)	Shake speed (rpm):
Buffer X	60	1000
Sample	1800	1000

Plate 1 (96 wells)

B

Advanced Quantitation Experiment - AAVX_96CH_96W

In this step, all the information about the sensor loading reagent p
First, check the assay settings. Then highlight one or more wells c

Read Head: 96 channels (high throughput)
Acquisition Rate: Standard (0.6 Hz)

Sensor Loading Settings
Assay: Advanced Quantitation
Standard Assay
Single analyte

	Time (s)	Shake speed (rpm):
Buffer X	60	1000
Sample	1800	1000

Plate 1 (96 wells)

Note. (A) Plate layout in the Octet® RH16, assuming each sample read step fully utilizes all 16 wells (2 adjacent columns). (B) Plate layout in RH96, assuming each sample read step fully utilizes all 96 wells (whole plate). Pink: samples; Red: matching reference wells. Each reference well is matched to the standards or samples within the same sample read step.

Factors that Determine Signal Window and Assay Precision

The signal window refers to the end point BLI signal difference (in nm) between full and empty reference materials (e.g., Figure 4C, Figure 5C). A bigger signal window provides higher precision and better sensitivity towards the low %Full range. A side-by-side comparison of three AAV serotypes and two DNA insert sizes is shown in Table 7. AAV genome size is the primary factor in determining the signal window, as can be expected by the change in capsid density. Serotype plays a minor role, with AAV2 and AAV5 generating bigger signal window than AAV8. Furthermore, producer cell does not significantly affect the signal window. Typically, samples greater than 20% full generate > 0.5 nm signal window, where CV < 10% can be expected. For samples that generate < 0.5 nm signal window, such as low % full samples or AAV with a small genome, larger variation such as 20–30% CV should be expected. In these scenarios, the assay should not be intended for absolute quantitation. Rather, it is better suited for screening applications where the ranking of candidates is desired.

Table 7: *Signal Window and Precision Comparison*

	2.4 kb AAV Genome (GFP)			**4.4 kb AAV Genome**		
Serotype	**Signal window (Full – Empty, nm)**	**%Full range**	**%CV range of calculated %Full**	**Signal window (Full – Empty, nm)**	**%Full range**	**%CV range of calculated %Full**
AAV2/AAV5	1.9–2.1	> 20% full	2–13%	2.5–2.7	> 20% full	2–9%
		< 20% full	11–25%		< 20% full	12–26%
AAV8	1.3–1.5	> 20% full	9–30%	2.3–2.5	> 20% full	3–12%
		< 20% full	10–20%		< 20% full	15–20%

Note. Each %Full standard was measured by 3–4 biosensors in separate aliquots, from which the standard curve, %Full recovery and CV is calculated. All measurements were made in 384-well microtiter plates in an Octet® BLI RH96 system using the 32-channel high throughput acquisition mode. AAVs with GFP insert produced from either HEK293 or Sf9 cells yield similar results.

Patent pending on methods disclosed in this Technical Note.

References

1. Technical Note: Octet® AAVX Biosensors for Quantitation of AAV Capsids.

Appendix

Example Workflow to Determine E/F Ratio of AAV8-GFP Samples

Goal: to rank E/F ratio of five crude cell lysate samples expressing AAV8-GFP (named Unknown 1 – 5), the %Full of which is expected to be < 20%.

1. Locate the Octet® instrument and AAVX biosensors.

Decision point (instrument choice): Throughput of the Octet® system impacts total assay length and design factors such as plate format, number of replicates and assay volume. See Materials Required for details. In this example, only Octet® R8 is available.

2. Locate Full & Empty AAV8 reference materials.
   a. Full: AAV8-GFP, 90% full (determined by third party), capsid titer of 1E13 vp/mL (determined by Octet® AAVX or ELISA)
   b. Empty: AAV8-Empty, 5% full (determined by third party), capsid titer of 2E13 vp/mL (determined by Octet® AAVX or ELISA)
3. Choose one of the two reference materials as titer standard for Octet® AAV Titer Assay.

Decision point (titering reference choice): Since unknown samples have expected %Full of < 20%, empty reference is better suited as the standard than the Full reference.

4. Create serial dilutions of the Empty reference and of each unknown samples in Octet® Sample Diluent (SD) buffer, according to instructions of Technical Note: Octet® AAVX Biosensors for Quantitation of AAV Capsids (1).
5. Run AAV Titer Assay and analyze data following instructions (1).
6. Record titer of each unknown sample:
   i. Unknown 1: 4E11 vp/mL
   ii. Unknown 2: 6E11 vp/mL
   iii. Unknown 3: 8E11 vp/mL
   iv. Unknown 4: 1E12 vp/mL
   v. Unknown 5: 1E11 vp/mL
7. Normalize capsid titer among unknown samples and a Matching Reference.

Decision point (sample titer choice): For AAV8, a minimum titer of 2E11 vp/mL is recommended to reach binding saturation in 30 min (see Materials Required). While assay time can be extended to accommodate lower titer, in this example the decision is to keep sample read time at 30 min to allow running multiple assays from the same sample plate and keep evaporation to minimum (see High Throughput Compatibility). Therefore, Unknown sample 5 is excluded from the rest of the assay due to insufficient titer. Among Unknown samples 1 – 4, the lowest titer of 4E11 vp/mL is chosen as the normalized titer, both for the unknown samples and for the matching Empty reference.

Decision point (sample diluent and volume choice): Since the samples are crude cell lysate themselves, dilutions (if any) are made with mock cell lysate (lysate made with identical lysis buffer on cells not transfected with AAV) to keep matrix constant between samples. In addition, there is no need to dilute the matrix per se because crude cell lysate can be used as neat (see Matrix Compatibility). Samples are titer-normalized to final volume of 420 µL because 200 µL is needed for each replicate well in 96-well plate (the only plate format compatible with Octet® R8, see Materials Required) and two replicates are chosen to provide more confidence in the ranking result (given expected CV of 10 – 20% for this serotype and insert size, see Factors that Determine Signal Window and Assay Precision).

Table 8: *Dilution Scheme to Normalize Sample Titer with the Matching Reference*

Sample	Starting titer (vp/mL)	Normalized titer (vp/mL)	Dilution factor	Vol. of original sample (µL)	Vol. of diluent (µL)	Final vol. (µL)
Unknown 1	4E11	4E11	1x	420	0	420
Unknown 2	6E11	4E11	1.5x	280	140	420
Unknown 3	8E11	4E11	2x	210	210	420
Unknown 4	1E12	4E11	2.5x	168	252	420
Empty reference	2E13	4E11	50x	8.4	411.6	420

8. Prepare EF standards.
   a. Follow Step 3: Prepare Standards from Full & Empty Reference Materials under Assay Steps in this Tech Note to set up mixing scheme using the Octet® EF Calculator App. The exact example is shown in Figure 2.

Decision point (number of standards, titer, diluent, and volume): In this example, 7 standards at %Full ranging from 9–90% were chosen, in addition to the matching Empty reference. If sensor or reagent availability is a concern, the number of standards can be reduced. Since the titers of standards and unknowns do not need to match, standards were mixed at 2E11 vp/mL, the minimum titer recommended for this serotype (see Materials Required Section) for cost saving purpose. For the same reason, dilutions are prepared for only one replicate well at each standard level (220 µL, Figure 2B). In addition, in order to reuse the standard curve for future experiments, standards and their Matching Reference are diluted in the Octet® Sample Diluent.

9. Set up method file to measure E/F ratio. Follow instructions described in Assay Settings under Step 4: Measure Sample E/F Ratio Using AAVX Biosensor to set up experimental method file. An example created for the Octet® R8 instrument is shown in Figure 9.
   a. Ensure that each sample read step has a designated Matching Reference well containing the Empty reference material. See Table 9 for details.
   b. Ensure that the buffer well used in the first "Buffer" read step contains the same matrix as the corresponding sample well in the second "Sample" read step.

Decision point (Buffer step option choice): Due to different matrices being included in this experiment, the buffer wells are not reused but rather set to "Use Once" under Step Options (instead of the default "Reuse position"). See Assay Settings.

Decision point (Biosensor reuse choice): When analyzing AAV8, only 2 rounds of regeneration is recommended (see Regeneration of Biosensor for E/F Ratio Measurement), less than the 3 back-to-back assays required to perform this experiment (Figure 9B). Assuming supply is sufficient, a new biosensor is used here for each sample read instead of going through regeneration.

10. Perform the assay. Follow instructions described in Performing the Assay under Step 4: Measure Sample E/F Ratio Using AAVX Biosensor.
11. Analyze the data. Follow instructions described in Data Analysis under Step 4: Measure Sample E/F Ratio Using the AAVX Biosensor.
    a. Select only the samples and matching reference belonging to the same sample read step to apply reference subtraction. In this example, three such groups exist (Figure 9A).
    b. %Full of Unknown samples 1–4 are calculated automatically based on the standard curve.

Table 9: *Description of the Plate Map and Well Content in Figure 9*

	Samples			Corresponding Buffer well		Sample read step
	Well no.	Titer	Matrix/Buffer	Well no.	Content	Assay no.
Standards 1–7	A1–G1	2E11	SD	A10–G10	SD	1
Empty Ref for Standards	H1	2E11	SD	H10	SD	1
Unknowns 1–4 Rep 1	A2–D2	4E11	Crude cell lysate	A11–D11	Mock cell lysate	2
Empty Ref for Unknowns Rep 1	E2	4E11	Mock cell lysate	E11	Mock cell lysate	2
Unknowns 1–4 Rep 2	A3–D3	4E11	Crude cell lysate	A12–D12	Mock cell lysate	3
Empty Ref for Unknowns Rep 2	E3	4E11	Mock cell lysate	E12	Mock cell lysate	3

Note. It is recommended to prepare samples in quantities sufficient for analysis of two replicates in 96 well plates.

Figure 9: *Method File to Carry Out the Example Experiment Using the Octet® R8 Instrument*

A

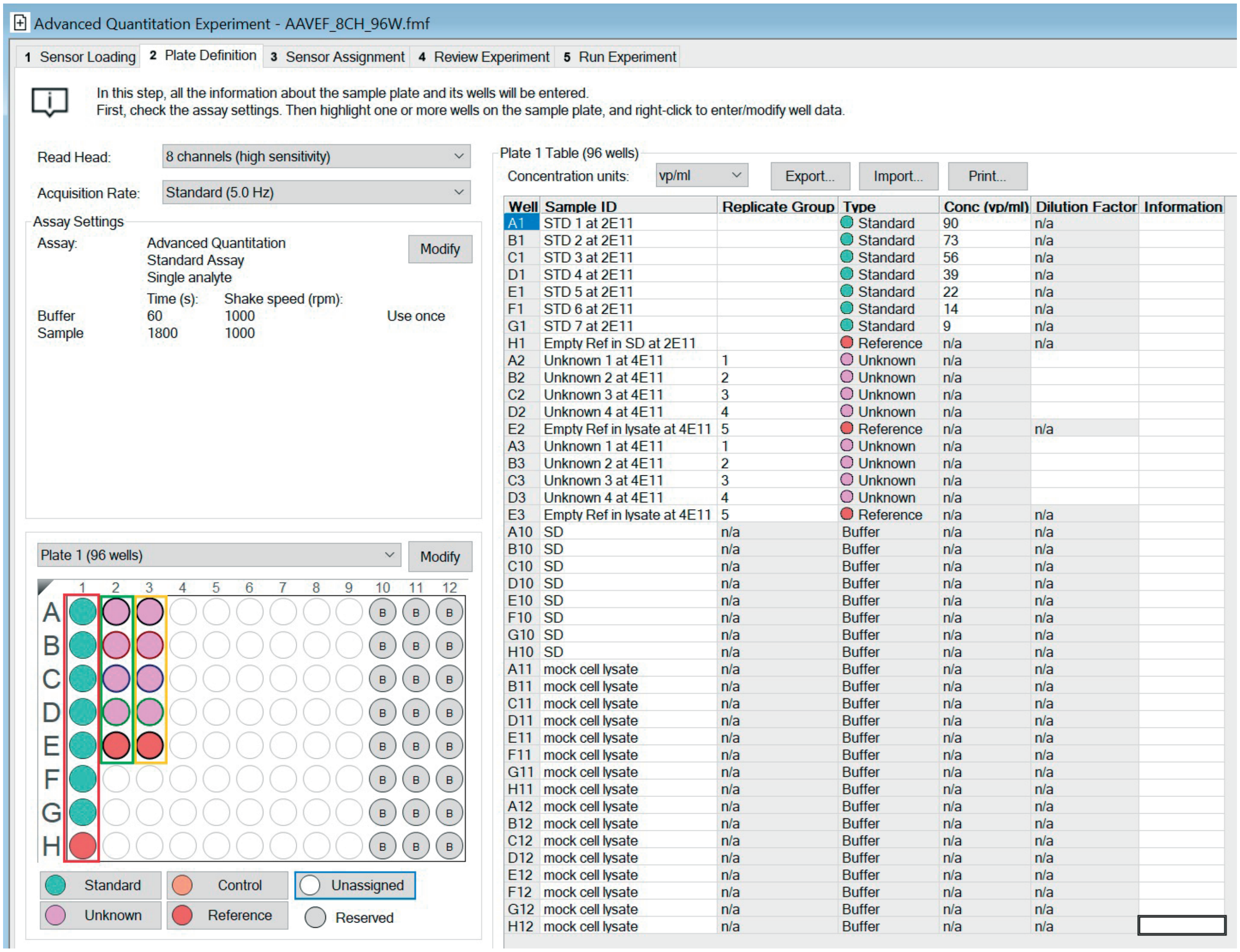

In this step, all the information about the sample plate and its wells will be entered.
First, check the assay settings. Then highlight one or more wells on the sample plate, and right-click to enter/modify well data.

Read Head: 8 channels (high sensitivity)

Acquisition Rate: Standard (5.0 Hz)

Assay Settings

Assay: Advanced Quantitation
Standard Assay
Single analyte

	Time (s):	Shake speed (rpm):	
Buffer	60	1000	Use once
Sample	1800	1000	

Plate 1 Table (96 wells)

Concentration units: vp/ml

Well	Sample ID	Replicate Group	Type	Conc (vp/ml)	Dilution Factor	Information
A1	STD 1 at 2E11		Standard	90	n/a	
B1	STD 2 at 2E11		Standard	73	n/a	
C1	STD 3 at 2E11		Standard	56	n/a	
D1	STD 4 at 2E11		Standard	39	n/a	
E1	STD 5 at 2E11		Standard	22	n/a	
F1	STD 6 at 2E11		Standard	14	n/a	
G1	STD 7 at 2E11		Standard	9	n/a	
H1	Empty Ref in SD at 2E11		Reference	n/a	n/a	
A2	Unknown 1 at 4E11	1	Unknown	n/a		
B2	Unknown 2 at 4E11	2	Unknown	n/a		
C2	Unknown 3 at 4E11	3	Unknown	n/a		
D2	Unknown 4 at 4E11	4	Unknown	n/a		
E2	Empty Ref in lysate at 4E11	5	Reference	n/a	n/a	
A3	Unknown 1 at 4E11	1	Unknown	n/a		
B3	Unknown 2 at 4E11	2	Unknown	n/a		
C3	Unknown 3 at 4E11	3	Unknown	n/a		
D3	Unknown 4 at 4E11	4	Unknown	n/a		
E3	Empty Ref in lysate at 4E11	5	Reference	n/a	n/a	
A10	SD	n/a	Buffer	n/a	n/a	
B10	SD	n/a	Buffer	n/a	n/a	
C10	SD	n/a	Buffer	n/a	n/a	
D10	SD	n/a	Buffer	n/a	n/a	
E10	SD	n/a	Buffer	n/a	n/a	
F10	SD	n/a	Buffer	n/a	n/a	
G10	SD	n/a	Buffer	n/a	n/a	
H10	SD	n/a	Buffer	n/a	n/a	
A11	mock cell lysate	n/a	Buffer	n/a	n/a	
B11	mock cell lysate	n/a	Buffer	n/a	n/a	
C11	mock cell lysate	n/a	Buffer	n/a	n/a	
D11	mock cell lysate	n/a	Buffer	n/a	n/a	
E11	mock cell lysate	n/a	Buffer	n/a	n/a	
F11	mock cell lysate	n/a	Buffer	n/a	n/a	
G11	mock cell lysate	n/a	Buffer	n/a	n/a	
H11	mock cell lysate	n/a	Buffer	n/a	n/a	
A12	mock cell lysate	n/a	Buffer	n/a	n/a	
B12	mock cell lysate	n/a	Buffer	n/a	n/a	
C12	mock cell lysate	n/a	Buffer	n/a	n/a	
D12	mock cell lysate	n/a	Buffer	n/a	n/a	
E12	mock cell lysate	n/a	Buffer	n/a	n/a	
F12	mock cell lysate	n/a	Buffer	n/a	n/a	
G12	mock cell lysate	n/a	Buffer	n/a	n/a	
H12	mock cell lysate	n/a	Buffer	n/a	n/a	

B

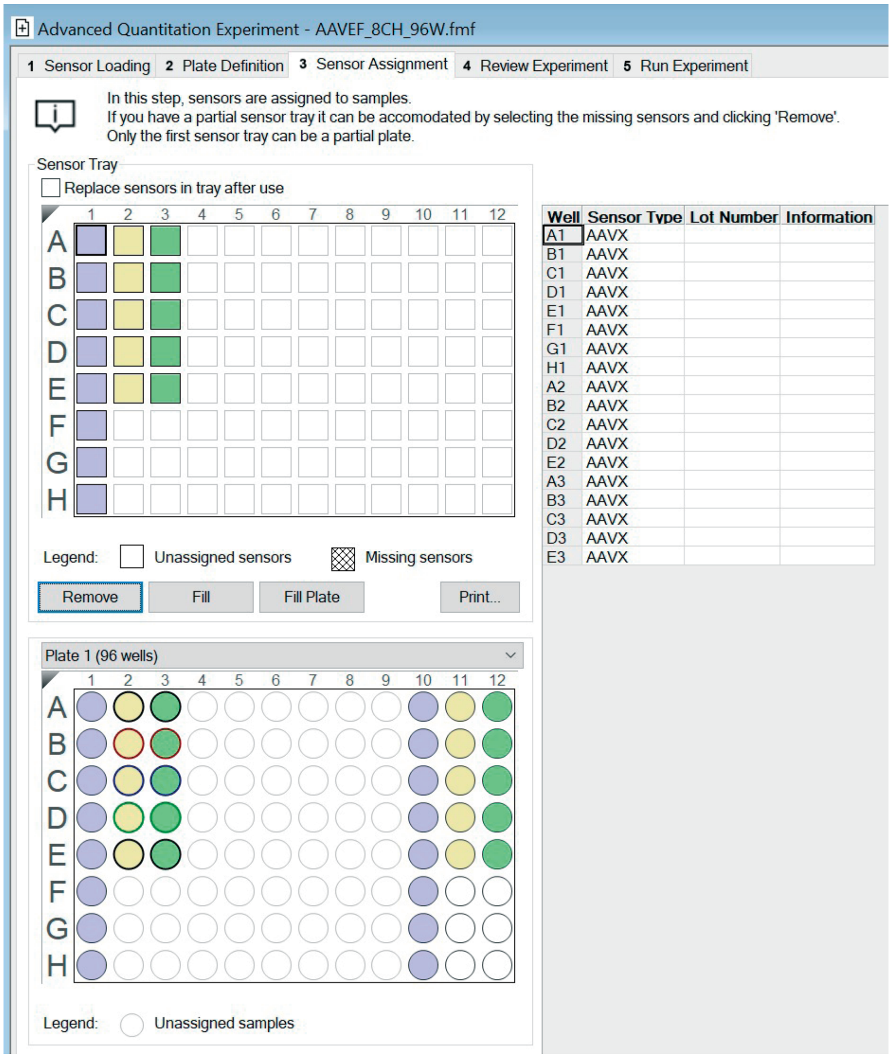

In this step, sensors are assigned to samples.
If you have a partial sensor tray it can be accomodated by selecting the missing sensors and clicking 'Remove'.
Only the first sensor tray can be a partial plate.

☐ Replace sensors in tray after use

Well	Sensor Type	Lot Number	Information
A1	AAVX		
B1	AAVX		
C1	AAVX		
D1	AAVX		
E1	AAVX		
F1	AAVX		
G1	AAVX		
H1	AAVX		
A2	AAVX		
B2	AAVX		
C2	AAVX		
D2	AAVX		
E2	AAVX		
A3	AAVX		
B3	AAVX		
C3	AAVX		
D3	AAVX		
E3	AAVX		

Germany
Sartorius Lab Instruments
GmbH & Co. KG
Otto-Brenner-Straße 20
37079 Göttingen
Phone +49 551 308 0

USA
Sartorius Corporation
565 Johnson Avenue
Bohemia, NY 11716
Phone +1 888 OCTET 75
Or +1 650 322 1360

For further contacts, visit
www.sartorius.com/octet-support

Status: 08 | 2024
Patent Pending


SARTORIUS
OCTET R8

WILEY Analytical Science

Imprint

Senior Account Manager: Joseph Tomaszewski

Editor: Dr. Christene A. Smith, *Wiley Analytical Science*